Observations of Atmospheric Gases Using Fourier Transform Spectrometers

by

Dejian Fu

A thesis
presented to the University of Waterloo
in fulfillment of the
thesis requirement for the degree of
Doctor of Philosophy
in
Chemistry

Waterloo, Ontario, Canada, 2007

AUTHOR'S DECLARATION

I hereby declare that I am the sole author of this thesis. This is a true copy of the thesis, including any required final revisions, as accepted by my examiners.

I understand that my thesis may be made electronically available to the public.

Abstract

Remote sensing of atmospheric gases improves our understanding of the state and evolution of the Earth's environment. At the beginning of the thesis, the basic principles for the retrieval of concentrations of atmospheric gases from spectra are presented with a focus on ground-based observations. An overview of the characteristic features of different platforms, viewing geometries, measurement sites, and Fourier Transform Spectrometers (FTSs) used in the measurements are provided. The thesis covers four main projects.

The first study of the global distribution of atmospheric phosgene was carried out using a total of 5614 measured profiles from the satellite-borne Atmospheric Chemistry Experiment FTS (ACE-FTS) spanning the period February 2004 through May 2006. The phosgene concentrations display a zonally symmetric pattern with the maximum concentration located approximately over the equator, at about 25 km in altitude, and the concentrations decrease towards the poles. A layer of enhanced concentration of phosgene spans the lower stratosphere at all latitudes, with volume mixing ratios of 20-60 pptv. The reasons for the formation of the phosgene distribution pattern are explained by the insolation, lifetime of phosgene and the Brewer-Dobson circulation. The ACE observations show lower phosgene concentrations in the stratosphere than were obtained from previous observations in the 1980s and 1990s due to a significant decrease in source species.

The Portable Atmospheric Research Interferometric Spectrometer for the Infrared (PARIS-IR) is a copy of the ACE-FTS that was designed for ground-based and balloon-borne measurements. The first balloon flight was part of the Middle Atmosphere Nitrogen TRend Assessment (MANTRA) 2004 balloon payload. Some useful engineering information was obtained on the thermal performance of the instrument during the flight. As part of the MANTRA program, a ground-based inter-instrument comparison campaign was conducted with the objective of assessing instrument performance, and evaluating data processing routines and retrieval codes. PARIS-IR provides similar quality results for stratospheric species as does the University of Toronto FTS.

An advanced study was carried out for the Carbon Cycle science by Fourier Transform Spectroscopy (CC-FTS) mission, which is a proposed future satellite mission to obtain a better understanding of the sources and sinks of greenhouse gases in the Earth's atmosphere by monitoring total and partial columns of CO_2, CH_4, N_2O, and CO in the near infrared together with the molecular O_2 column. To evaluate the spectral regions, resolution, optical components, and spectroscopic parameters required for the mission, ground-based Fourier transform spectra, recorded at Kiruna, Kitt Peak, and Waterloo, were used. Dry air volume mixing ratios of CO_2 and CH_4 were retrieved from the ground-based observations. A FTS with a spectral resolution of 0.1 cm^{-1}, operating between 2000 and 15000 cm^{-1}, is suggested as the primary instrument for the mission. Further progress in improving the atmospheric retrievals for CO_2, CH_4 and O_2 requires new laboratory measurements to improve the spectroscopic line parameters.

Atmospheric observations were made with three FTSs at the Polar Environment Atmospheric Research Laboratory (PEARL) during spring 2006. The vertical column densities of O_3, HCl, HNO_3, HF, NO_2, $ClONO_2$ and NO from PARIS-IR, the Eureka DA8 FTS, and the ACE-FTS show good agreement. Chorine activation and denitrification in the Arctic atmosphere were observed in the extremely cold stratosphere near Eureka, Nunavut, Canada. The observed ozone depletion during the 2006 campaign was attributed to chemical removal.

Acknowledgements

I would like to express the sincerest and foremost thanks to my thesis supervisor, Dr. Peter F. Bernath. I feel very fortunate to have had the opportunity to study and work under the supervision of such a distinguished teacher and scientist. His encouragement and patience are indispensable to my successful completion of the Ph.D. His pleasant personality made my graduate study a very enjoyable experience.

I wish to thank other members of my Ph.D. advisory committee, Drs. Robert J. Le Roy, Kaley A. Walker, James P. Martin and Nick C. Westwood, for their suggestions and comments during the course of my Ph.D. I would like to thank Dr. Takayoshi Amano for his kindness to share his invaluable experience on many things. I would also like to thank the Natural Sciences and Engineering Research Council (NSERC) of Canada and Canada Space Agency (CSA) for providing funding support.

I am grateful to Dr. Chris D. Boone for his continuous support during my Ph.D studies, especially, for providing the retrieved phosgene profiles, and giving wonderful suggestions regarding the carbon cycle study. I thank Dr. Keeyoon Sung, who collaborated in the carbon cycle study by providing the results observed at Kitt Peak, and for helpful discussions on the data analysis of the 2006 Canadian Arctic ACE Validation Campaign. I appreciate Dr. Kimberly Strong, Dr. Hans Fast, Richard Mittermeier, Dr. Pierre Fogal, Paul Loewen, Oleg Mikhailov and other members in the 2006 Canadian Arctic ACE Validation Campaign team and all of staff at the Eureka Arctic weather station for their help in making my Arctic experience an exciting one. I thank Dr. Debra Wunch and Jeff Taylor for their generous support during the instrument comparison campaign at the University of Toronto. I also thank Dr. Aldona Wiacek for providing the *a priori* volume mixing ratio profiles of atmospheric gases. I would also like to acknowledge Yony Bresler, Ian Young, and Michelle Seguin, who provided the software to make the balloon-borne measurements of PARIS-IR possible. I thank Felicia Kolonjari for discussion of latitude calculation of sampled atmosphere as shown in the data analysis of the 2006 Canadian Arctic ACE Validation Campaign. I appreciate Dr. Gloria Manney who provided scaled potential vorticity data over Eureka for the 2006 Canadian Arctic ACE Validation Campaign.

I enjoyed my life immensely with Ray Nassar, Iouli Gordon, Michael Dick, Alireza Shayesteh, Philip Sheridan, Jin-Guo Wang and Dominique Appadoo. They were always ready to share their experience whenever I came to them with questions. I thank Sean McLeod for help on a lot of software and for fixing numerous computer problems for me. I thank other current and former members of the Bernath group for their help and friendship.

I had the outstanding luck to marry Shanshan at a key time in my life, when we decided to study in Canada. I thank Shanshan for being a wonderful wife and colleague. Her love, intellect and insight inspire and encourage me to explore the unknown world in my study. Without her, life would not mean much to me.

Finally, I'd like to express my deepest appreciation to my parents, to my sister and to the Chinese community in University of Waterloo for their support and encouragement in every aspect of my life.

For Shanshan

Table of Contents

List of Figures

List of Tables

Chapter 1

Introduction and Theory

1.1 Introduction

Observations of the gaseous constituents of the Earth's atmosphere are important in the study of atmospheric chemistry and in the development of models that can predict the possible evolution of this complicated system. Gases from volcanic eruptions, biomass burning, and industrial sources are perturbing the environment. Conventional atmospheric measurements involve direct sampling, which is not always straightforward or risk-free, and is inconvenient for long-term monitoring. An atmospheric absorption spectrum recorded using the sun as a source contains spectral features that are characteristic of atmospheric composition. The intensity of the observed features provides quantitative information on the constituent concentrations.

In the infrared spectral region, Fourier transform spectrometers (FTSs) are the usual choice for atmospheric remote sensing because of their inherent advantages of high energy throughput and wide spectral coverage, relative to a grating spectrometer with a single detector element. In general, FTSs also have a "multiplex" advantage, at least in the thermal infrared [*Davis et al.*, 2001]. FTSs have been deployed on various satellites and planetary probes [*Persky* 1995; *Kobayashi et al.*, 1999; *Beer* 2006], on balloon gondolas [*Camy-Peyret*, 1995; *Friedl-Vallon et al.*, 2004], and on the ground for volcanic gas measurements [*Oppenheimer et al.*, 1998; 2002] and pollutant emission studies [*Griffiths et al.*, 2000; *Hong et al.,* 2004; *Koehler et al.*, *2001*; *Todd et al.*, 2001]. They are used in long term monitoring programs for atmospheric species that are changing the climate on the Earth [*Griffith et al.*, 2003; *Rinsland et al.*, 2003; *Yang et al.*, 2002; *Washenfelder et al.*, 2003]. Remote sensing from a satellite such as the Atmospheric Chemistry Experiment (ACE) mission [*Bernath et al*., 2005] and the Orbiting Carbon Observatory (OCO) mission [*Crisp et al.*, 2004] can provide a global picture of changes in atmospheric composition. The ACE mission provides temperature and pressure profiles and volume mixing ratio (VMR) profiles with 3-4 km vertical resolution of about 30 atmospheric constituents, as well as of multiple isotopologues of some of these species [*Bernath*, 2006]. The use of spectrometers in space has, in turn, spurred the need for measurements from the ground or balloons, in order to verify the calibration and performance of satellite instruments [*Fu et al.*, 2007; *Fu et al.*, in preparation].

This work describes the remote sensing of atmospheric gases using Fourier transform spectroscopy from satellites, balloons and the ground. In Chapter 2, the characteristic features of observation geometries, platforms and instrumentation used will be introduced. In Chapter 3, the global phosgene observations from ACE, a Canadian satellite mission, are given [*Fu et al.*, 2007]. In Chapter 4, preparation and deployment of PARIS-IR (Portable Atmospheric Research Interferometric Spectrometer for the Infrared) for the MANTRA (Middle Atmosphere Nitrogen TRend Assessment) 2004 balloon campaign are presented. Chapter 5 discusses the ground-based solar absorption studies that have been used to plan for a possible future satellite mission, Carbon Cycle Science by Fourier Transform Spectroscopy (CC-FTS) [submitted to *J. Quant. Spectrosc. Radiat. Trans.*]. In Chapter 6, simultaneous atmospheric measurements from the ground using two Fourier transform infrared spectrometers during the 2006 Canadian Arctic ACE Validation Campaign are presented [*Fu et al.*, in preparation].

Ground-based observations have been used in most of the work in this thesis. Hence, the following sections will describe Fourier transform spectroscopy, spectral lineshapes, simulation of atmospheric absorption spectra, and the retrieval process which is used to obtain concentration information from atmospheric absorption spectra. In the following section, matrices and matrix functions are denoted by bold-face upper-case fonts, vectors by bold-face lower-case, the transpose by a superscript T, and a matrix inverse is denoted by a superscript ‘-1’.

1.2 Fourier Transform Spectroscopy

Fourier transform spectroscopy is a measurement technique in which spectra are collected based on interference of the light from a radiative source. The heart of a FTS is a Michelson interferometer that was first designed about 120 years ago [*Michelson*, 1891; 1892]. A schematic diagram of a Michelson interferometer is presented in Figure 1.1. Radiation from a source such as the sun is split by a beamsplitter into two beams. One beam is reflected off a fixed mirror (M1) and one off a moving mirror (M2) which introduces a time delay. After the two beams recombine at the beamsplitter and interfere with each other, allowing the temporal coherence of the light to be measured at different time delay settings, that is, at different optical path differences. By recording the signal intensity at many discrete positions of the moving mirror, an interferogram is obtained. The spectrum can be obtained by performing a Fourier transform on the interferogram. The principles and development of Fourier transform spectroscopy have been discussed in many books, such as *Griffiths and de Haseth* [1986], *Davis et al.* [2001] and *Thorne et al.* [1991] and hence only a brief description is given here.

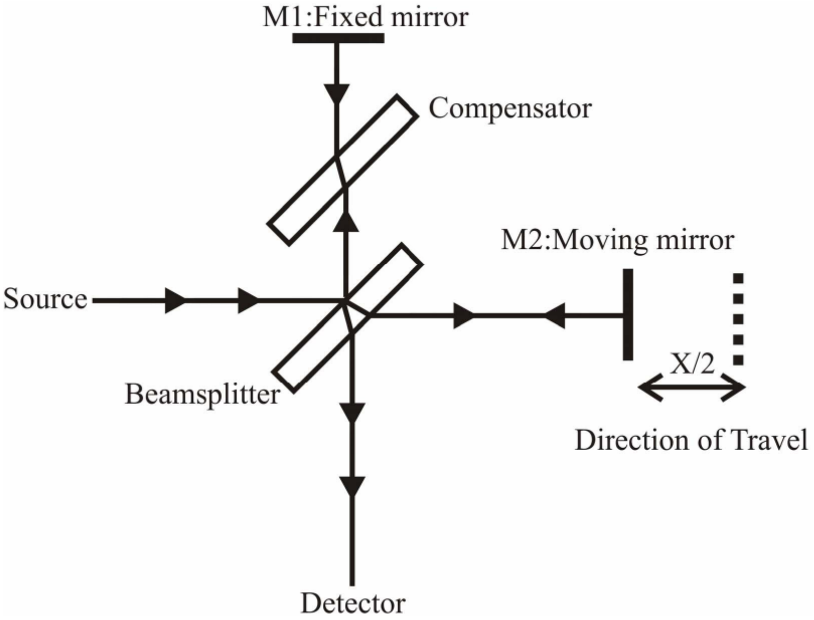

Figure 1.1 A schematic diagram of a classical Michelson interferometer.

When the light source is monochromatic, that is a single frequency, the two beams will interfere at the beamsplitter due to the optical path difference x, and the intensity of the interferogram can be written as

$$\mathrm{I(x)} = \mathrm{B}(\tilde{v})\left[1 + \cos(2\pi\tilde{v}\mathrm{x})\right]. \tag{1.2.1}$$

$\mathrm{B}(\tilde{v})$ is the spectral intensity of the monochromatic source as a function of wavenumber $\tilde{v}$.

When the source is polychromatic, that is, contains more than one frequency, the right hand side of Eq. (1.2.1) needs to be integrated in order to describe the intensity of the interferogram as

$$\mathrm{I(x)} = \int_0^{+\infty} \mathrm{B}(\tilde{v})\left[1 + \cos\left(2\pi\tilde{v}\right)\right] \mathrm{d}\tilde{v} \tag{1.2.2}$$

$$= \int_0^{+\infty} \mathrm{B}(\tilde{v})\mathrm{d}\tilde{v} + \int_0^{+\infty} \mathrm{B}(\tilde{v})\cos(2\pi\tilde{v}\mathrm{x})\, \mathrm{d}\tilde{v}\,. \tag{1.2.3}$$

The first term in the right hand side of Eq. (1.2.3) is the mean intensity of the interferogram, and is constant if the source is stable. The second term, also known as the AC component, contains all the information in the spectrum. Let us define

$$\mathrm{I'(x)} = \int_0^{+\infty} \mathrm{B}(\tilde{v})\cos(2\pi\tilde{v}\mathrm{x})\, \mathrm{d}\tilde{v}\,, \tag{1.2.4}$$

with $\mathrm{B}(\tilde{v}) = 0$ for $\tilde{v} < 0$. Hence, Eq. (1.2.4) can be written as

$$\mathrm{I'(x)} = \int_{-\infty}^{+\infty} \mathrm{B}(\tilde{v})\cos(2\pi\tilde{v}\mathrm{x})\, \mathrm{d}\tilde{v}\,. \tag{1.2.5}$$

To obtain the source spectrum $\mathrm{B}(\tilde{v})$, Fourier transformation gives

$$\mathrm{B}(\tilde{v}) = \int_{-\infty}^{+\infty} \mathrm{I'(x)}\cos(2\pi\tilde{v}\mathrm{x})\, \mathrm{dx}\,. \tag{1.2.6}$$

For real observations, only finite optical path differences can be attained and hence, Eq. (1.2.6) will be rewritten as

$$\mathrm{B}(\tilde{v}) = \int_{-\mathrm{MOPD}}^{+\mathrm{MOPD}} \mathrm{I'(x)}\cos(2\pi\tilde{v}\mathrm{x})\, \mathrm{dx}\,, \tag{1.2.7}$$

where, MOPD stands for maximum optical path difference. The MOPD value depends on the maximum distance that the moving mirror travels in the interferometer. Each FTS has a finite spectral resolution $\Delta\tilde{\nu}$ due to its finite MOPD. For this thesis, the spectral resolution is defined as $\Delta\tilde{\nu} = 0.5/\mathrm{MOPD}$.

1.3 Lineshape Functions

When sunlight travels through the Earth's atmosphere, it can be absorbed by the gaseous species, and in the infrared this absorption is associated with vibration-rotation transitions of molecules. An atmospheric absorption spectrum, which is the solar radiation as a function of wavenumber, contains many absorption features called lines. However, the absorption features do not occur at a single wavelength, and each line has a definite width and characteristic shape. In the atmosphere, line broadening is mainly due to collisions between molecules and to their thermal motions [*Bernath*, 2005].

Doppler broadening is the broadening of spectral lines due to the Doppler effect in which the thermal movement shifts the apparent frequency of each emitter or absorber. The many different velocities of the molecules result in many small shifts, and the combined effect is to broaden the line. The resulting line profile is known as a Doppler lineshape function,

$$g_D(\tilde{\nu} - \tilde{\nu}_0) = \frac{1}{\sqrt{a\pi}} \exp\left(- \frac{(\tilde{\nu} - \tilde{\nu}_0)^2}{a^2} \right) \qquad (1.3.1)$$

$$a = \frac{\tilde{\nu}_0}{c}\sqrt{\frac{2k_B T}{m}} \qquad (1.3.2)$$

which is a Gaussian function, where $\tilde{\nu}_0$ is the wavenumber at the line center, k_B is the Boltzmann constant (1.381×10^{-23}J/K), T is the ambient temperature, m is the molecular mass, and the full width at half maximum (FWHM) of the line is $\Delta\tilde{\nu}_D = a\sqrt{\ln 2}$ [*Bernath*, 2005].

The line broadening that arises from collisions between molecules, either due to the same type of molecule or to different species, can be presented as a Lorentzian lineshape function

$$g_L(\tilde{\nu}-\tilde{\nu}_0)=\frac{1}{\pi}\frac{\Delta\tilde{\nu}_L}{\left(\tilde{\nu}-\tilde{\nu}_0-\delta_L\right)^2+\left(\Delta\tilde{\nu}_L\right)^2}\,, \tag{1.3.3}$$

in which $\tilde{\nu}_0$ is the line center at zero pressure, δ_L is a line position shift, and $\Delta\tilde{\nu}_L$ is the line width parameter. For air at temperature T and pressure p, the line width is

$$\Delta\nu_L(T,p)=\left(\frac{T_0}{T}\right)^{n_{air}}\left[\gamma_{air}(T_0,p_0)(p-p_s)+\gamma_{self}(T_0,p_0)p_s\right]\,. \tag{1.3.4}$$

In Eq. (1.3.3), $\delta_L=\delta_{air}p$ is line shift with δ_{air} the line shift parameter in air measured at the reference temperature T_0 (296 K) and pressure p_0 (1 atm). $2\Delta\nu_L$, is the FWHM of the Lorentz lineshape at the specified temperature T and pressure p. In Equation 1.3.4, γ_{air} and γ_{self}, are the air-broadening and self-broadening coefficients, respectively. They are also measured at the reference temperature T_0 (296 K) and pressure p_0 (1 atm); p_s is the partial pressure of the gas that absorbed the solar radiation at wavenumber $\tilde{\nu}$. n_{air} is the temperature exponent coefficient, and its value depends on the nature of the gases in the collision and on the particular transition.

The Voigt lineshape function is the convolution of a Lorentz broadening lineshape and a Doppler broadening lineshape,

$$g_V(\tilde{\nu}-\tilde{\nu}_0)=\int_{-\infty}^{+\infty}g_D(\tilde{\nu}_0'-\tilde{\nu}_0)\,g_L(\tilde{\nu}-\tilde{\nu}_0')\,d\tilde{\nu}_0'\,. \tag{1.3.5}$$

It is a general form that can include purely Lorentz or Doppler broadening lineshapes as limiting cases [*Bernath*, 2005]. The Voigt lineshape function is widely used in atmospheric remote sensing, for example in the SFIT2 retrieval program, which will be described in Section 1.8. For example, at low altitudes, where pressure broadening dominates the lineshape function, $\Delta\tilde{\nu}_L >> \Delta\tilde{\nu}_D$, so $g_D(\tilde{\nu}_0'-\tilde{\nu}_0)\approx\delta(\tilde{\nu}_0'-\tilde{\nu}_0)$ and

$$g_v(\tilde{\nu}-\tilde{\nu}_0)=\int_{-\infty}^{+\infty}g_L\left(\tilde{\nu}-\tilde{\nu}_0'\right)\delta\left(\tilde{\nu}-\tilde{\nu}_0'\right)d\tilde{\nu}_0'=g_L\left(\tilde{\nu}-\tilde{\nu}_0\right). \tag{1.3.6}$$

Lorentz broadening decreases rapidly as the altitude increases due to the exponential decrease in the atmospheric pressure. It becomes comparable to Doppler broadening at about 25 km (for CO_2), and is negligible at about 45 km, that is, $\Delta\tilde{\nu}_L << \Delta\tilde{\nu}_D$. In this limit $g_L(\tilde{v}-\tilde{v}_0^{'}) \approx \delta(\tilde{v}-\tilde{v}_0^{'})$, and

$$g_v(\tilde{v}-\tilde{v}_0) = \int_{-\infty}^{+\infty} g_D\left(\tilde{v}-\tilde{v}_0^{'}\right)\delta\left(\tilde{v}-\tilde{v}_0^{'}\right)d\tilde{v}_0^{'} = g_D\left(\tilde{v}-\tilde{v}_0\right). \qquad (1.3.7)$$

When Lorentz and Doppler broadening are both important, as in the stratosphere, the Voigt lineshape function becomes

$$g_V(\tilde{v}-\tilde{v}_0) = \frac{\Delta\tilde{v}_L}{a^2}\frac{1}{\pi^{3/2}}\int_{-\infty}^{+\infty}\frac{e^{-y^2}}{\left(\Delta\tilde{v}_L/\Delta\tilde{v}_D\right)^2 + \left(y-\left(\tilde{v}-\tilde{v}_0\right)/\Delta\tilde{v}_D\right)^2}dy. \qquad (1.3.8)$$

The absorption coefficient $k_{\tilde{v}}$ is the product of the line strength $S(\tilde{v}_0)$ and lineshape function,

$$k_{\tilde{v}}(\tilde{v}) = S(\tilde{v}_0)\times g_V(\tilde{v}-\tilde{v}_0). \qquad (1.3.9)$$

Line parameters such as $\tilde{v}_0, \gamma_{air}, \gamma_{self}, \delta_{air}$, and n_{air} are measured by many research groups, and are collected in the HITRAN (HIigh-resolution TRANsmission) database [*Rothman et al.*, 2005] and in the GEISA (Gestion et Etude des Informations Spectroscopiques Atmosphériques) database [*Jacquinet-Husson et al.*, 2005].

1.4 Simulation of Atmospheric Absorption Spectra

The transmittance of sunlight through the atmosphere is the ratio of the intensity at the top of the atmosphere (TOA) to the intensity measured at the ground,

$$\tau = \frac{I(\tilde{v})}{I_0(\tilde{v})}. \qquad (1.4.1)$$

Atmospheric absorption is described by the Bouguer-Lambert-Beer law, usually called Beer's law:

$$\tau = \frac{I(\tilde{\nu})}{I_0(\tilde{\nu})} = \exp(-\int_{\text{surface}}^{\text{TOA}} k(\tilde{\nu}, x)\, n_x ds) \qquad (1.4.2)$$

for the transmission due to molecule x with molecular density n_x at wavenumber $\tilde{\nu}$ at position x along the optical path. The optical path, ds, can be calculated by the auxiliary "FSCATM" subroutine [*Gallery et al.*, 1983; *Meier et al.*, 2004] of the SFIT2 algorithm which performs ray tracing calculations by taking account of the effects of atmospheric curvature and refraction. 100 km above sea level is commonly defined as TOA.

The atmospheric absorption spectrum of trace gas x can be calculated using Eq. (1.4.2) if the vertical distribution of the gas x is known. The vertical distribution of gas x can be obtained from balloon or satellite observations. For example, many vertical profiles of more than 30 atmospheric gases are available from the measurements made using the MkIV balloon Fourier transform infrared spectrometer [*Peterson* and *Margitan*, 1995]. The HALogen Occultation Experiment (HALOE) v.19 satellite data provide O_3, HCl, HF, CH_4, H_2O, NO, and NO_2 volume mixing ratio (VMR) profiles [*Russell et al.*, 1994; *Grooß and Russell*, 2005]. In many cases, the vertical distributions of atmospheric gases are given in VMRs as a function of altitude or pressure. They can be easily transformed to number density units (molecules/m^3) using the idea gas equation

$$n_x = \frac{p}{k_B T} C_{vmr}, \qquad (1.4.3)$$

in which k_B is the Boltzmann constant (1.381×10^{-23} J/K) and C_{vmr} (dimensionless) is the VMR value for gas x. The p (in pascal) and T (in K) profiles, which are used in Eq. (1.4.3) and in the previous calculations of absorption coefficients, can be obtained from National Centers for Environmental Prediction (NCEP)/National Center for Atmospheric Research (NCAR) analyses provided by the NASA Goddard Space Flight Centre (GSFC) automailer (science@hyperion.gsfc.nasa.gov) [*McPherson et al.*, 1979; *Kalnay et al.*, 1996] and the Mass-Spectrometer-Incoherent-Scatter model (MSIS-2000) [*Picone et al.*, 2002]. NCEP covers the altitude range from surface to about 50 km, and the output of MSIS is used from 50 km to 100 km.

The total column amount of gas x in the slant optical path from the TOA to the observatory at the surface M_x, can be obtained along the optical path from the integral

$$M_x = \int_{\text{surface}}^{\text{TOA}} n_x(s)\, ds\,. \tag{1.4.3}$$

The vertical total column of gas x, $M_{\text{tot\_x}}$, can be calculated from

$$M_{\text{tot\_x}} = \int_{\text{surface}}^{\text{TOA}} n_x(z) \frac{dz}{ds} ds \tag{1.4.4}$$

using the vertical coordinate, z. If an altitude range is used in the integral of Eq. (1.4.4) instead of from the surface to the top of the atmosphere (e.g. from 10 km to 50 km), a partial vertical column will be obtained for the gas x. In this thesis, total vertical columns and partial columns of several gases are reported in Chapters 4 to 6.

After normalization, an atmospheric absorption spectrum can be used as a transmittance spectrum if the effects of atmospheric scattering and emission can be neglected. This approximation is generally used in the infrared region where atmospheric scattering is relatively weak. The simulated spectra make use of *a priori* VMR profiles, such as those recorded by the MkIV or HALOE instruments, but the observed profiles are expected to be different. By adjusting the simulated profile, the differences between the calculated absorption spectrum and the measured one will be minimized. The final adjusted profile is reported as the VMR profile of gas x. The procedure for finding the desired quantities (VMR vertical distributions of target gas x) from the measured spectra is often called an "inverse problem". In the retrievals employed in Chapters 4 to 6, the Optimal Estimation Method (OEM) developed by *Rodgers* [2000] is used.

1.5 Retrievals Using the Optimal Estimation Method

The retrieval of a VMR profile for an atmospheric gas from a ground-based solar absorption spectrum is inherently an ill-posed problem. This is because the spectral absorption features contain only enough information to determine the gas concentrations in a few independent vertical layers, while the atmosphere must be modeled with about 30 layers to minimize severe errors in the simulated spectra due to possible misrepresentation of physical conditions such as p and T in the atmosphere. The vertical resolution of ground-based observations is limited by many factors such as the observation geometry and the maximum spectral resolution. The OEM provides a suitable procedure to solve the under-determined problem of deriving a VMR profile from an observed absorption spectrum.

In the OEM formulation of atmospheric sounding, the *a priori* VMR, $\mathbf{x}_\mathbf{a}$, which is an n dimensional state vector, contains VMR values of the target gas on a specified altitude grid obtained from previous observations. The m-dimensional measurement vector **y** contains the measured spectral intensities in the wavenumber domain, while the vector **x** contains the observed vertical VMR values of the target gas. The forward model **F**(**x**, **b**) relates the state vector **x** to the measurement vector **y** through

$$\mathbf{y} = \mathbf{F}(\mathbf{x},\mathbf{b}) + \boldsymbol{\varepsilon}, \tag{1.5.1}$$

in which, **b** are parameters used in the forward model, such as the spectroscopic parameters and temperature profiles, and **ε** is the random spectral measurement noise. The goal is determine the profile **x** from the spectrum, **y**.

Eq. (1.5.1) can be linearized about the *a priori* state, $\mathbf{x}_\mathrm{a}$, which is taken as the reference state,

$$\mathbf{y} = \mathbf{F}(\mathbf{x}_\mathrm{a},\mathbf{b}) + \mathbf{K}(\mathbf{x} - \mathbf{x}_\mathrm{a}) + \boldsymbol{\varepsilon}, \tag{1.5.2}$$

in which, $\mathbf{K} = \partial\mathbf{F}(\mathbf{x},\mathbf{b})/\partial\mathbf{x}$, is an m by n matrix. Eq. (1.5.2) can be further expanded to

$$\mathbf{y} = \mathbf{F}(\mathbf{x}_\mathbf{a},\mathbf{b}_\mathbf{a}) + \frac{\partial\mathbf{F}}{\partial\mathbf{x}}(\mathbf{x} - \mathbf{x}_\mathbf{a}) + \frac{\partial\mathbf{F}}{\partial\mathbf{b}}(\mathbf{b} - \mathbf{b}_\mathrm{a}) + \boldsymbol{\varepsilon} = \mathbf{F}(\mathbf{x}_\mathbf{a},\mathbf{b}_\mathbf{a}) + \mathbf{K}(\mathbf{x} - \mathbf{x}_\mathbf{a}) + \mathbf{K}_\mathbf{b}(\mathbf{b} - \mathbf{b}_\mathbf{a}) + \boldsymbol{\varepsilon} \tag{1.5.3}$$

by including a linearization about a set of model parameters $\mathbf{b}_\mathrm{a}$. **K** contains the sensitivity of the forward model to the true state of VMR, and $\mathbf{K}_\mathrm{b}$ defines the sensitivity of the forward model to the model parameters. **K** is called the weighting function matrix or Jacobian matrix.

It is possible to determine an inverse model **R** which relates the spectra **y** to the desired estimate of the atmospheric state, $\hat{\mathbf{x}}$:

$$\hat{\mathbf{x}} = \mathbf{R}(\mathbf{y}, \mathbf{b})\,. \tag{1.5.4}$$

The inverse model can also be linearized as

$$\hat{\mathbf{x}} = \mathbf{R}(\mathbf{y}_\mathrm{a}, \mathbf{b}_\mathrm{a}) + \frac{\partial \mathbf{R}}{\partial \mathbf{y}}(\mathbf{y} - \mathbf{y}_\mathrm{a}) + \frac{\partial \mathbf{R}}{\partial \mathbf{b}}(\mathbf{b} - \mathbf{b}_\mathrm{a}) = \mathbf{R}(\mathbf{y}_\mathrm{a}, \mathbf{b}_\mathrm{a}) + \mathbf{G}(\mathbf{y} - \mathbf{y}_\mathrm{a}) + \mathbf{G}_\mathrm{b}(\mathbf{b} - \mathbf{b}_\mathrm{a}) \tag{1.5.5}$$

about the measurement $\mathbf{y}_\mathbf{a}$, which is the expected measured spectrum when the VMR profile in the given atmosphere is $\mathbf{x}_\mathrm{a}$. **G** is an n by m matrix called the gain or contribution function matrix, since it shows the contribution to the solution due to a unit change in the corresponding element of **y**. $\mathbf{G}_\mathrm{b}$ represents the sensitivity of the inverse model to its model parameters.

The retrieved profile $\hat{\mathbf{x}}$ can be related to the true profile $\mathbf{x}$ using a transfer function **T**,

$$\hat{\mathbf{x}} = \mathbf{R}(\mathbf{F}(\mathbf{x}, \mathbf{b}), \mathbf{b}) = \mathbf{T}(\mathbf{x}, \mathbf{b})\,, \tag{1.5.6}$$

by ignoring the errors in the measurements and model parameters.

Eq. (1.5.6) can be linearized about the *a priori* state, $\mathbf{x}_\mathrm{a}$,

$$\hat{\mathbf{x}} = \mathbf{T}(\mathbf{x}_\mathrm{a}, \mathbf{b}) + \frac{\partial \mathbf{T}}{\partial \mathbf{x}}(\mathbf{x} - \mathbf{x}_\mathrm{a}) = \mathbf{T}(\mathbf{x}_\mathrm{a}, \mathbf{b}) + \frac{\partial \mathbf{R}}{\partial \mathbf{F}}\frac{\partial \mathbf{F}}{\partial \mathbf{x}}(\mathbf{x} - \mathbf{x}_\mathrm{a}) = \mathbf{T}(\mathbf{x}_\mathrm{a}, \mathbf{b}) + \mathbf{GK}(\mathbf{x} - \mathbf{x}_\mathrm{a}) \tag{1.5.7}$$

and since $\mathbf{T}(\mathbf{x}_\mathrm{a}, \mathbf{b}) = \mathbf{x}_\mathrm{a}$, Eq. (1.5.7) can be further simplified to

$$\hat{\mathbf{x}} = \mathbf{x}_\mathrm{a} + \mathbf{GK}(\mathbf{x} - \mathbf{x}_\mathrm{a}) = \mathbf{x}_\mathrm{a} + \mathbf{A}(\mathbf{x} - \mathbf{x}_\mathrm{a}) = \mathbf{Ax} + (\mathbf{I} - \mathbf{A})\mathbf{x}_\mathrm{a} \tag{1.5.8}$$

with **A** defined as $\mathbf{GK}$. Thus $\hat{\mathbf{x}}$, which is the solution of the retrieval, is weighted by the n by n matrix $\mathbf{A} = \mathbf{GK} = \frac{\partial \mathbf{R}}{\partial \mathbf{F}}\frac{\partial \mathbf{F}}{\partial \mathbf{x}} = \frac{\partial \hat{\mathbf{x}}}{\partial \mathbf{x}}$. The rows of the square matrix **A** are called the averaging kernel [*Backus and Gilbert*, 1970], and they represent the sensitivity of the retrieved state to the true state. To find the solution $\hat{\mathbf{x}}$, the **G** and **K** matrices need to be determined, since the reference state $\mathbf{x}_\mathbf{a}$ can be easily obtained from previous observations.

The procedure for finding the solution $\hat{\mathbf{x}}$ is to find the probability of obtaining the VMR profile $\mathbf{x}$ from given a measurement $\mathbf{y}$ using Bayes' theorem [*Rodgers*, 2000]:

$$\mathbf{P}(\mathbf{x} \mid \mathbf{y}) = \frac{\mathbf{P}(\mathbf{x}, \mathbf{y})}{\mathbf{P}(\mathbf{y})}. \tag{1.5.9}$$

$\mathbf{P}(\mathbf{x} \mid \mathbf{y})$ is the conditional probability of obtaining **x** given **y**. $\mathbf{P}(\mathbf{y})$ is the probability of obtaining **y,** and $\mathbf{P}(\mathbf{x}, \mathbf{y})$ is joint probability of obtaining **x** and **y**.

Given a VMR profile **x**, the probability of measurement can be written as

$$\mathbf{P}(\mathbf{y} \mid \mathbf{x}) = \frac{\mathbf{P}(\mathbf{x}, \mathbf{y})}{\mathbf{P}(\mathbf{x})}, \tag{1.5.10}$$

or

$$\mathbf{P}(\mathbf{x}, \mathbf{y}) = \mathbf{P}(\mathbf{y} \mid \mathbf{x})\mathbf{P}(\mathbf{x}) . \tag{1.5.11}$$

Combining Eq (1.5.11) and Eq. (1.5.9) gives

$$\mathbf{P}(\mathbf{x} \mid \mathbf{y}) = \frac{\mathbf{P}(\mathbf{y} \mid \mathbf{x})\mathbf{P}(\mathbf{x})}{\mathbf{P}(\mathbf{y})}. \tag{1.5.12}$$

In practice, all observations have experimental error or 'measurement noise', so retrievals must take this into account. The experimental error can be written in terms of probability density functions. For example, consider a single variable z. Our knowledge of the true value of the measured parameter is described by a probability density function $\mathrm{P(z)}$ with mean $\bar{\mathrm{z}}$ and variance σ^2, with

$$\bar{\mathrm{z}} = \int \mathrm{zP(z)\,d\,z} \tag{1.5.13}$$

and

$$\sigma^2 = \int (\mathrm{z} - \bar{\mathrm{z}})^2\, \mathrm{P(z)dz}. \tag{1.5.14}$$

Hence, the probability that z lies in the interval (z, z + dz) is P(z)dz. The form of P(z)dz is almost always taken to be Gaussian,

$$P(z) = N(z-\bar{z},\sigma) = \frac{1}{(2\pi)^{1/2}\sigma}\exp\left[-\frac{(z-\bar{z})^2}{2\sigma^2}\right], \tag{1.5.15}$$

since it is a good approximation for experimental error, and is very convenient for algebraic manipulations [*Rodgers*, 2000].

When the measured quantity is a vector, a probability density function can still be defined over a measurement space $\mathbf{P}(\mathbf{z})$. In this case, $\mathbf{P}(\mathbf{z})\mathrm{d}\mathbf{z}$ gives the probability that the true value of the measurement lies in a multidimensional interval ($\mathbf{z}$, $\mathbf{z}$ + d$\mathbf{z}$) in measurement space. Different elements of a vector may be correlated, as

$$S_{ij} = \mathcal{E}[(z_i-\bar{z}_i)(z_j-\bar{z}_j)] \neq 0, \tag{1.5.16}$$

where S_{ij} is called the covariance of z_i and z_j, and $\mathcal{E}$ is the expected value operator. A matrix denoted by $\mathbf{S}_z$ is used to express the covariance matrix of $\mathbf{z}$. The Gaussian distribution for a vector $\mathbf{z}$ is written as

$$\mathbf{P}(\mathbf{z}) = \frac{1}{(2\pi)^{n/2}|\mathbf{S}_z|^{1/2}}\exp\left[-\frac{1}{2}(\mathbf{z}-\bar{\mathbf{z}})^T\mathbf{S}_z{}^{-1}(\mathbf{z}-\bar{\mathbf{z}})\right]. \tag{1.5.17}$$

Similarly, $\mathbf{P}(\mathbf{x})$, $\mathbf{P}(\mathbf{y})$, and $\mathbf{P}(\mathbf{y}\,|\,\mathbf{x})$ in our case can be described using Gaussian functions as

$$\mathbf{P}(\mathbf{x}) = \frac{1}{(2\pi)^{n/2}|\mathbf{S}_a|^{1/2}}\exp\left[-\frac{1}{2}(\mathbf{x}-\mathbf{x}_\mathbf{a})^T\mathbf{S}_\mathbf{a}{}^{-1}(\mathbf{x}-\mathbf{x}_\mathbf{a})\right], \tag{1.5.18}$$

in which $\mathbf{S}_\mathbf{a}$ is the n by n covariance matrix of the *a priori* VMR, and describes how much the VMR of two layers vary together,

$$\mathbf{P}(\mathbf{y}) = \frac{1}{(2\pi)^{n/2}|\mathbf{S}_\varepsilon|^{1/2}}\exp\left[-\frac{1}{2}(\mathbf{y}-\bar{\mathbf{y}})^T\mathbf{S}_\varepsilon{}^{-1}(\mathbf{y}-\bar{\mathbf{y}})\right], \tag{1.5.19}$$

and

$$\mathbf{P}(\mathbf{y}\,|\,\mathbf{x}) = \frac{1}{(2\pi)^{m/2}|\mathbf{S}_\varepsilon|^{1/2}}\exp\left[-\frac{1}{2}(\mathbf{y}-\mathbf{Kx})^T\mathbf{S}_\varepsilon{}^{-1}(\mathbf{y}-\mathbf{Kx})\right], \tag{1.5.20}$$

respectively [*Rodgers*, 2000]. In Eqs. (1.5.19) and (1.5.20), $\mathbf{S}_\varepsilon$ is the measurement noise covariance matrix, an m by m matrix describing how much the measurement error of two spectral points varies together. The off-diagonal elements in $\mathbf{S}_\varepsilon$ can be assumed to be zero since the measurement errors are mostly independent of each other, i.e., they are random, and the diagonal elements in $\mathbf{S}_\varepsilon$ are usually set to 1/(signal-to-noise ratio)^2.

Using Equations (1.5.12), (1.5.18), (1.5.19) and (1.5.20), one obtains:

$$\mathbf{P}(\mathbf{x}\,|\,\mathbf{y}) = \frac{\exp\left[\frac{1}{2}\left(\mathbf{y}-\overline{\mathbf{y}}\right)^{\mathrm{T}}\mathbf{S}_\varepsilon^{-1}\left(\mathbf{y}-\overline{\mathbf{y}}\right)-\frac{1}{2}\left(\mathbf{y}-\mathbf{K}\mathbf{x}\right)^{\mathrm{T}}\mathbf{S}_\varepsilon^{-1}\left(\mathbf{y}-\mathbf{K}\mathbf{x}\right)-\frac{1}{2}\left(\mathbf{x}-\mathbf{x}_{\mathrm{a}}\right)^{\mathrm{T}}\mathbf{S}_{\mathrm{a}}^{-1}\left(\mathbf{x}-\mathbf{x}_{\mathrm{a}}\right)\right]}{\left(2\pi\right)^{n/2}\left|\mathbf{S}_{\mathrm{a}}\right|^{1/2}}$$

(1.5.21)

and taking the logarithm of Eq. (1.5.21) yields,

$$-2\ln\mathbf{P}(\mathbf{x}\,|\,\mathbf{y}) = \left(\mathbf{y}-\mathbf{K}\mathbf{x}\right)^{\mathrm{T}}\mathbf{S}_\varepsilon^{-1}\left(\mathbf{y}-\mathbf{K}\mathbf{x}\right)+\left(\mathbf{x}-\mathbf{x}_{\mathrm{a}}\right)^{\mathrm{T}}\mathbf{S}_{\mathrm{a}}^{-1}\left(\mathbf{x}-\mathbf{x}_{\mathrm{a}}\right)+\mathrm{C}_1\ , \qquad (1.5.22)$$

in which, C_1 is a constant since it does not depend on **x**. Eq. (1.5.22) is quadratic in **x**, so it must be possible to write

$$-2\ln\mathbf{P}(\mathbf{x}\,|\,\mathbf{y}) = \left(\mathbf{x}-\hat{\mathbf{x}}\right)^{\mathrm{T}}\hat{\mathbf{S}}^{-1}\left(\mathbf{x}-\hat{\mathbf{x}}\right)+\mathrm{C}_2\ . \qquad (1.5.23)$$

Eq. (1.5.22) and Eq. (1.5.23) can be related by equating terms. Equating terms that are quadratic in **x**, gives

$$\mathbf{x}^{\mathrm{T}}\mathbf{K}^{\mathrm{T}}\mathbf{S}_\varepsilon^{-1}\mathbf{K}\mathbf{x}+\mathbf{x}^{\mathrm{T}}\mathbf{S}_{\mathrm{a}}^{-1}\mathbf{x} = \mathbf{x}^{\mathrm{T}}\mathbf{S}^{-1}\mathbf{x} \qquad (1.5.24)$$

and hence,

$$\mathbf{S}^{-1} = \mathbf{K}^{\mathrm{T}}\mathbf{S}_\varepsilon^{-1}\mathbf{K}+\mathbf{S}_{\mathrm{a}}^{-1} \qquad (1.5.25)$$

Likewise, equating the terms linear in $\mathbf{x}^{\mathrm{T}}$ using Eq. (1.5.22) and Eq. (1.5.23), gives

$$\left(-\mathbf{K}\mathbf{x}\right)^{\mathrm{T}}\mathbf{S}_\varepsilon^{-1}\left(\mathbf{y}\right)+\left(\mathbf{x}\right)^{\mathrm{T}}\mathbf{S}_{\mathrm{a}}^{-1}\left(-\mathbf{x}_{\mathbf{a}}\right) = \mathbf{x}^{\mathrm{T}}\mathbf{S}^{-1}\left(-\hat{\mathbf{x}}\right) \qquad (1.5.26)$$

and removing the $\mathbf{x}^{\mathrm{T}}$ in Eq. (1.5.26) gives

$$\mathbf{K}^{\mathrm{T}}\mathbf{S}_{\varepsilon}^{-1}\mathbf{y}+\mathbf{x}^{\mathrm{T}}\mathbf{S}_{\mathrm{a}}^{-1}\mathbf{x}_{\mathrm{a}}=\mathbf{S}^{-1}\hat{\mathbf{x}} \tag{1.5.27}$$

Substituting Eq. (1.5.25) into Eq. (1.5.27) gives

$$\mathbf{K}^{\mathrm{T}}\mathbf{S}_{\varepsilon}^{-1}\mathbf{y}+\mathbf{x}^{\mathrm{T}}\mathbf{S}_{\mathrm{a}}^{-1}\mathbf{x}_{\mathrm{a}}=\left(\mathbf{K}^{\mathrm{T}}\mathbf{S}_{\varepsilon}^{-1}\mathbf{K}+\mathbf{S}_{\mathrm{a}}^{-1}\right)\hat{\mathbf{x}} \tag{1.5.28}$$

and hence

$$\begin{aligned}\hat{\mathbf{x}}&=\left(\mathbf{K}^{\mathrm{T}}\mathbf{S}_{\varepsilon}^{-1}\mathbf{K}+\mathbf{S}_{\mathrm{a}}^{-1}\right)^{-1}\left(\mathbf{K}^{\mathrm{T}}\mathbf{S}_{\varepsilon}^{-1}\mathbf{y}+\mathbf{x}^{\mathrm{T}}\mathbf{S}_{\mathrm{a}}^{-1}\mathbf{x}_{\mathrm{a}}\right)\\&=\mathbf{x}_{\mathrm{a}}+\mathbf{S}_{\mathrm{a}}\mathbf{K}^{\mathrm{T}}\left(\mathbf{K}\mathbf{S}_{\mathrm{a}}\mathbf{K}^{\mathrm{T}}+\mathbf{S}_{\varepsilon}\right)^{-1}\left(\mathbf{y}-\mathbf{K}\mathbf{x}_{\mathrm{a}}\right).\end{aligned} \tag{1.5.29}$$

Since $\mathbf{y}=\mathbf{K}\mathbf{x}$, Eq. (1.5.29) can be written as

$$\hat{\mathbf{x}}=\mathbf{x}_{\mathrm{a}}+\left(\mathbf{K}^{\mathrm{T}}\mathbf{S}_{\varepsilon}^{-1}\mathbf{K}+\mathbf{S}_{\mathrm{a}}^{-1}\right)^{-1}\mathbf{K}^{\mathrm{T}}\mathbf{S}_{\varepsilon}^{-1}\mathbf{K}(\mathbf{x}-\mathbf{x}_{\mathrm{a}}) \tag{1.5.30}$$

or

$$\hat{\mathbf{x}}=\mathbf{x}_{\mathrm{a}}+\mathbf{S}_{\mathrm{a}}\mathbf{K}^{\mathrm{T}}\left(\mathbf{K}\mathbf{S}_{\mathrm{a}}\mathbf{K}^{\mathrm{T}}+\mathbf{S}_{\varepsilon}\right)^{-1}\mathbf{K}\left(\mathbf{x}-\mathbf{x}_{\mathrm{a}}\right). \tag{1.5.31}$$

Eqs. (1.5.30) and (1.5.31) can be compared with Eq. (1.5.8) and the matrix **G** is found to be

$$\mathbf{G}=\left(\mathbf{K}^{\mathrm{T}}\mathbf{S}_{\varepsilon}^{-1}\mathbf{K}+\mathbf{S}_{\mathrm{a}}^{-1}\right)^{-1}\mathbf{K}^{\mathrm{T}}\mathbf{S}_{\varepsilon}^{-1}=\mathbf{S}_{\mathrm{a}}\mathbf{K}^{\mathrm{T}}\left(\mathbf{K}\mathbf{S}_{\mathrm{a}}\mathbf{K}^{\mathrm{T}}+\mathbf{S}_{\varepsilon}\right)^{-1} \tag{1.5.32}$$

Eq. (1.5.32) shows that the gain matrix (also known as contribution function), **G**, can be calculated given the Jacobian matrix **K**, the measurement error covariance matrix $\mathbf{S}_{\varepsilon}$, and the *a priori* VMR covariance $\mathbf{S}_{\mathrm{a}}$. Notice, however, that equation (1.5.31) assumes Gaussian error probabilities and a linear relationship between **y** and **x** (**y** = **Kx**), which is not generally the case in practice [*Rodgers*, 2000]. In general, there is a non-linear relationship $\mathbf{y}=\mathbf{F}(\mathbf{x})$ between the spectrum **y** and the profile **x**, and the most probable solution is determined by

$$\nabla_{\mathrm{x}}\left[-2\ln\mathbf{P}(\mathbf{x}|\mathbf{y})\right]=\nabla_{\mathrm{x}}\{[\mathbf{y}-\mathbf{F}(\mathbf{x})]^{\mathrm{T}}\mathbf{S}_{\varepsilon}^{-1}\left(\mathbf{y}-\mathbf{F}(\mathbf{x})\right)+(\mathbf{x}-\mathbf{x}_{\mathrm{a}})\mathbf{S}_{\mathrm{a}}^{-1}\left(\mathbf{x}-\mathbf{x}_{\mathrm{a}}\right)+\mathrm{C}_1\} \tag{1.5.33}$$

$$=\nabla_{\mathrm{x}}\left[(-\mathbf{F}(\mathbf{x}))\right]^{\mathrm{T}}\mathbf{S}_{\varepsilon}^{-1}\left(\mathbf{y}-\mathbf{F}(\mathbf{x})\right)+\mathbf{S}_{\mathrm{a}}^{-1}\left(\mathbf{x}-\mathbf{x}_{\mathrm{a}}\right) \tag{1.5.34}$$

$$= -[\nabla_{x}\mathbf{F}(\mathbf{x})]^{T}\mathbf{S}_{\varepsilon}{}^{-1}\left(\mathbf{y}-\mathbf{F}(\mathbf{x})\right)+\mathbf{S}_{a}{}^{-1}\left(\mathbf{x}-\mathbf{x}_{a}\right)=0 \tag{1.5.35}$$

Eq. (1.5.35) is an implicit equation for **x**, that is, the value of **y** is obtained from **x** by solving the equation $-[\nabla_{x}\mathbf{F}(\mathbf{x})]^{T}\mathbf{S}_{\varepsilon}{}^{-1}\left(\mathbf{y}-\mathbf{F}(\mathbf{x})\right)+\mathbf{S}_{a}{}^{-1}\left(\mathbf{x}-\mathbf{x}_{a}\right)=0$. It must be solved numerically, and the difficulty involved depends on the degree of non-linearity of the forward model $\mathbf{F}(\mathbf{x})$.

Let us define the cost function **J** as

$$\mathbf{J}(\mathbf{x})=\left(\mathbf{y}-\mathbf{Kx}\right)^{T}\mathbf{S}_{\varepsilon}{}^{-1}\left(\mathbf{y}-\mathbf{Kx}\right)+\left(\mathbf{x}-\mathbf{x}_{a}\right)^{T}\mathbf{S}_{a}{}^{-1}\left(\mathbf{x}-\mathbf{x}_{a}\right). \tag{1.5.36}$$

According to equation Eq. (1.5.30), the gradient of the cost function $\mathbf{J(x)}$ gives

$$\nabla_{x}\mathbf{J}(\mathbf{x})=-\left[\nabla_{x}\mathbf{F}(\mathbf{x})\right]^{T}\mathbf{S}_{\varepsilon}{}^{-1}\left(\mathbf{y}-\mathbf{F}(\mathbf{x})\right)+\mathbf{S}_{a}{}^{-1}\left(\mathbf{x}-\mathbf{x}_{a}\right). \tag{1.5.37}$$

Newtonian iteration is a straightforward numerical method for finding the zero of the gradient of the cost function $\mathbf{J(x)}$. For $\nabla_{x}\mathbf{J(x)}=0$, the (i+1)th iteration of **x** gives

$$\mathbf{x}_{i+1}=\mathbf{x}_{i}-\left[\nabla_{x}\nabla_{x}\mathbf{J}(\mathbf{x}_{i})\right]^{-1}\nabla_{x}\mathbf{J}(\mathbf{x}_{i}) \tag{1.5.38}$$

The derivative of $\nabla_{x}\mathbf{J(x)}$ can be written as

$$\nabla_{x}\nabla_{x}\mathbf{J(x)}=\mathbf{S}_{a}{}^{-1}+\left[\nabla_{x}\left(\mathbf{F}(\mathbf{x})\right)\right]^{T}\mathbf{S}_{\varepsilon}{}^{-1}\mathbf{K}-\left\{\nabla_{x}\left[\nabla_{X}\left(\mathbf{F}(\mathbf{x})\right)\right]^{T}\right\}\mathbf{S}_{\boldsymbol{\varepsilon}}{}^{-1}\left[\mathbf{y}-\mathbf{F}(\mathbf{x})\right] \tag{1.5.39}$$

and if the last term in Eq. (1.5.39) is small enough to be neglected, then

$$\nabla_{x}\nabla_{x}\mathbf{J(x)}=\mathbf{S}_{a}{}^{-1}+\left[\nabla_{x}\left(\mathbf{F}(\mathbf{x})\right)\right]^{T}\mathbf{S}_{\varepsilon}{}^{-1}\mathbf{K} \tag{1.5.40}$$

Substituting Eqs. (1.5.37) and (1.5.40) into Eq. (1.5.38) gives

$$\mathbf{x}_{i+1}=\mathbf{x}_{i}+\left\{\mathbf{S}_{a}{}^{-1}+\left[\nabla_{x}\mathbf{F}(\mathbf{x}_{i})\right]^{T}\mathbf{S}_{\boldsymbol{\varepsilon}}{}^{-1}\nabla_{x}\mathbf{F}(\mathbf{x}_{i})\right\}\left\{\left[\nabla_{x}\mathbf{F}\left(\mathbf{x}_{i}\right)\right]^{T}\mathbf{S}_{\boldsymbol{\varepsilon}}{}^{\mathbf{-1}}\left[\mathbf{y}-\mathbf{F}(\mathbf{x}_{i})\right]+\mathbf{S}_{\mathbf{a}}{}^{\mathbf{-1}}\left(\mathbf{x}_{i}-\mathbf{x}_{a}\right)\right\}$$

(1.5.41)

By expressing $\mathbf{x}_{i+1}$ as a departure from $\mathbf{x}_{a}$ rather than from $\mathbf{x}_{i}$, Eq. (1.5.41) can be rearranged as

$$\mathbf{x}_{i+1}=\mathbf{x}_{a}+\left\{\mathbf{S}_{a}{}^{-1}+\left[\nabla_{x}\mathbf{F}(\mathbf{x}_{i})\right]^{T}\mathbf{S}_{\varepsilon}{}^{-1}\nabla_{x}\mathbf{F}(\mathbf{x}_{i})\right\}\left[\nabla_{x}\mathbf{F}\left(\mathbf{x}_{i}\right)\right]^{T}\mathbf{S}_{\boldsymbol{\varepsilon}}{}^{-1}\left\{\mathbf{y}-\mathbf{F}(\mathbf{x}_{i})+\left[\nabla_{x}\mathbf{F}\left(\mathbf{x}_{i}\right)\right]^{-1}\left(\mathbf{x}_{i}-\mathbf{x}_{a}\right)\right\}$$

$$= \mathbf{x}_{\mathrm{a}} + \mathbf{S}_{\mathrm{a}}\left[\nabla_{\mathrm{x}}\mathbf{F}(\mathbf{x}_{\mathrm{i}})\right]^{\mathrm{T}}\left\{\nabla_{\mathrm{x}}\mathbf{F}(\mathbf{x}_{\mathrm{i}})\mathbf{S}_{\mathrm{z}}\left[\nabla_{\mathrm{x}}\mathbf{F}(\mathbf{x}_{\mathrm{i}})\right]^{\mathrm{T}}\right\}\left\{(\mathbf{y}-\mathbf{y}_{\mathrm{i}}) + \left[\nabla_{\mathrm{x}}\mathbf{F}(\mathbf{x}_{\mathrm{i}})\right]^{-1}(\mathbf{x}_{\mathrm{i}}-\mathbf{x}_{\mathrm{a}})\right\} \qquad (1.5.42)$$

in which, $\mathbf{y}_{\mathrm{i}} = \mathbf{F}(\mathbf{x}_{\mathrm{i}})$ is produced by the forward model using the i$^{\mathrm{th}}$ estimate of the VMR profile. It is the calculated spectrum at the i$^{\mathrm{th}}$ iteration.

A convergence criterion is required to determine when the iterations should be terminated. A commonly used test is to compare the difference between the calculated spectrum $\mathbf{y}_{\mathrm{i}} = \mathbf{F}(\mathbf{x}_{\mathrm{i}})$ and the measured spectrum $\mathbf{y}$ with the expected measurement error. When the difference is smaller than the expected measurement error m

$$\chi^2\left[\mathbf{y}-\mathbf{F}(\mathbf{x}_{\mathrm{i}})\right] = \left[\mathbf{y}-\mathbf{F}(\mathbf{x}_{\mathrm{i}})\right]\mathbf{S}_{\varepsilon}^{-1}\left[\mathbf{y}-\mathbf{F}(\mathbf{x}_{\mathrm{i}})\right]^{-1} \leq m \qquad (1.5.43)$$

the iteration will be terminated at the i$^{\mathrm{th}}$ step, and the solution $\mathbf{x}_{\mathrm{i}}$ is the retrieved VMR $\hat{\mathbf{x}}$.

1.6 Retrieval Characterization

The Eq. (1.5.8) shows that the retrieved VMR profile is actually a combination of the *a priori* VMR and the measurements, in which the *a priori* VMR is weighted by the matrix **A**. The n by n matrix **A**, called the averaging kernel matrix, gives the sensitivity of the retrieval to the VMR profile. The averaging kernel matrix is the product of the contribution function **G**, which is given by Eq. (1.5.32), and the weighting function $\mathbf{K} = \dfrac{\partial \mathbf{F}(\mathbf{x})}{\partial \mathbf{x}}$.

The averaging kernel matrix characterizes the retrievals, since its rows describe the sensitivity of the retrieval to each atmospheric layer. In the ideal case, **A** is a unit matrix, that is, the measurement is sensitive to each layer with perfect sensitivity, and the retrieved VMR profiles do not use any information from the *a priori* ones. The vertical resolution in the ideal case is the vertical layer spacing. However, in reality, such as for the retrievals of ground-based observations, the rows of **A** are generally peaked functions. The diagonal elements of **A** are not equal to one and the off-diagonal elements are not equal to zero. The *a priori* VMR profile thus makes a contribution to the retrieved VMR profiles. The half-width of the peaked function is usually defined as the vertical resolution of the observations. The sum of the elements in the n^{th} row of the $\mathbf{A}$ matrix gives the sensitivity of the observations at the n^{th} layer. For example, the retrieved VMR value at the n^{th} layer is solely determined by the observations when the sum is close to 1. In contrast, if the sum is close to 0 the retrieved VMR value is mainly from the *a priori* VMR.

The VMR profiles of trace gases observed using ground-based instruments or satellite-borne nadir-viewing spectrometers have a limited vertical resolution, and typically provide about 1 to 4 independent layers. The trace of the averaging kernel matrix $\mathbf{A}$, called the degrees of freedom (DOFS) for signal and labeled as $\mathrm{DOFS}\left(=\mathrm{tr}(\mathbf{A})\right)$, determines the number of independently resolved pieces of information in the atmosphere obtained from the measurement, that is, the amount of a trace gas in a certain altitude range, which is a partial column. For example, when $\mathrm{DOFS}=\mathrm{tr}(\mathbf{A})=3$ three partial columns representing three different altitude ranges in the atmosphere can be obtained from the observations.

1.7 Retrieval Error Analysis

Taking errors into account, Eq. (1.5.6) can be rewritten as

$$\hat{\mathbf{x}} = \mathbf{R}\left[\mathbf{F}(\mathbf{x},\mathbf{b}), \boldsymbol{\Delta}\mathbf{f}(\mathbf{x},\mathbf{b},\mathbf{b}') + \boldsymbol{\varepsilon}, \mathbf{b}\right]. \tag{1.7.1}$$

Here, $\boldsymbol{\Delta}\mathbf{f}(\mathbf{x},\mathbf{b},\mathbf{b}')$ is the difference between the best known forward model $\mathbf{F}(\mathbf{x},\mathbf{b})$ and the perfect forward model; $\mathbf{b}'$ are the unknown forward model parameters, but should be included in the best known physical model; $\boldsymbol{\varepsilon}$ is the random measurement noise.

Performing a linearization of the forward model $\mathbf{F}(\mathbf{x},\mathbf{b})$ about $\mathbf{x}_a$ and $\mathbf{b}_a$ (subscript a indicates that the parameters are from *a priori* information), we can rewrite Eq. (1.7.1) as

$$\hat{\mathbf{x}} = \mathbf{R}\left[\mathbf{F}(\mathbf{x}_a,\mathbf{b}_a) + \mathbf{K}(\mathbf{x}-\mathbf{x}_a) + \mathbf{K}_b(\mathbf{b}-\mathbf{b}_a) + \Delta\mathbf{f}(\mathbf{x},\mathbf{b},\mathbf{b}') + \boldsymbol{\varepsilon}, \mathbf{b}_a\right]. \tag{1.7.2}$$

A linearization about $\mathbf{y}_a$ for Eq. (1.7.2) yields,

$$\hat{\mathbf{x}} = \mathbf{R}\left[\mathbf{F}(\mathbf{x}_a,\mathbf{b}_a) + \frac{\partial\mathbf{R}}{\partial\mathbf{F}}(\mathbf{x}-\mathbf{x}_a) + \mathbf{K}_b(\mathbf{b}-\mathbf{b}_a) + \Delta\mathbf{f}(\mathbf{x},\mathbf{b},\mathbf{b}') + \boldsymbol{\varepsilon}, \mathbf{b}_a\right], \tag{1.7.3}$$

and assuming that the retrieval method does not introduce a bias, has $\mathbf{x}_a = \mathbf{R}\left[\mathbf{F}(\mathbf{x}_a, \mathbf{b}_a), \mathbf{b}_a\right]$. As given in section 1.5, $\mathbf{G} = \frac{\partial \mathbf{R}}{\partial \mathbf{F}}$ so

$$\hat{\mathbf{x}} = \mathbf{x}_a + \mathbf{GK(x - x}_a) + \mathbf{GK}_b(\mathbf{b - b}_a) + \mathbf{G}\Delta\mathbf{f}(\mathbf{x}, \mathbf{b}, \mathbf{b}') + \mathbf{G}\boldsymbol{\varepsilon} \tag{1.7.4}$$

Since $\mathbf{A} = \mathbf{GK}$, subtracting $\mathbf{x}$ from both sides of Eq. (1.7.4) and denoting the n by n unity matrix as **I**, we obtain

$$\begin{aligned} \hat{\mathbf{x}} - \mathbf{x} &= (\mathbf{A} - \mathbf{I})(\mathbf{x - x}_a) && \text{smoothing error} \\ &+ \mathbf{GK}_b(\mathbf{b - b}_a) && \text{model parameter error} \\ &+ \mathbf{G}\Delta\mathbf{f}(\mathbf{x}, \mathbf{b}, \mathbf{b}') && \text{forward model parameter error} \\ &+ \mathbf{G}\boldsymbol{\varepsilon}. && \text{retrieval noise} \end{aligned} \tag{1.7.5}$$

The left hand side of Eq. (1.7.5) is the total error in an observation, since it presents the difference between the retrieved or observed VMR profile and the real VMR profile of the target gas in the atmosphere. The right hand side indicates the various error sources which consist of smoothing error, model parameter error, forward model parameter error, and retrieval noise error.

Since we do not know the real VMR profile in the atmosphere, only the error covariance matrices can be obtained as

$$\mathbf{S}_S = (\mathbf{A - I})\mathbf{S}_a(\mathbf{A - I})^T \tag{1.7.6}$$

$$\mathbf{S}_F = \mathbf{GK}_b\mathbf{S}_b\mathbf{K}_b{}^T\mathbf{G}^T \tag{1.7.7}$$

$$\mathbf{S}_M = \mathbf{GS}_\varepsilon\mathbf{G}^T. \tag{1.7.8}$$

$\mathbf{S}_S$ is the covariance of the smoothing of the real VMR profile through the use of an averaging kernel matrix. It is a systematic error on a short time scale, but random on long time scales since its estimate is only correct as $\mathbf{S}_a$ becomes the covariance of a real ensemble of atmospheric VMR profiles and $\mathbf{x}_a$ gives the true mean atmospheric VMR profile. $\mathbf{S}_M$ is the covariance error arising from the random measurement noise propagating into the retrievals, and is a random error. The model parameter error covariance $\mathbf{S}_F$ is caused by biases in forward model parameters, and can contain random errors such as those from the temperature and pressure profiles and solar zenith angle used in the model, together with systematic errors such as those from spectroscopic parameters. The forward model error is usually neglected, since evaluating it without knowing **x** and **b** is extremely difficult.

1.8 Retrievals Using SFIT2 Program

The SFIT2 program [*Hase et al.*, 2004; *Pougatchev et al.*, 1995; *Rinsland et al.*, 1998] is widely used for the analysis of ground-based solar absorption spectra. It was jointly developed at the NASA-Langley Research Center and at the National Institute of Water and Atmospheric Research at Lauder, New Zealand. It is a retrieval program that employs the OEM of C. D. Rodgers [*Rodgers* 1976, 1990, 2000; *Rodgers et al.*, 2003]. The OEM is coded into the program to include *a priori* VMR profiles as a function of altitude in the retrievals. SFIT2 allows the simultaneous retrieval of a vertical profile and column density of the target molecule, together with the total columns of interfering species.

To run the SFIT2 program, we need the following input information: 1) a model atmosphere; 2) line parameters; 3) instrumental parameters which simulate the performance of the spectrometer used in the observation, such as the MOPD (the parameter that determines the spectral resolution for an FTS), and the effective apodization parameters (EAP); 4) segments of observed atmospheric absorption spectrum, called “microwindows”.

To obtain the initial input information, a forward model, named FSCATM [*Gallery et al.*, 1983*; Meier et al.*, 2004], is applied to generate model atmospheres using *a priori* VMR profiles containing the concentrations of most atmospheric gases as a function of altitude, pressure and temperature profiles, longitude and latitude of the observation site, and the time of each observation. It is needed to conduct refractive ray tracing, and a calculation of the air mass distribution (which is the number of molecules as a function of altitude) for each model atmosphere. The *a priori* VMR profiles $\mathbf{x}_a$ and covariance matrices $\mathbf{S}_a$ for each atmospheric constituent are constructed using a combination of climatological profiles measured by satellite-borne or balloon-borne instruments. For example, the *a priori* VMR profiles that are used for the observations at Waterloo Atmospheric Observatory (WAO) were provided by A. Wiacek, who combined the HALogen Occultation Experiment (HALOE) v.19 satellite data [*Russell et al.*, 1994], mid-latitude daytime 2001 Michelson Interferometer for Passive Atmospheric Sounding (MIPAS) reference profiles [*Carli et al.*, 2004], and the VMR profiles obtained for northern mid-latitudes by *Toon et al.* using the MkIV FTS measurements during balloon flights [*Peterson and Margitan*, 1995]. Pressure and temperature profiles obtained from NCEP/NCAR, as provided by the NASA GSFC automailer (science@hyperion.gsfc.nasa.gov) [*McPherson et al.*, 1979; *Kalnay et al.*, 1996] and the MSIS-2000 [*Picone et al.*, 2002] are also the input information for the retrievals. Typically, NCEP provides the pressure and temperature information from the surface to 50 km and the output of MSIS covers from 50 km to 100 km. The *a priori* VMR, pressure and temperature profiles used in the data analysis of the ground-based observations will be specified in the retrieval sections in Chapters 4-6. The retrievals of atmospheric phosgene VMR profiles as shown in Chapter 3 were performed by C. D. Boone using an iterative nonlinear least squares fitting procedure, which differs with the OEM approach and does not require *a priori* VMR profiles as an input information [*Boone et al.*, 2005]. In all of the retrievals used by this work, HITRAN 2004, which contains the latest released version of the HITRAN data compilation (http://cfa-www.harvard.edu/hitran/welcometop.html) [*Rothman et al.*, 2005], were used.

In order to find the best estimate, that is, to find the VMR profile $\hat{\mathbf{x}}$ that satisfies Eqs. 1.5.35 and 1.5.43, SFIT2 uses the Newton iteration approach as given in Eq. 1.5.42. During each iteration, input information is used in the forward model of the SFIT2 program to simulate the infrared absorption spectrum of the target gas along with the interfering gases which produce absorption features within the specified microwindow or microwindows. In the first iteration, the SFIT2 program uses $\mathbf{x}_1 = \mathbf{x}_a$ to simulate the first absorption spectrum. In the ith iteration, the simulated spectrum, which is the $\mathbf{y}_i$ or $\mathbf{F(x}_i\mathbf{)}$ term in Eq. (1.5.42), is calculated using the i^th^ estimated VMR profile $\mathbf{x}_i$. The $\mathbf{y}_i$, $\mathbf{F(x}_i\mathbf{)}$, the $\mathbf{S}_\varepsilon$ covariance matrix (which has only diagonal elements that are all equal to the reciprocal of the square of signal-to-noise ratio), together with the input observed spectrum $\mathbf{y}$, are used in the Eq. (1.5.43) to evaluate the convergence. If the convergence criterion is satisfied, then the program will output the ith estimated VMR profile $\mathbf{x}_i$ as the retrieved VMR profile $\hat{\mathbf{x}}$ for the target species. The weighting function matrix $\mathbf{K}_i = \frac{\partial \mathbf{F}}{\partial \mathbf{x}} | \mathbf{x}_i$ is also written in the output file. Since the weighting function matrix is already obtained from the retrieval and the $\mathbf{S}_a$ and $\mathbf{S}_\varepsilon$ matrices are also known, the contribution function $\mathbf{G}$ can be calculated using Eq. (1.5.32). Finally, the averaging kernel matrix **A** can be obtained simply because we know $\mathbf{A} = \mathbf{GK}$, and **A** is used in the retrieval characterization and the retrieval error analysis using Eqs. (1.7.6) to (1.7.8).

1.9 References

Backus G.E. and Gilbert J.F., (1970), Uniqueness in the inversion of inaccurate gross Earth data, *Trans. R. Soc. Lon, Ser. A*, **266**, 123-192.

Beer R., (2006), TES on the Aura mission: scientific objectives, measurements, and analysis overview, *IEEE Trans. Geosci. Remote Sensing*, **44**, 1102-1105.

Bernath P.F., (2005), *Spectra of Atoms and Molecules*, 2nd edition, Oxford University Press, New York.

Bernath P.F., McElroy C.T., Abrams M.C., Boone C.D., Butler M., Camy-Peyret C., Carleer M., Clerbaux C., Coheur P.-F., Colin R., DeCola P., DeMazière M., Drummond J.R., Dufour D., Evans W.F.J., Fast H., Fussen D., Gilbert K., Jennings D.E., Llewellyn E.J., Lowe R.P., Mahieu E., McConnell J.C., McHugh M., McLeod S.D., Michaud R., Midwinter C., Nassar R., Nichitiu F., Nowlan C., Rinsland C.P., Rochon Y.J., Rowlands N., Semeniuk K., Simon P., Skelton R., Sloan J.J., Soucy M.-A., Strong K., Tremblay P., Turnbull D., Walker K.A., Walkty I., Wardle D.A., Wehrle V., Zander R., and Zou J., (2005), Atmospheric Chemistry Experiment (ACE): Mission Overview, *Geophys. Res. Lett.*, **32**, L15S01, doi:10.1029/2005GL022386.

Bernath P.F., (2006), Atmospheric Chemistry Experiment (ACE): Analytical Chemistry from Orbit, *Tren. Anal. Chem.*, **25**, 647-654.

Boone C.D., Nassar R., Walker K.A., Rochon Y., McLeod S.D., Rinsland C.P., and Bernath P.F., (2005), Retrievals for the Atmospheric Chemistry Experiment Fourier transform spectrometer, *Appl. Opt.*, **44**, 7218-7231.

Camy-Peyret C., (1995), Balloon-borne infrared Fourier transform spectroscopy for measurements of atmospheric trace species, *Spectrochim. Acta, Part A*: *Mol. Spectrosc.*, **51A**, 1143-1152.

Carli B., Alpaslan D., Carlotti M., Castelli E., Ceccherini S., Dinelli B.M., Dudhia A., Flaud J.M., Hoepfner M., Jayd V., Magnani L., Oelhaf H., Payne V., Piccolo C., Prosperi M., Raspollini P., Remedios J., Ridolfic M., and Spang R., (2004), First results of MIPAS/ENVISAT with operational Level 2 code, *Adv. Space Res.*, **33**, 1012-1019.

Crisp D., Atlas R.M., Breon F.M., Brown L.R., Burrows J.P., Ciais P., Connor B.J., Doney S.C., Fung I.Y., Jacob D.J., Miller C.E., O'Brien D., Pawson S., Randerson J.T., Rayner P., Salawitch R.J., Sander S.P., Sen B., Stephens G.L., Tans P.P., Toon G.C., Wennberg P.O., Wofsy S.C., Yung Y.L., Kuang Z., Chudasama B., Sprague G., Weiss B., Pollock R., Kenyon D., and Schroll S., (2004), The Orbiting Carbon Observatory (OCO) mission, *Adv. Space Res.*, **34**, 700-709.

Davis S.P., Abrams M.C., and Brault J.W., (2001), *Fourier Transform Spectrometry*, Academic Press, San Diego.

Friedl-Vallon F., Maucher G., Seefeldner M., Trieschmann O., Kleinert A., Lengel A., Keim C., Oelhaf H., and Fischer H., (2004), Design and characterization of the balloon-borne Michelson Interferometer for Passive Atmospheric Sounding (MIPAS-B2), *Appl. Opt.* **43**, 3335-3355.

Fu D., Walker K.A., Sung K., Boone C.D., Soucy M-A, and Bernath P.F., (2007), The Portable Atmospheric Research Interferometric Spectrometer for the Infrared, PARIS-IR, *J. Quant. Spectrosc. Radiat. Trans.*, **103**, 362-370.

Fu D., Boone C.D., Bernath, P.F., Walker K.A., Nassar R., Manney G.L., and S.D. McLeod (2007), Global phosgene observations from the Atmospheric Chemistry Experiment (ACE) mission, Geophys. Res. Lett., 34, L17815, doi:10.1029/2007GL029942.

Fu D., Sung K., Walker K.A., Boone C.D., and Bernath P.F., Ground-based solar absorption studies for the Carbon Cycle science by Fourier Transform Spectroscopy (CC-FTS) mission, Submitted to *J. Quant. Spectrosc. Radiat. Trans.*

Fu D., Mittermeier R., Sung K., Walker K.A., Boone C.D., Bernath P.F., Fast H., and Strong K., Simultaneous atmospheric measurements using Fourier transform infrared spectrometers at the Polar Environment Atmospheric Research Laboratory (PEARL) during spring 2006, (in preparation for *Atmos. Chem. Phys.*).

Gallery W.O., Kneizys F.X., and Clough S.A., (1983), Air mass computer program for atmospheric transmittance/radiance calculation: FSCATM, *Environ. Res. Pap.*, **828** (AFGL-TR-83-0065), U.S. Air Force Geophysics Laboratory, Bedford, Massachusetts.

Griffith D.W.T., Jones N.B., McNamara B., Walsh C.P., Bell W., and Bernardo C., (2003) Intercomparison of NDSC ground-based solar FTIR measurements of atmospheric gases at Lauder, New Zealand, *J. Atmos. Oceanic Technol.*, **20**, 1138-1153.

Griffiths P.R. and de Haseth J.A., (1986), *Fourier Tansform Infrared Spectrometry*, John Wiley & Sons, Toronto.

Griffiths P.R., Hart B.K., Yang H., and Berry R.J., (2000), Open-path FT-IR spectrometry: is completely unattended operation feasible? *Talanta*, **53**, 223-231.

Grooß J.U. and Russell III J., (2005), Technical note: A stratospheric climatology for O_3, H_2O, CH_4, NO_x, HCl and HF derived from HALOE measurements, *Atmos. Chem. Phys.*, **5**, 2797-2807.

Hase F., Hannigan J.W., Coffey M.T., Goldman A., Höpfner M., Jones N.B., Rinsland C.P, and Wood S.W., (2004), Intercomparison of retrieval codes used for the analysis of high-resolution, ground-based FTIR measurements, *J. Quant. Spectrosc. Radiat. Trans.*, **87**, 25-52.

Heise H.M., Muller U., Gartner A.G., and Holscher N., (2001), Improved chemometric strategies for quantitative FTIR spectral analysis and applications in atmospheric open-path monitoring, *Field Anal. Chem. Technol.* **5**, 13-28.

Hong D.W., Heob G.S., Hanc J.S., and Choa S.Y., (2004), Application of the open path FTIR with COL1SB to measurements of ozone and VOCs in the urban area, *Atmos. Environ.*, **38**, 5567–-5576.

Jacquinet-Husson N., Scott N.A., Chedin A., Garceran K., Armante R., Chursin A.A., Barbe A., Birk M., Brown L.R., Camy-Peyret C., Claveau C., Clerbaux C., Coheur P.F., Dana V., Daumont L., Debacker-Barilly M.R., Flaud J.M., Goldman A., Hamdouni A., Hess M., Jacquemart D., Kopke P., Mandin J.Y., Massie S., Mikhailenko S., Nemtchinov V., Nikitin A., Newnham D., Perrin A., Perevalov V.I., Regalia-Jarlot L., Rublev A., Schreier F., Schult I., Smith K.M., Tashkun S.A., Teffo J. L., Toth R.A., Tyuterev Vl.G., Vander Auwera J., Varanasi P., and Wagner G., (2005), The 2003 edition of the GEISA/IASI spectroscopic database, *J. Quant. Spectrosc. Radiat. Trans.*, **95**, 429-467.

Kalnay E., Kanamitsu M., Kistler R., Collins W., Deaven D., Gandin L., Iredell M., Saha S., White G., Woollen J., Zhu Y., Chelliah M., Ebisuzaki W., Higgins W., Janowiak J., Mo K., Ropelewski C., Wang J., Leetmaa A., Reynolds R., and Joseph D., (1996), The NCEP/NCAR 40-year reanalysis project, *Bull, Amer, Meteor, Soc.*, **77**, 437 - 471.

Kobayashi H., Shimota A., Yoshigahara C., Yoshida I., Uehara Y., and Kondo K., (1999), Satellite-borne high-resolution FTIR for lower atmosphere sounding and its evaluation, *IEEE Trans. Geosci. Remote Sens.*, **37**, 1496-1507.

Koehler F.W., Small G.W., Combs R.J., Knapp R.B., and Kroutil R.T., (2001), Automated detection of sulfur dioxide in stack emissions by passive Fourier transform infrared spectrometry, *Vib. Spectrosc.*, **27**, 97-107.

McPherson R.D., Bergan K.H., Kistler R.E., Rasch G.E., Gordon D.S., (1979), The NMC operational global data assimilation system, *Mon. Wea. Rev.*, **107**, 1445-1461.

Meier A., Goldman A., Manning P.S., Stephen T.M., Rinsland C.P., Jones N.B., and Wood S.W., (2004), Improvements to air mass calculations for ground-based infrared measurements, *J. Quant. Spectrosc. Radiat. Trans.*, **83**, 109-113.

Michelson A.A., (1891), On the application of interference methods to spectroscopic measurements-I, *Philos. Mag.*, **31**, 338-346.

Michelson A.A., (1892), On the application of interference methods to spectroscopic measurements-II, *Philos. Mag.*, **34**, 280-299.

Oppenheimer C., Francis P., Burton M., Maciejewski A.J.H., and Boardman L., (1998), Remote measurement of volcanic gases by Fourier transform infrared spectroscopy, *Appl. Phys. B.*, **67**, 505-515.

Oppenheimer C., Burton M.R., Durieux J., and Pyle D.M., (2002), Open-path Fourier transform spectroscopy of gas emissions from Oldoinyo Lengai volcano, Tanzania. *Opt. and Lasers Eng.*, **37**, 203-214.

Persky M.J., (1995), A review of spaceborne infrared Fourier transform spectrometers. *Rev. Sci. Instrum.*, **66**, 4763-4797.

Peterson D.B. and Margitan J.M., (1995), *Upper atmospheric satellite correlative measurement program (UARS-CMP) balloon data atlas*, NASA, Washington, DC.

Picone J.M., Hedin A.E., Drob D.P., and Aikin A.C., (2002), NRLMSISE-00 empirical model of the atmosphere: statistical comparison and scientific issues, *J. Geophys. Res.*, **107**, 1468-1483.

Pougatchev N.S., Connor B.J., and Rinsland C.P., (1995), Infrared measurements of the ozone vertical distribution above Kitt Peak, *J. Geophys. Res.*, **100**, 16689-16698.

Rinsland C.P., Mahieu E., Zander R., Jones N.B., Chipperfield M.P., Goldman A., Anderson J., Russell III J.M., Demoulin P., Notholt J., Toon G.C., Blavier J.-F., Sen B., Sussmann R., Wood S.W., Meier A., Griffith D.W.T., Chiou L.S., Murcray F.J.,. Stephen T.M, Hase F., Mikuteit S., Schulz A., and Blumenstock T., (2003), Long-term of inorganic chlorine from ground-based infrared solar spectra: past increases and evidence for stabilization, *J. Geophys. Res.*, **108**, 4252-4273.

Rodgers, C.D., (1976), Retrieval of atmospheric temperature and composition from remote measurements of thermal radiation, *Rev. Geophys. Space. Phys.*, **14**, 609-624.

Rodgers, C.D., (1990), Characterization and error analysis of profiles retrieved from remote sounding measurements, *J. Geophys. Res.*, **95**, 5587-5595.

Rodgers, C.D., (2000), *Inverse methods for atmospheric sounding: Theory and practice*, World Scientific, Singapore.

Rodgers C.D. and Connor B.J., (2003), Intercomparison of remote sounding instruments, *J. Geophys, Res.*, **108**, 4116, doi: 10.1029/2002JD002299.

Rothman L.S., Jacquemart D., Barbe A., Benner D.C., Birk M., Brown L.R., Carleer M.R., Chackerian Jr. C., Chance K., Coudert L.H., Dana V., Devi V.M., Flaud J.M., Gamache R.R., Goldman A., Hartmann J.M., Jucks K.W., Maki A.G., Mandin J.Y., Massie S.T., Orphal J., Perrin A., Rinsland C.P., Smith M.A.H., Tennyson J., Tolchenov R.N., Toth R.A., Auwera J.V., Varanasi P., Wagner G., (2005), The HITRAN 2004 molecular spectroscopic database, *J. Quant. Spectrosc. Rad. Transfer.* **96**, 139-204.

Russell J.M., Gordley L.L., Deaver L.E., Thompson R.E., and Park J.H., (1994), An overview of the HALogen Occultation Experiment (HALOE) and preliminary results, *Adv. Space Res.*, **14**, 913.

Thorne A., Litzen U. and Johansson S., (1991), *Spectrophysics*, 2nd edition, Springer-Verlag Berlin, Heidelberg.

Todd L.A., Ramanathan M., Mottus K., Katz R., Dodson A., and Mihlan G., (2001), Measuring chemical emissions using open-path Fourier transform infrared (OP-FTIR) spectroscopy and computer-assisted tomography, *Atmos. Environ.* **35**, 1937-1947.

Yang Z., Toon G.C., Margolis J.S., and Wennberg P.O., (2002), Atmospheric CO_2 retrieved from ground-based near IR solar spectra, *Geophys. Res. Lett.*, **29**, 1339, doi:10.1029/2001GL014537.

Washenfelder R.A., Wennberg P.O., and Toon G.C., (2003), Tropospheric methane retrieved from ground-based near-IR solar absorption spectra, *Geophys. Res. Lett.,* **30**, 2226, doi:10.1029/2003GL017969.

Chapter 2

Overview of Observations and Instrumentation

2.1 Platform and Geometry Used in the Observations

Atmospheric remote sensing can be performed from different types of platforms, which generally can be classified into three categories: ground-based, air-borne and space-based. The space-borne platforms, such as satellites provide an excellent view in the nadir and limb directions. Satellites are very stable and have predictable orbital motions. However, satellites are expensive to launch and to operate, and are difficult to repair. Air-borne platforms such as aircraft and balloons offer a cheaper way to observe the atmosphere with a better view than from the ground. Air-borne platforms, however, can be unstable, and in the case of balloons, the flight direction is difficult to control. Ground-based platforms provide the lowest costs and easiest instrumental access.

Spatial resolution is important in the study of chemical processes in the atmosphere, and is related to the viewing geometry used for the observations. For example, a limb-viewing geometry can provide a higher vertical resolution than a nadir-viewing geometry or a ground-based solar viewing geometry. The solar occultation geometry is available only for measurements taken from a space-borne or an air-borne platform. The solar occultation geometry usually provides lower spatial resolution in the horizontal direction and poorer sampling in the troposphere than does a nadir-viewing geometry or the solar-viewing geometry used in a ground-based observatory.

Since each platform and geometry has its own characteristic features, they are selected based on the specific scientific problems to be addressed. It is common to utilize many platforms and multiple viewing geometries in atmospheric observation programs. The following subsections will focus on the descriptions of the platforms and viewing geometries used in this thesis.

2.1.1 SCISAT-1 and Solar Occultation Viewing Geometry

The Atmospheric Chemistry Experiment (ACE) satellite, also known as SCISAT-1 (shown in Figure 2.1), is a Canadian satellite which was launched on August 12th, 2003. It is being used for remote sensing of the Earth's atmosphere from a low Earth circular orbit (perigee 642 km, apogee 654 km, inclination 73.9º, period 97.7 minutes) [*Bernath et al.*, 2005]. SCISAT-1 is a small satellite that uses a circular instrument/component aluminum mounting plate (1.12 m in diameter) as the main structure element. It was designed, built and integrated by Bristol Aerospace Ltd. of Winnipeg, Manitoba, a division of Magellan Aerospace Corporation. The spacecraft is 3-axis stabilized as shown in Figure 2.1. SCISAT-1 has a total mass of 150 kg, a low power usage of 70 W supplied by a single solar panel, and total data storage capacity of 1.5 gigabytes.

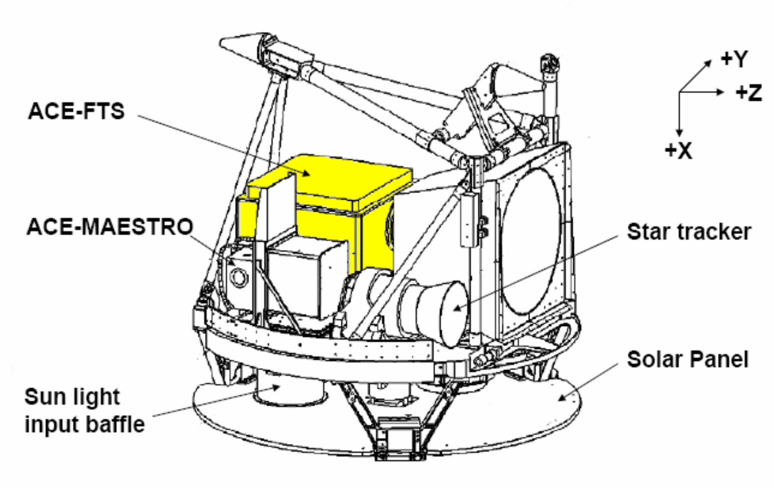

Figure 2.1 A schematic diagram of ACE satellite, SCISAT-1. Figure was adapted from the schematic diagram provide by Bristol Aerospace.

The ACE mission studies primarily the upper troposphere and stratosphere. It measures chemical constituents that influence the distribution of stratospheric ozone, a major chemical species that absorbs the sun's biologically-damaging ultraviolet radiation. To obtain the vertical concentration profiles of atmospheric species, ACE measures the absorption of sunlight using solar occultation geometry, in which the sun is used as a light source, and interferograms are recorded during sunrise and sunset as shown in Figure 2.2.

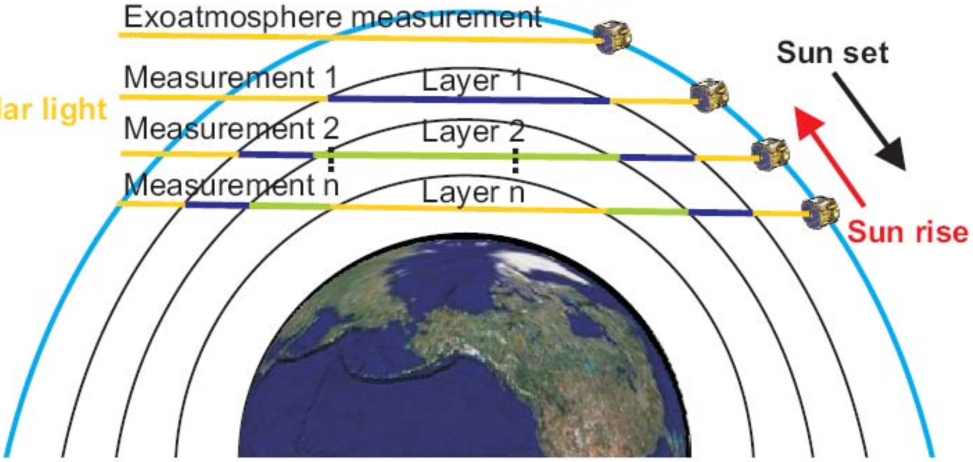

Figure 2.2 A schematic diagram showing the solar occultation geometry used in the ACE mission. Note that the distances are not to scale. Solar radiation passes through space and arrives at the upper boundary of the Earth's atmosphere. The blue, green and gray lines indicate the atmospheric absorption path lengths in layers 1, 2 and n, respectively. The attenuated solar radiation is recorded by the instruments on SCISAT-1 for a set of tangent heights during an occultation.

As SCISAT-1 orbits the Earth, the scientific instruments, which will be described in Section 2.2.1, point toward the sun and measure the intensity of solar radiation as shown in Figure 2.2. At high sun, that is, at the end of a sunrise or at the beginning of a sunset, the instruments record the solar radiation without attenuation by the atmosphere to obtain a reference spectrum exoatmosphere measurement. During a sunset, when the spacecraft moves towards the horizon, the instruments record the intensity of solar radiation which passes through the atmosphere and is attenuated by aerosols and gases that scatter and absorb sunlight. These spectra are recorded at different tangent heights, which are the minimum distances from the Earth's surface to the optical paths followed by the rays from the sun to the instrument. The atmospheric spectra are divided by the reference spectra to obtain transmittances. The sequence of atmospheric transmittances provides information on the concentrations of atmospheric constituents in each layer. The details of how the information is retrieved from the atmospheric transmittances are provided for ACE Fourier Transform Spectrometer (ACE-FTS) and ACE Measurement of Aerosol Extinction in the Stratosphere and Troposphere Retrieved by Occultation (ACE-MAESTRO) instruments in *Boone et al.* [2005] and *McElroy et al.* [2007], respectively. The vertical resolution is determined by the field-of-view (FOV) of the instrument, which is 3 to 4 km for the ACE-FTS and 1 to 2 km for ACE-MAESTRO.

SCISAT-1 has now exceeded its 2-year design lifetime, and no degradation of performance or functionality of the FTS instrument has been observed since launch. Satellite operations have been extended to 2009. Due to its excellent performance, SCISAT-1 is now moving beyond its original mission goals, and is providing excellent data related not only to ozone chemistry, but also to climate change and air pollution. In Chapter 3, the results on the first global observation of phosgene, a highly toxic atmospheric gas, will be presented.

2.1.2 MANTRA 2004 Balloon and Solar Occultation Viewing Geometry

The Middle Atmosphere Nitrogen TRend Assessment (MANTRA) is an international atmospheric observation program that uses a series of high-altitude balloon flights to study ozone chemistry in the mid-latitude stratosphere. Four balloon campaigns were held at Vanscoy (52.02ºN, 107.03ºW, and 510 m above sea level), Saskatchewan, in August 1998, August 2000, September 2002, and September 2004. In each flight, a high-altitude balloon carried instruments to measure vertical concentration profiles of stratospheric trace gases from a float altitude of about 35 km. The launch of the MANTRA 2004 balloon is shown in Figure 2.3.

A new portable FTS, an instrument built for the validation program of the ACE mission, was launched for the first time on a high altitude balloon in MANTRA 2004. The FTS was to observe the vertical concentration profiles of thirteen traces gases (O_3, CH_4, N_2O, H_2O,

HNO_3, HCl, NO, NO_2, CCl_3F, CCl_2F_2, HF, CO and N_2O_5) for the ACE validation program. To obtain a vertical resolution similar to that used in the ACE mission, this FTS was to use a solar occultation viewing geometry from the balloon gondola. The instrument description of the FTS is given in Section 2.2.2. The entire instrument configuration on the balloon platform, instrument tests, and its performance during two MANTRA 2004 balloon flights are given in Chapter 4.

Figure 2.3 MANTRA 2004 balloon was launched on September 1st, 2004. It contains 330208 m^3 (11.8 million cubic feet) of helium gas and carried 13 scientific instruments with a total weight of 658 kg (1450 lb) to the float altitude of about 37 km. Figure was downloaded from http://www.atmosp.physics.utoronto.ca/MANTRA.

2.1.3 CC-FTS, Nadir and Glint Viewing Geometries

The Carbon Cycle science by Fourier Transform Spectroscopy (CC-FTS) mission is a second-generation mission proposed to follow the Orbiting Carbon Observatory (OCO) mission [*Crisp et al.*, 2004] and the Greenhouse Gases Observing Satellite (GOSAT) mission

[*Hamazaki et al.*, 2005]. It aims to provide highly precise simultaneous observations of CO_2, CH_4, CO, N_2O and O_2 with a small pixel size of 1 km square by recording the solar radiation reflected by the Earth's surface from orbit.

The primary observation modes of CC-FTS are nadir viewing and glint viewing geometries for land and water surfaces, respectively (Figure 2.4 A). Glint viewing geometry corresponds to mirror-like specular reflection of sunlight from a flat water surface. The reason for using the glint viewing geometry is that in the short wave infrared bands (about 4000 – 6500 cm^{-1}) used to measure the principal greenhouse gases and the precursor CO, the albedo (the ratio of reflected to incident radiation) of water is too low, <1%, to provide a suitable source of radiance. The glint viewing geometry provides a high radiance similar to the nadir view over land.

In the nadir viewing geometry, the CC-FTS will scan from west to east to obtain cross track observations and will have a FOV with a dimension of 8 by 8 km (indicated by blue boxes in Figure 2.4 B). An array of 64 detectors placed in an 8 by 8 matrix will be used for the observation of greenhouse gases. A single scan of the FTS lasting 6.5 seconds yields a set of 64 interferograms for each FOV. Each detector pixel is identical and observes 1 km^2 within the 8 km square as shown in Figure 2.4 C-D. During the interferometer scan and recovery period, the satellite moves forward by ~50 km. Image motion compensation is necessary, so during each FTS scan the instrument pointing system views a single scene on the ground by scanning back along the satellite path by ~2.2º (Figure 2.4 B).

Contiguous coverage is not needed, and the CC-FTS mission is able to collect enough information to sample CO_2 on a regional scale. For example, a set of 64 interferograms per FOV will be able to cover the area of Kitchener-Waterloo, a Canadian twin city with a population of 300,000 (Figure 2.4 C). For example, a measurement over the University of Waterloo campus can provide information on the difference in greenhouse gas column densities between the student accommodation area near Columbia Lake (indicated by the orange box on the left in Figure 2.4 D) and the main campus of the University of Waterloo (indicated by the orange box on the right in Figure 2.4 D). In Chapter 4 the results of ground-based observations needed to select the spectral regions, spectral resolution and spectroscopic line parameter requirements for the CC-FTS mission are reported.

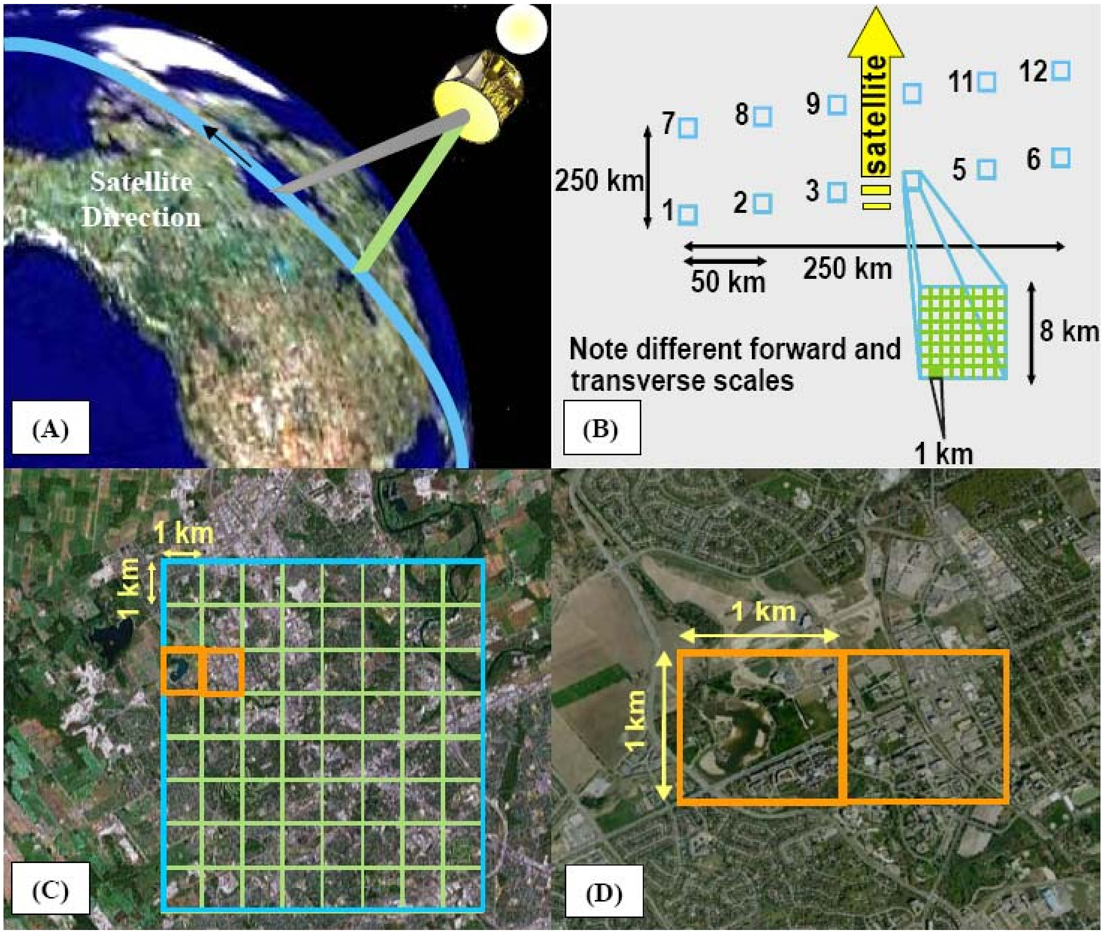

Figure 2.4 A schematic diagram of the operation modes, scan patterns and spatial coverage strategy to be used in the proposed CC-FTS mission as shown in (A) CC-FTS satellite orbiting the Earth and observing greenhouse gases in the nadir (shown by the green line) and glint viewing geometries (shown by the gray line); (B) During a single cross-track scan in the nadir viewing geometry, the CC-FTS makes 6 measurements in the cross track direction; (C) An array of 64 detectors placed in an 8 x 8 matrix will be used in the observations with a FOV that covers an area of 8 km square. Observations with a single FOV of CC-FTS are able to cover Kitchener-Waterloo (image courtesy of Google Earth); (D) Each detector pixel observes 1 km^2 which, for example, covers the Columbia Lake student accommodation (left pixel) or the main campus of University of Waterloo (right pixel).

2.1.4 WAO, NSO at Kitt Peak, PEARL (also known as ASTRO) and Ground-based Solar Viewing Geometry

The Waterloo Atmospheric Observatory (WAO) is located on the roof of the Centre for Environmental and Information Technology (CEIT), University of Waterloo (43.47ºN, 80.54ºW, and 319 m above sea level). WAO is currently equipped with the following instruments: the Portable Atmospheric Research Interferometric Spectrometer for the Infrared (PARIS-IR), an ABB-Bomem DA8 FTS, an ABB-Bomem sun tracker, a sun tracker built by Denver University, and a commercially available weather station (Vantage Pro Plus manufactured by Davis Instruments Corp) that records the local metrological conditions, UV radiation and solar irradiance. Figure 2.5 shows how observations were performed using the two FTSs. The description of PARIS-IR and the ABB-Bomem FTS will be given in Section 2.2.2 and Section 2.2.3, respectively. WAO has four major goals: (1) to function as the home base of PARIS-IR to prepare for field campaigns and to carry out instrument maintenance; (2) to monitor concentrations of atmospheric trace gases related to ozone chemistry and to observe their trends at mid-latitudes; (2) to perform ground-based observations needed for future satellite missions such as CC-FTS; (4) to validate satellite missions such as the on-going ACE mission and the CC-FTS mission in the future.

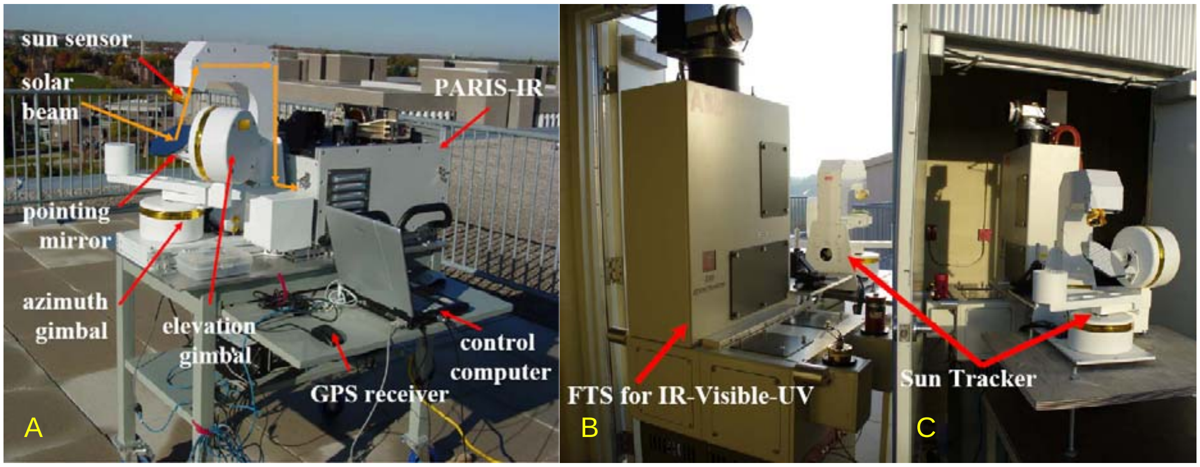

Figure 2.5 PARIS-IR (A) and the ABB-Bomem DA8 FTS for IR-Visible-UV (B: rear view; C: front view) observing the atmosphere at WAO, Waterloo, Ontario, Canada.

The National Solar Observatory (NSO) has facilities at Kitt Peak (31.96°N, 111.59°W, and 2096 m above sea level), Arizona, USA. The primary goal of the NSO is to advance knowledge of the sun, both as an astronomical object and as the dominant external influence on the Earth, by providing observational opportunities to the research community (http://www.nso.edu/general/docs/ar2006_final.pdf). The two major facilities of NSO at Kitt Peak are Synoptic Optical Long-term Investigations of the Sun (SOLIS) and the McMath-Pierce Telescope Complex (MPTC) (http://nsokp.nso.edu/). The McMath-Pierce 1-meter FTS is located in MPTC, and has provided atmospheric absorption measurements over 28 years. It was also used as part of the advanced study for the CC-FTS mission. The description of this instrument will be given in Section 2.2.4.

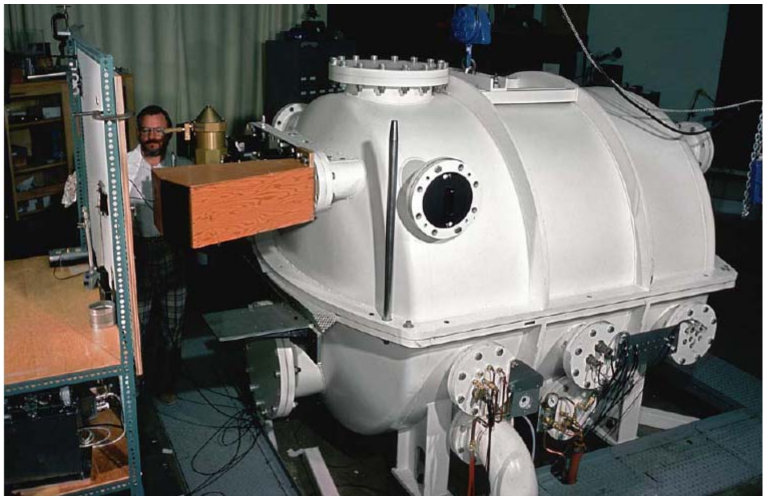

Figure 2.6 The McMath-Pierce 1-meter FTS housed in a vacuum vessel in the McMath-Pierce Telescope Complex at Kitt Peak, Arizona, USA. Courtesy of Dr. Peter F. Bernath.

The Arctic STratospheric Ozone Observatory (ASTRO) is an atmospheric observatory built in 1992 at Eureka, Nunavut (80.05°N, 86.42°W, and 619 m above sea level) Canada. It was operated by Environment Canada until 2002. It was renamed the Polar Environment Atmospheric Research Laboratory (PEARL) in 2005 and is currently operated by the

Canadian Network for the Detection of Atmospheric Change (CANDAC, http://www.candac.ca/). CANDAC is carrying out studies on atmospheric chemistry and the environment in the Canadian Arctic. It is equipped with a number of scientific instruments such as LIght Detection and Ranging (LIDAR) [*Bird et al.*, 1996], Brewer spectrophotometer [*Savasktiouk and McElroy*, 2005], ozonesondes [*Davies et al.*, 2000], UV-visible spectrometers [*Kerzenmacher et al.*, 2005; *Bassford et al.*, 2001; 2005], high resolution FTS [*Donovan et al.*, 1997; *Farahani et al.*, 2007], and other optical equipment [*Pommereau and Goutail*, 1988]. Atmospheric absorption spectra have been recorded since 1993 using an ABB-Bomem DA8 FTS. The laboratory also is used for validation of satellite instrument performance. For example, it has been used in the validation of satellite missions such as the ACE since 2004 [*Bernath et al.*, 2005; *Kerzenmacher et al.*, 2005; *Fu et al.*, in preparation for *Atmos. Phys. Chem.*]. The description of this instrument is given in Section 2.2.5. Atmospheric observations, together with analysis of FTS data from the DA8 FTS and PARIS-IR, are described in Chapter 6.

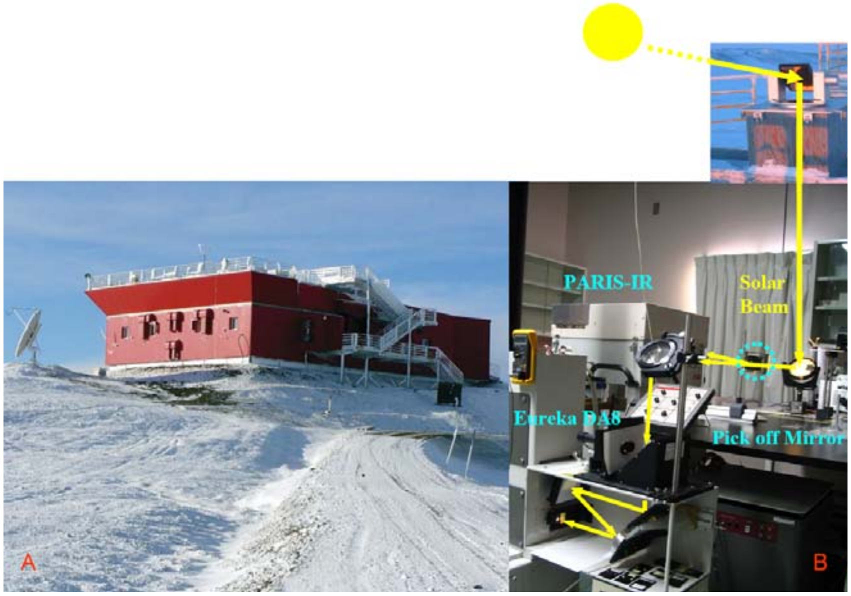

Figure 2.7 Overview of the PEARL and two FTSs in the Eureka 2006 campaign. (A) PEARL located at Eureka, Nunavut Canada; (B) the ABB-Bomem DA8 spectrometer and PARIS-IR simultaneously observing the Arctic atmosphere in PEARL from February 21st to March 8th, 2006.

Solar radiation passes through the entire atmosphere and is attenuated by atmospheric constituents due to absorption and scattering. When using FTSs to observe the atmosphere from the ground at WAO, NSO at Kitt Peak, and at PEARL, the sun is used as a light source and atmospheric absorption spectra are recorded in the solar viewing geometry as shown in Figure 2.8. Measurements using FTSs on the ground provide a way to observe the atmosphere with good sensitivity, relatively low cost and with instrumental accessibility for maintenance over the long term. However, the ground-based solar viewing geometry on the ground provides low vertical resolution relative to the solar occultation viewing geometry used by space-borne instruments, especially for the middle and upper atmosphere where the pressure is low. Height information in ground-based absorption spectra comes from the observation of pressure-broadening of the lines. The total column density of a trace gas in the optical path through the atmosphere can be obtained by the application of the Beer's law. However, the vertical distribution of a trace gas is difficult to obtain from the line shape which contains pressure-broadening information from each atmospheric layer. The retrieval of a height profile from a ground-based solar spectrum is an under-constrained or ill-posed problem. As explained in Chapter 1, Rodgers developed a method, called the Optical Estimation Method (OEM), to solve this type of problem [*Rodgers*, 2000].

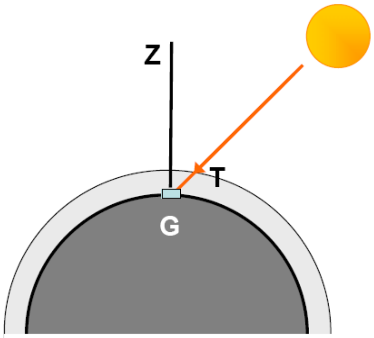

Figure 2.8 A schematic diagram of the ground-based solar viewing geometry. G is the location of the observatory. GZ indicates the zenith. Solar radiation arrives at the point T, the top of atmosphere, and then arrives at the input optics of the instrument on the ground after attenuation by absorption and scattering by atmospheric constituents.

2.2 Instrumentation

Remote sensing instruments can be classified into two groups: Passive instruments, which measure the electromagnetic radiation emitted or absorbed by an object, and active instruments, which emit electromagnetic radiation and compare it with the back scattered or reflected signal. In this thesis, five passive instruments that make use of Fourier transform spectroscopy were utilized for atmospheric remote sensing: 1) a satellite-borne high resolution FTS (ACE-FTS) was used for the first global phosgene observations; 2) a new compact, portable FTS (PARIS-IR) was used on the ground and on a balloon; 3) an ABB Bomem DA8 IR-Visible-near UV FTS located at the WAO; 4) a folded cat's-eye Michelson interferometer located at the NSO together with the third instrument were utilized in the advanced study for the CC-FTS mission; 5) an ABB Bomem DA8 Fourier transform IR spectrometer located at Polar Environment Atmospheric Research Laboratory (PEARL) was also used in during the 2006 Canadian Arctic ACE Validation Campaign.

2.2.1 Atmospheric Chemistry Experiment Fourier Transform Spectrometer

The primary instrument on SCISAT-1, the ACE-FTS, is a Fourier transform spectrometer coupled with an auxiliary 2-channel visible (525 nm) and near infrared imager (1020 nm). The imagers provide important information on pointing and help to detect the presence of clouds in the FOV. The other instrument onboard SCISAT-1 is ACE-MAESTRO shown in Figure 2.1, a small UV-Visible-Near Infrared spectrophotometer. Since the results used in this thesis are not from ACE-MAESTRO, the following section will focus only on the ACE-FTS.

The ACE-FTS was designed and built by ABB-Bomem in Québec City. The ACE-FTS has two photovoltaic detectors (InSb: indium antimonide; MCT: mercury cadmium telluride) covering the 750 to 4400 cm^{-1} spectral region with a resolution of 0.02 cm^{-1} (±25 cm MOPD, maximum optical path difference).

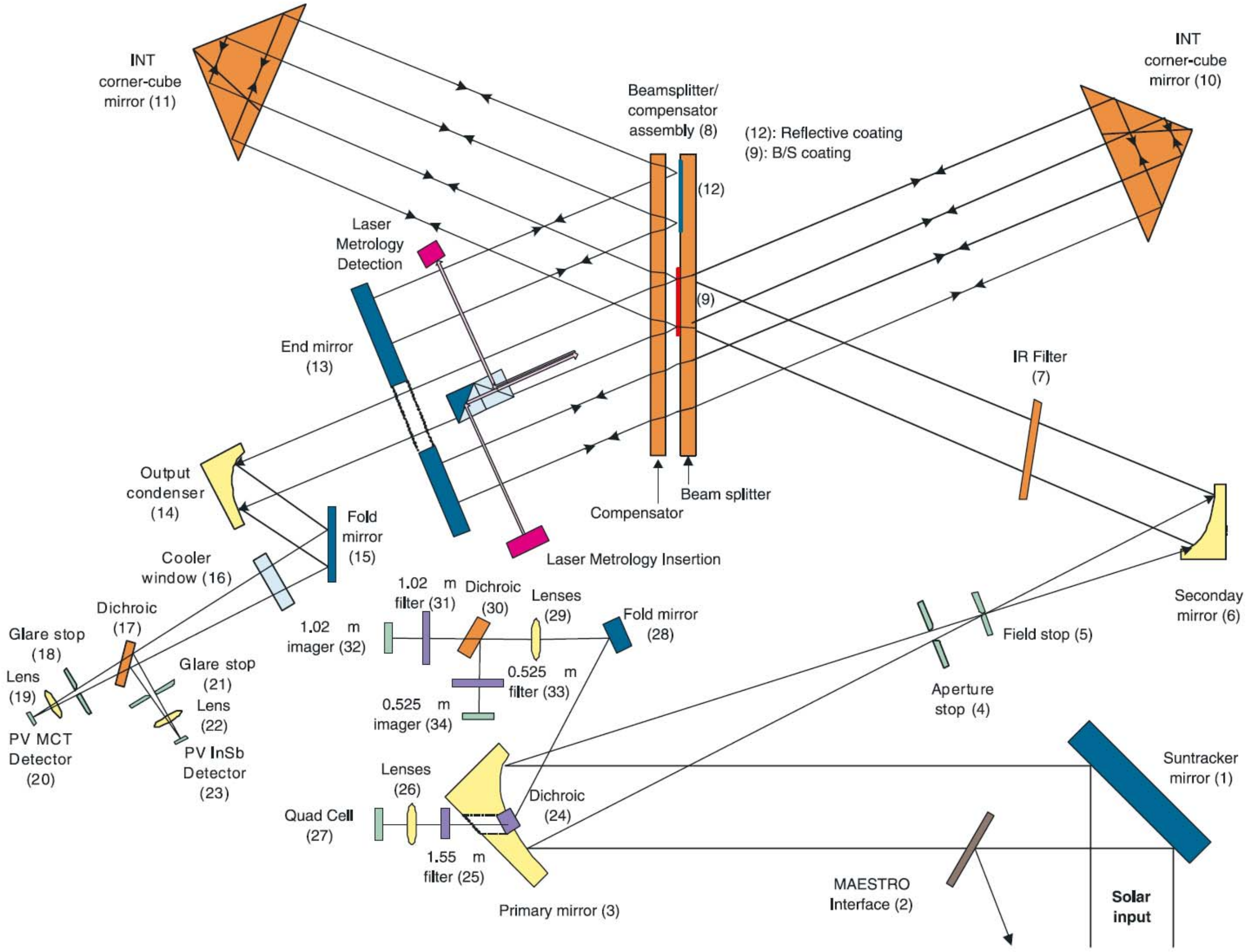

Figure 2.9 Illustration of the ACE-FTS optical layout, courtesy of ABB-Bomem.

The Optical Path Difference (OPD) was generated by two cube corners rotating on a central flex pivot. An “end” mirror was placed inside the interferometer to increase the OPD by double-passing solar radiance (shown in Figure 2.9). The ACE-FTS records double-sided interferograms by solar occultation, and interferograms are recorded in the limb geometry during sunrise and sunset. A pointing mirror, controlled by a quad cell servo-loop, locks on the sun center and tracks it when making measurements. Fourier transformation of interferograms is carried out on the ground at the ACE Science Operation Center (SOC) to obtain the desired atmospheric spectra. The Signal-to-Noise Ratio (SNR) of each solar spectrum from a 2 second scan is typically 300. The measured spectra are processed to obtain the volume mixing ratio (VMR) profiles of trace gases in the Earth's atmosphere, as well as pressure and temperature profiles at the SOC at the University of Waterloo [*Boone et al.*, 2005].

2.2.2 Portable Atmospheric Research Interferometric Spectrometer for the Infrared

Portable Atmospheric Research Interferometric Spectrometer for the Infrared (PARIS-IR), a new portable high resolution Fourier transform spectrometer, was built by ABB-Bomem, Inc., in Québec City for the Waterloo Atmosphere Observatory (WAO). It has relatively high spectral resolution (0.02 cm^{-1}) with a very compact design. A suntracker, also from ABB-Bomem, is used to direct radiance from the sun into the spectrometer, and atmospheric absorption measurements can be made from sunrise to sunset. PARIS-IR is being used regularly to monitor atmospheric trace gases from WAO. It has also participated in Canadian ground-based field campaigns at PEARL in Eureka, Nunavut and in the MANTRA 2004 balloon campaign in Vanscoy, Saskatchewan. From these solar absorption results, total column densities are obtained for key atmospheric constituents such as ozone and other species involved in ozone chemistry such as HNO_3, NO_2 and HCl, together with measurements of primarily tropospheric species such as N_2O and CH_4.

PARIS-IR has a design similar to that of ACE-FTS, and measurements recorded by PARIS-IR are being used to validate data from the ACE-FTS [*Kerzenmacher et al.*, 2005; *Sung et al.*, 2007; *Fu et al.*, in preparation for *Atmos. Phys. Chem.*]. PARIS-IR has the same resolution (0.02 cm^{-1}) and spectral coverage region (750 to 4400 cm^{-1}) as the ACE-FTS due to their similar design and the use of components such as the beam splitter that were flight spares for the satellite instrument. PARIS-IR has a mass of about 66 kg, dimensions of 60 cm x 60 cm x 42 cm, and an average power consumption of 62 W. The instrument has a circular field of view (FOV) of 3.32 mrad. It can sustain a mechanical shock of up to 10g (g = 9.8 m/s^2). These features make PARIS-IR an excellent instrument for field measurements.

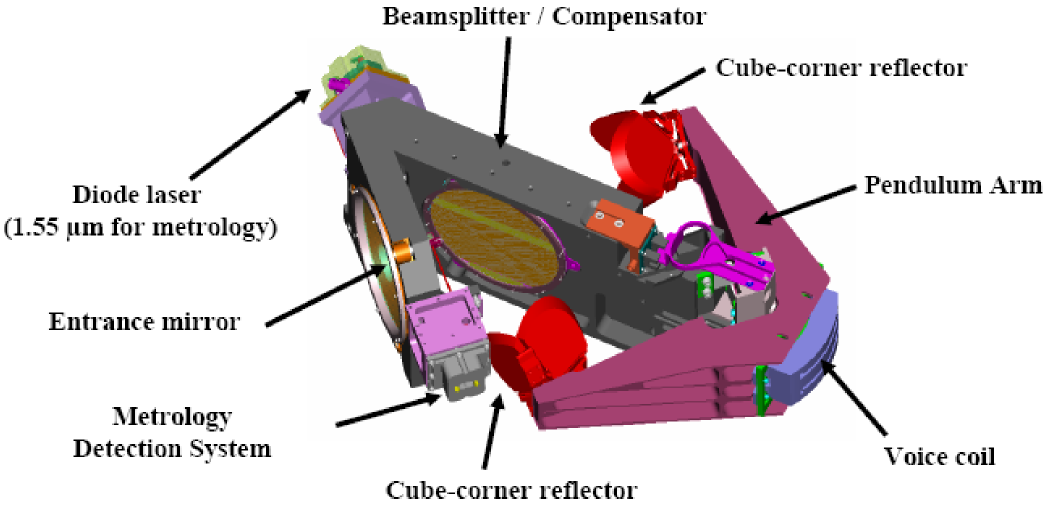

Figure 2.10 Double-pendulum interferometer for the PARIS-IR instrument. Two cube-corner reflectors mounted on a rotating structure driven by a magnetic voice coil around a pivot are used as moving elements to generate the optical path difference. Courtesy of ABB-Bomem.

The core of this compact, high resolution spectrometer is a “double pendulum” interferometer (DPI; shown in Figure 2.10). Two cube-corner reflectors mounted on a rotating structure driven by a magnetic voice coil around a pivot are used as moving elements to generate the optical path difference. The first DPI interferometer design was developed in the 1980's [*Burkert et al.*, 1983]. The advantages of DPI-type instruments are compact size, low power consumption, and insensitivity to linear acceleration. The beamsplitter is made from zinc selenide (ZnSe). The corner cubes are coated with protected gold, and the only moving components are the cube-corner reflectors. A diode laser operating at 1.55 μm provides interference fringes to measure the optical path difference (OPD), and these fringes are used to trigger the sampling of the interferogram. There are eight options for the MOPD setting, corresponding to 0.02, 0.1, 0.2, 1.0, 2.0, 5.0, 10.0, and 25 cm. These MOPD values correspond to spectral resolutions (defined as 0.5/MOPD) of approximately 25.0, 5.0, 2.5, 0.5, 0.25, 0.10, 0.05, and 0.02 cm^{-1}, respectively. The spectral observation time varies according to the MOPD setting and the scan speed of the interferometer. Four options for the scanning speed of the interferometer are available: 0.83 cm/s, 1.25 cm/s, 1.67 cm/s and 2.5 cm/s.

The optical path layout of PARIS-IR is illustrated in Figure 2.11. The PARIS-IR optical design is fully compensated for tilt and shear of both moving and stationary optics inside the interferometer, mainly because the radiation is double-passed through the FTS using the "entrance mirror" (shown in Figure 2.11). The pointing mirror in the sun tracker, controlled by the sun tracker servo-loop, locks on the radiometric center of the sun and provides fine tracking while PARIS-IR is taking measurements. The solar beam is sent through the PARIS-IR input window by the sun tracker. The 44 mm diameter solar beam is directed to the optical bench by two flat mirrors (73 mm x 73 mm) coated with protected gold. The solar beam is then directed to the 1.73X magnification telescope primary mirror. The primary mirror reflects the solar beam through the entrance aperture (5 mm diameter) and field stop (0.5 mm diameter) to the secondary collimator mirror. The collimated beam with a diameter of 25.4 mm is then directed towards the interferometer. An infrared filter (30 mm diameter) is installed between the input optics and the interferometer to minimize the thermal load. The IR signal goes through a 25.4 mm diameter port in the entrance mirror. In order to mount the optics in a relatively small volume, the interferometer is double-passed and cube corner mirrors in both arms of the interferometer are scanned. The output of the interferometer is

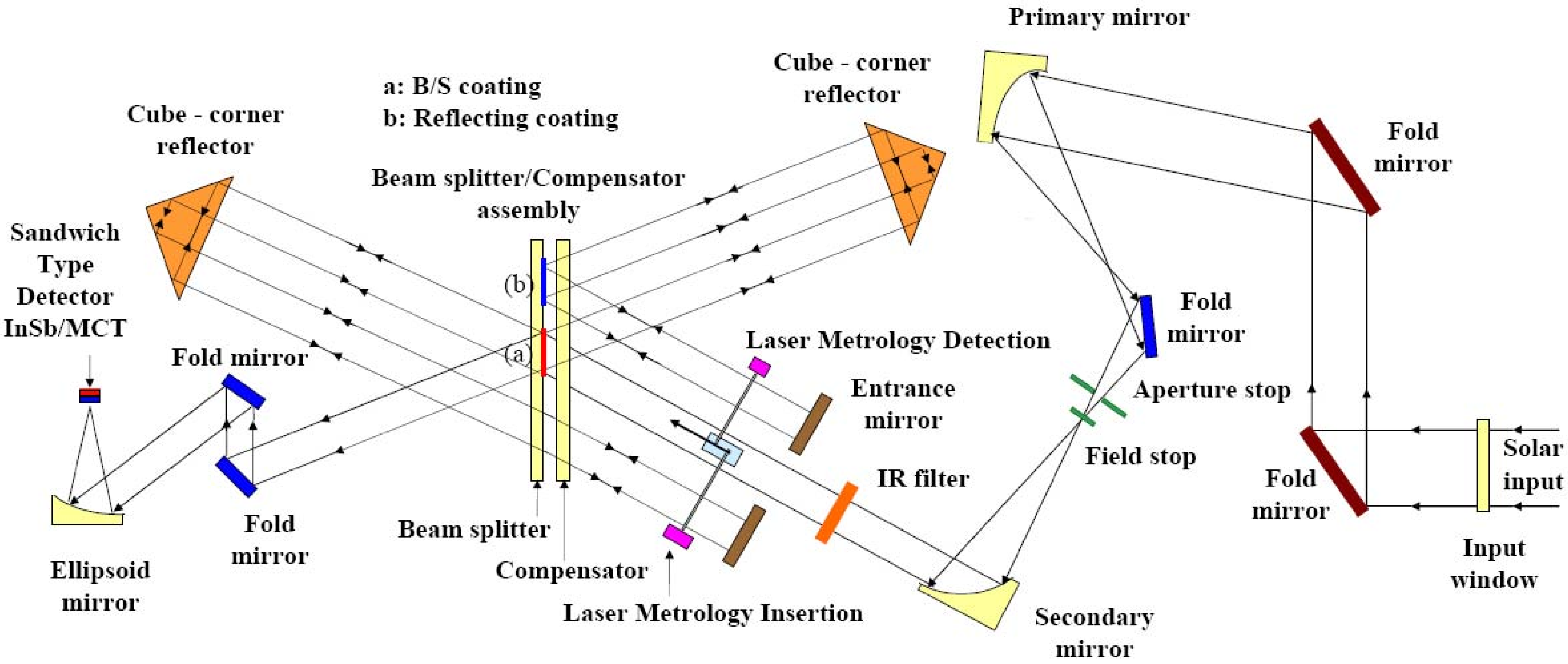

Figure 2.11 Schematic diagram showing optical layout of the PARIS-IR instrument. The PARIS-IR optical design is fully compensated for tilt and shear of both moving and stationary optics inside the interferometer, mainly because the radiation is double-passed through the FTS using the “entrance mirror”.

then directed by a series of flat mirrors and an ellipsoidal mirror into the detector. The stainless-steel detector dewar has a capacity of 0.4 liters of liquid N_2 and a hold time of approximately 48 hours. The two detectors (from Judson), a photovoltaic indium antimonide (InSb) and a photoconductive mercury cadmium telluride (MCT) detector, are mounted in a sandwich arrangement. Using these two detectors simultaneously, PARIS-IR covers the spectral region from 750 to 4400 cm^{-1}. Double sided interferogams are stored on the hard disk of the main control computer inside the PARIS-IR case. These data are transferred to an external data processing computer using a 10 Mb/s Ethernet communication port.

Using ABB-Bomem's software package L1bDPS (version 1.3), the desired atmospheric spectra were generated from the double-sided interferograms recorded by PARIS-IR. The L1bDPS includes several necessary processes including wavenumber calibration, phase correction, detector nonlinearity correction, channel spectrum correction, residual DC removal, and Fourier transformation. The L1bDPS program is based on the level 0 (raw interferograms) to level 1 (calibrated spectra) software developed by ABB-Bomem for the ACE-FTS instrument [*Bernath et al.*, 2005].

The output frequency of PARIS-IR's diode laser, which is used to control the sampling of the interferogram, is affected by the ambient temperature. The spectra recorded by PARIS-IR thus require careful wavenumber calibration because of the drift of the diode laser frequency. The L1bDPS program can obtain the calibration factor needed for each interferogram based on unsaturated atmospheric lines of species such as N_2O. The measured interferogram is not a real symmetric function because of experimental, instrumental, and computational limitations. A complete reconstruction of the spectrum thus requires a complex Fourier transformation to handle both amplitude and phase information. The needed phase correction, to obtain a real spectrum with only noise in the imaginary plane, is made by the L1bDPS program. In addition, the nonlinear response of the photoconductive MCT detector must be corrected. The L1bDPS program obtains non-linearity characterization parameters by minimizing the out-of-band optical artifacts, and uses them for nonlinearity correction of the interferogram [*Jeseck et al.*, 1998].

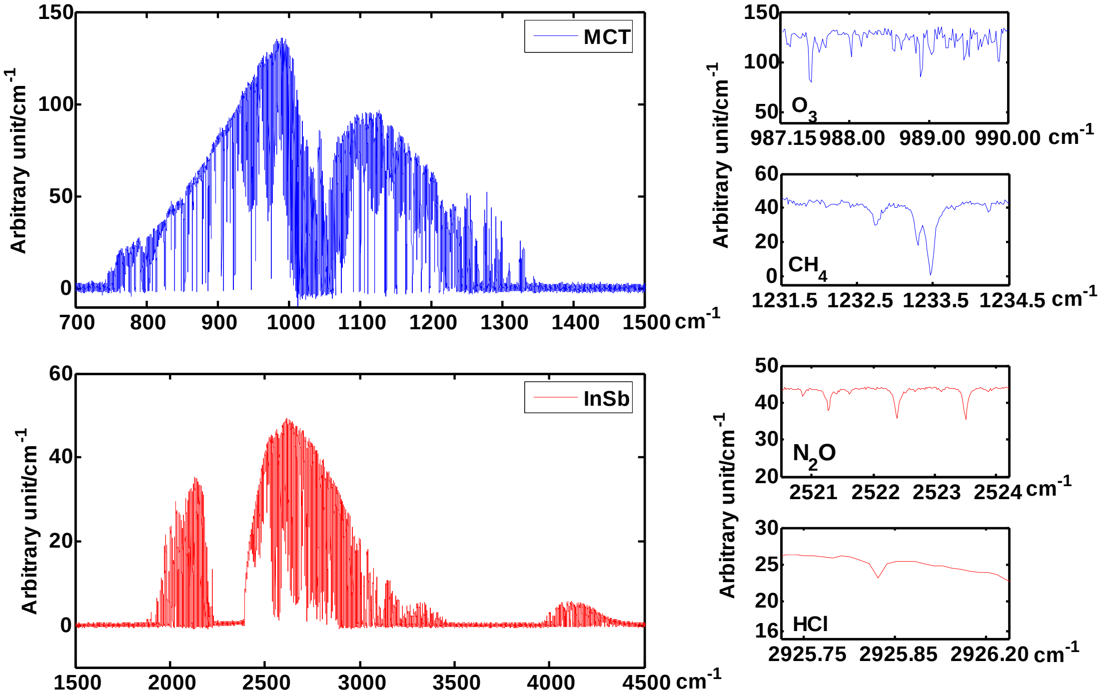

Figure 2.12 Sample solar absorption spectra recorded using PARIS-IR observed with a solar zenith angle of 65.77° at WAO on November 3rd, 2004. Spectra are from the co-addition of 20 scans (400 second observation).

Figure 2.12 displays typical ground-based infrared atmospheric solar absorption spectra generated from interferograms using the L1bDPS program. They have a 0.02 cm^{-1} resolution and were observed at WAO in November 3rd, 2004 with a solar zenith angle of 65.77°. The left side in Figure 2.12 shows the overview of a typical spectrum recorded using MCT (upper plot) and InSb (lower plot) detectors. The range of signal-to-noise ratios (SNR) over the 750-4400 cm^{-1} spectral region is from 150:1 to 300:1 (typically 20 scans recorded in 400 seconds are coadded to obtain these spectra). The right side of Figure 2.12 shows several spectral segments (microwindows) used in the retrieval process. The retrieval process uses the SFIT2 program to extract the column densities of O_3, CH_4, N_2O and HCl target molecules from the appropriate microwindows (O_3: 987.15 - 990.0 cm^{-1}; CH_4: 1231.5 - 1234.5 cm^{-1}; N_2O: 2520.5 - 2524.2 cm^{-1}; HCl: 2925.65 - 2926.20 cm^{-1}). In these microwindows, the absorption lines of the target species are well isolated, i.e., the absorption lines of the target molecules are minimally affected by absorption of the interfering species such as H_2O and CO_2.

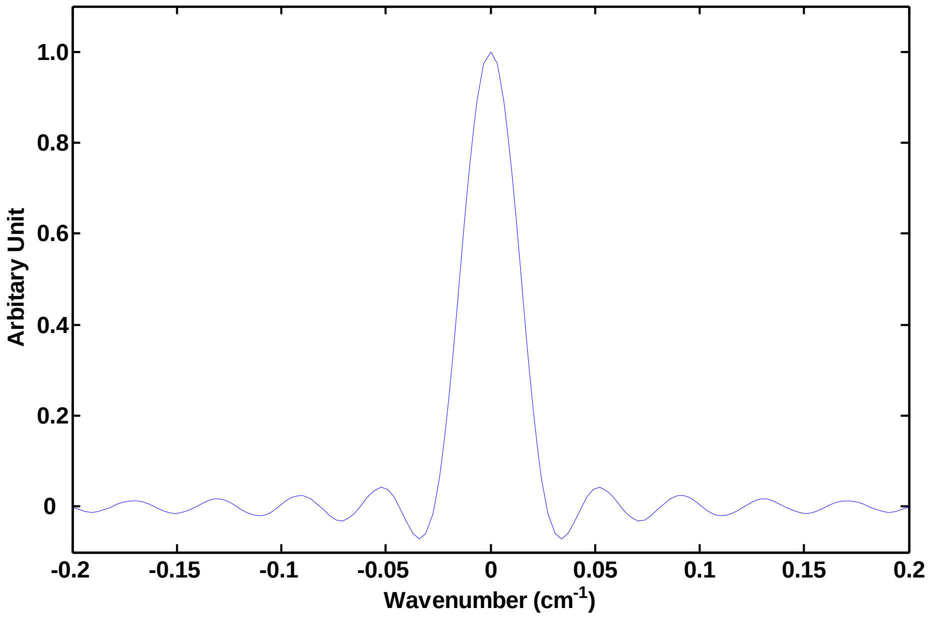

Figure 2.13 ILS of the PARIS-IR instrument, which was derived from a N_2O gas cell spectrum around 2500 cm^{-1}. The PARIS-IR line shape is symmetric and is nearly a sinc function.

The observed spectral lines shapes can be affected by instrumental effects (such as optical misalignment) and by the observing conditions (e.g. clouds in the FOV). These effects are considered by including an Empirical Apodization Parameter Function (EAPF) in the spectral analysis [*Pougatchev et al.*, 1995; *Rinsland et al.*, 1998]. Figure 2.13 shows the instrument line shape function (ILS) of PARIS-IR obtained by Fourier transformation of the EAPF. The EAPF was derived from a N_2O gas cell spectrum in the 2500 cm^{-1} region. The PARIS-IR line shape is symmetric and is nearly a sinc (sinx/x) function.

2.2.3 The ABB Bomem DA8 FTS (IR-Visible-near UV) at WAO

An ABB Bomem DA8 FTS was installed at WAO in July 2005 and used for atmospheric remote sensing. The DA8 spectrometer is a plane mirror Michelson interferometer with a maximum optical path difference of 25 cm, providing a maximum spectral resolution of 0.02 cm^{-1}. The interferometer inside the DA8 is a modified Michelson interferometer that uses the Dynamical Alignment Technique (DAT) from ABB-Bomem, as shown in Figure 2.14. DAT compensates for the angular instability of the scanning mirror by adjusting the stationary mirror M1 which is typically fixed in a classical Michelson interferometer. The DAT provides a fixed optical axis through the beam splitter which helps to keep the modulation efficiency constant.

Table 2.1 Spectral coverage of the detectors, beamsplitters, internal sources for the DA8 FTS.

Detector	Spectral Range[b] (cm^{-1})	Beam Splitter	Spectral Range[b] (cm^{-1})	Internal Source	Spectral Range[b] (cm^{-1})
Mercury Cadmium Telluride[a]	800 – 5000	KBr	450 – 5000	Mercury Lamp	5 – 200
Indium Antimonide[a]	1800 – 11000	CaF_2	1200 – 10000	Globar	450 – 8500
Indium Gallium Arsenide[a]	6350 – 11000	Quartz (Visible)	4000 – 27000	Quartz/ Halogen Lamp	2500 – 15000
Silicon	8500 – 52000	Quartz (UV)	8500 – 55000	Deuterium Lamp[c]	9500 – 55000

[a] Liquid nitrogen-cooled.

[b] The spectral ranges are optimum values.

[c] Deuterium lamp is an externally mounted source.

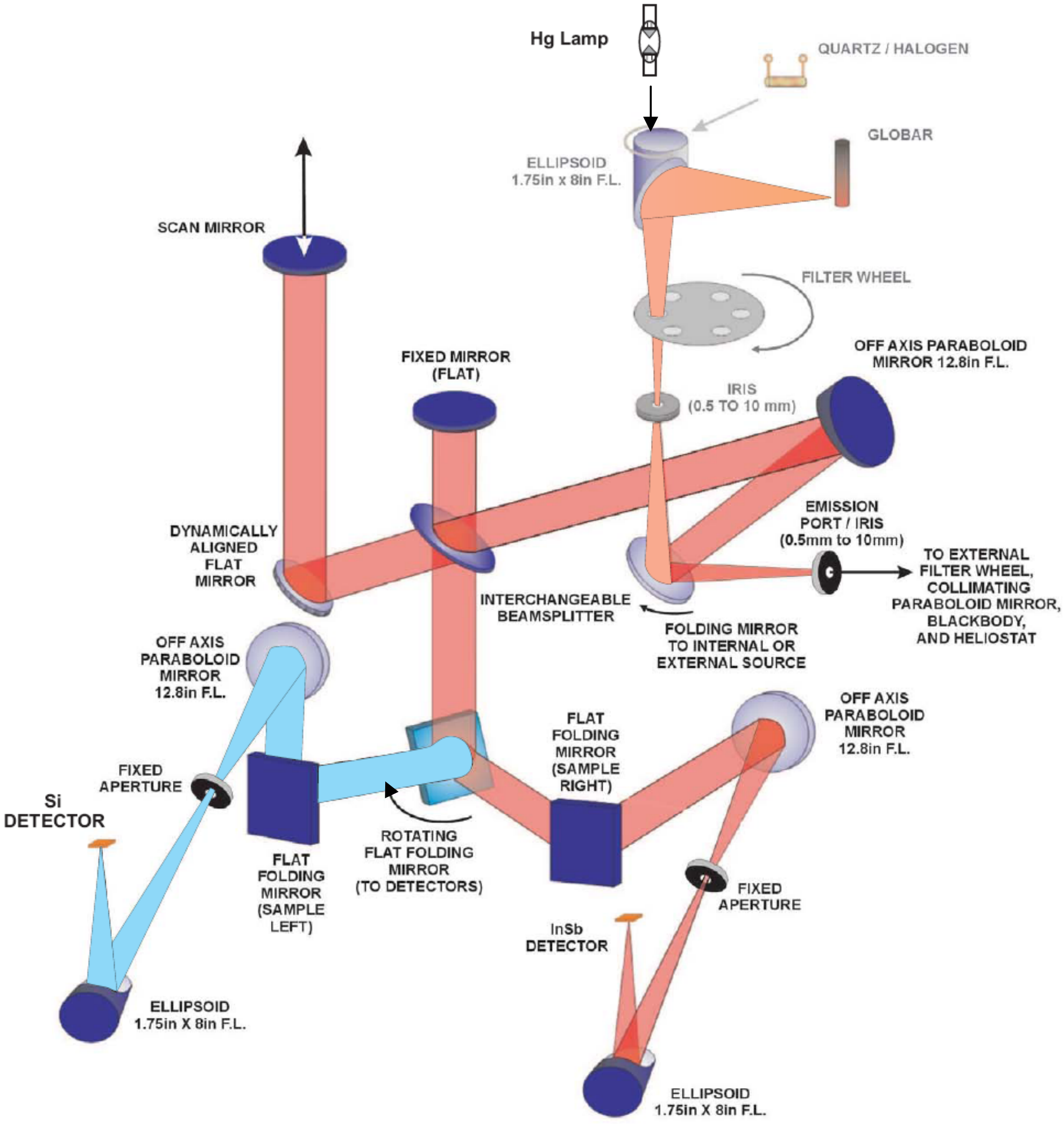

Figure 2.14 The ABB-Bomem DA8 FTS at WAO is a plane mirror Michelson interferometer (see text for details). A movable folding mirror selects between the emission port used for solar absorption measurements and the internal sources used for instrument alignment. A rotating mirror selects between the detector in left chamber and the one in right chamber to record spectra with the desired spectral range. Figure was adapted from optical path schematic plot provided by ABB-Bomem Inc.

A movable folding mirror selects between the emission port used for solar absorption measurements and the internal sources used for instrument alignment and tests of instrument performance. A rotating mirror selects between the detector in the left chamber and the one in the right chamber to record spectra with the desired spectral range. The DA8 FTS at WAO is currently equipped with four detectors and four beam splitters. This combination makes the DA8 at WAO capable of recording atmospheric spectra from the infrared to ultraviolet (500 – 55,000 cm^{-1}). The spectral coverage of detectors, beam splitters, internal sources and external sources used with the WAO DA8 are shown in Table 2.1.

2.2.4 The McMath-Pierce FTS in NSO at Kitt Peak

The McMath-Pierce FTS is housed in a vacuum vessel located at the NSO at Kitt Peak. It is available for use either in conjunction with the solar beam from the McMath-Pierce telescope or with laboratory sources. It can provide a broad spectral coverage of 550 to 45,000 cm^{-1} with the available optical configurations (see Table 2.2).

Table 2.2 Spectral coverage of the detectors and beamsplitters of the McMath-Pierce FTS[a].

Detector	**Spectral Range cm^{-1}**	**Beam Splitter**	**Spectral Range cm^{-1}**
Arsenic-Doped Silicon	500 – 1850	KCl	550 – 3000
Indium Antimonide Diode	1850 – 15000	CaF_2	1250 – 9000
Silicon PIN Diode	9000 – 45000	Visible Quartz	4000 – 27000
		UV Quartz	6500 – 45000

[a] Data obtained from http://nsokp.nso.edu/mp/fts/aboutFTS.html.

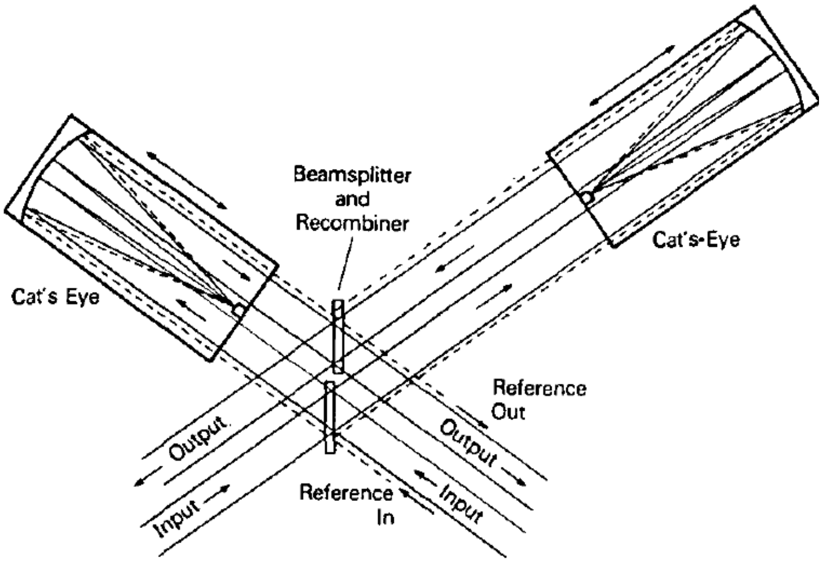

A.) Dual-Beam Configuration

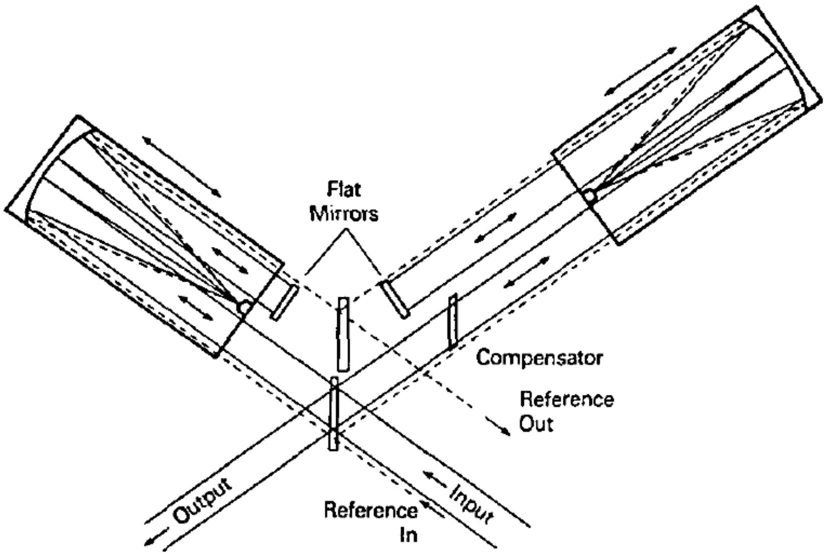

B.) Double-Pass Configuration

Figure 2.15 A schematic diagram of the McMath-Pierce Fourier transform spectrometer at Kitt Peak, Arizona, USA. (A) the dual-input and output configuration and (B) in the double-pass, single-input/output configuration, courtesy of *Jennings et al.* [1985].

The heart of the McMath-Pierce FTS is a folded cat’s-eye Michelson interferometer. It is a modified version of the classical Michelson interferometer that uses cat's eye retroreflectors instead of plane mirrors. In normal operation the instrument has a maximum spectral resolution of 0.005 cm^{-1} (MOPD = 100 cm), but it can also be operated in a double pass mode with a maximum spectral resolution of 0.0025 cm^{-1} (MOPD = 200 cm) [*Jennings et al.*, 1985].

The dual-input and output configuration is the standard mode of the McMath-Pierce FTS as shown in Figure 2.15 (A). The input beams from two input apertures are divided at a beam splitter and sent to two cat's-eyes. The beams returning from the cat's-eyes are recombined at a second beam splitter and the two output beams are sent to a pair of detectors. Each cat's-eye travels a maximum of 25 cm, yielding a MOPD of 100 cm. In this mode, the instrument receives radiation from two input apertures and is able to detect the difference between two input intensities at the two output apertures. The use of two input ports helps in subtracting a large background common to both inputs from a small signal present at only one input (e.g. for stellar observations).

For the double-pass, single-input and output mode, a flat mirror is placed in the output beam from each cat's-eye, reflecting the beams back through the cat's-eyes to the first beam splitter. This configuration is shown in Figure 2.15 (B). A single detector is placed at the second input port shown in Figure 2.15 (A), which is now the output port of the FTS. A compensator, matched to the beam splitter substrate, is used in the double-pass configuration. This double-pass configuration gives a MOPD of 200 cm from the 25 cm movement of the cat's-eyes.

2.2.5 ABB-Bomem DA8 Fourier Transform Spectrometer at PEARL

An ABB-Bomem DA8 FTS was installed at PEARL in February 1993 [*Donovan et al.*, 1997; *Farahani et al.*, 2007]. It has the same design as the ABB Bomem DA8 FTS at WAO shown in Figure 2.7. However, the DA8 FTS in PEARL has a narrower spectral range and a higher maximum spectral resolution than the DA8 at WAO. The DA8 FTS has a maximum spectral resolution of 0.004 cm^{-1} (MOPD = 250 cm) and is equipped with two detectors, MCT and InSb, covering the spectral range from 700 to 5100 cm^{-1}. Nine consecutive optical filters are used with the DA8 FTS to improve the SNR. The filters, spectral ranges, and detectors used in the DA8 spectrometer are shown in Table 2.3. A mirror-tracking system, which is mounted on the rooftop of the PEARL facility, is used to direct sunlight into the input optics of the DA8 spectrometer.

Table 2.3 Filters, their spectral ranges, and detectors used for the DA8 FTS at PEARL.

Filter	Spectral Range (cm^{-1})	Maximum Optical Path Difference (cm)	Detector
S0	3900 - 5100	166.67	InSb
S1	3950 - 4300	250.00	InSb
S2	2500 - 3500	250.00	InSb
S3	2400 - 3300	250.00	InSb
S4	1950 - 2800	250.00	InSb
S5	1800 - 2050	250.00	InSb
S6	700 - 1300	250.00	MCT
S7	2750 - 3100	250.00	InSb
S8	2400 - 3100	250.00	InSb

2.3 References

Bassford M.R., McLinden C.A., and Strong K., (2001), Zenith-Sky Observations of Stratospheric Gases: The Sensitivity of Air Mass Factors to Geophysical Parameters and the Influence of Tropospheric Clouds, *J. Quant. Spectrosc. Radiat. Transfer*, **68**, 657-677.

Bassford M.R., Strong K., McLinden C.A., and McElroy C.T. (2005), Ground-based measurements of ozone and NO_2 during MANTRA 1998 using a new Zenith-Sky spectrometer, *Atmos. Ocean.*, **43**, 325-338.

Bernath P.F., McElroy C.T., Abrams M.C., Boone C.D., Butler M., Camy-Peyret C., Carleer M., Clerbaux C., Coheur P.-F., Colin R., DeCola P., DeMazière M., Drummond J.R., Dufour D., Evans W.F.J., Fast H., Fussen D., Gilbert K., Jennings D.E., Llewellyn E.J., Lowe R.P., Mahieu E., McConnell J.C., McHugh M., McLeod S.D., Michaud R., Midwinter C., Nassar R., Nichitiu F., Nowlan C., Rinsland C.P., Rochon Y.J., Rowlands N., Semeniuk K., Simon P., Skelton R., Sloan J.J., Soucy M.-A., Strong K., Tremblay P., Turnbull D., Walker K.A., Walkty I., Wardle D.A., Wehrle V., Zander R., and Zou J., (2005), Atmospheric Chemistry Experiment (ACE): Mission Overview, *Geophys. Res. Lett.*, **32**, L15S01, doi:10.1029/2005GL022386.

Bird J.C., Carswell A.I., Donovan D.P., Duck T.J., Pal S.R., Whiteway J.A., and Wardle D.I., (1996), Stratospheric studies at the Eureka NDSC station using a Rayleigh/Raman differential absorption lidar, paper presented at XVIII Quadrennial Ozone Symposium-96, Univ. of L'Aquila, L'Aquila, Italy.

Boone C.D., Nassar R., Walker K.A., Rochon Y., McLeod S.D., Rinsland C.P., and Bernath P.F., (2005), Retrievals for the Atmospheric Chemistry Experiment Fourier transform spectrometer, *Appl. Opt.*, **44**, 7218-7231.

Burkert P., Fergg F., and Fischer H., (1983), A compact high-resolution Michelson interferometer for passive atmospheric sounding (MIPAS), *IEEE Trans. Geosci. Remote Sens.*, **21**, 345-349.

Crisp D., Atlas R.M., Breon F.M., Brown L.R., Burrows J.P., Ciais P., Connor B.J., Doney S.C., Fung I.Y., Jacob D.J., Miller C.E., O'Brien D., Pawson S., Randerson J.T., Rayner P., Salawitch R.J., Sander S.P., Sen B., Stephens G.L., Tans P.P., Toon G.C., Wennberg P.O., Wofsy S.C., Yung Y.L., Kuang Z., Chudasama B., Sprague G., Weiss B., Pollock R., Kenyon D., and Schroll S., (2004), The Orbiting Carbon Observatory (OCO) mission, *Adv. Space Res.*, **34**, 700-709.

Davies J., Tarasick D.W., McElroy C.T., Kerr J.B., Fogal P.F., and Savastiouk V., (2000), Evaluation of ECC Ozonesonde Preparation Methods from Laboratory Tests and Field Comparisons during MANTRA, *Proceedings of the Quadrennial Ozone Symposium*, Hokkaido University, Sapporo, Japan, July 3-8, 2000. Bojkov RD, Kazuo S. eds., 137-138.

Donovan D.P., Fast H., MakinoY., Bird J.C., Carswell A.I., Davies J., Duck T.J., Kaminski J.W., McElroy C.T., and Mittermeier R.L., (1997), Ozone, column ClO, and PSC measurements made at the NDSC Eureka observatory (80°N, 86°W) during the spring of 1997, *Geophys. Res. Lett.*, **24**, 2709-2712.

Farahani E., Fast H., Mittermeier R.L., Makino Y., Strong K., McLandress C., Shepherd T.G., Chipperfield M.P., Hannigan J.W., Coffey M.T., Mikuteit S., Hase F., Blumenstock T., and Raffalski U., (2007), Nitric acid measurements at Eureka obtained in winter 2001–2002 using solar and lunar Fourier transform infrared absorption spectroscopy: Comparisons with observations at Thule and Kiruna and with results from three-dimensional models, *J. Geophys. Res.*, **112**, D01305, doi:10.1029/2006JD007096.

Fu D., Walker K.A., Sung K., Boone C.D., Soucy M-A, and Bernath P.F., (2007), The Portable Atmospheric Research Interferometric Spectrometer for the Infrared, PARIS-IR, *J. Quant. Spectrosc. Radiat. Trans.*, **103**, 362-370.

Fu D., Sung K., Walker K.A., Boone C.D., and Bernath P.F., Ground-based solar absorption studies for the Carbon Cycle science by Fourier Transform Spectroscopy (CC-FTS) mission, Submitted to *J. Quant. Spectrosc. Radiat. Trans.*.

Fu D., Mittermeier R., Sung K., Walker K.A., Boone C.D., Bernath P.F., Fast H., and Strong K., Simultaneous atmospheric measurements using Fourier transform infrared spectrometers at the Polar Environment Atmospheric Research Laboratory (PEARL) during spring 2006, (in preparation for *Atmos. Chem. Phys.*).

Hamazaki T., Kaneko Y., Kuze A., and Kondo K., (2005), Fourier transform spectrometer for Greenhouse Gases Observing Satellite (GOSAT), *SPIE*, **5659**, 73-80.

Jennings D.E., Hubbard R., and Brault J.W., (1985), Double passing the Kitt Peak 1-m Fourier transform spectrometer, *Appl. Opt.*, **24**, 3438-3440.

Jeseck P., Camy-Peyret C., Payan S., and Hawat T., (1998), Detector nonlinearity correction scheme for the LPMA Balloon-borne Fourier transform spectrometer, *Appl. Opt.*, **37**, 6544-6549.

Kerzenmacher T.E., Walker K.A., Strong K., Berman R., Bernath P.F., Boone C.D., Drummond J.R., Fast H., Fraser A., MacQuarrie K., Midwinter C., Sung K., McElroy C.T., Mittermeier R.L., Walker J., and Wu H., (2005), Measurements of O_3, NO_2 and temperature during the 2004 canadian arctic ACE validation campaign, *Geophys. Res. Lett.*, **32**, L16S07, doi:10.1029/2005GL023032.

Pommereau J.P. and Goutail F., (1988), O_3 and NO_2 ground-based measurements by visible spectrometry during Arctic winter and spring, *Geophys. Res. Lett.*, **15**, 891-894.

Pougatchev N.S., Connor B.J., and Rinsland C.P., (1995), Infrared measurements of the ozone vertical distribution above Kitt Peak, *J. Geophys. Res.*, **100**, 16689-16698.

Rinsland C.P., Jones N.B., Connor B.J., Logan J.A., Pougatchev N.S., Goldman A., Murcray F.J., Stephen T.M., Pine A.S., and Zande R., (1998), Northern and southern hemisphere ground-based infrared spectroscopic measurements of tropospheric carbon monoxide and ethane, *J. Geophy. Res.*, **103**, 28197-28217.

Rodgers C.D. (2000), *Inverse methods for atmospheric sounding: Theory and practice*, World Scientific, Singapore.

Savasktiouk V. and McElroy C.T., (2005), Brewer spectrophotometer total ozone measurements made during the 1998 Middle Atmosphere Nitrogen Trend Assessment (MANTRA) campaign, *Atmos. Ocean.*, **43**, 315-324.

Sung K., Skelton R., Walker K.A., Boone C.D., Fu D., and Bernath P.F., (2007), N_2O and O_3 Arctic column amounts from PARIS-IR observations: Retrievals, characterization and error analysis, *J. Quant. Spectrosc. Radiat. Trans.*, **107**, 385-406.

Chapter 3

Global Phosgene Observations from the Atmospheric Chemistry Experiment (ACE) Mission

3.1 Introduction

Phosgene, also known as carbonyl chloride ($COCl_2$), was synthesized by the chemist John Davy in 1812 using sunlight and a mixture of carbon monoxide and chlorine [*Leonard*, 1945]. Phosgene is a highly toxic colorless gas. It gained infamy through its use as a chemical weapon during World War I, and was stockpiled as part of US military arsenals until well after World War II in the form of aerial bombs and mortar rounds. Phosgene plays a major role in the chemical industry, particularly in the preparation of pharmaceuticals, herbicides, insecticides, synthetic foams, resins, and polymers. Considering the health hazards associated with phosgene, the chemical industry is trying to find substitutes to eliminate its use [*Aresta et al.*, 1997].

Phosgene is produced from the decomposition of chlorocarbon compounds. In the troposphere, phosgene is mainly formed by the OH-initiated oxidation of chlorinated hydrocarbons such as CH_3CCl_3 and C_2Cl_4, and is removed by water droplets in clouds or by deposition onto the ocean and other water surfaces [*Singh* 1976; *Helas and Wilson*, 1992]. In the stratosphere, phosgene is produced from the photochemical decay of CCl_4 together with oxidization of its tropospheric source gases [*Crutzen et al.*, 1978; *Wilson et al.*, 1988]. Phosgene can be slowly oxidized through ultraviolet photolysis to form ClO_x, which plays an important role in stratospheric ozone depletion [*Wilson et al.*, 1988]. However, this process is slower than the vertical transport of phosgene, since it is a weak absorber in the near ultraviolet and does not react with OH [*Kindler et al.*, 1995].

The first measurement of atmospheric phosgene was performed in situ by *Singh et al.* [1977]. They obtained surface concentrations at six stations in California. *Wilson et al.* [1988] then measured phosgene during the flight of a Lear Jet aircraft between Germany and Spitzbergen. *Toon et al.* [2001] reported twelve volume mixing ratio (VMR) profiles of phosgene using the solar occultation technique from data recorded during nine MkIV spectrometer balloon flights near 34ºN and 68ºN between 1992 and 2000. There have been no previous reports of the global distribution of phosgene.

3.2 Observations and Retrievals

The Atmospheric Chemistry Experiment (ACE) satellite, also known as SCISAT-1, is a Canadian satellite for remote sensing of the Earth's atmosphere from a low Earth circular orbit (altitude 650 km, inclination 74º). The primary instrument on SCISAT-1, ACE-FTS, is a Fourier transform spectrometer (FTS) covering the spectral region 750 to 4400 cm^{-1} with a resolution of 0.02 cm^{-1} (±25 cm maximum optical path difference) [*Bernath et al.*, 2005]. ACE-FTS records spectra by solar occultation in which the sun is used as a light source and spectra are recorded in the limb geometry during sunrise and sunset. The measured spectra are inverted to obtain the VMR profiles of trace gases in the Earth's atmosphere, along with pressure and temperature profiles [*Boone et al.*, 2005]. The ACE-FTS version 2.2 data contains temperature and pressure profiles, and VMR profiles with 3-4 km vertical resolution of 27 atmospheric constituents including H_2O, O_3, N_2O, CO, CH_4, NO, NO_2, HNO_3, HF, HCl, OCS, N_2O_5, $ClONO_2$, HCN, CH_3Cl, CF_4, CCl_2F_2, CCl_3F, COF_2, C_2H_6, C_2H_2, CHF_2Cl, SF_6, ClO, HO_2NO_2, CCl_4, and N_2, and multiple isotopologues of some of these species. Details of the ACE mission and measurement geometry are given in Chapter 2.

$COCl_2$ VMR retrievals were performed using the spectral region 831 to 864 cm^{-1} with spectroscopic line parameters taken from *Brown et al*. [1996] and *Toon et al*. [2001]. The spectroscopic parameters include data for both the main isotopologue ($CO^{35}Cl_2$) and the most abundant minor isotopologue ($CO^{35}Cl^{37}Cl$). The altitude range of the retrievals extends from 8 to 30 km. Pressure and temperature for the retrievals were taken from ACE-FTS version 2.2 results. Molecules with interferences in the retrieval window are CCl_3F (CFC-11), HNO_3, O_3, CO_2, OCS, C_2H_6, $H_2{}^{16}O$, and $H_2{}^{18}O$. For molecules other than $COCl_2$, spectroscopic line parameters and cross sections (CFC-11) were taken from the HITRAN 2004 database [*Rothman et al.*, 2005].

During $COCl_2$ retrievals, VMR profiles are retrieved simultaneously for the interferers CFC-11, HNO_3, O_3, and H_2O. The VMR for CO_2 is fixed to its assumed profile [*Boone et al.*, 2005], while the VMR profiles for OCS and C_2H_6 are fixed to ACE-FTS version 2.2 results. Note that the isotopologue $H_2{}^{18}O$ is a minor interference, only significant below ~9 km for tropical occultations and negligible for polar occultations. Contributions to the spectrum from CFC-11 are calculated from 55 cross section files in the HITRAN 2004 database that cover the pressure and temperature range of 0.01-1 atm and 190-296 K.

Following the procedure outlined in *Dufour et al.* [2006], Table 3.1 presents an estimate of uncertainties associated with the retrievals for a representative set of occultations: tropical occultations with latitudes 15 to 20°N. The column labeled "measurement noise" is the statistical fitting error in the least squares analysis. Deficiencies in the retrieval of interferences analyzed simultaneously (CFC-11, HNO_3, O_3, and H_2O) are reflected in this column. Contributions from errors in temperatures, pointing, and interferences fixed during the retrieval (CO_2, OCS, and C_2H_6) are also considered. The uncertainty of 30% on the $COCl_2$ spectroscopic parameters was deduced from information provided in the article by *Toon et al.* [2001], where average quantities were calculated from two sources that differed by up to 60% (much higher than the quoted precisions of 2 and 10%). Interferences analyzed simultaneously (CFC-11, HNO_3, O_3, and H_2O) are not considered separately. The random errors from deficiencies in the retrievals of these molecules are reflected in the measurement noise column, and systematic contributions to the error are neglected. Of particular concern for $COCl_2$ retrievals is the broad, overlapping CFC-11 absorption feature. Note, however, that a systematic scaling of the CFC-11 cross sections in HITRAN 2004 would only affect the retrieved CFC-11 VMR profile. Systematic errors in the $COCl_2$ retrievals from errors in CFC-11 spectroscopy would only arise if the shape of the calculated CFC-11 absorption feature was wrong, and there is no indication of such problems in the fitting residuals.

It is worth noting that the numbers in Table 3.1 represent the uncertainties on the retrieval of a single VMR profile, including both random and systematic contributions. Uncertainties are a large percentage of the retrieved VMR values, and they exceed 100 percent at the highest retrieval altitude, where the magnitude of the $COCl_2$ spectral signature approaches the noise level. Random contributions to the uncertainty (such as measurement noise) are greatly reduced (generally to less than 5 pptv) through averaging results for many occultations, as was done for the plots presented in this article.

Table 3.1 Sensitivity study for the $COCl_2$ retrieval, evaluated from a representative set of occultations in the latitude range 15-20°N. $COCl_2$ VMR values and uncertainties in the VMR are expressed in parts per trillion by volume (pptv). The total error is expressed as a percentage of the mean VMR.

Altitude (km)	Mean VMR	Measurement noise	Spectr. Data[a]	Pointing[b]	T[c]	CO_2[d]	OCS[e]	C_2H_6[f]	Total Error
8.5	21.6	13.5	6.5	3.0	0.5	0.01	0.02	0.14	71%
11.5	19.0	13.1	5.7	2.0	0.7	0.002	0.01	0.04	76%
14.5	15.3	10.8	4.6	1.0	0.9	0.002	0.003	0.03	77%
17.5	18.2	13.1	5.5	2.0	0.5	0.001	0.003	0.02	79%
20.5	23.3	21.0	6.2	1.5	0.5	0.001	0.005	0.005	94%
23.5	36.8	32.9	11.0	2.0	1.0	0.002	0.004	0.005	94%
26.5	32.6	41.6	9.8	3.0	0.5	0.003	0.003	0.01	131%
29.5	3.7	44.9	1.1	2.0	0.3	0.005	0.004	0.015	1215%

[a] Based on spectroscopic uncertainty of 30 % for $COCl_2$ (see text).

[b] Based on a tangent height uncertainty of 150 m.

[c] Based on a temperature uncertainty of 2 K.

[d] Based on an uncertainty of 1%.

[e] Based on an uncertainty of 5%.

[f] Based on an uncertainty of 10%.

During polar winter/spring, the airmass contained within the polar vortex experiences a significant subsidence. As a consequence, VMR profiles of $COCl_2$ measured inside or at the edge of the polar vortex are smaller than those observed outside the vortex at a particular altitude [*Toon et al.*, 2001]. In order to avoid this temporary dynamical effect, occultations within the polar vortex or on the vortex edge were excluded from analysis. Using the potential vorticity derived from the Met Office meteorological analyses [*Davies et al.*, 2005], a two-step approach similar to that described by *Nassar et al.* [2005] was used to classify each of the 6758 occultations collected during the period February 2004 to May 2006 as being inside, outside, or on the edge of the vortex. Filtering out occultations inside or on the edge of the vortex yielded 5614 extravortex occultations, which were then used in the evaluation of the $COCl_2$ global distribution. The geographic locations of these 5614 occultations are shown in Figure 3.1.

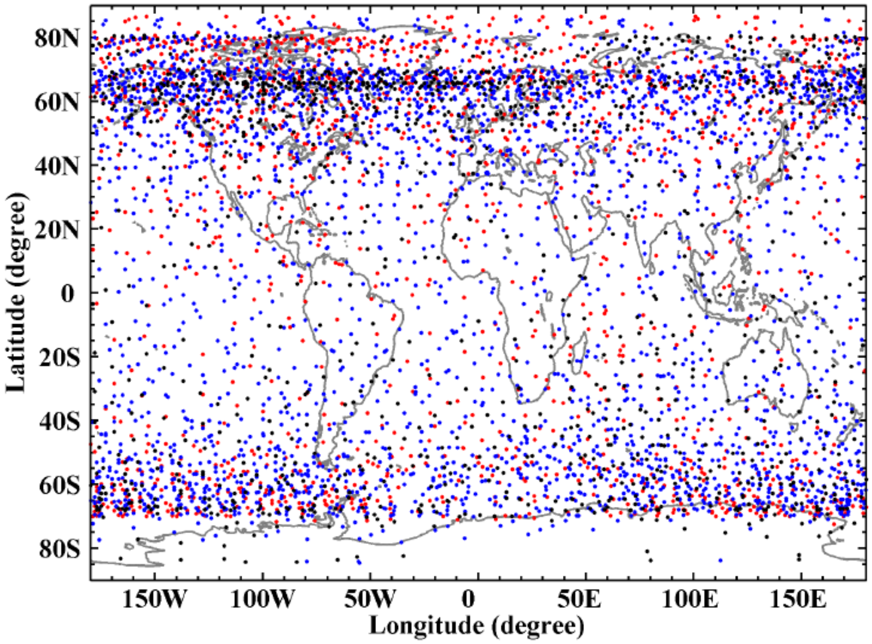

Figure 3.1 The locations of 30 km geometric tangent points for 5614 ACE-FTS occultations during the period February 2004 to May 2006 are illustrated with dots. The color of each marker indicates the year of the observation was made (Red: 2004; Blue: 2005 and Black: 2006).

3.3 Results and Discussion

Within 5 degree latitudinal zones, the observed VMR profiles of $COCl_2$ show very similar characteristics in terms of peak altitude and VMR values at the peak. For this initial work, the predicted small seasonal cycle [*Kindler et al.*, 1995] and the expected annual decrease due to the decline in atmospheric chlorine loading were not considered. The entire data set was therefore separated into 5 degree latitude bins, and all of the profiles within a given bin were averaged to generate a single profile with reduced noise. Although there are 36 bins between 90ºN and 90ºS, only 35 of the bins were used because there were no profiles in the region 85 to 90ºS.

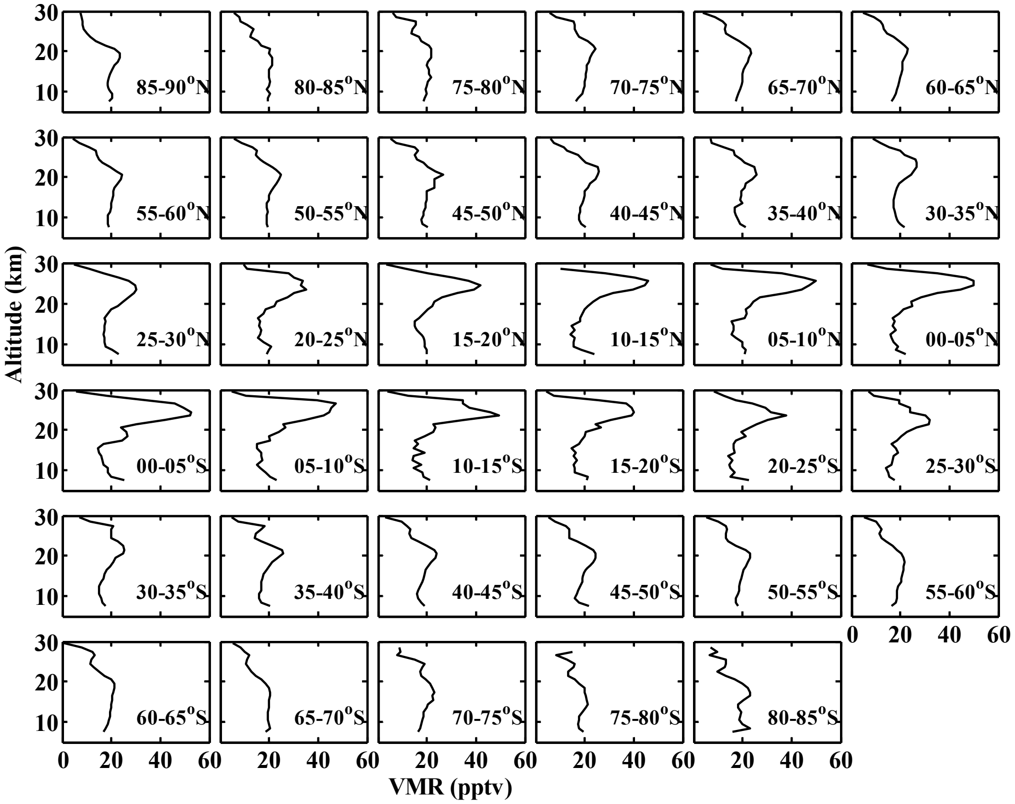

Figure 3.2 The 35 averaged $COCl_2$ VMR profiles for 5 degree latitudinal zones spanning from 90ºN to 85ºS during the period February 2004 to May 2006 are presented. There were no profiles in the region 85 to 90ºS.

The 35 averaged $COCl_2$ VMR profiles shown in Figure 3.2 were used to generate the contour plot shown in Figure 3.3. In the troposphere, phosgene has a generally even distribution, with VMR values of roughly 15 to 20 pptv. In the lower stratosphere, $COCl_2$ exhibits a layer of higher concentration (25 to 60 pptv) with a thickness of 5 to 10 km. Within this layer, $COCl_2$ concentrations are highest near the equator and decline poleward. There is a core of strongly enhanced $COCl_2$ (VMRs 40 to 60 pptv) between 22 and 27 km in the region 20ºN to 20ºS. For all latitudes, the retrieved VMR drops rapidly to zero for altitudes above the $COCl_2$ enhancement layer.

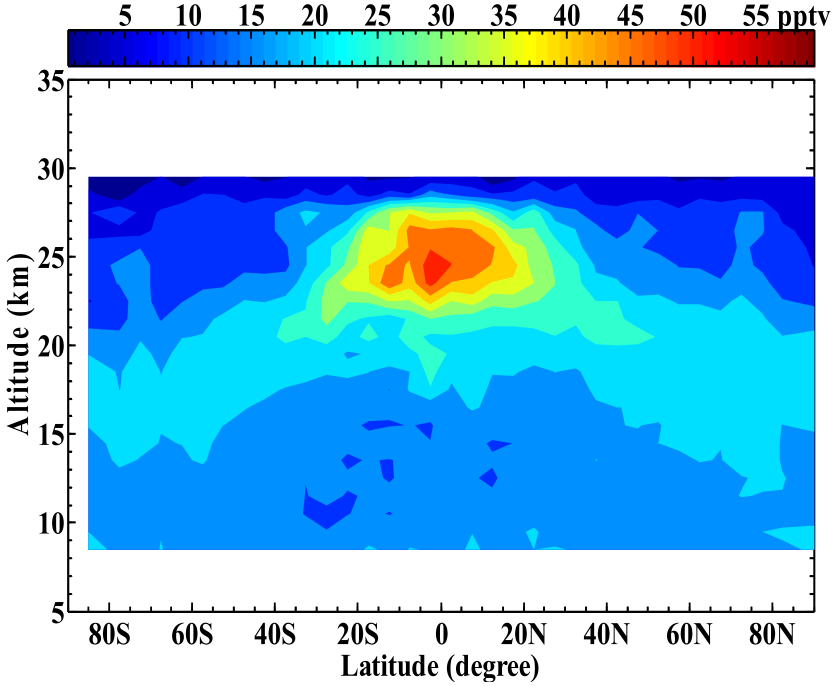

Figure 3.3 The latitudinal distribution of averaged $COCl_2$ VMR profiles spanning 8 to 30 km from ACE-FTS observations during the period February 2004 to May 2006 are displayed.

The phosgene distribution pattern is determined by its chemical production and lifetime. $COCl_2$ is believed to have five main precursor molecules. In the troposphere, $COCl_2$ is produced primarily from the OH-initiated oxidation of CH_3CCl_3, $CHCl_3$, C_2Cl_4, and C_2HCl_3

[*Helas and Wilson*, 1992]. In addition to these sources, the largest source of $COCl_2$ is attributed to the photolysis of CCl_4 which contributes about 68% of the total $COCl_2$ budget in the stratosphere, according to model simulation results [*Kindler et al.*, 1995]. Tropospheric $COCl_2$ has a lifetime of about 70 days due to fast wet removal [*Singh*, 1976; *Singh et al.*, 1977; *Kindler et al.*, 1995]. Stratospheric $COCl_2$, on the other hand, is expected to have a lifetime of several years, since phosgene decomposes slowly through UV photolysis and has no reaction with OH. Interestingly, *Kindler et al.* [1995] predict that a substantial amount of phosgene is returned to the troposphere from the stratosphere, where it is removed primarily by wet deposition.

Based on the distribution in Figure 3.3, the bulk of the $COCl_2$ appears over the tropics, likely because the tropics receive more insolation than higher latitudes, due to a smaller solar zenith angle. Because of its long lifetime, $COCl_2$ in the tropics can then be transported poleward by the Brewer-Dobson circulation. Hence, the high concentration of phosgene appears in the tropics, decreases poleward, and shows a zonally symmetric pattern centered on the equator.

Figure 3.4 shows $COCl_2$ profiles corresponding to five different latitudinal zones (90-60ºN, 60-30ºN, 30ºS-30ºN, 30-60ºS and 60-85ºS) averaged from the observed profiles spanning February 2004 through May 2006. In the stratosphere, the peak values of $COCl_2$ VMR decrease significantly from the tropics to the poles. In a recent global inventory of stratospheric chlorine [*Nassar et al.*, 2006], mean $COCl_2$ profiles were estimated from the MkIV measurements spanning September 1992 to March 2000 [*Toon et al.* 2001], but with limited latitudinal coverage in those measurements, the presently observed latitudinal distribution of stratospheric $COCl_2$ was not discerned. In the troposphere, the $COCl_2$ VMR increases slightly from the tropics to the poles. This may result from the fact that the troposphere at higher latitudes contains less liquid water than the tropical atmosphere, providing less opportunity for wet removal. In addition, larger tropospheric phosgene mixing ratios at higher latitudes may be a result of recirculation from the stratosphere by Brewer-Dobson circulation. The averaged VMR profiles for northern (0-90°N) and southern (0-85°S) hemispheres seen in Figure 3.4 are very similar, suggesting that both hemispheres have similar amounts of $COCl_2$. This observation is at variance with the model results of *Kindler et al.* [1995], which predict a significant hemispheric asymmetry with an enhancement in the troposphere of the Northern Hemisphere, though the hemispheric differences of source gases are much smaller than they were in the 1980s and 1990s.

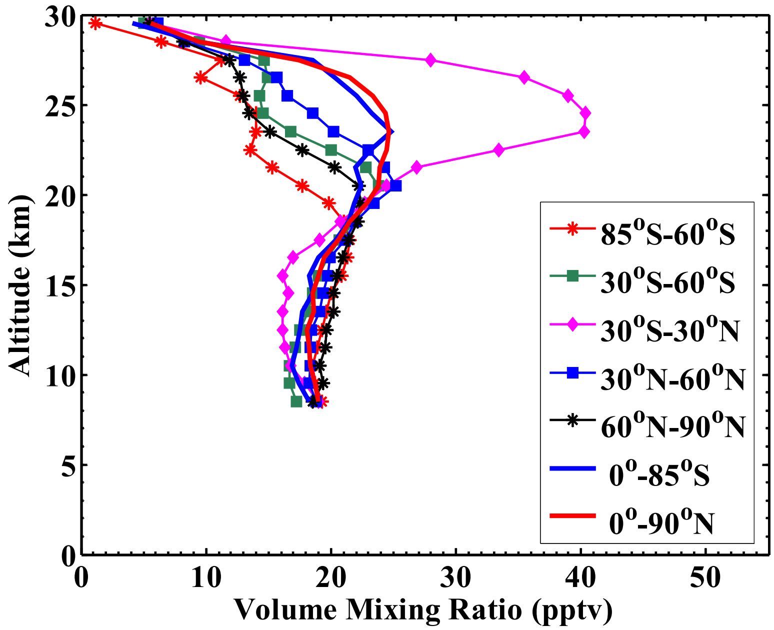

Figure 3.4 The averaged $COCl_2$ VMR profiles for 90-60°N, 60-30°N, 30°S-30°N, 30-60°S and 60-85°S latitudinal zones, southern hemisphere and northern hemisphere observed by the ACE mission during the period February 2004 to May 2006 are presented.

Above the peak in all of the averaged ACE-FTS $COCl_2$ profiles, around 22 to 25 km depending on the latitude range, $COCl_2$ VMR decreases rapidly with increasing altitude and becomes essentially zero above 28 km. This is consistent with the results from the MkIV spectrometer [*Toon et al.*, 2001] measured near 34°N and 68°N between September 1992 and March 2000. Both ACE-FTS and MkIV results are inconsistent with the model results [*Kindler et al.*, 1995], which are plotted as red dotted line in Figure 3.5. Results from aircraft observations collected by *Wilson et al.* [1988] between Germany and Spitzbergen (50°-78°N) at altitudes of 5-12 km are also included in Figure 3.5 $COCl_2$ VMRs in the stratosphere from ACE-FTS are smaller than the observations from both *Wilson et al.* [1988] and *Toon et al.* [2001].

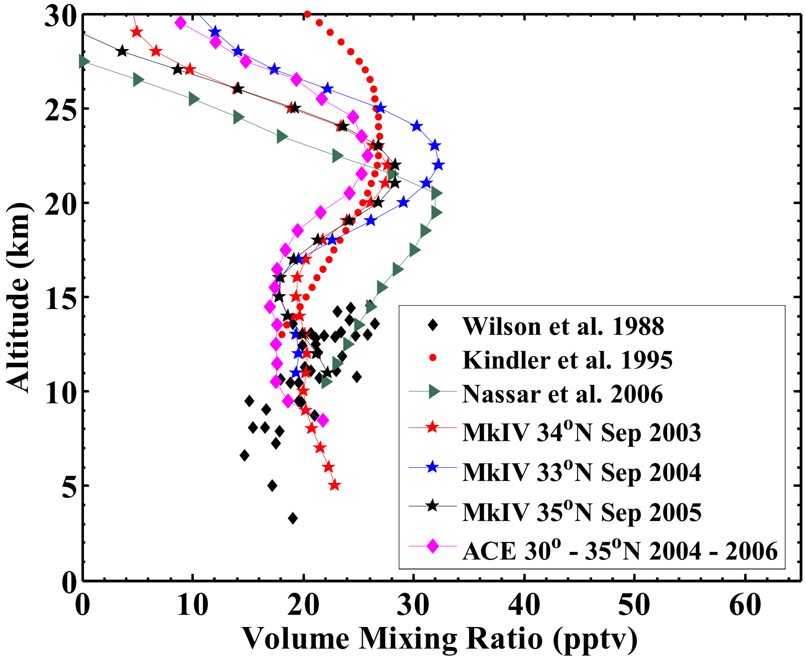

Figure 3.5 The averaged $COCl_2$ VMR profiles (filled magenta diamond line) for 30-35°N, latitudinal zone observed by ACE mission during the period February 2004 to May 2006 are presented along with *in situ* aircraft measurements of *Wilson et al.* [1988] between Germany and Spitzbergen (50°-78°N) at altitudes of 5-12 km (filled black diamonds), plus the results presented in Figure 11 in the model prediction of *Kindler et al.* [1995] (dotted red line), the *Nassar et al.* [2006] (filled green triangle line) estimates for 2004 based on a best-fit line to the *Toon et al.* [2001] MkIV points in the 10-30 km range measured near 34°N and 68°N between September 1992 and March 2000, and phosgene profiles measured in 2003, 2004, and 2005 using MkIV spectrometer by *Toon et al.* [private communication, 2007].

The differences of the ACE-FTS $COCl_2$ VMR from values obtained in previous studies likely arise from changes in the concentrations of sources species. Ground based studies indicate sharp declines in a number of the "parent" molecules of $COCl_2$ over the past 10 to 15 years as a result of emission restrictions on its two major sources CH_3CCl_3 and CCl_4 required by the Montreal Protocol and its amendments. For example, the Atmospheric Lifetime Experiment, the Global Atmospheric Gases Experiment and the Advanced Global Atmospheric Gases Experiment (ALE/GAGE/AGAGE) [*Prinn et al.*, 2000, 2005; *Simmonds et al.*, 2006; WMO, 2006], the National Oceanic and Atmospheric Administration Climate Monitoring and Diagnostics Laboratory (NOAA/CMDL) [*Montzka et al.*, 1996, 1999; *Thompson et al., 2004*; WMO, 2006], and the University of California at Irvine (UCI) [*Blake et al.,* 1996; *Blake et al.*, 2001; WMO, 2006] measure the concentrations of the five main phosgene precursor molecules.

From these *in situ* data sets, CCl_4 concentrations dropped 10% between 1988 and 2005 [*Montzka et al.*, 1996, 1999; *Blake et al.*, 1996; *Blake et al.*, 2001; *Thompson et al.*, *2004*; *Prinn et al.*, 2000, 2005; WMO, 2006]. Levels of tropospheric CH_3CCl_3 declined rapidly between 1991 and 2004. During this period, the CH_3CCl_3 mixing ratio declined 85% [*Prinn et al.*, 2000, 2005; WMO, 2006]. Between 1989 and 2002, annual mean C_2Cl_4 mixing ratios for the extratropical northern hemisphere dropped from 13.9 pptv to less than half this value (6.5 pptv), and global averages declined from 6.3 pptv to 3.5 pptv [*Simpson et al.*, 2004; WMO, 2006]. Recent ambient atmospheric data suggest that the amounts of $CHCl_3$ and C_2HCl_3 are also declining. *Prinn et al.* [2000] reported data for $CHCl_3$ from 1983-1998 with a trend ranging from –0.1 to –0.4 ppt/year. The rate of decrease for C_2HCl_3 was reported as 0.01 ppt/year during the period July 1999 to December 2004 [*Simmonds et al.*, 2006]. Given these significant changes in atmospheric chlorine content, differences on the order of 25% for $COCl_2$ as compared to older data sets are quite reasonable.

3.4 Summary

The first study of the global distribution of atmospheric phosgene ($COCl_2$) has been performed using data from the ACE satellite mission. A total of 5614 profiles from the period

February 2004 to May 2006 were used, after filtering out occultations that were inside or near the polar vortex. No seasonal variation was observed in the data, but there was a significant variation as a function of latitude.

A major source region for atmospheric phosgene appears in the stratosphere over the tropics (around 25 km), where the highest VMRs (40-60 pptv) are observed. There are also likely enhanced abundances of the $COCl_2$ parent species in this region, but an in-depth study of the parent species is beyond the scope of this discussion. The Brewer-Dobson circulation transports the $COCl_2$ toward the poles. A long lifetime in the lower stratosphere leads to an enhanced layer in this region. For altitudes above the enhancement layer, VMR values are small because the molecule undergoes UV photolysis. In the troposphere, $COCl_2$ VMR values are relatively low (17-20 pptv) as a result of the 70-day lifetime which is governed by fast wet removal.

Comparisons of $COCl_2$ VMRs between ACE-FTS observations and measurements from previous work [*Wilson et al.,* 1988; *Toon et al.,* 2001] show reasonable agreement. ACE-FTS results indicate a decline in $COCl_2$ concentrations since those studies, as one would expect from the decline in parent species [*Blake et al.*, 1996; *Montzka et al.*, 1996, 1999; *Blake et al.*, 2001; *Simpson et al.*, 2004; *Thompson et al.*, *2004*; *Prinn et al.*, 2000, 2005; *Simmonds et al.*, 2006; WMO, 2006].

3.5 References

Aresta M. and Quaranta E., (1997), Carbon dioxide: a substitute for phosgene, *Chem. Tech.*, **27**, 32-40.

Bernath P.F., McElroy C.T., Abrams M.C., Boone C.D., Butler M., Camy-Peyret C., Carleer M., Clerbaux C., Coheur P.-F., Colin R., DeCola P., DeMazière M., Drummond J.R., Dufour D., Evans W.F.J., Fast H., Fussen D., Gilbert K., Jennings D.E., Llewellyn E.J., Lowe R.P., Mahieu E., McConnell J.C., McHugh M., McLeod S.D., Michaud R., Midwinter C., Nassar R., Nichitiu F., Nowlan C., Rinsland C.P., Rochon Y.J., Rowlands N., Semeniuk K., Simon P., Skelton R., Sloan J.J., Soucy M.-A., Strong K., Tremblay P., Turnbull D., Walker K.A., Walkty I., Wardle D.A., Wehrle V., Zander R., and Zou J., (2005), Atmospheric Chemistry Experiment (ACE): Mission Overview, *Geophys. Res. Lett.*, **32**, L15S01, doi:10.1029/2005GL022386.

Blake D.R., Chen T.-Y., Smith Jr. T.W., Wang C.J.-L., Wingenter O.W., Blake N.J., Rowland F.S., and Mayer E.W., (1996), Three-dimensional distribution of nonmethane hydrocarbons and halocarbons over the northwestern Pacific during the 1991 Pacific Exploratory Mission (PEM-West A), *J. Geophys. Res.*, **101**, 1763-1778.

Blake N.J., Blake D.R., Simpson I.J., Lopez J.P., Johnston N.A.C., Swanson A.L., Katzenstein A.S., Meinardi S., Sive B.C., Colman J.J., Atlas E., Flocke F., Vay S.A., Avery M.A., and Rowland F.S., (2001), Large-scale latitudinal and vertical distributions of NMHCs and selected halocarbons in the troposphere over the Pacific Ocean during the March-April 1999 Pacific Exploratory Mission (PEM-Tropics B), *J. Geophys. Res.*, **106**, 32627-32644.

Boone C.D., Nassar R., Walker K.A., Rochon Y., McLeod S.D., Rinsland C.P., and Bernath P.F., (2005), Retrievals for the Atmospheric Chemistry Experiment Fourier transform spectrometer, *Appl. Opt.*, **44**, 7218-7231.

Brown L.R., Gunson M.R., Toth R.A., Irion F.W., Rinsland C.P., and Goldman A., (1996), The 1995 Atmospheric Trace Molecule Spectroscopy (ATMOS) linelist, *Appli. Opt.*, **35**, 2828-2848.

Crutzen P.J., Isaksen I.S.A., and McAfee J.R. (1978), The impact of the chlorocarbon industry on the ozone layer, *J. Geophys. Res.*, **83**, 345-363.

Davies T., Cullen M.J.P., Malcolm A.J., Mawson M.H., Staniforth A., White A.A., and Wood N., (2005), A new dynamical core for the Met Office's global and regional modelling of the atmosphere, *Q. J. R. Meteorol. Soc.*, **131**, 1759-1782.

Dufour G., Boone C.D., Rinsland C.P., and Bernath P.F., (2006), First space-borne measurements of methanol inside aged southern tropical to mid-latitude biomass burning plumes using the ACE-FTS instrument, *Atmos. Chem. Phys.*, **6**, 3463-3470 .

Helas G. and Wilson S.R., (1992), On source and sinks of phosgene in the troposphere, *Atmos. Envir.*, **26A**, 2975-2982.

Kindler T.P., Chameides W.L., Wine P.H., Cunnold D.M., Alyea F.N., and Franklin J.A., (1995), The fate of atmospheric phosgene and the stratospheric chlorine loading of its parent compounds: CCl_4, C_2Cl_4, C_2HCl_3, CH_3CCl_3, and $CHCl_3$, *J. Geophys. Res.*, **100**, 1235-1251.

Leonard D., (1945), The history of the discovery of phosgene, *Annals of Science.* **5**, 270-287.

Montzka S.A., Butler J.H., Myers R.C., Thompson T.M., Swanson T.H., Clarke A.D., Lock L.T., and Elkins J.W., (1996), Decline in tropospheric abundance of halogen from halocarbons: Implications for stratospheric ozone depletion, *Science*, **272**, 1318-1322.

Montzka S.A., Butler J.H., Elkins J.W., Thompson T.M., Clarke A.D., and Lock L.T., (1999), Present and future trends in the atmospheric burden of ozone-depleting halogens, *Nature*, **398**, 690-694.

Nassar R., Bernath P.F., Boone C.D., Manney G.L., McLeod S.D., Rinsland C.P., Skelton R., and Walker K.A., (2005), ACE-FTS measurements across the edge of the winter 2004 Arctic vortex, *Geophys. Res. Lett.*, **32**, L15S05, doi:10.1029/2005GL022671.

Nassar R., Bernath P.F., Boone C.D., Clerbaux C., Coheur P.F., Dufour G., Froidevaux L., Mahieu E., McConnell J.C., McLeod S.D., Murtagh D.P., Rinsland C.P., Semeniuk K., Skelton R., Walker K.A., and Zander R., (2006), A global inventory of stratospheric chlorine in 2004, *J. Geophys. Res.*, **111**, D22312, doi:10.1029/2006JD007073.

Prinn R.G., Weiss R.F., Fraser P.J., Simmonds P.G., Cunnold D.M., Alyea F.N., O'Doherty S., Salameh P., Miller B.R., Huang J., Wang R.H.J., Hartley D.E., Harth C., Steele L.P., Sturrock G., Midgley P.M., McCulloch A., (2000), A history of chemically and radiatively important gases in air deduced from ALE/GAGE/AGAGE, *J. Geophys. Res.*, **105**, 17751-17792.

Prinn R.G., Huang J., Weiss R.F., Cunnold D.M., Fraser P.J., Simmonds P.G., McCulloch A., Harth C., Reimann S., Salameh P., O’Doherty S., Wang R.H.J., Porter L.W., Miller B.R., and Krummel P.B., (2005), Evidence for variability of atmospheric hydroxyl radicals over the past quarter century, *Geophys. Res. Lett.*, **32**, L07809, doi:10.1029/2004GL022228.

Rothman L.S., Jacquemart D., Barbe A., Benner C., Birk M., Brown L.R., Carleer M.R., Chackerian Jr.C., Chance K., Coudert L.H., Dana V., Devi V.M., Flaud J.M., Gamache R.R., Goldman A., Hartmann J.M., Jucks K.W., Maki A.G., Mandin J.Y., Massie S.T., Orphal J., Perrin A., Rinsland C.P., Smith M.A.H., Tennyson J., Tolchenov R.N., Toth R.A., Vander J., Varanasi P., and Wagner G., (2005), The HITRAN 2004 molecular spectroscopic database, *J. Quant. Spec. Radi. Trans.*, **96**, 139-204.

Simmonds P.G., Manning A.J., Cunnold D.M., McCulloch A., O’Doherty S., Derwent R.G., Krummel P.B., Fraser P.J., Dunse B., Porter L.W., Wang R.H.J., Greally B.R., Miller B.R., Salameh P., Weiss R.F., and Prinn R.G., (2006), Global trends, seasonal cycles, and European emissions of dichloromethane, trichloroethene, and tetrachloroethene from the

AGAGE observations at Mace Head, Ireland, and Cape Grim, Tasmania, *J. Geophys. Res.*, **111**, D18304, doi:10.1029/2006JD007082.

Simpson I.J., Meinardi S., Blake N.J., Rowland F.S., and Blake D.R., (2004), (2004), Long-term decrease in the global atmospheric burden of tetrachloroethene (C_2Cl_4), *Geophys. Res. Lett.*, **31**, L08108, doi: 10.1029/2003GL019351.

Singh H.B., (1976), Phosgene in ambient air, *Nature*, **265**, 428-429.

Singh H.B., Salas L., Shigeishi H., and Crawford A., (1977), Urban-nonurban relationships of halo-carbons, SF_6, N_2O and other atmospheric trace constituents, *Atmos. Envir.*, **11**, 819-828.

Thompson T.M., Butler J.H., Daube B.C., Dutton G.S., Elkins J.W., Hall B.D., Hurst D.F., King D.B, Kline E.S., LaFleur B.G., Lind J., Lovitz S., Mondeel D.J., Montzka S.A., Moore F.L., Nance J.D., Neu J.L., Romashkin P.A., Scheffer A., and W.J. Snible, (2004), Halocarbons and other atmospheric trace species, section 5, in Climate Monitoring and Diagnostics Laboratory: summery report No. 27, 2002-2003, edited by R. Schnell, A.-M. Buggle and R. Rosson, 115-135, NOAA/Climate Monitoring and Diagnostics Laboratory, Boulder, Colo.

Toon G.C., Blavier J.-F., Sen B., and Drouin B.J., (2001), Atmospheric $COCl_2$ measured by solar occultation spectrometry, *Geophys. Res. Lett.*, **28**, 2835-2838.

Wilson S.R., Crutzen P.J., Schuster G., Griffith D.W.T., Helas G., (1988), Phosgene measurements in the upper troposphere and lower stratosphere, *Nature*, **334**, 689-691.

WMO (World Meteorological Organization) (2006), *Scientific assessment of ozone depletion: 2006,* Geneva, Switzerland.

Chapter 4

Preparation and Deployment of PARIS-IR for the MANTRA 2004 Balloon Campaign

4.1 Introduction

The Portable Atmospheric Research Interferometric Spectrometer (PARIS-IR), is a high resolution Fourier Transform Spectrometer (FTS) built for atmospheric remote sensing measurements. The instrument description was given in section 2.2.2. PARIS-IR makes atmospheric measurements from the ground and also participates in balloon campaigns [*Fu et al.*, 2007]. During August and September 2004, PARIS-IR was part of the payload for the Middle Atmosphere Nitrogen TRend Assessment (MANTRA 2004) balloon campaign. MANTRA has four major scientific goals: 1) to measure key stratospheric species that control the mid-latitude ozone amounts, particularly species in the NO_y (HNO_3, NO, NO_2, N_2O_5, HNO_4 and $ClONO_2$) and Cl_y (ClO, HOCl, HCl and $ClONO_2$) families as well as the dynamical tracers N_2O and HF; 2) to measure the long term changes in the composition of the stratosphere by combining measurements from MANTRA with those from previous balloon flights at northern mid-latitudes; 3) to investigate instrument differences by comparing the measurements of the same species recorded by different instruments on the balloon platform; 4) to validate satellite measurements such as those from SCISAT-1 [*Strong et al.*, 2005].

To achieve these goals, measurements were made by thirteen different instruments from a single platform in 2004. These instruments are listed in Table 4.1. The measurements from the three FTSs (including PARIS-IR) are able to provide vertical concentration profiles of thirteen of the “baseline” traces gases (O_3, CH_4, N_2O, H_2O, HNO_3, HCl, NO, NO_2, CCl_3F, CCl_2F_2, HF, CO and N_2O_5) required to validate [*Walker et al.*, 2005] the Atmospheric Chemistry Experiment, a Canadian satellite mission [*Bernath et al.*, 2005]. As described in Section 2.1.2 the balloon campaign took place at Environment Canada’s Balloon Launch Facility in Vanscoy, Saskatchewan (52.02ºN, 107.03ºW, and 510 m above sea level).

Table 4.1 Instruments onboard the MANTRA 2004 balloon payload[a].

Primary Balloon-Borne Instruments	Secondary Balloon-Borne Instruments
MSC[b] emission radiometer (thermal infrared)	Second MSC[b] emission radiometer (thermal infrared)
MSC[b] SPS[c]-B1 (UV-Vis)	MSC[b] FTS (infrared)
MAESTRO-B[d] (UV-Vis)	PARIS-IR FTS (infrared)
U of Denver FTS (infrared)	MSC[b] SPS[c]-B2 (UV-Vis)
Service d'Aéronomie SAOZ[e] (UV-Vis)	MSC[b] OH spectrometer (UV)
MSC[b] ozonesonde[f] (*in situ*)	AIR[g] (near infrared)
aerosol sonde (*in situ*)	

[a] The spectral ranges of the instruments are given in the brackets.

[b] Meteorological Service of Canada

[c] SunPhotoSpectrometer [*McElroy*, 1995]

[d] Measurement of Aerosol Extinction in the Stratosphere and Troposphere Retrieved by Occultation- Balloon [*McElroy et al.*, 2007]

[e] Système d'Analyse par Observations Zènithales [*Pommereau and Piquard*, 1994]

[f] [*Davies et al.*, 2000]

[g] Airglow Infrared Radiometer [*Yee et al.*, 2003]

4.2 Measurements Made from a Balloon

There are several environmental factors which have to be taken into account when putting an instrument on a high-altitude balloon platform. The low pressure (~3 mbar at ~38 km) significantly decreases the efficiency of cooling by convection, the typical method used for cooling electronic equipment on the ground. Only radiative and conductive methods can be used to remove heat from balloon-borne instruments. The low pressure also limits the types of data storage devices that can be used. A standard hard drive requires an ambient pressure of one atmosphere for the rotating mechanism to operate properly. Either a solid-state device, such as a compact flash memory card, or a hard drive with a pressurized case must be used for the balloon flight. The instrument must be able to sustain a wide range of temperatures: these range from an ambient temperature of -60°C as the payload passes through the tropopause (at a height of ~10 to 20 km) to high temperatures (up to +60°C) due to heating from direct solar radiation at float altitude (~37 km), where the balloon does not change its height significantly relative to the surface. The instrument also has to be able to survive large mechanical shocks both at launch (~2.5 g) and when the parachute opens during descent (~10 g). These factors were taken into consideration when designing and constructing the PARIS-IR instrument.

4.3 PARIS-IR Balloon Configuration

Two computers are required to operate PARIS-IR remotely from the ground. An onboard computer (mini-ATX 600 MHz) is on the gondola to provide communication between PARIS-IR and the ground computer. Two SanDisk 2 GB flash cards are used for data storage in the onboard computer instead of hard drives. The ground computer is used for receiving, processing and displaying the instrument status information and for storing the measurement data sent down from the balloon. Three serial (RS-232) communication links are used to send data between the onboard computer/PARIS-IR and the ground computer. These are an instrument status information downlink (9600 baud), a shared high speed data downlink (115.2 kbaud), and a command uplink (300 baud) (Figure 4.1). These data stream are transmitted and received using the shared microwave communication system used by all of the instruments on the balloon platform. This system is provided and operated by the launch contractor, Scientific Instrumentation Ltd.

To remotely control the instrument, control and commanding software was developed for the onboard computer and the ground computer. This software was jointly developed by Yony Bresler, Ian Young, and Michelle Seguin, who were undergraduate co-op and 4th year project students in Dr. Bernath's group. This software allows PARIS-IR to make measurements using an onboard auto scheduler. It executes a batch file prepared before the flight which contains all the required instrument commands. The instrument status information can be monitored as the parameters are collected and sent down to the ground computer automatically by the onboard computer every few seconds. When necessary, the

PARIS-IR instrument can be sent commands from the ground using the command uplink. When requested, the measured scientific data are sent down to the ground through the data downlink channel. This process is not automatic because the high speed downlink channel is shared between the three FTS instruments. The scientific data also can be downloaded using the instrument status data downlink when this request is excuted by the auto scheduler. In this download mode, the instrument status is not updated, since the down link is occupied by the scientific data.

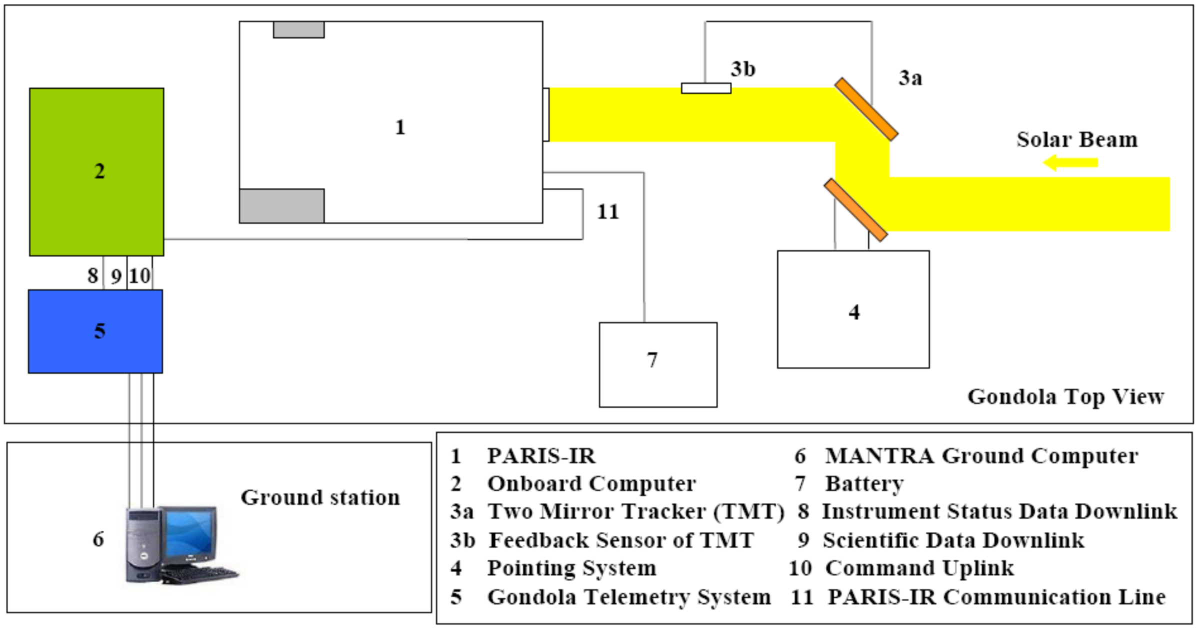

Figure 4.1 PARIS-IR balloon configuration.

4.4 Preflight Vacuum Testing

The whole PARIS-IR system had to be tested under simulated flight conditions to determine if it could withstand the low pressures present at float altitude. Two sets of tests were carried out at the Space Instrument Characterization Facility (SICF) in the Physics Department at the University of Toronto in April and July 2004. The SICF has a class 100000 clean room with a large (2 m diameter and 5 m length) thermal-vacuum chamber (TVAC) which was used for all tests, as shown in Figure 4.2. The pumping system can easily evacuate the TVAC chamber to pressures of ~3 mbar with all of the PARIS-IR components inside.

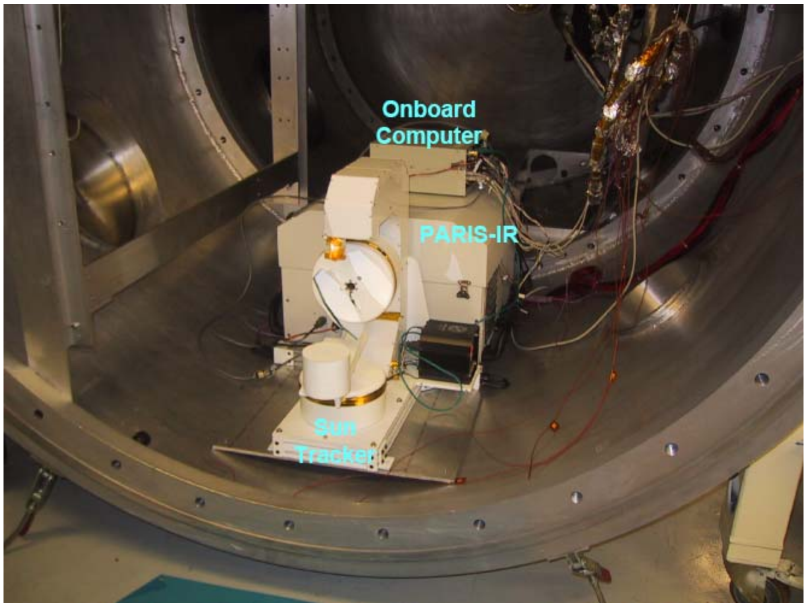

Figure 4.2 PARIS-IR system in the thermal-vacuum chamber (TVAC) at the Space Instrument Characterization Facility (SICF) located in University of Toronto.

The temperatures of electronic components and optical components of the PARIS-IR system must be maintained within the recommended ranges given by their manufacturers. For example, when the temperatures of the Central Processing Unit (CPU), which is the main component in a digital computer that interprets computer program instructions and processes data, is higher than 95ºC, it may not respond to input commands, and instrument control will be compromised. In addition, the optical alignment of PARIS-IR will change if the temperature of the optical bench on which most of the optical components are mounted is out of the nominal 20 to 35ºC range.

Several thermistors were installed in PARIS-IR and the onboard computer so that their temperatures could be measured during flight. For the tests, PARIS-IR and the onboard computer were operated at low pressure (~3 mbar) in the TVAC for several hours, or until the rate of the temperature increase for the main components was nearly zero, as shown in Figure 4.3. An additional set of thermocouples were used to monitor several of the same points during testing, to verify the thermistor readings.

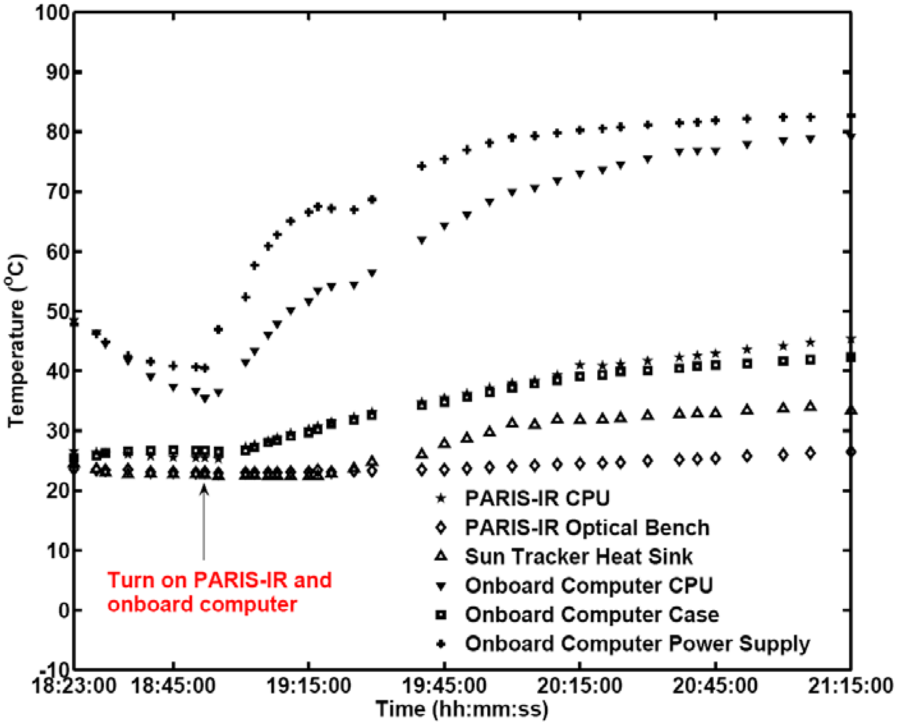

Figure 4.3 The temperature measurements for the major components in the PARIS-IR system. They were obtained from the tests on July 12th, 2004. The tests were performed in the TVAC at the SICF located at University of Toronto. The onboard computer, PARIS-IR and sun tracker were powered up on 18:55:00 (local time). After operating for two hours, the temperature increases of the various components had slowed significantly.

During the April tests, it was apparent that the heat sink on the CPU of the onboard computer needed to be improved. A new larger aluminum heat sink was installed above the CPU and North Bridge chipset. The new heat sink reduced the operating temperature of the components by 5-10°C. The flight model DC-DC power converter for the onboard computer was only tested in July. The results during this pre-flight test showed that the heat sink of this component needed to be improved as shown in the Figure 4.3 (computer power supply). The ground-based suntracker used with PARIS-IR was tested in the TVAC to ensure that it could withstand the temperature and pressure conditions expected during the balloon flight. The temperatures of all of the CPUs achieved a stable operating value below 80°C. The PARIS-IR optical bench temperature was lower than 30 °C.

4.5 Preflight Preparation at Vanscoy, Saskatchewan

Field preparations started one month prior to the balloon launch. Tests were made to verify the performance of each instrument and then the payload was integrated and tested as a unit. Some ground-based measurements were taken near the beginning of the campaign using PARIS-IR and the sun tracker.

Figure 4.4 PARIS-IR and the ABB-Bomem sun tracker on the gondola of the MANTRA 2004 balloon during mechanical tests.

One of the first tests to be conducted with all of the instruments was to determine if the PARIS-IR ground-based sun tracker caused any mechanical interference with other instruments on the balloon platform. The sun tracker has two stepping motors which move the tracking mirror in azimuth and elevation (Figure 4.4). When tested on the balloon gondola, the vibration from the stepping motors produced artifacts in the measurements of the other two FTS instruments. Because of this, the sun tracker was replaced by a two-mirror tracker system coupled to the gondola pointing system (Figure 4.5). This required an alignment procedure to be developed and then to be verified outdoors by using the gondola pointing system to track the Sun. However, there proved to be very few opportunities to perform these tests because of cloudy and rainy weather during much of August.

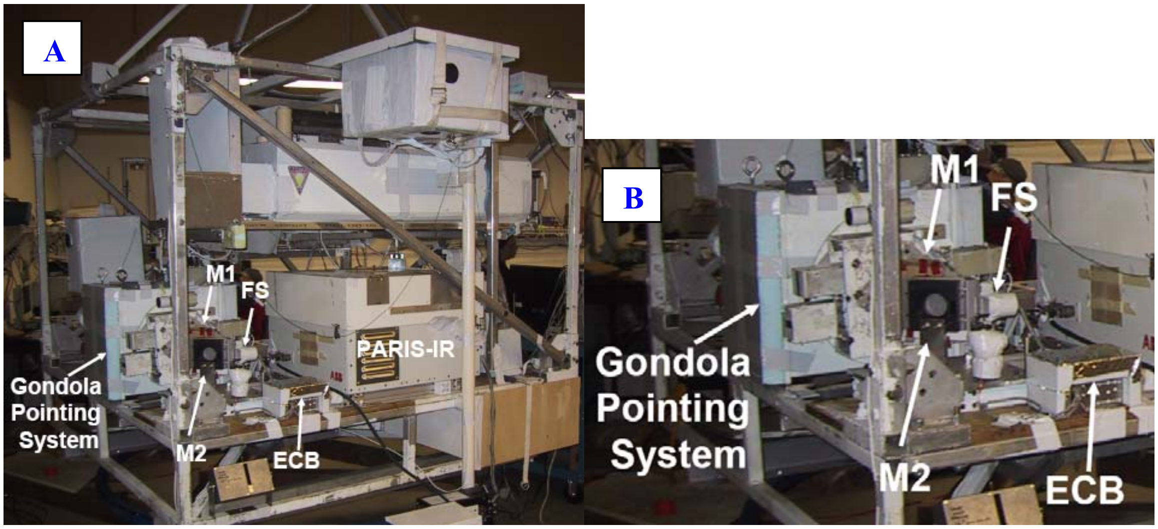

Figure 4.5 PARIS-IR and the two mirror tracker on the gondola of the MANTRA 2004 balloon. M1: a flat mirror (4 by 6 inches) mounted on the pointing system; M2: a flat mirror driven by a stepper motor; FS: feed back sensor; ECB: electronic control box for the stepper motor. A: overview B: expanded view.

Tests were done to ensure that the gondola power and communication systems and all instruments could be powered by the 28 V power supplied from the lithium battery packs and that the communication uplink and downlinks were operational using the onboard telemetry system. Tests were also carried out verify that there was no radio frequency interference from the instruments or the gondola systems onboard. Foam insulation was used to cover some of the instrument surfaces to reduce the impact of the large ambient temperature fluctuations during the flight. The foam not only kept heat in the instrument and the onboard computer during ascent, but it also insulated the sun-facing side of the instrument from the strong solar radiation at float altitude. Parts attached to heat sinks were not covered by foam, in order to allow the excess heat to more easily radiate from the instrument during flight.

4.6 MANTRA 2004 Balloon Flights

The first flight of the MANTRA 2004 payload was launched on September 1st, 2004 at 8:30:00 (local time). There was a problem with the uplink antenna that made it impossible to send commands to the gondola after the first 15 minutes of the flight. The instrument status information downlink showed that PARIS-IR was operating as expected using the auto scheduler. The observed instrument temperatures were slightly lower than those measured during the TVAC tests (Figure 4.6). Good performance was obtained from the heat sink on the DC-DC power supply.

Because of the loss of the command uplink, there was some concern that several of the instruments might overheat because they could not be turned off when they were not in use. It turned out that instrument temperatures were not a major problem, but the continuous operation of the instruments shortened the length of the flight by consuming the battery power. PARIS-IR measurements were attempted at solar noon and during sunset. A command glitch and problems with the solar alignment prevented usable spectra from being recorded on this flight. In addition, the gondola pointing system failed at 16:20:00, apparently due to overheating. Without active pointing control, the gondola started to rotate with a period of 30 minutes, thus making it impossible for any of the FTSs to record sunset spectra. The flight was terminated at 20:40:00. The payload was recovered the next morning and returned to the launch facility. All of the instruments were removed from the gondola and checked. PARIS-IR was found to have minimal damage, although its surface was rather dirty from landing in a wheat field.

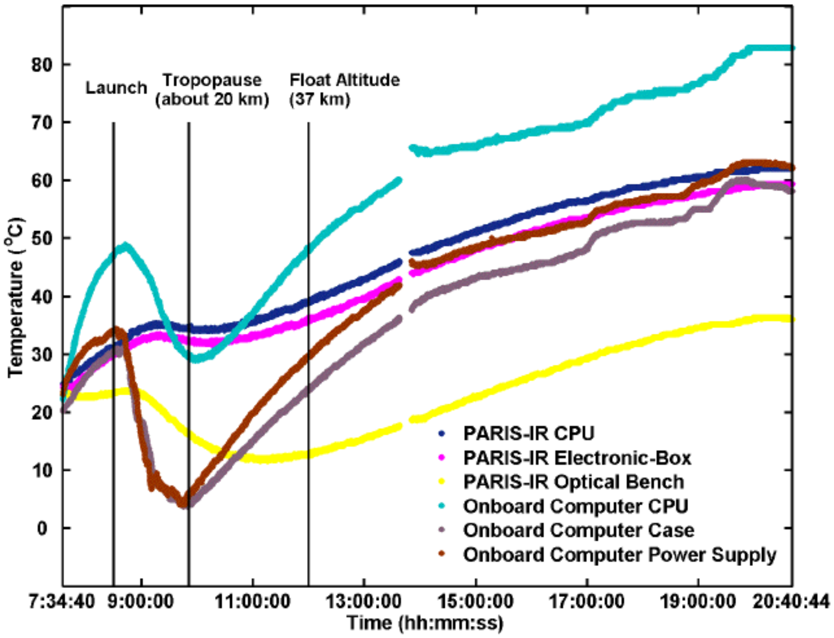

Figure 4.6 The temperature records of the major components in the PARIS-IR system obtained during the MANTRA 2004 balloon flight on September 1st, 2004. From 13:38:02 to 13:50:53 (local time), the instrument status information was not updated since its downlink system was used to transmit interferograms obtained at solar noon by PARIS-IR. The instrument temperatures varied with the ambient temperature significantly from the surface at launch to the float altitude.

Preparations were made for a second flight. PARIS-IR and the two mirror tracking system were realigned and extensively tested outdoors with the pointing system. The MANTRA 2004 payload was launched a second time on September 14th, 2004 at 2:16:00 (local time). Unfortunately, the flight ended after 5 minutes when the termination mechanism fired, separating the balloon from the gondola. The maximum altitude reached was 2.0906 km, as shown in Figure 4.7. The cause of this failure was investigated and remains unknown.

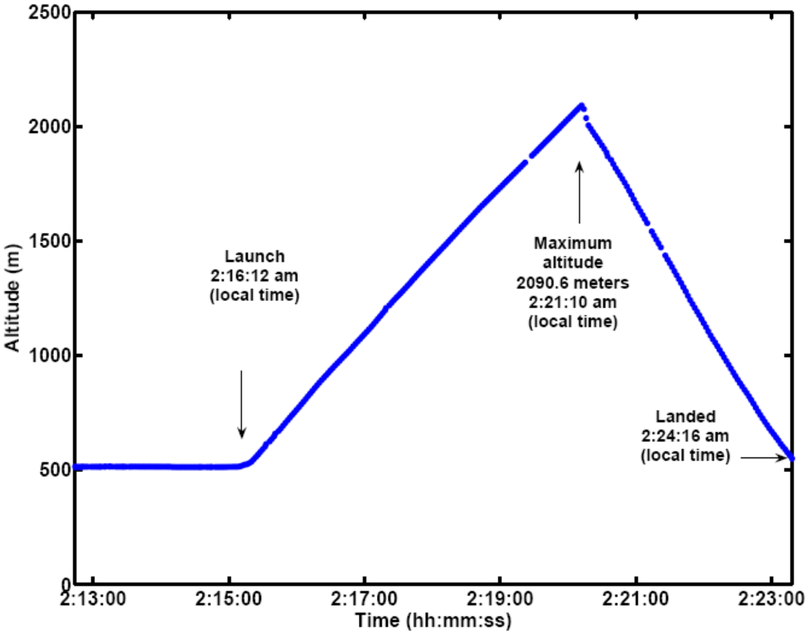

Figure 4.7 The altitude records of the PARIS-IR system obtained during the MANTRA 2004 balloon flight on September 14th, 2004. The termination system fired prematurely on 2:21:10 (local time).

4.7 Ground-based Measurements Made during MANTRA 2004

Ground-based measurements were carried out on August 13th, 2004 at the MSC Balloon Launch Facility in Vanscoy, Saskatchewan as part of the PARIS-IR prelaunch testing. The data were analyzed using the SFIT2 (version 3.81) program [*Pougatchev et al.*, 1995; *Rinsland et al.*, 1998], which uses the Optimal Estimation Method (OEM) to derive atmospheric composition information from spectra as discussed in Chapter 1. The total column of ozone observed by PARIS-IR at Vanscoy on August 13th, 2004 was 307.4 Dobson Units. For the same day, total column amounts of ozone obtained from the Brewer spectrophotometer [*Savastiouk and McElroy*, 2005], SAOZ (Systeme d'Analyse par d'Observation Zenithale, a lightweight UV-visible diode array spectrometer) [*Pommereau et al.*, 1988] and UV-visible grating spectrometer [*Bassford et al.*, 2001; 2005] at the same campaign station were 307.7, 305.8 and 288.0 Dobson Units (1 Dobson Unit = 2.6867 x 10^{16} molecules/cm^2), respectively [*Fraser et al.*, 2007]. The partial column amount of ozone (from the surface to 33.82 km) measured by an ozonesonde [*Davies et al.*, 2000] was 270.2 Dobson Units [*Fraser et al.*, 2007]. The partial column of ozone from the surface to 33.5 km retrieved from PARIS-IR observations was 261.3 Dobson Units. The discrepancies between PARIS-IR, Brewer spectrophotometer, SAOZ, ozonesonde and the UV-visible grating spectrometer are less than 6.5%. The uncertainty in the retrieved PARIS-IR results is 2.6%. The uncertainty in the retrieved PARIS-IR results for ozone include contributions from the spectral noise, interfering molecules, uncertainties in the viewing geometry and uncertainties in atmospheric temperature profiles which are described in Section 1.7.

4.8 PARIS-IR Observations during the mini-MANTRA Campaign

Simultaneous observations were performed by three FTSs on August 24th, August 26th, September 1st and September 2nd, 2005 from the Toronto Atmospheric Observatory (TAO, 43.66ºN, 79.4ºW, and 174 m above sea level), a complementary measurement station in the Network for the Detection of Atmospheric Composition Change (NDACC) (http://www.ndsc.ncep.noaa.gov/) as part of an intercomparison campaign. This activity was developed as a part of the MANTRA 2004 campaign and was called the mini-MANTRA campaign. The goal of the campaign was to investigate the impact of instrumental differences among PARIS-IR, U of T FTS, and TAO-FTS, such as instrument resolution (maximum optical path difference (MOPD) = 25 cm, 50 cm, and 250 cm, respectively for the three instruments), on the retrieved column amounts [*Wunch et al.*, 2007].

The observations were performed simultaneously using PARIS-IR (operator: Dejian Fu), the U of T FTS (operator: Debra Wunch), and the TAO-FTS (operator: Jeff Taylor). TAO-FTS, a high-resolution ABB-Bomem FTS, has a design similar to the ABB-Bomem DA8 Fourier transform spectrometer at PEARL (Section 2.2.5) and has been operating in the TAO since May 2002 [*Wiacek et al.*, 2007]. U of T FTS was adapted from a commercial ABB-Bomem DA5 FTS using updated software and electronics. It is a FTS that is appropriate for both ground-based and balloon-based measurements [*Wunch et al.*, 2006]. To ensure the differences observed in the mini-MANTRA results were solely due to instrument differences, simultaneous measurements were taken from the same location, (i.e., same optical path for three FTSs), in the same spectral range, and using similar retrieval methods with identical a priori information, line parameters and forward model. Retrievals for all three instruments were performed using SFIT2 (v.3.82beta3) [*Pougatchev et al.*, 1995; *Rinsland et al.*, 1998] and the same input parameters. More details on the data analysis using SFIT are given in Chapter 1. The experimental setup is shown in Figure 4.8.

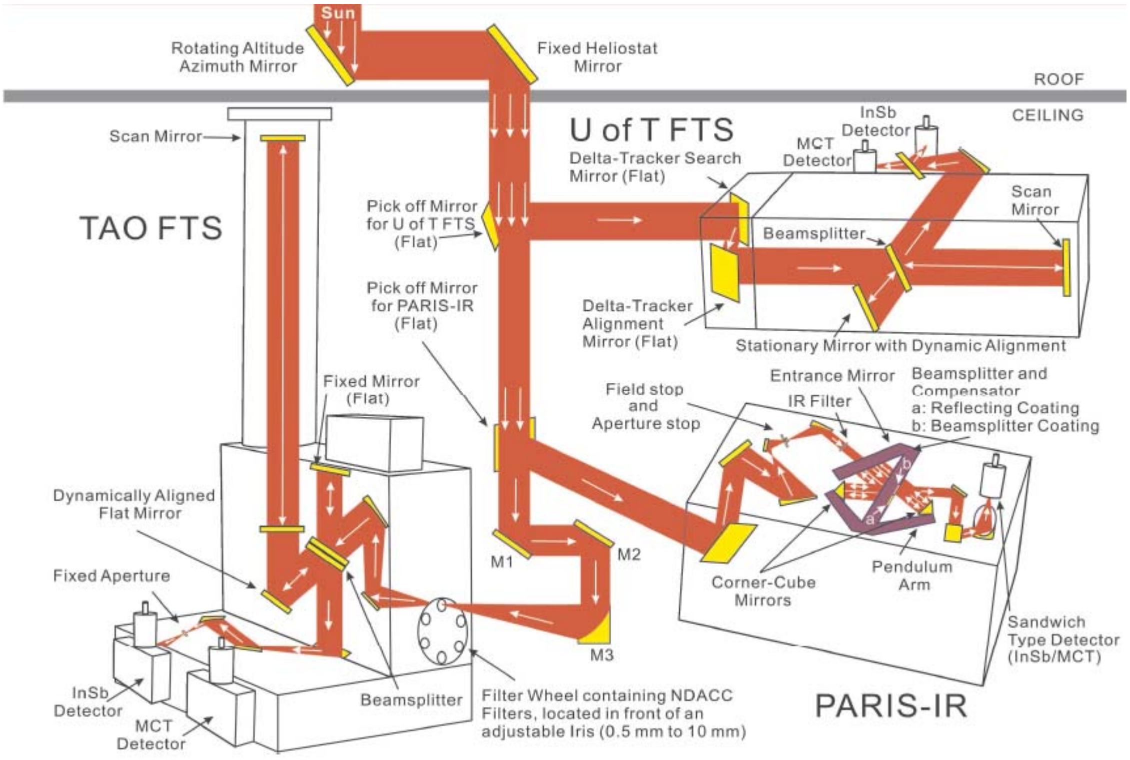

Figure 4.8 Diagram of the experimental setup in mini-MANTRA.

Total column amounts of O_3, HCl, N_2O and CH_4 were retrieved from PARIS-IR, the U of T FTS, and the TAO-FTS. Measurements were averaged during coincident 20-min periods, and the total column amounts retrieved from these averaged spectra were compared directly. The results for the three FTSs are given in Table 4.2. These show that the lower-resolution instruments can measure total columns of O_3, CH_4, HCl and N_2O to within 4%, on average, of the “true” values (taken here as the results from the high-resolution TAO-FTS) from the ground [*Wunch et al.*, 2007]. The largest errors are obtained for the stratospheric species, and these errors can be attributed to the averaging kernels of the lower-resolution instruments, since PARIS-IR has lower spectral resolution than others. It suggests that using other spectral ranges with higher line densities of target species will help to improve the observations made using PARIS-IR. A new set of microwindows, the spectral segments used in the retrievals, have been selected and used in the data analysis of spectra recorded at Eureka in 2006 [*Fu et al.*, in preparation] and shown in Chapter 6. The errors from the methane retrievals are possibly due to uncertainties in the spectroscopic parameters. Using better instrument information by retrieving Instrument Line Shape (ILS) parameters from SFIT2 significantly improves the column comparisons of the stratospheric species for the lower-resolution instruments over retrievals performed assuming an ideal ILS [*Wunch et al.*, 2007]. The ILS information is less important for the wider lines of pressure-broadened tropospheric species (N_2O and CH_4) in the observations using PARIS-IR.

Table 4.2 Percentage differences of mean total column values among PARIS-IR, U of T FTS, and TAO-FTS together with results from previous intercomparisons is shown. Measurements with solar zenith angle > 40 degrees were used. Table courtesy of D. Wunch.

	O_3		HCl	N_2O	CH_4
	3040[a]	2775[a]	2925[a]	2482[a]	2859[a]
PARIS-IR percentage difference from TAO	0.9	1.2	4.5	0.4	0.5
U of T FTS percentage difference from TAO	3.3	0.7	1.7	0.4	2.3
U of T FTS percentage difference from PARIS-IR	4.3	2.8	2.6	0.8	1.7

[a] Central wavenumber of the spectral segments used in analysis.

4.9 Summary and conclusions

The PARIS-IR instrument was adapted for balloon-based measurements. Its first flights were part of the MANTRA 2004 balloon payload and some useful engineering information was obtained on the thermal performance of the instrument. For future flights, improvements will have to be made to the PARIS-IR suntracker to provide a system that is more easily aligned. To achieve the MANTRA goals, a ground-based inter-instrument comparison campaign was conducted with the objective of assessing instrument performance and evaluating data processing routines and retrieval codes. Based on the results from the intercomparison campaign, PARIS-IR provides similar quality results for the stratospheric species as does the U of T FTS, a portable FTS that was deployed in MANTRA 2004. It also suggests that using an accurate ILS improves the observations using a portable FTS such as PARIS-IR, for which the spectral resolution is typically 5-10 times lower than for a laboratory FTS.

4.10 References

Bernath P.F., McElroy C.T., Abrams M.C., Boone C.D., Butler M., Camy-Peyret C., Carleer M., Clerbaux C., Coheur P.-F., Colin R., DeCola P., DeMazière M., Drummond J.R., Dufour D., Evans W.F.J., Fast H., Fussen D., Gilbert K., Jennings D.E., Llewellyn E.J., Lowe R.P., Mahieu E., McConnell J.C., McHugh M., McLeod S.D., Michaud R., Midwinter C., Nassar R., Nichitiu F., Nowlan C., Rinsland C.P., Rochon Y.J., Rowlands N., Semeniuk K., Simon P., Skelton R., Sloan J.J., Soucy M.-A., Strong K., Tremblay P., Turnbull D., Walker K.A., Walkty I., Wardle D.A., Wehrle V., Zander R., and Zou J., (2005), Atmospheric Chemistry Experiment (ACE): Mission Overview, *Geophys. Res. Lett.*, **32**, L15S01, doi:10.1029/2005GL022386.

Bassford M.R., McLinden C.A., and Strong K., (2001), Zenith-Sky Observations of Stratospheric Gases: The Sensitivity of Air Mass Factors to Geophysical Parameters and the Influence of Tropospheric Clouds, *J. Quant. Spectrosc. Radiat. Transfer*, **68**, 657-677.

Bassford M.R., Strong K., McLinden C.A., and McElroy C.T. (2005), Ground-based measurements of ozone and NO_2 during MANTRA 1998 using a new Zenith-Sky spectrometer, *Atmos. Ocean.*, **43**, 325-338.

Davies J., Tarasick D.W., McElroy C.T., Kerr J.B., Fogal P.F., and Savastiouk V., (2000), Evaluation of ECC ozonesonde preparation methods from laboratory tests and field comparisons during MANTRA, *Proceedings of the Quadrennial Ozone Symposium*, Hokkaido University, Sapporo, Japan, July 3-8, 2000. Bojkov RD, Kazuo S. eds., 137-138.

Fraser A., Bernath P.F., Blatherwick R.D., Drummond J.R., Fogal P.F., Fu D., Goutail F., McElroy C.T., Midwinter C., Olson J.R., Strong K., Walker K.A., Wunch D., and Young I., (2007) Intercomparison of ground-based ozone and NO_2 measurements during the MANTRA 2004 campaign, *Atmos. Chem. Phys.*, **7**, 10205–10234.

Fu D., Walker K.A., Sung K., Boone C.D., Soucy M-A, and Bernath P.F., (2007), The Portable Atmospheric Research Interferometric Spectrometer for the Infrared, PARIS-IR, *J. Quant. Spectrosc. Radiat. Trans.*, **103**, 362-370.

Fu D., Mittermeier R., Sung K., Walker K.A., Boone C.D., Bernath P.F., Fast H., and Strong K., Simultaneous atmospheric measurements using Fourier transform infrared spectrometers at the Polar Environment Atmospheric Research Laboratory (PEARL) during spring 2006, (in preparation for *Atmos. Chem. Phys.*).

McElroy C.T., (1995), A spectroradiometer for the measurement of direct and scattered solar irradiance from on-board the NASA ER-2 high-altitude research aircraft, *Geophys. Res. Lett.*, **22**, 1361-1364.

McElroy C.T., Nowlan C.R., Drummond J.R., Bernath P.F., Barton D.V., Dufour D.G., Midwinter C., Hall R.B., Ogyu A., Ullberg A., Wardle D.I., Kar J., Zou J., Nichitiu F., Boone C.D., Walker K.A., and Rowlands N., (2007), The ACE-MAESTRO instrument on SCISAT: description, performance, and preliminary results, *Appl. Opt.*, **46**, 4341-4356.

Pommereau J.P. and Goutail F., (1988), O_3 and NO_2 ground-based measurements by visible spectrometry during Arctic winter and spring, *Geophys. Res. Lett.*, **15**, 891-894.

Pommereau J.P. and Piquard J. (1994), Ozone and nitrogen dioxide vertical distributions by UV-visible solar occultation from balloons, *Geophys. Res. Lett.*, **21**(13), 1227-1230.

Pougatchev N.S., Connor B.J., and Rinsland C.P., (1995), Infrared measurements of the ozone vertical distribution above Kitt Peak, *J. Geophys. Res.*, **100**, 16689-16698.

Rinsland C.P., Jones N.B., Connor B.J., Logan J.A., Pougatchev N.S., Goldman A., Murcray F.J., Stephen T.M., Pine A.S., and Zande R., (1998), Northern and southern hemisphere ground-based infrared spectroscopic measurements of tropospheric carbon monoxide and ethane, *J. Geophy. Res.*, **103**, 28197-28217.

Savasktiouk V. and McElroy C.T., (2005), Brewer spectrophotometer total ozone measurements made during the 1998 Middle Atmosphere Nitrogen Trend Assessment (MANTRA) campaign, *Atmos. Ocean.*, **43**, 315-324.

Strong K., Bailak G., Barton D., Bassford M.R., Blatherwick R.D., Brown S., Chartrand D., Davies J., Drummond J.R., Fogal P.F., Forsberg E., Hall R., Jofre A., Kaminski J., Kosters J., Laurin C., McConnell J.C., McElroy C.T., McLinden C.A., Melo S.M.L., Menzies K., Midwinter C., Murcray F.J., Nowlan C., Olson J.R, Quine B.M., Rochon Y., Savastiouk V., Solheim B., Sommerfeldt D., Ullberg A., Werchohlad S., Wu H., and Wunch D., (2005), MANTRA - A balloon mission to study the odd-nitrogen budget of the stratosphere, *Atmos. Ocean*, **43**, 283-299.

Walker, K.A., Randall C.E., Trepte C.R., Boone C.D., and Bernath P.F., (2005), Initial validation comparisons for the Atmospheric Chemistry Experiment (ACE-FTS) *Geophys. Res. Lett.*, **32**, L16S04, doi:10.1029/2005GL022388.

Wiacek A., Taylor J.R., Strong K., Saari R., Kerzenmacher T.E., Jones N.B., and Griffith D.W.T., (2007), Ground-based solar absorption FTIR spectroscopy: Characterization of retrievals and first results from a novel optical design instrument at a new NDACC complementary station, *J. Atmos. Ocean. Tech.* **24**, 432-448.

Wunch D., Midwinter C., Drummond J.R., McElroy C.T., Bagès A-F, (2006), University of Toronto's balloon-borne Fourier transform spectrometer, *Rev. Sci. Instrum.*, **77**, 093104.

Wunch D., Taylor J.R., Fu D., Bernath P., Drummond J.R., Midwinter C., Strong K., and Walker K.A., (2007), Simultaneous ground-based observations of O_3, HCl, N_2O, and CH_4 over Toronto, Canada by three Fourier transform spectrometers with different resolutions, *Atmos. Chem. Phys.*, **7**, 1275-1292.

Yee J.-H., Talaat E.R., Christensen A.B., Killeen T.L., Russell J.M., and Woods T.N., (2003), TIMED instruments, Johns Hopkins APL technical digest, **24**, 156-164.

Chapter 5

Ground-based Solar Absorption Studies for the Carbon Cycle Science by Fourier Transform Spectroscopy (CC-FTS) Mission

5.1 Introduction

Emissions from human activities such as combustion of fossil fuel, production of cement and changes in land use are changing the Earth's atmosphere. The primary anthropogenic contribution to the change in atmospheric composition is the emission of the greenhouse gases CO_2, CH_4, and N_2O [*Etheridge et al.*, 1998; *Cunnold et al.*, 2002; *Hofmann et al.*, 2006; *IPCC*, 2007]. Greenhouse gas concentrations in the atmosphere have increased significantly in the past few decades [*Cunnold et al.*, 2002; *Hofmann et al.*, 2006; IPCC 2007; *Keeling et al.*, 1996, 2005; *Yang et al.*, 2002; *Washenfelder et al.*, 2003; *Dufour et al.*, 2004]. The first high precision measurements of atmospheric CO_2 concentrations on a continuous basis were taken by C.D. Keeling, starting in 1958 at Mauna Loa, Hawaii [*Keeling*, 1960; *Keeling et al.*, 2005]. The record of CO_2 concentrations at Mauna Loa, now known as the "Keeling curve", indicates a 21% increase in the mean annual concentration from 315 ppmv in 1958 to 381 ppmv in 2006, as shown in Figure 5.1 [Source data are available at ftp://ftp.cmdl.noaa.gov/ccg/co2/in-situ/]. The persistent year-to-year increase has an associated wave-like pattern in each year. These annual cycles are due to the effect of the biosphere on the CO_2 concentration. The atmospheric CO_2 concentration is higher in winter due to biospheric respiration, and has low values in summer because of drawdown by photosynthesis [*Keeling et al.*, 1996, 2005]. The increase in greenhouse gases has important consequences for air quality, meteorology and climate [*Etheridge et al.*, 1998; *Cunnold et al.*, 2002; *Hofmann et al.*, 2006; *IPCC*, 2007; *Houghton et al.*, 2000].

Since the 1970s, a world-wide network consisting of more than 100 stations has been organized to monitor greenhouse gases. For example, air samples are collected through the National Ocean and Atmospheric Administration (NOAA) / Earth System Research Laboratory (ESRL) global network, including a cooperative program for carbon containing gases which provides samples from 30 fixed stations and at 5 degree latitude intervals from three ship routes [*Cunnold et al.*, 2002; *Hofmann et al.*, 2006]. In North America, solar absorption spectra recorded containing information on CH_4 and CO_2 have been recorded since 1978 at Kitt Peak, Arizona, USA [*Yang et al.*, 2002; *Washenfelder et al.*, 2003; *Dufour et al.*, 2004]. The tropospheric CH_4 and atmospheric CO_2 total columns were retrieved from these spectra. In 1992, the Kyoto Protocol was established as an international treaty on climate change, assigning mandatory greenhouse gas emission limitations to the signatory countries [*Hofmann et al.*, 2006; *Houghton et al.*, 2000].

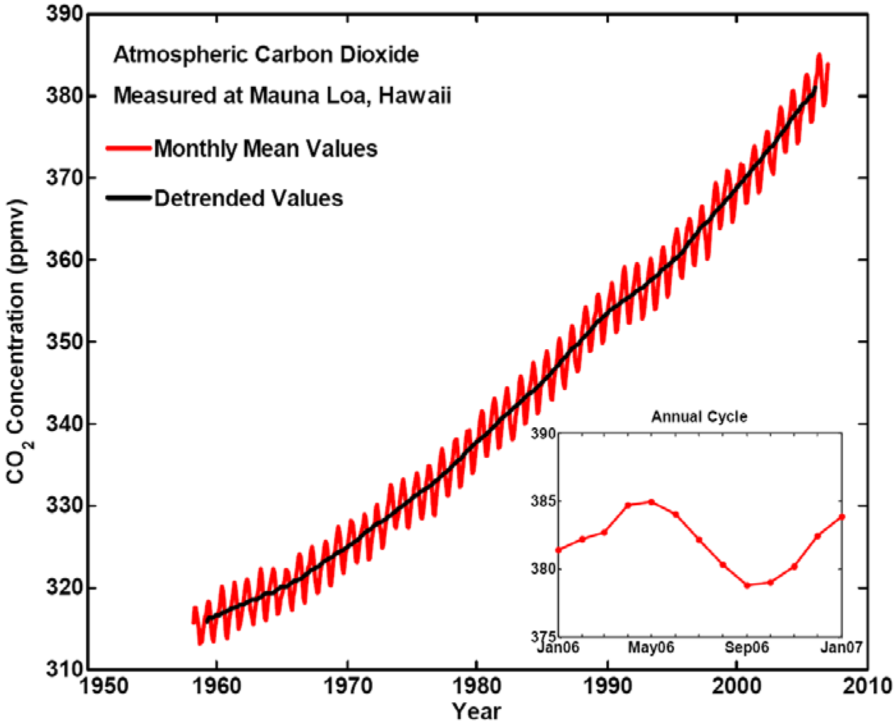

Figure 5.1 The 48-year record of atmospheric CO_2 monthly mean concentrations in dry air at Mauna Loa, also known as the Keeling curve, shows a 21% increase of the mean annual concentration from 315 ppmv in 1958 to 381 ppmv in 2006. The annual cycle of CO_2 at Mauna Loa in 2006 is shown in the subplot. Source data were downloaded from the following link: ftp://ftp.cmdl.noaa.gov/ccg/co2/in-situ/.

Detailed knowledge of the carbon cycle is necessary to implement the Kyoto Protocol and successor agreements. Measurements from ground-based instruments provide long-term records of concentrations of major greenhouse gases, but with limited spatial coverage. Furthermore, in the transport models used to identify the regional sources and sinks, errors within models are bigger than those between models [*Gurney et al.*, 2002]. However, the requirement to monitor sources and sinks of greenhouse gases, which helps to achieve the goal of controlling the amount of greenhouse gases, makes the knowledge of the global spatial distributions important [*Rayner and O'Brien*, 2001]. Observations from space using Fourier transform spectroscopy provide an effective method to obtain global distributions of greenhouse gases with high spatial resolution and accuracy. Current satellite instruments such as TOVS [*Chédin et al.*, 2002, 2003], IASI [*Turquety et al.*, 2004], AIRS [*Aumann et al.*, 2003], TES [*Beer* 2006], MOPITT [*Drummond and Mand*, 1996; *Deeter et al.*, 2004], and particularly SCIAMACHY [*Buchwitz et al.*, 2005], are carrying out pioneering studies on global carbon. However, measurements from these missions have a limitation in that they provide a precision not better than 1% for the columns and, except for SCIAMACHY, all of them have poor sampling of the planetary boundary layer [*Crisp et al.*, 2004]. Since differential column distributions are needed to identify regional sources and sinks of CO_2, it is the precision of the measurements that is more important than absolute accuracy. In 1997, *Park et al.* [1997] showed that a precision of better than 1% in the CO_2 column-averaged volume mixing ratio can be achieved for a FTS when the O_2 A-band and three CO_2 bands at 4.3, 2.7, and 2.0 μm are employed. More recent studies by *Rayer et al.* in 2001 demonstrated that a precision of 2.5 ppm (0.7%) is needed to improve on the current knowledge of sources and sinks based on the existing flask network. The absolute accuracy can be improved by a ground-based calibration-validation program associated with a satellite mission.

The Orbiting Carbon Observatory (OCO) mission will make the first global, space-based measurements of atmospheric carbon dioxide (CO_2) with the precision, resolution, and coverage required to characterize CO_2 sources and sinks on regional scales. Starting in 2008 the OCO mission will measure global CO_2 column densities using three near infrared grating spectrometers (spectral resolution of about 0.3 cm^{-1}) in a 98.2° polar sun-synchronous orbit in the 'A-train' [*Crisp et al.*, 2004]. The Greenhouse Gases Observing Satellite (GOSAT) mission will also be launched in 2008, and will use a Fourier transform spectrometer (FTS) (resolution of 0.2 cm^{-1}, MOPD = 2.5 cm) to make measurements of additional gases such as CH_4 as well as CO_2 [*Hamazaki et al.*, 2005]. GOSAT will use observations in the thermal infrared as well as the near infrared, but has a pixel size of 10 km by 10 km compared to the 1 km by 1 km pixel used by OCO [*Crisp et al.*, 2004; *Hamazaki et al.*, 2005]. Smaller pixel sizes suffer from less cloud contamination. The Carbon Cycle science by Fourier Transform Spectroscopy (CC-FTS) mission is a second-generation mission proposed to follow OCO and GOSAT. It aims to provide highly precise simultaneous observations of CO_2, CH_4, CO, N_2O and O_2 with a small pixel size of 1 km by 1 km, similar to the OCO mission. This chapter reports on the results of ground-based observations needed to select the spectral regions, spectral resolution, and spectroscopic line parameter requirements for this proposed mission.

Ground-based solar absorption spectra recorded in the near infrared have been analysed to obtain CH_4 and CO_2 columns [*Yang et al.*, 2002; *Washenfelder et al.*, 2003; *Dufour et al.*, 2004]. However, the spectroscopic parameters from HITRAN 1996 and 2000 used in their work are substantially different from more recent values [*Henningsen and Simonsen*, 2000; *Miller and Brown*, 2004; *Miller et al.*, 2004, 2005; *Toth et al.*, 2006]. In the near infrared, nadir satellite observations are based on the measurement of reflected sunlight [*O'Brien et al.*, 1998; *Heidinger and Stephens*, 2000; *Kuze and Chance*, 1994; *Asano et al.*, 1995; *Yang et al.*, 2005]. Solar photons experience significant scattering in the atmosphere from clouds and aerosols, and therefore have an effective optical path different from that calculated using the observation geometry. The retrieved column densities of the greenhouse gases can be corrected for the variations in optical path caused by clouds and aerosols by dividing them by the simultaneously observed O_2 total column. O_2 is a well mixed gas with a known constant volume mixing ratio. However, no published work has analyzed the O_2 A-band at 0.76 μm and the greenhouse gas absorptions in the near infrared region (such as CH_4 near 1.68 μm and CO_2 near 1.57 μm and 2.06 μm) using simultaneously observed spectra. Most of the ground-based FTSs, such as those used in the Network for the Detection of Atmospheric

Composition Change (NDACC, http://www.ndsc.ncep.noaa.gov/) only observe in the infrared spectral region from 700 to 7000 cm^{-1}. Recently automated observatories with the capability of measuring atmospheric column abundances of CO_2 and O_2 simultaneously using near-infrared FTS solar absorption spectra of the sun have been developed in the Total Carbon Column Observing Network (TCCON). The first observations at Park Falls, Wisconsin have just been published, but they did not use the O_2 A-band recorded in their analyses [*Washenfelder et al.*, 2006]. Simultaneously observed spectra are able to provide the total column of CO_2, CH_4, CO, N_2O and O_2 under the same atmospheric conditions of optical path and ambient pressure. Our work presents first results from ground-based measurements over broad spectral region spanning 2000 to 15000 cm^{-1}.

5.2 Instrumentation and Observations

The effect of spectral resolution has been considered in order to determine an optimum value for a greenhouse gas mission. Ground-based atmospheric absorption spectra in the 3950 cm^{-1} to 7140 cm^{-1} region with a spectral resolution of 0.0042 cm^{-1} (120 cm MOPD) recorded using a Bruker IFS 120 HR spectrometer at Kiruna (67.84ºN, 20.41ºE, and 419 m above sea level), Sweden on April 1st, 1998 were used for this study. The observed interferogram was truncated at 50 cm, 5 cm and 5/3 cm MOPD and Fourier transformed to generate spectra with resolution of 0.01 cm^{-1}, 0.1 cm^{-1}, 0.3 cm^{-1}, respectively. Figures 5.2-5.5 present expanded views of observed and resolution degraded spectra in six spectral regions including CO_2 at 4911 and 6238 cm^{-1}, CH_4 at 4264 and 5891 cm^{-1}, CO at 4274 cm^{-1} and N_2O at 4429 cm^{-1}. Typical molecular line widths due to pressure broadening are 0.1 cm^{-1} in the troposphere, so there is little change in the spectra as the resolution changes from 0.0042 cm^{-1} to 0.01 cm^{-1}, or even to 0.1 cm^{-1} for these molecules. The change in resolution from 0.1 cm^{-1} to 0.3 cm^{-1}, however, has a more significant effect, and in all cases, except for the very clean CO_2 band near 6239 cm^{-1} that has been selected as the primary candidate for CO_2 column measurements, there is a serious loss of information at the lower spectral resolution of 0.3 cm^{-1} for the atmospheric species of CH_4, CO and N_2O. In particular, the lines of interest

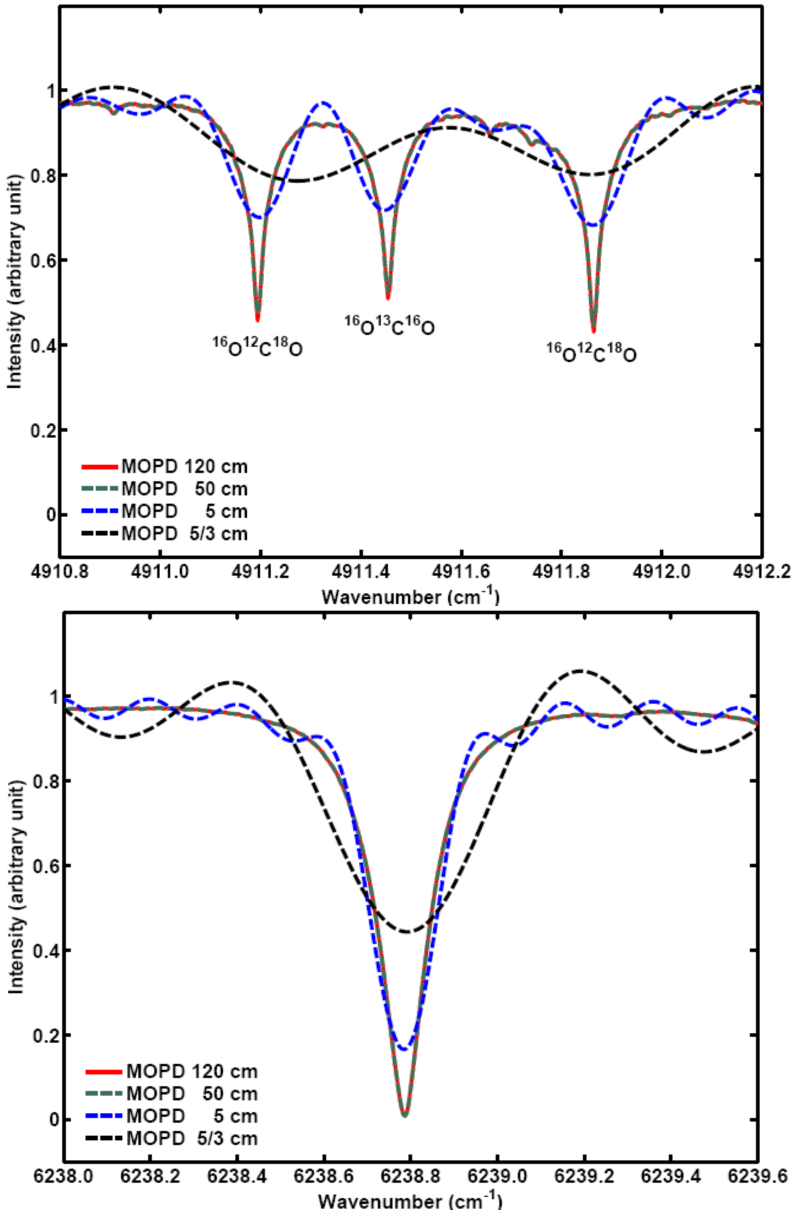

Figure 5.2 Observed and resolution-degraded atmospheric absorption spectra of CO_2 near 4911 cm^{-1} at 2.06 μm (upper plot) and near 6238 cm^{-1} at 1.57 μm (lower plot) are shown. Solid lines indicate spectra recorded with a commercial Bruker IFS 120 HR spectrometer by Meier at Institutet för rymdfysik (IRF) Kiruna (67.84ºN, 20.41ºE, and 419 m above sea level) on April 1st, 1998. Solar zenith angle is 65.02º, and spectral resolution is 0.0042 cm^{-1} (MOPD = 120 cm). Spectra with resolution degraded from 0.0042 cm^{-1} (MOPD = 120 cm) to 0.01 cm^{-1} (MOPD = 50 cm), 0.1 cm^{-1} (MOPD = 5 cm) and 0.3 cm^{-1} (MOPD = 5/3 cm) are presented by red solid line, green dashed line, blue dashed line and black dashed line, respectively.

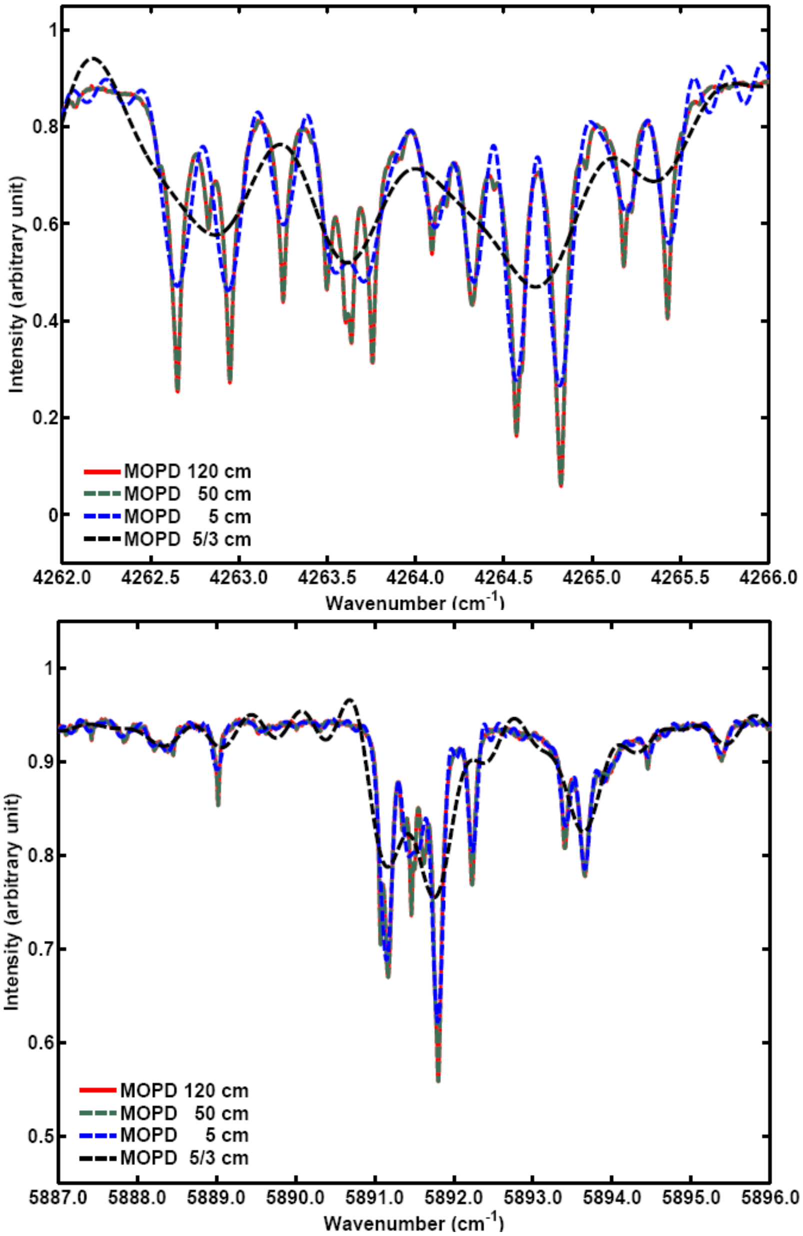

Figure 5.3 Observed and resolution-degraded atmospheric absorption spectra of CH_4 near 4264 cm^{-1} at 2.34 μm (upper plot) and near 5891 cm^{-1} at 1.69 μm (lower plot) are shown. Solid lines indicate spectra recorded with a commercial Bruker IFS 120 HR spectrometer by Meier at IRF Kiruna (67.84°N, 20.41°E, and 419 m above sea level) on April 1st, 1998. Solar zenith angle is 65.02°, and spectral resolution is 0.0042 cm^{-1} (MOPD = 120 cm). Spectra with resolution degraded from 0.0042 cm^{-1} to 0.01 cm^{-1} (MOPD = 50 cm), 0.1 cm^{-1} (MOPD = 5 cm) and 0.3 cm^{-1} (MOPD = 5/3 cm) are shown by red solid line, green dashed line, blue dashed line and black dashed line, respectively.

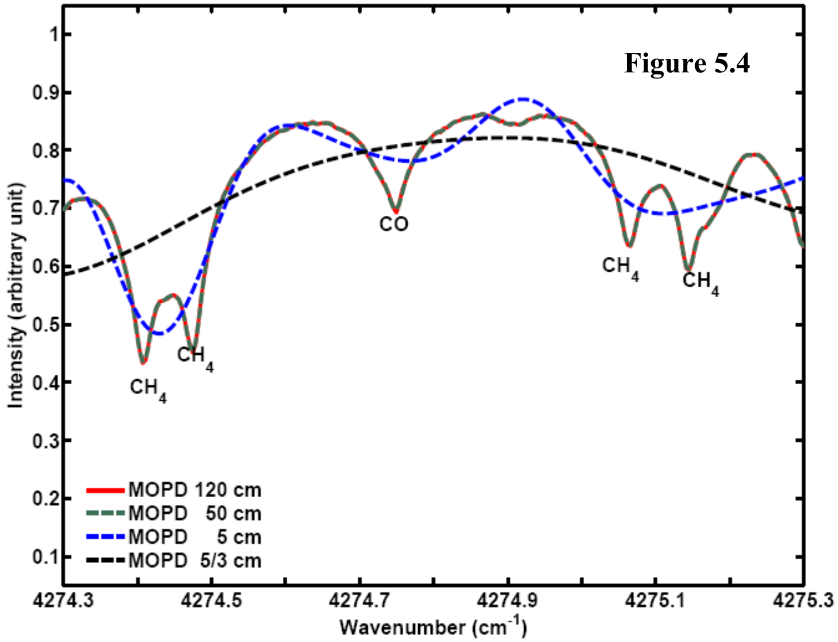

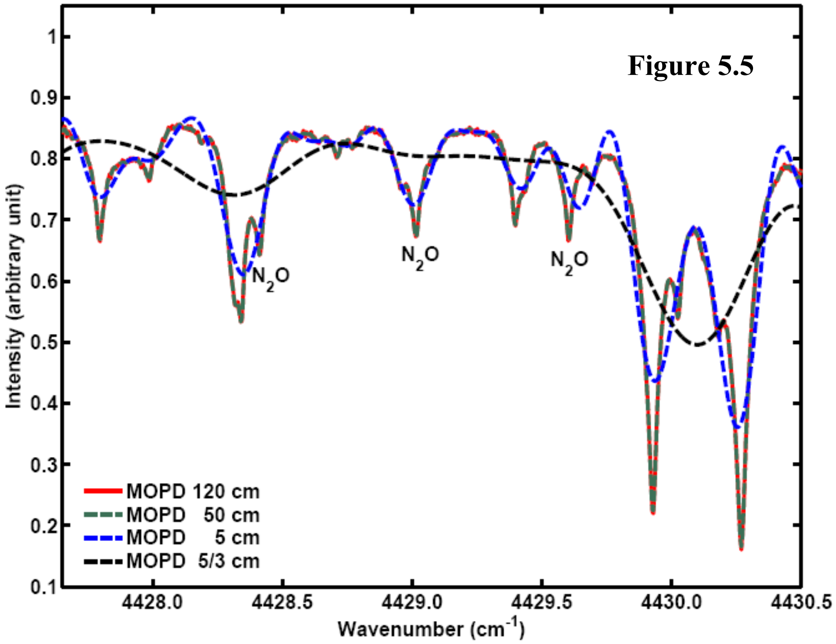

Figure 5.4 Observed and resolution-degraded atmospheric absorption spectra of CO near 4274 cm^{-1} at 2.34 μm are shown. Solid lines indicate spectra recorded with a commercial Bruker IFS 120 HR spectrometer by Meier at IRF Kiruna (67.84ºN, 20.41ºE, and 419 m above sea level) on April 1st, 1998. Solar zenith angle is 65.02º, and spectral resolution is 0.0042 cm^{-1} (MOPD = 120 cm). Spectra with resolution degraded from 0.0042 cm^{-1} to 0.01 cm^{-1} (MOPD = 50 cm), 0.1 cm^{-1} (MOPD = 5 cm) and 0.3 cm^{-1} (MOPD = 5/3 cm) are presented by red solid line, green dashed line, blue dashed line and black dashed line, respectively.

Figure 5.5 Observed and resolution-degraded atmospheric absorption spectra of N_2O near 4429 cm^{-1} at 2.26 μm are shown. Solid lines indicate spectra recorded with a commercial Bruker IFS 120 HR spectrometer by Meier at IRF Kiruna (67.84ºN, 20.41ºE, and 419 m above sea level) on April 1st, 1998. Solar zenith angle is 65.02°, and spectral resolution is 0.0042 cm^{-1} (MOPD = 120 cm). Spectra with resolution degraded from 0.0042 cm^{-1} to 0.01 cm^{-1} (MOPD = 50 cm), 0.1 cm^{-1} (MOPD = 5 cm) and 0.3 cm^{-1} (MOPD = 5/3 cm) are presented by solid line, triangle-dashed line, dashed line and dotted line, respectively.

become blended with water lines, and the baseline is no longer clear; this will degrade the retrieval precision. To monitor concentrations of major greenhouse species other than CO_2 with high precision, the spectral resolution should be better than 0.3 cm^{-1}. Spectra recorded at about 0.1 cm^{-1} (MOPD = 5 cm) are satisfactory.

For additional studies, we recorded atmospheric absorption spectra with resolutions of 0.01 cm^{-1} and 0.1 cm^{-1} at the National Solar Observatory (NSO) at Kitt Peak in Arizona (31.9°N, 111.6°W, and 2.1 km above sea level) and Waterloo Atmospheric Observatory (WAO) at Waterloo in Ontario (43.5°N, 80.6°W, and 0.3 km above sea level). A series of spectra were obtained on July 25th, 2005 using the McMath-Pierce FTS, a folded cat's-eye Michelson interferometer (MOPD = 100 cm) housed in a vacuum vessel in the McMath-Pierce solar telescope facility. An ABB Bomem DA8 Fourier transform spectrometer, a plane mirror Michelson interferometer (25 cm MOPD), was used for the observations in the WAO on November 22nd, 2006. Details of descriptions for these two FTSs are given in Chapter 2.

For the observations at NSO, an indium antimonide (InSb) detector and calcium fluoride (CaF_2) beamsplitter were used to record atmospheric absorption spectra from 2000 cm^{-1} to 15000 cm^{-1}. Each spectrum recorded is the coaddition of 2 scans (about 30 minutes) at a spectral resolution of 0.01 cm^{-1}. A RG715 red pass filter was used to cut the spectra at 15000 cm^{-1}. At WAO, the observations were also recorded in the near-infrared spectral region from 2000 to 15000 cm^{-1} in order to obtain spectroscopic signatures of O_2, CH_4, CO_2, CO, and N_2O. A filter (713 nm or 14000 cm^{-1} red pass) in front of the entrance window of the DA8 spectrometer was used to block visible light. InSb and semiconductor silicon (Si) detectors were used (InSb: 2,000 to 15,000 cm^{-1}, Si: 8,500 to 15,000 cm^{-1}) in alternation. Each spectrum is based on the coaddition of 20 scans (about 15 minutes).

The left hand panel of Figure 5.6 shows an overview of the atmospheric absorption spectra recorded at WAO covering the broad spectral region from mid infrared to visible. The spectral segments indicated by the solid bars are the regions containing a high density of absorption features of CH_4, CO_2, CO, N_2O and O_2. The right hand panel in Figure 5.6 provides enlarged views of three spectral regions of interest. Starting from the top, they are

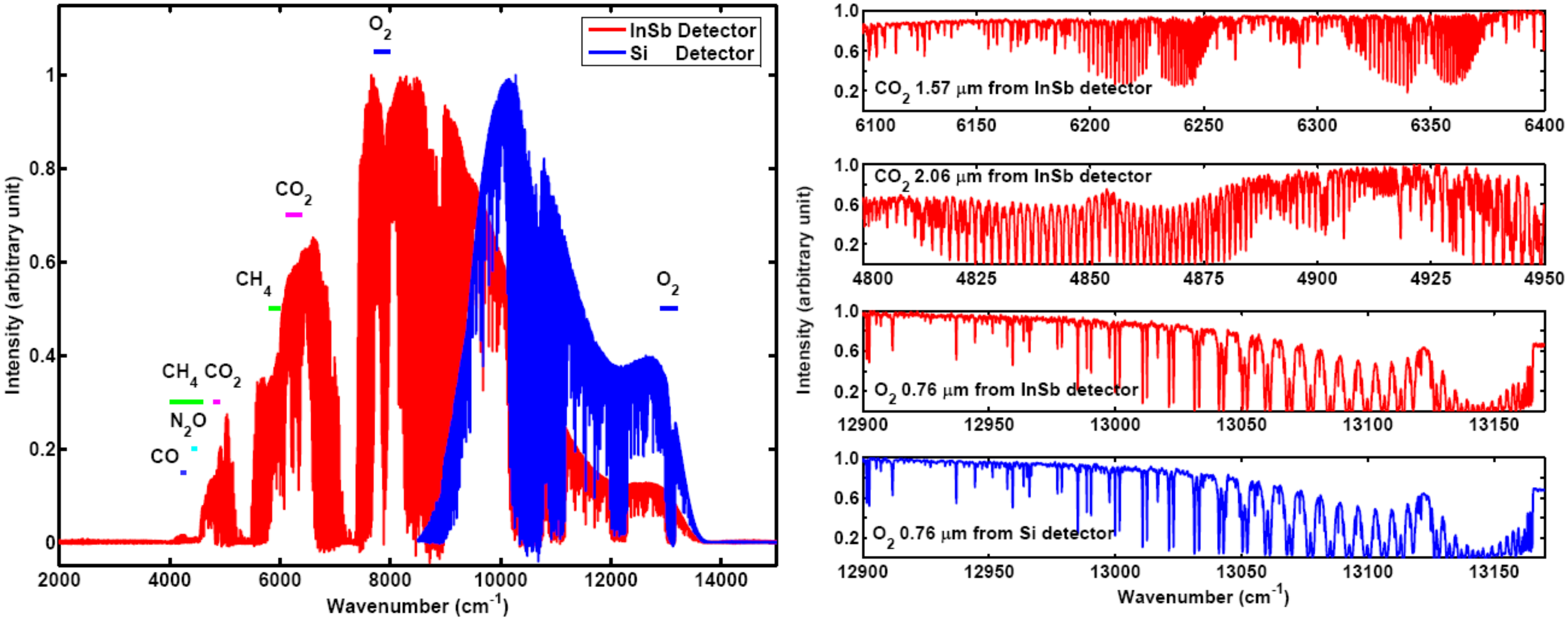

Figure 5.6 Overview (on the left) and enlarged view (on the right) of the atmospheric absorption spectra recorded on November 22nd, 2006 using the ABB-Bomem DA8 spectrometer at WAO (43.5°N, 80.6°W, and 0.3 km above sea level) are shown. Spectral resolution is 0.1 cm^{-1} (MOPD = 5 cm). InSb and Si detectors are used to record spectra covering the spectral region from 4000 to 14000 cm^{-1} (red line in left plot) and 8500 to 14000 cm^{-1} (blue line in left plot), respectively. Solar zenith angles are 66.61° and 67.33° for InSb and Si data, respectively. In the overview of spectra, solid bars with species names indicate the spectral regions containing suitable absorption features. From top to bottom in the right plot, expanded spectral sections from the overview spectra are shown for CO_2 at 1.57 μm and 2.06 μm, O_2 A-band at 0.76 μm from InSb and Si detectors, respectively.

CO_2 at 1.58 μm, CO_2 at 2.06 μm and O_2 at 0.76 μm recorded with the InSb detector. The bottom plot of right hand panel of Figure 5.6 shows O_2 at 0.76 μm recorded using the Si detector. The O_2 A-band recorded using the InSb detector has a signal-to-noise ratio of 150:1. Although the 0.76 μm spectral region is not optimal for the InSb detector, spectra recorded with the InSb detector are similar in quality as those acquired using the Si detector. The highest precision will be obtained by using spectra covering all regions of interest (including the A-band) that are recorded at the same time [*Yang et al.*, 2002; *Washenfelder et al.*, 2003; *Dufour et al.*, 2004; *Washenfelder et al.*, 2006]. Hence, the analysis only includes spectra recorded using the InSb detector.

5.3 Spectral Analysis and Retrievals

Spectra recorded at the two observatories were analyzed using SFIT2 (version 3.91) [*Pougatchev et al.*, 1995; *Rinsland et al.*, 1998]. SFIT2 was jointly developed at the NASA-Langley Research Center and at the National Institute of Water and Atmospheric Research at Lauder, New Zealand and is widely used for the analysis of ground-based solar absorption spectra. SFIT2 is a retrieval algorithm that employs the Optimal Estimation Method (OEM) of *Rodgers et al*. [*Rodger*, 1976; 1990; 2000; *Rodgers and Connor*, 2003]. It makes use of the OEM to include *a priori* constituent profiles as a function of altitude in the retrievals in a statistically sound manner. SFIT2 allows the simultaneous retrieval of a vertical profile and column density of the target molecule, together with the total columns of interfering species. Details of SFIT2 program were described in Chapter 1.

Model atmospheres are used in the SFIT2 program to simulate spectra during the retrievals. A program called FSCATM [*Meier et al., 2004*] was used to carry out refractive ray tracing needed to generate the model atmospheres using *a priori* Volume Mixing Ratio (VMR) estimates, pressure profiles and temperature profiles. A combination of a climatology estimated from the HALogen Occultation Experiment (HALOE) v.19 satellite data [*Russell et al.*, 1994] and mid-latitude daytime 2001 Michelson Interferometer for Passive Atmospheric Sounding (MIPAS) reference profiles [*Carli et al.*, 2004] were used to construct the *a priori* state estimates of VMR profiles and columns. Details of the *a priori* construction are available in Section 4.1 of Wiacek's thesis [*Wiacek*, 2006]. These *a priori* VMRs are used in the retrievals of spectra recorded at WAO. The *a priori* VMRs from Mark IV balloon FT-IR spectra [*Peterson and Margitan*, 1995] obtained in northern mid-latitudes by *G. C. Toon et al.* are use in the retrievals of Kitt Peak spectra. Two sets of *a priori* VMR estimates are used in retrievals, because there are significant environmental differences between the two sites. Pressure and temperature profiles were obtained from the National Centers for Environmental Prediction/National Center for Atmospheric Research analyses provided by the NASA Goddard Space Flight Centre automailer (obtained from the Goddard Automailer: science@hyperion.gsfc.nasa.gov) [*McPherson et al.*, 1979; *Kalnay et al.*, 1996] and the Mass-Spectrometer-Incoherent-Scatter model (MSIS-2000) [*Picone et al.*, 2002]. NCEP covers the surface to 50 km, and the output of MSIS is used from 50 km to 100 km. The spectroscopic line parameters used in this work are from the HIgh resolution TRANsmission molecular absorption database (HITRAN) 2004 [*Rothman et al.*, 2005].

In our analysis, we mainly focus on CO_2 and CH_4, two greenhouse gases that are identified in the IPCC report as the first and second most important species in altering the balance of incoming and outgoing energy in the Earth-atmosphere system [*IPCC*, 2007]. Total columns of CO_2 were retrieved from three spectral bands: two bands at 1.57 μm and one band at 2.06 μm. The absorption features at 1.57 μm consist of 30013-00001 and ($\nu_1 + 4\nu_2 + \nu_3$, $\nu_0 = 6228$ cm^{-1}) and 30012-00001 ($2\nu_1 + 2\nu_2 + \nu_3$, $\nu_0 = 6348$ cm^{-1}) transitions. They will be referred to as the CO_2 6228 cm^{-1} and CO_2 6348 cm^{-1} bands. In the spectral region at 1.57 μm there are numerous absorption features from CO_2, with weak absorption by H_2O, HDO and additionally from CH_4 for the 30013-00001 transition. These CO_2 bands consist of many lines with a wide range of intensities, which provides good retrieval sensitivities in both the stratosphere and troposphere. Thermal emission from the atmosphere and instrument are also negligible at these short wavelengths [*Kuang et al.*, 2002]. The 2.06 μm CO_2 absorption band has a weaker dependence on the CO_2 concentration, and greater sensitivity to airborne particles and the temperature profile than does the weaker absorption in the 1.57 μm bands [*Dufour and Bréon*, 2003]. The spectral region from 5880 to 5996 cm^{-1} is investigated for the CH_4 retrieval, taking advantage of its weak dependence on the temperature profile [*Washenfelder et al.*, 2003]. The total column of O_2 will be used to overcome the common systematic bias in CH_4 and CO_2 retrievals arising from air mass errors and surface pressure variations. Spectra of the O_2 A-band at 0.76 μm provide constraints on both the surface pressure and optical path length variations associated with scattering by aerosols in the atmosphere [*O'Brien et al.*, 1998; *Heidinger and Stephens*, 2000; *Kuze and Chance*, 1994; *Asano et al.*, 1995; *Yang et al.*, 2005]. By taking the ratio of columns of CH_4 and CO_2 to O_2 columns, systematic errors will be reduced as long as they are measured under the same conditions. The O_2 total columns are retrieved from the $^1\Delta_g - {}^3\Sigma_g^-$ IR band ($\nu_0 = 7882$ cm^{-1}) at 1.27 μm, and from the $b^1\Sigma_g^+ - X^3\Sigma_g^-$ band ($\nu_0 = 13121$ cm^{-1}) (A-band) at 0.76 μm. Two sets of line intensity parameters for the O_2 7882 cm^{-1} band are used, based on the work of Goldman [*Goldman*, private communication] and the values in HITRAN 2004 [*Rothman et al.*, 2005].

5.4 Results and Discussion

Figures 5.7 to 5.12 show sample fits for CO_2, CH_4, and O_2 using spectra recorded at NSO and WAO. The largest discrepancies between the calculated and the measured transmittances are on the order of a few percent (about 2 % for CO_2, CH_4 and O_2 1.27 micron band and 5% for O_2 0.76 micron band), and are observed in the vicinity of the absorption line centers. Similar systematic fitting residual patterns in terms of positions and amplitudes also appeared in the results of previous work [*Yang et al.*, 2002; *Washenfelder et al.*, 2003; *Dufour et al.*, 2004; *Yang et al.*, 2005]. They mainly arise from the spectroscopic parameters including line intensity, self- and air-broadening coefficients, and self- and air-shift coefficients. Away from the absorption lines, the fitting residuals from spectra recorded at NSO are generally larger than those obtained using spectra recorded at WAO. This is because the WAO spectra have a higher Signal-to-Noise Ratio (SNR), mainly because of their lower spectral resolution.

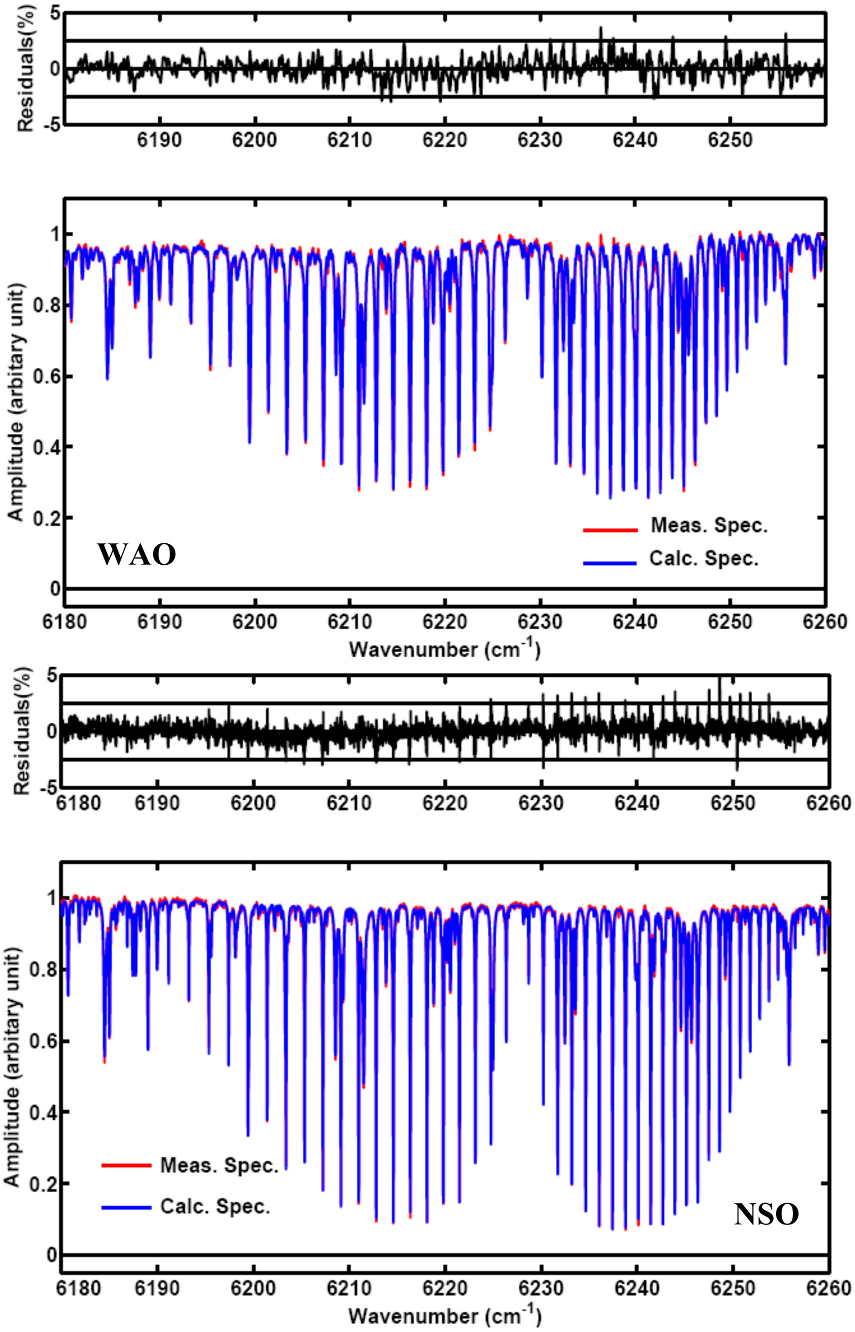

Figure 5.7 Fitting residuals for the CO_2 6228 cm^{-1} band at 1.57 μm obtained using spectra recorded at WAO, Waterloo, Ontario on November 22nd, 2006 (spectral resolution: 0.1 cm^{-1}, solar zenith angle: 66.6°) and obtained using spectra recorded at NSO (31.9°N, 111.6°W, and 2.1 km above sea level) at Kitt Peak, Arizona on July 25th, 2005 (spectral resolution: 0.01 cm^{-1}, solar zenith angle: 49.1°) are shown in the upper and lower plot, respectively.

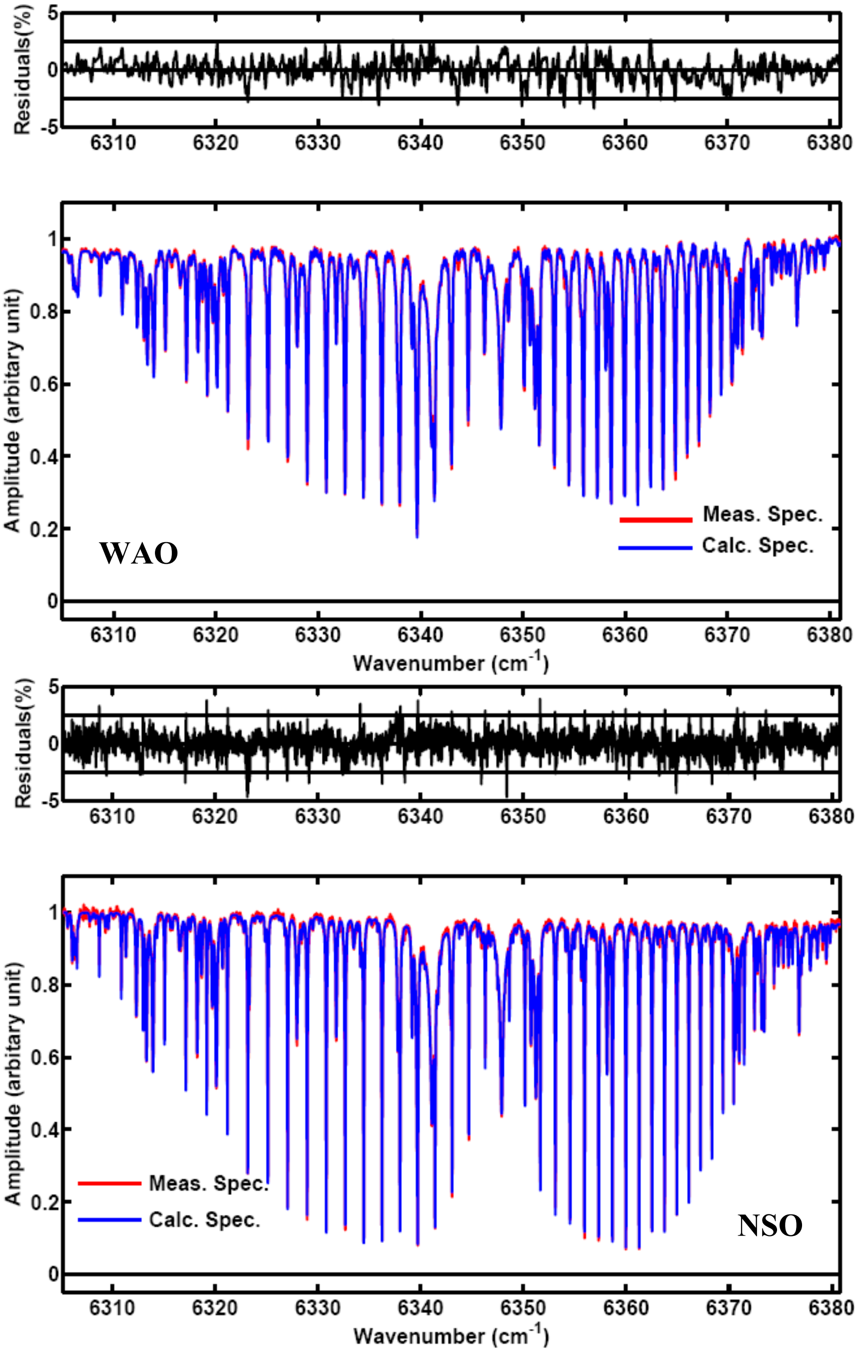

Figure 5.8 Fitting residuals for the CO_2 6348 cm^{-1} band at 1.57 μm obtained using spectra recorded at WAO on November 22nd, 2006 (spectral resolution: 0.1 cm^{-1}, solar zenith angle: 66.6°) and obtained using spectra recorded at NSO on July 25th, 2005 (spectral resolution: 0.01 cm^{-1}, solar zenith angle: 49.1°) are shown in the upper and lower plot, respectively.

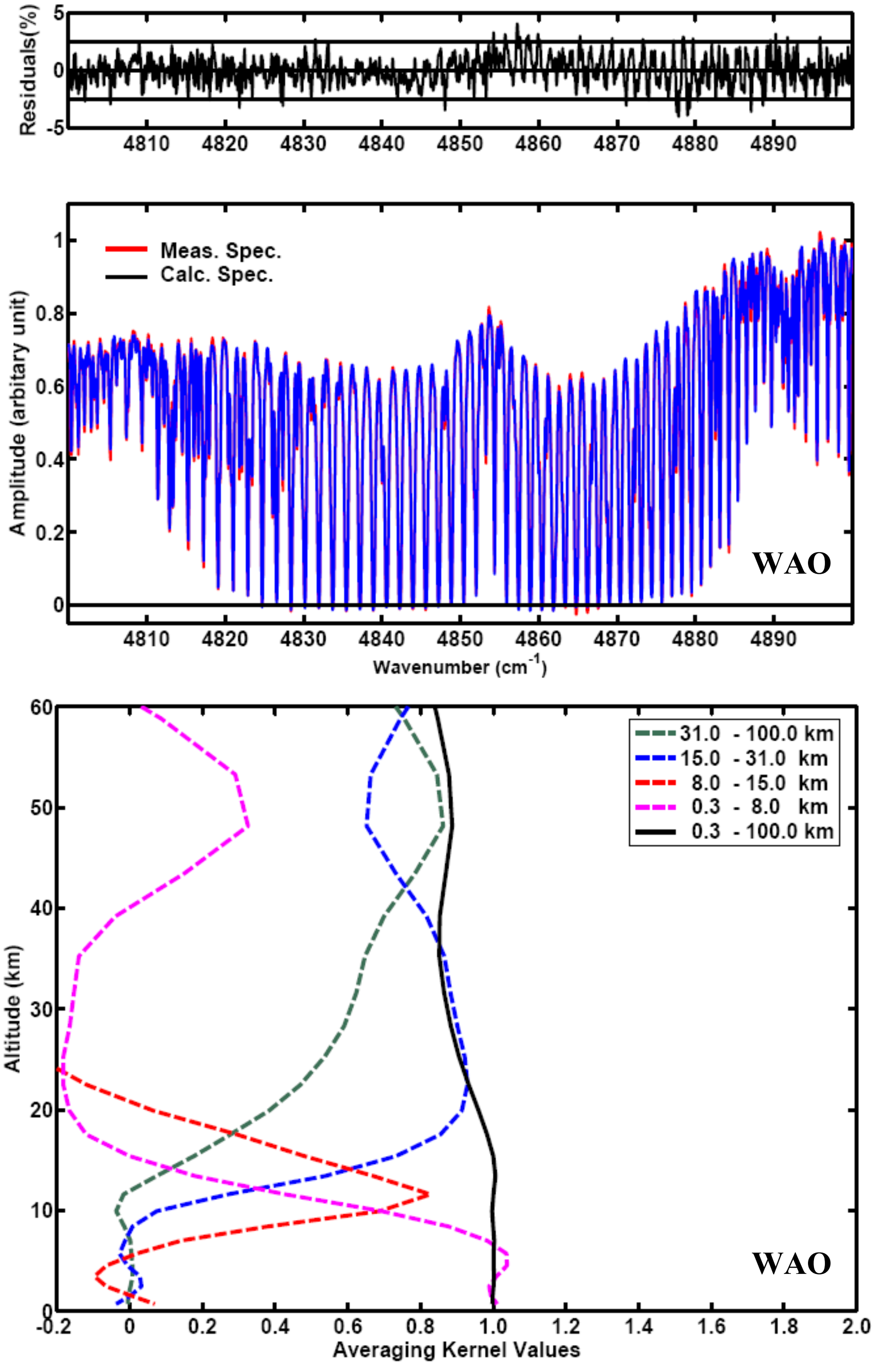

Figure 5.9 Fitting residuals for CO_2 at 2.06 μm obtained using spectra recorded at WAO on November 22nd, 2006 (spectral resolution: 0.1 cm^{-1}, solar zenith angle: 66.6°) and averaging kernel profiles corresponding to the retrievals are shown in the upper and lower plot, respectively.

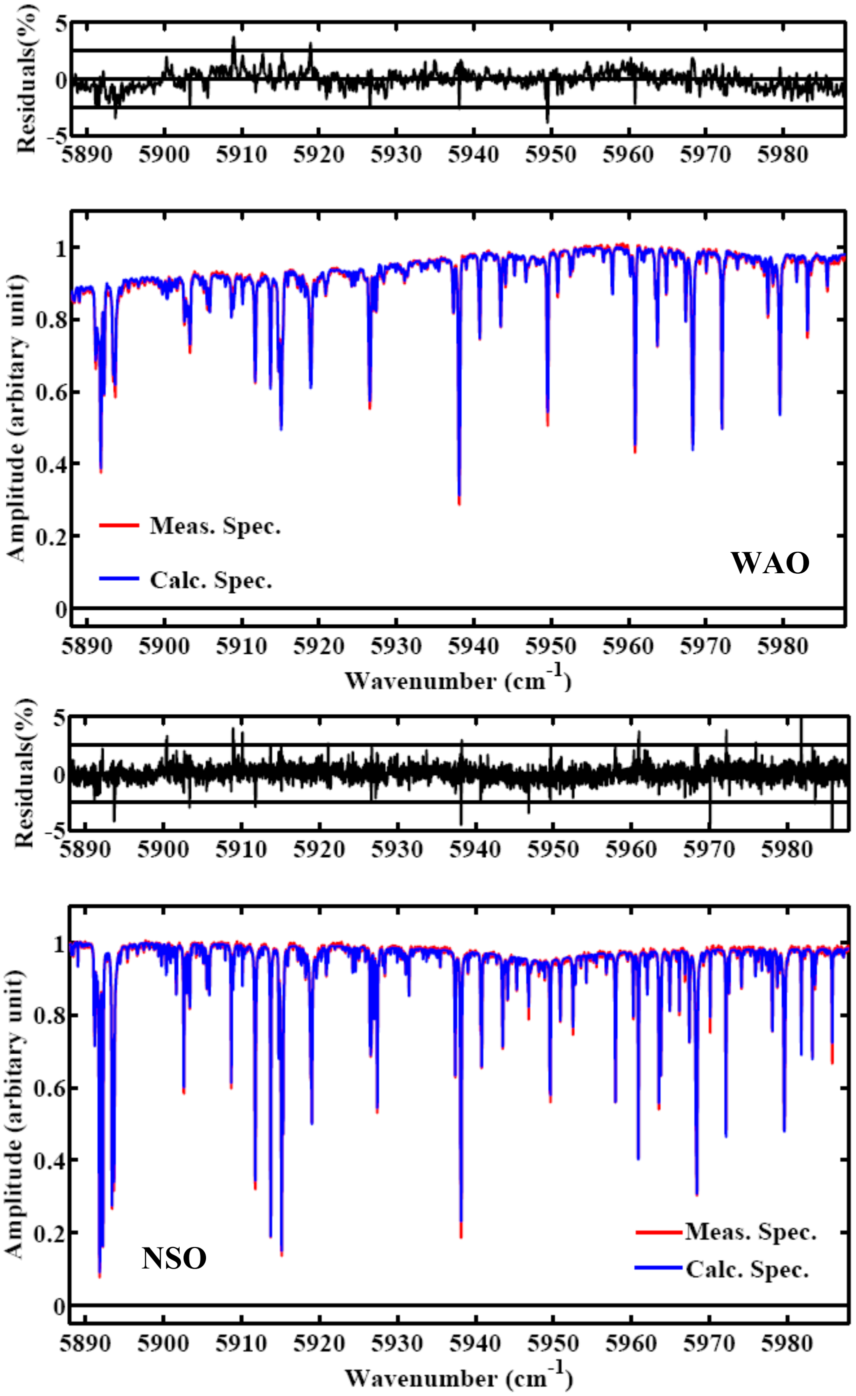

Figure 5.10 Fitting residuals for CH_4 at 1.68 μm obtained using spectra recorded at WAO on November 22nd, 2006 (spectral resolution: 0.1 cm^{-1}, solar zenith angle: 66.6°) and obtained using spectra recorded at NSO on July 25th, 2005 (spectral resolution: 0.01 cm^{-1}, solar zenith angle: 49.1°) are shown in the upper and lower plot, respectively.

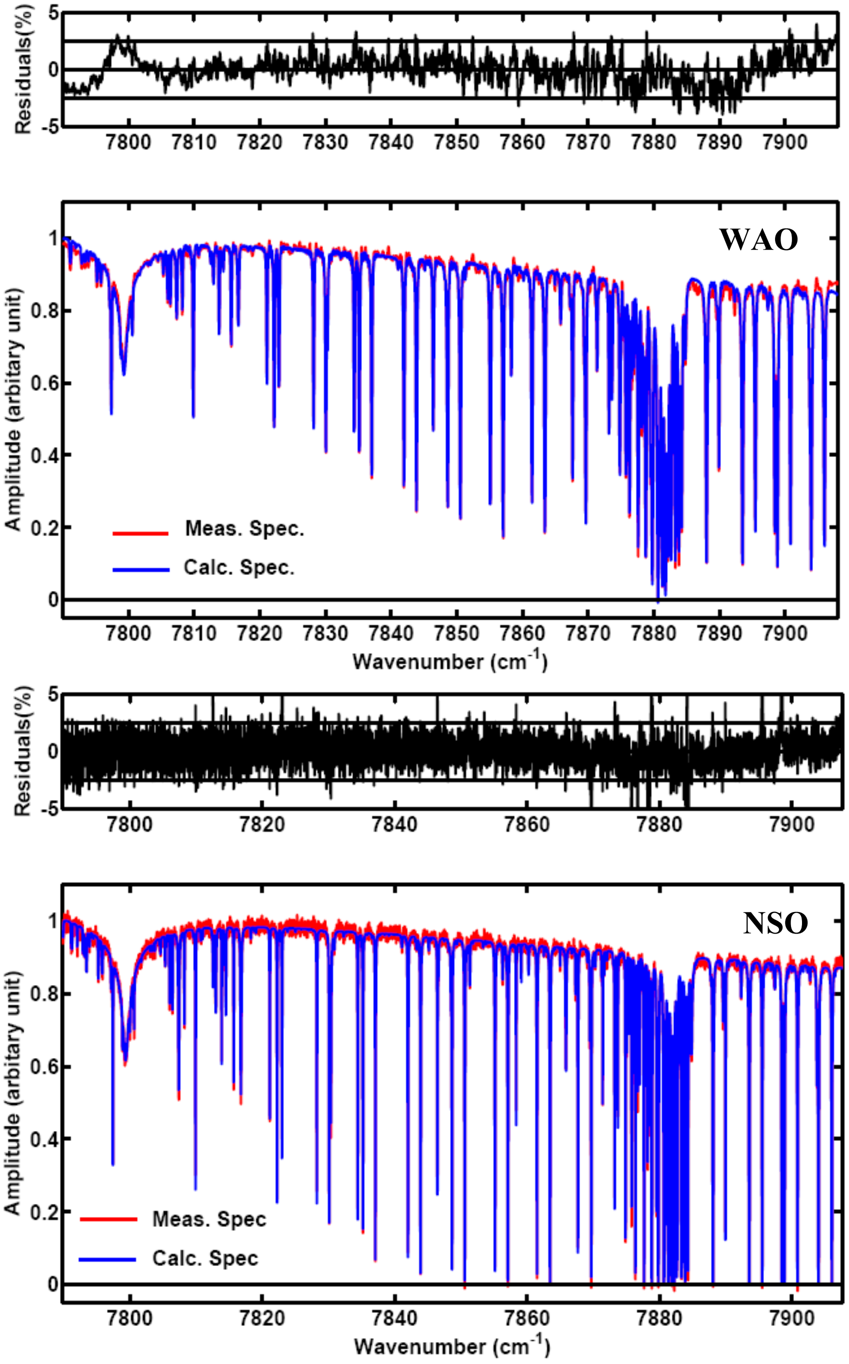

Figure 5.11 Fitting residuals for O_2 at 1.27 μm obtained using spectra recorded at WAO on November 22nd, 2006 (spectral resolution: 0.1 cm^{-1}, solar zenith angle: 66.6°) and obtained using spectra recorded at NSO on July 25th, 2005 (spectral resolution: 0.01 cm^{-1}, solar zenith angle: 49.1°) are shown in the upper plot and lower plot, respectively.

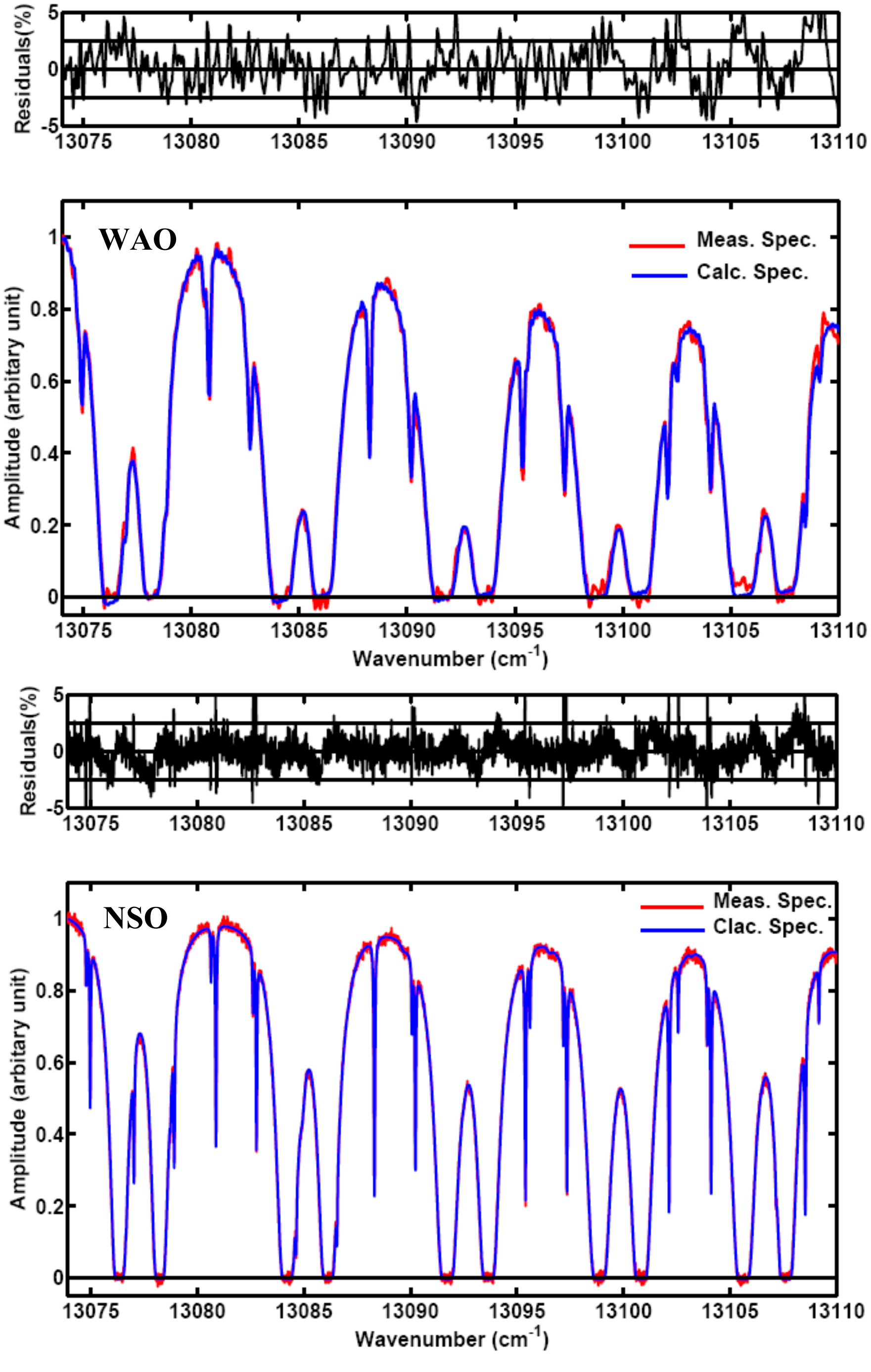

Figure 5.12 Fitting residuals for the O_2 A-band at 0.76 μm obtained using spectra recorded at WAO on November 22nd, 2006 (spectral resolution: 0.1 cm^{-1}, solar zenith angle: 66.6°) and obtained using spectra recorded at NSO on July 25th, 2005 (spectral resolution: 0.01 cm^{-1}, solar zenith angle: 49.1°) are shown in the upper and lower plot, respectively.

The absolute accuracy of the CO_2 retrievals obtained using spectroscopic parameters from HITRAN 2004 is expected to be limited to ~2% [*Devi et al.*, 2007]. Recent studies show the improvements in the CO_2 spectroscopic parameters in the spectral region of 4550 to 7000 cm^{-1} with a precision of 1% or better [*Miller and Brown*, *Miller et al.*, 2004, 2005; *Toth et al.*, 2006; *Devi et al.*, in press]. *Devi et al.* in 2007 made further improvements in the CO_2 spectroscopic parameters for the 6348 cm^{-1} band by considering line mixing and using speed-dependent Voigt line shape functions. The work of *Devi et al.* provides the possibility of remote sensing CO_2 with ~ 0.3% precision. As demonstrated by *Boone et al.* [*Boone et al.*, 2007], the use of speed-dependent Voigt line shape functions improves tropospheric remote sensing, but such a modification of SFIT2 is beyond the scope of this work. Deficiencies in spectroscopic parameters are also found for the CH_4 and O_2 retrievals. For example, the fitting residuals show obvious difficulty in fitting the O_2 continuum (not included in our forward model) for both the 1.27 μm and 0.76 μm bands. However, no recent published work has presented improvements to the spectroscopic parameters for CH_4 and O_2 over those in HITRAN 2004.

Sources and sinks for greenhouse gases are located primarily in the boundary layer. Hence, it is critical for any satellite mission to obtain good sensitivity near the surface. The vertical sampling of a particular measurement is quantified by computing the averaging kernel, as defined in the Rodgers optimal estimation approach [*Rodgers*, 2000]. The Rodgers approach for a retrieval such as the vertical profile of CO_2 combines information from observations and the *a priori* values in a statistically sound manner. The averaging kernel is the derivative of a derived parameter with respect to its *a priori* state value, i.e., when this derivative is small (nearly 0), all of the information comes from the *a priori* and when it is large (near 1), then the information in the retrieval comes mainly from the measured data [*Rodgers*, 2000]. When observing the atmosphere with a nadir viewing geometry, a spectrometer with higher spectral resolution is expected to provide better vertical information than one with low spectral resolution [*Rodgers*, 2000]. Typical vertical averaging kernels for CO_2 at 2.06 μm and 1.57 μm and for CH_4 at 1.68 μm from ground-based observations at NSO and WAO are shown in Figures 5.9 and 5.13-5.15. They demonstrate that observations

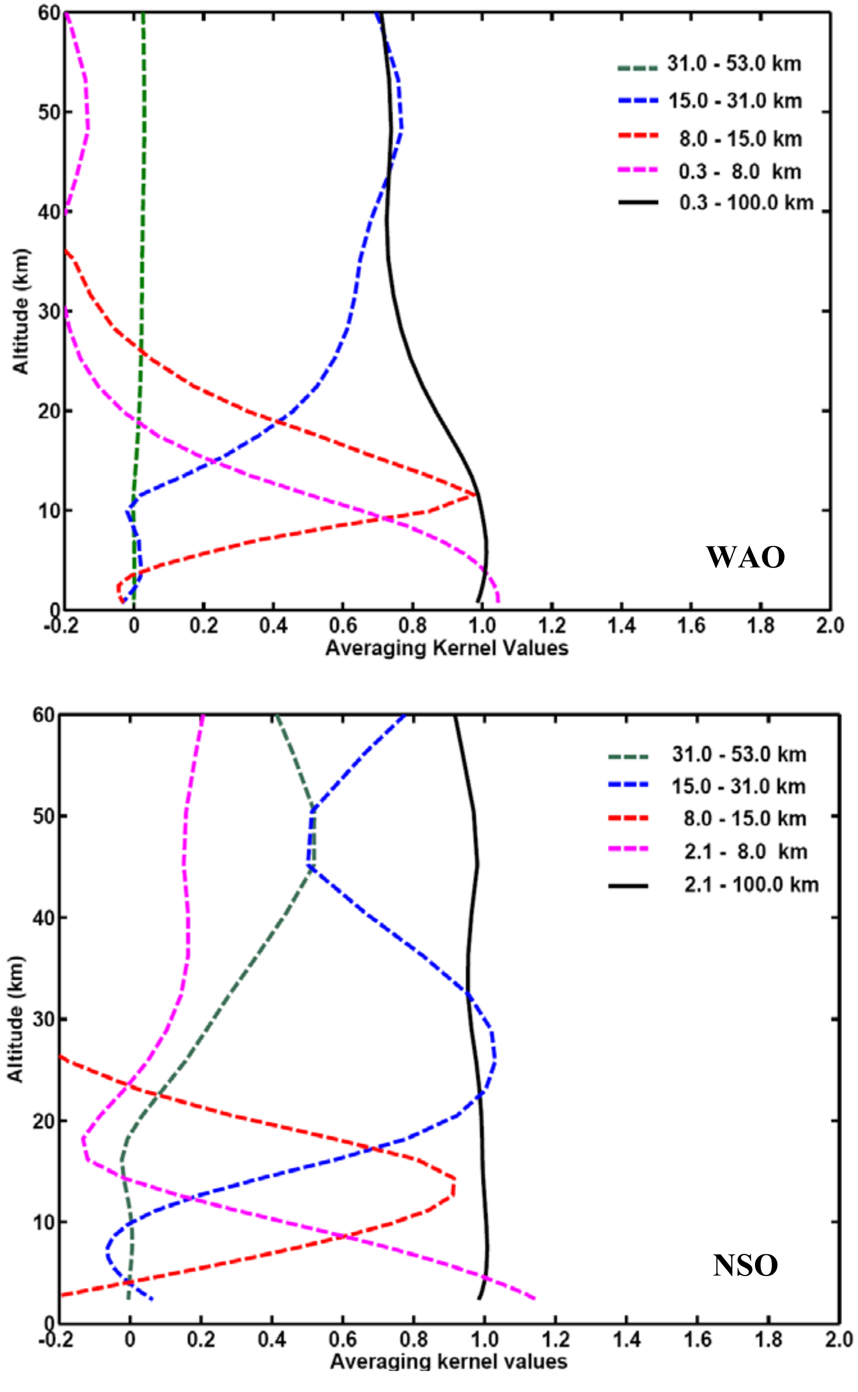

Figure 5.13 **Averaging kernel profiles for the retrievals using CO_2 6228 cm^{-1} band at 1.57 μm recorded at WAO on November 22nd, 2006 (spectral resolution: 0.1 cm^{-1}, solar zenith angle: 66.6°) and using spectra recorded at NSO on July 25th, 2005 (spectral resolution: 0.01 cm^{-1}, solar zenith angle: 49.1°) are shown in the upper and lower plot, respectively.**

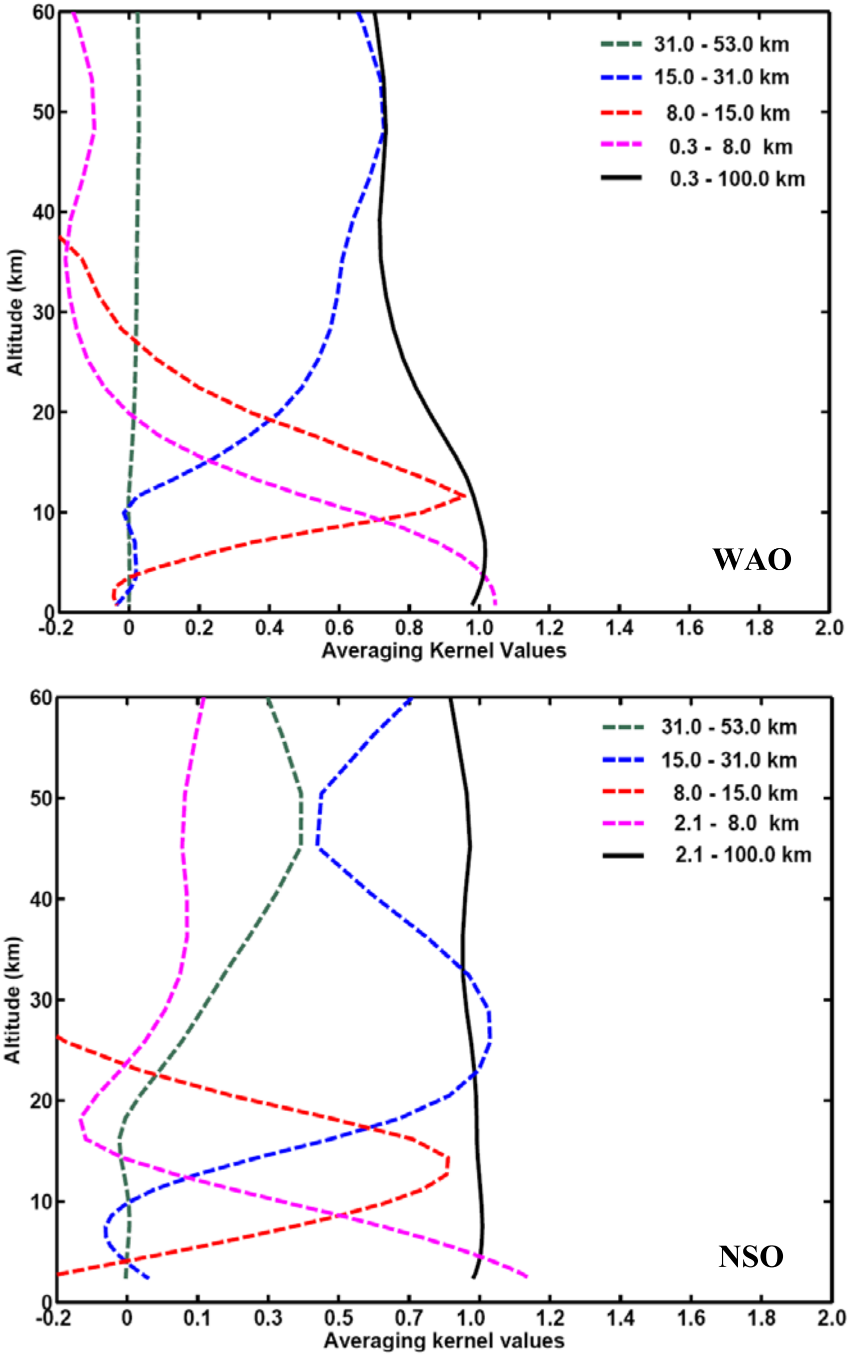

Figure 5.14 Averaging kernel profiles for the retrievals using CO_2 6348 cm^{-1} band at 1.57 μm recorded at WAO on November 22nd, 2006 (spectral resolution: 0.1 cm^{-1}, solar zenith angle: 66.6°) and using spectra recorded at NSO on July 25th, 2005 (spectral resolution: 0.01 cm^{-1}, solar zenith angle: 49.1°) are shown in the upper and lower plot, respectively.

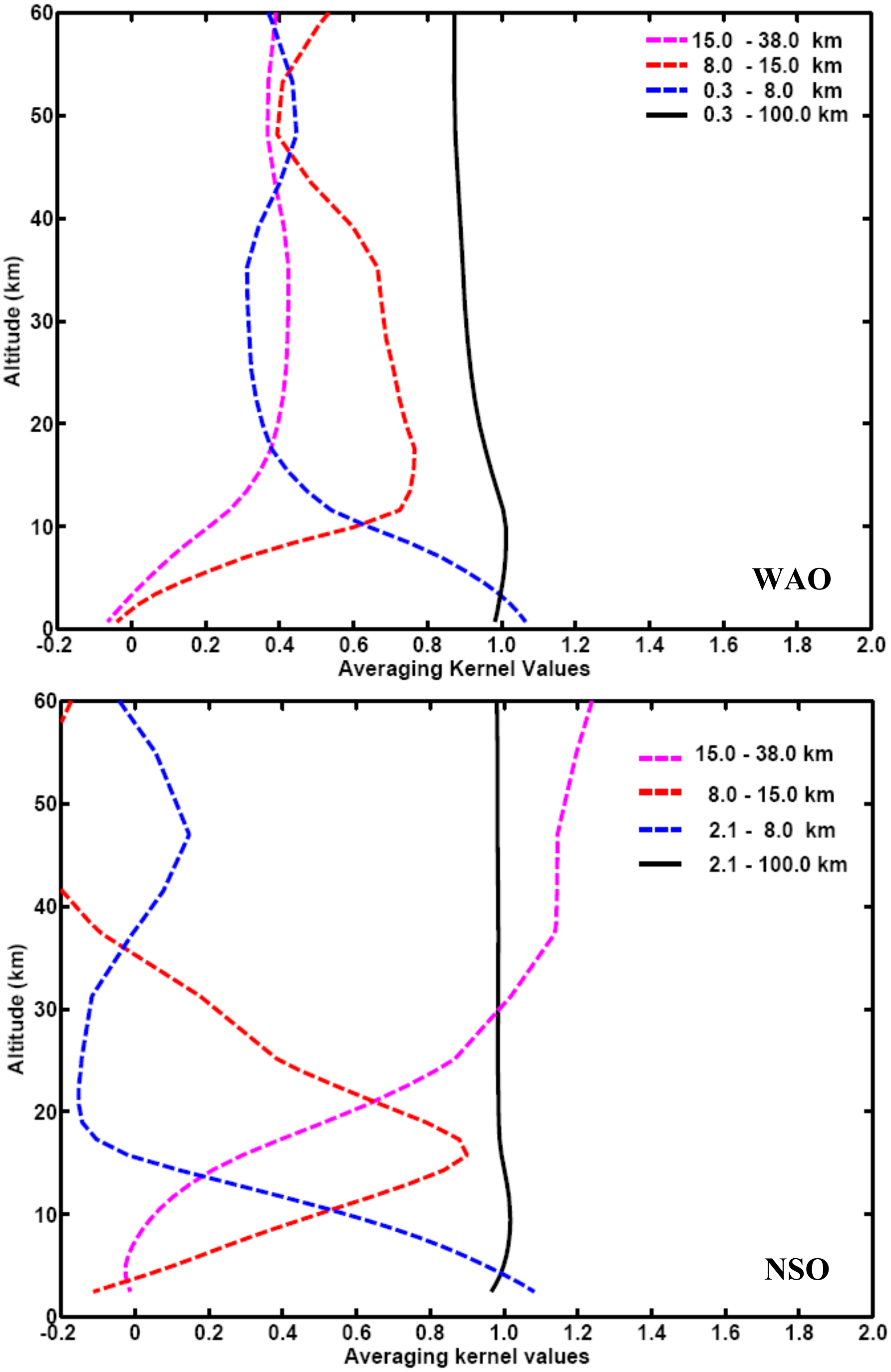

Figure 5.15 Averaging kernel profiles for the retrievals using CH_4 at 1.68 μm recorded at WAO on November 22nd, 2006 (spectral resolution: 0.1 cm^{-1}, solar zenith angle: 66.6°) and using spectra recorded at NSO on July 25th, 2005 (spectral resolution: 0.01 cm^{-1}, solar zenith angle: 49.1°) are shown in the upper and right plot, respectively.

achieved the required near surface sensitivity, i.e., averaging kernel values are near one from the surface to the upper troposphere. In this altitude range, only minor differences are seen between spectra with resolutions of 0.01 cm^{-1} and 0.1 cm^{-1}. The retrieval of a tropospheric partial column with spectral resolution 0.1 cm^{-1} is as feasible as that for a spectrum with 0.01 cm^{-1} resolution. There is enough information to split the total CO_2 column and the CH_4 column into four layers and two layers, respectively. A FTS with lower spectral resolution (0.1 cm^{-1}) will provide spectra with a higher signal-to-noise ratio, and is much cheaper to build than one with a higher resolution (0.01 cm^{-1}).

The retrievals using the SFIT2 program provide the total vertical column density of CO_2, and the VMR of CO_2 can be calculated using

$$\mathrm{VMR}_{\mathrm{CO_2}} = \frac{\mathrm{C}_{\mathrm{CO_2}}}{\mathrm{C}_{\mathrm{air}}}. \tag{5.4.1}$$

However, the VMRs have only limited precision because the measurements are influenced by a number of factors such as variations in surface pressure and light path in the atmosphere. Humidity can increase the total column of air by 0.5%, but does not change the CO_2 total column. Essentially, the CO_2 gets ‘diluted’ by the H_2O. Fortunately, the O_2 total vertical column density is diluted in the same way as that for CO_2, and has a similar optical path. The VMR of CO_2 in dry-air is more directly related to sources and sinks, and is a better tracer because it is not influenced by evaporation or condensation of H_2O. The VMR of O_2 in dry air can be assumed to be constant at 0.2095, so the total column of dry air is given by

$$\mathrm{C}_{\mathrm{dry-air}} = \frac{\mathrm{C}_{\mathrm{O_2}}}{0.2095}. \tag{5.4.2}$$

The retrieved O_2 total vertical column density obtained from the O_2 A-band is used in Eq. (5.4.2). By replacing the total vertical column density of air in Eq. (5.4.1) with the total columns of dry air obtained from Eq. (5.4.2), the VMR of CO_2 in dry is

$$\mathrm{VMR}_{\mathrm{dry\text{-}CO_2}} = \frac{0.2095 \times \mathrm{C}_{\mathrm{CO_2}}}{\mathrm{C}_{\mathrm{O_2}}}. \tag{5.4.3}$$

Eq. (5.4.3) can be adapted to give the CH_4 VMR in dry air as

$$\mathrm{VMR}_{\text{dry-CH}_4} = \frac{0.2095 \times \mathrm{C}_{\mathrm{CH}_4}}{\mathrm{C}_{\mathrm{O}_2}}. \tag{5.4.4}$$

Common systematic errors such as surface pressure and scattering effects of large particles in the solar beam are removed by using Eqs. (5.4.3) and (5.4.4). Figure 5.16 shows the retrieved total column of CO_2 and O_2 together with the column-averaged VMR of CO_2 in dry air observed at the two sites. Figure 5.17 presents the retrieved total column and column averaged VMR in dry air of CH_4. The precision of the observations can be estimated from the standard deviations of the results of repeated measurements under similar conditions. The measurements at each site were performed in a single day with uniform weather conditions. The precisions of the column-averaged VMRs of CO_2 and CH_4 in dry air are found to be better than 1.07% and 1.13%, respectively. The observed total columns of CO_2, CH_4 and O_2 at NSO in all spectral regions are less than those in WAO by about 12%, 15% and 11%, respectively. These differences are reasonable because of the different altitudes of the two observation sites (NSO: 2.1 km above sea level; WAO: 0.3 km). The column densities of CO_2 from the 6348 cm^{-1} band are consistently higher than those derived from the 6228 cm^{-1} and 2.06 μm bands by about 7%. The Goldman spectroscopic parameters for the O_2 1.27 μm band provide O_2 amounts 12% lower than those obtained using the values in HITRAN 2004. The systematic residuals that are observed in our analysis are due to deficiencies in the line parameters.

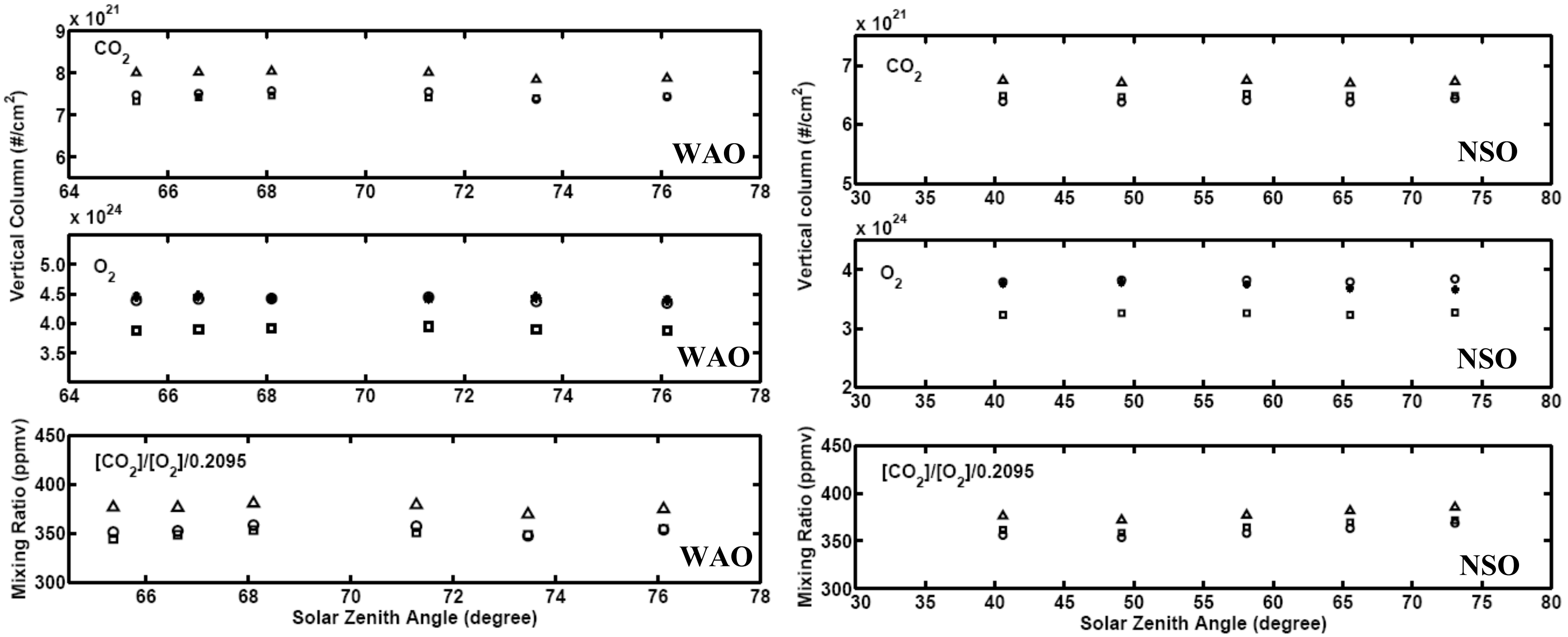

Figure 5.16 Retrieved total vertical column densities of CO_2, O_2 and column ratios in dry air of CO_2 to O_2 obtained using spectra recorded at WAO on November 22nd, 2006 (spectral resolution: 0.1 cm^{-1}) and using spectra recorded at NSO on July 25th, 2005 (spectral resolution 0.01 cm^{-1}) are shown in the left and right plots respectively, as a function of solar zenith angles. In both plots, top panels contain retrieved total columns of CO_2 at 1.57 μm and 2.06 μm (triangles: 6348 cm^{-1} band at 1.57 μm; circles: 6228 cm^{-1} band at 1.57 μm; squares: 2.06 μm band); middle panels present retrieved total columns of O_2 at 1.27 μm and at 0.76 μm (circles: 1.27 μm band with HITRAN 2004 spectroscopic parameters; squares: 1.27 μm band with Goldman spectroscopic parameters; stars: 0.76 μm band with HITRAN 2004 spectroscopic parameters); bottom panels show Volume Mixing Ratios (VMR) of CO_2 in dry air at 1.57 μm and 2.06 μm corrected with simultaneously observed total columns of O_2 at 0.76 μm (triangles: 6348 cm^{-1} band at 1.57 μm; circles: 6228 cm^{-1} band at 1.57 μm; squares: 2.06 μm band).

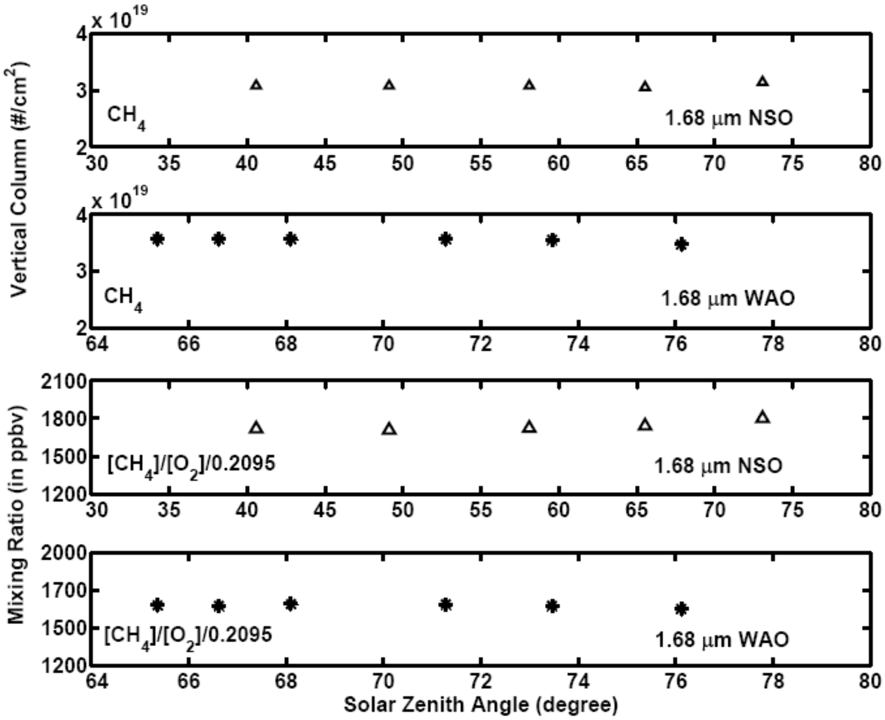

Figure 5.17 Retrieved total columns of CH_4 at 1.68 μm from observations at NSO and WAO, column ratios in dry air of CH_4 (1.68 μm) to O_2 (0.76 μm) at NSO and WAO are shown in plots from the top to the bottom, respectively. Observations at WAO and NSO were made on November 22nd, 2006 with a spectral resolution of 0.1 cm^{-1} and on July 25th, 2005 with a spectral resolution of 0.01 cm^{-1}, respectively.

5.5 Summary and Conclusions

Atmospheric spectra with resolutions of 0.0042 cm^{-1}, 0.01 cm^{-1}, 0.1 cm^{-1} and 0.3 cm^{-1} in the 3950 cm^{-1} to 7140 cm^{-1} region recorded at IRF Kiruna, Sweden were compared. The spectral features of CH_4, N_2O, CO and CO_2 2.06 μm band are under-resolved in most spectral regions at a resolution of 0.3 cm^{-1}, which is similar to that used in the OCO mission. Spectra with a resolution of 0.1 cm^{-1} are sufficient to resolve the absorption features of CO_2, CH_4, N_2O, and CO.

In order to obtain the near infrared absorption features of CH_4, CO_2, CO and N_2O together with the O_2 A-band in a single spectrum, further observations over a broad spectral region from 2000 to 15000 cm^{-1} were taken at Kitt Peak and Waterloo at resolutions of 0.01 cm^{-1} and 0.1 cm^{-1}, respectively. The vertical sampling of these observations is quantified by computing averaging kernels as defined in the Rodgers optimal estimation method. The vertical sampling of observations with a spectral resolution of 0.1 cm^{-1} is similar to those with a spectral resolution of 0.01 cm^{-1}. A spectral resolution of 0.1 cm^{-1} (MOPD = 5 cm) is recommended for the CC-FTS mission.

Systematic fitting residuals are obvious in all of our retrievals, and have been noted previously [*Yang et al.*, 2002; *Washenfelder et al.*, 2003; *Dufour et al.*, 2004; *Washenfelder et al.*, 2006]. These residuals are due to the deficiencies in the spectroscopic line parameters in the HITRAN 2004 database. To improve the precision of atmospheric observations, new laboratory measurements on the spectroscopic parameters are required.

5.6 References

Asano S., Shiobara M., and Uchiyama A., (1995), Estimation of cloud physical parameters from airborne solar spectral reflectance measurements for stratocumulus clouds, *J. Atmos. Sci.*, **52**, 3556-3576.

Aumann H.H., Chahine M.T., Gautier C., Goldberg M.D., Kalnay E., McMillin L.M., Revercomb H., and Rosenkranz PW., (2003), AIRS/AMSU/HSB on the Aqua mission: design, science objectives, data products, and processing systems, *IEEE Trans. Geosci. Remote Sensing*, **41**, 253-264.

Beer R., (2006), TES on the Aura mission: scientific objectives, measurements, and analysis overview, *IEEE Trans. Geosci. Remote Sensing*, **44**, 1102-1105.

Boone C.B., Walker K.A., and Bernath P.F., (2007), Speed-dependent Voigt profile for water vapor in infrared remote sensing applications, *J. Quant. Spectrosc. Radiat. Trans.*, **105**, 525-532.

Buchwitz M., Beek R.D., Noël S., Burrows J.P., Bovensmann H., Bremer H., Bergamaschi P., Körner S., and Heimann M., (2005), Carbon monoxide, methane and carbon dioxide columns retrieved from SCIAMACHY by WFM-DOAS: year 2003 initial data set, *Atmos. Chem. Phys.*, **5**, 3313-3329.

Carli B., Alpaslan D., Carlotti M., Castelli E., Ceccherini S., Dinelli B.M., Dudhia A., Flaud J.M., Hoepfner M., Jayd V., Magnani L., Oelhaf H., Payne V., Piccolo C., Prosperi M., Raspollini P., Remedios J., Ridolfic M., and Spang R., (2004), First results of MIPAS/ENVISAT with operational Level 2 code, *Adv. Space Res.*, **33**, 1012-1019.

Chédin A., Hollingsworth A., Scott N.A., Serrar S., Crevoisier C., and Armante R., (2002), Annual and seasonal variations of atmospheric CO_2, N_2O and CO concentrations retrieved from NOAA/TOVS satellite observations, *Geophys. Res. Lett.*, **29**, 1269, doi:10.1029/2001GL014082.

Chédin A., Saunders R., Hollingsworth A., Clerbaux N.C., Armante R., and Crevoisier C., (2003), The feasibility of monitoring CO_2 from high-resolution infrared sounders. *J. Geophys. Res.*, **108**, 4064, doi:10.1029/2001JD001443.

Crisp D., Atlas R.M., Breon F.M., Brown L.R., Burrows J.P., Ciais P., Connor B.J., Doney S.C., Fung I.Y., Jacob D.J., Miller C.E., O'Brien D., Pawson S., Randerson J.T., Rayner P., Salawitch R.J., Sander S.P., Sen B., Stephens G.L., Tans P.P., Toon G.C., Wennberg P.O., Wofsy S.C., Yung Y.L., Kuang Z., Chudasama B., Sprague G., Weiss B., Pollock R., Kenyon D., and Schroll S., (2004), The Orbiting Carbon Observatory (OCO) mission, *Adv. Space Res.*, **34**, 700-709.

Cunnold D.M., Steele L.P., Fraser P.J., Simmonds P.G., Prinn R.G., Weiss R.F., Porter L.W., O'Doherty S., Langenfelds R.L., Krummel P.B., Wang H.J., Emmons L., Tie X.X., and Dlugokencky E.J., (2002), In situ measurements of atmospheric methane at GAGE/AGAGE sites during 1985-2000 and resulting source inferences, *J. Geophys. Res.*, **107**, 4225, doi:10.1029/2001JD001226.

Deeter M.N., Emmons L.K., Edwards D.P., Gille J.C., and Drummond J.R., (2004), Vertical resolution and information content of CO profiles retrieved by MOPITT, *Geophys. Res. Lett.*, **31**, L15112, doi:10.1029/2004GL020235.

Devi V.M., Benner D.C., Brown L.R., Miller C.E., and Toth R.A., (2007), Line mixing and speed dependence in CO_2 at 6348 cm^{-1}: positions, intensities and air- and self-broadening derived with constrained multispectrum analysis, *J. Mol. Spectrosc.*, **242**, 90-117.

Drummond J.R. and Mand G.S., (1996), The Measurements of Pollution in the Troposphere (MOPITT) Instrument: overall performance and calibration requirements, *J. Atmos. Oceanic. Technol.*, **13**, 314-320.

Dufour E. and Bréon F., (2003), Spaceborne estimate of atmospheric CO_2 column by use of the differential absorption method: error analysis, *Appl. Opt.*, **42**, 3595-3609.

Dufour E., Bréon F., and Peylin P., (2004), CO_2 column averaged mixing ratio from inversion of ground-based solar spectra, *J. Geophys. Res.*, **109**, doi:10.1029/2003JD004469.

Etheridge D.M., Steele L.P., Francey R.J., and Langenfelds R.L., (1998), Atmospheric methane between 1000 A.D. and present: Evidence of anthropogenic emissions and climate variability, *J. Geophys. Res.*, **103**, 15979-15993.

Gurney K.R., Law R.M., Denning A.S., Rayner P.J., Baker D., Bousquet P., Bruhwilerk L., Chen Y.H., Ciais P., Fan S., Fung I.Y., Gloor M., Heimann M., Higuchi K., John J., Maki T., Maksyutov S., Masariek K., Peylin P., Pratherkk M., Pak B.C., Randerson J., Sarmiento J., Taguchi S., Takahashi T., and Yuen C.W., (2002), Towards robust regional estimates of CO_2 sources and sinks using atmospheric transport models, *Nature*, **415**, 626-630.

Hamazaki T., Kaneko Y., Kuze A., and Kondo K., (2005), Fourier transform spectrometer for Greenhouse Gases Observing Satellite (GOSAT), *SPIE*, **5659**, 73-80.

Heidinger A.K. and Stephens G.L., (2000), Molecular line absorption in a scattering atmosphere. Part II: application to remote sensing in the O_2 A-band, *J. Atmos. Sci.*, **57**, 1615-1634.

Henningsen J. and Simonsen H., (2000), The (22^01-00^00) band of CO_2 at 6348 cm^{-1}: Linestrengths, broadening parameters, and pressure shifts, *J. Mol. Spectrosc.*, **203**, 16-17.

Hofmann D.J., Butler J.H., Dlugokencky E.J., Elkins J.W., Masarie K., Montzka S.A., and Tans P., (2006), The role of carbon dioxide in climate forcing from 1979 to 2004: Introduction of the Annual Greenhouse Gas Index, *Tellus B*, **58B**, 614-619.

Houghton J.T., Ding Y., Griggs D.J., Noguer M., Linden P.J., Dai X., Maskell K., and Johnson C.A., (2000), Climate Change 2001: The Scientific Basis. Cambridge: Cambridge University Press.

Intergovernmental Panel on Climate Change (IPCC) 2007. Climate Change 2007: The Physical Science Basis, IPCC Secretariat, Geneva, Switzerland (http://www.ipcc.ch/).

Kalnay E., Kanamitsu M., Kistler R., Collins W., Deaven D., Gandin L., Iredell M., Saha S., White G., Woollen J., Zhu Y., Chelliah M., Ebisuzaki W., Higgins W., Janowiak J., Mo K., Ropelewski C., Wang J., Leetmaa A., Reynolds R., and Joseph D., (1996), The NCEP/NCAR 40-year reanalysis project, *Bull, Amer, Meteor, Soc.*, **77**, 437-471.

Keeling, C.D., (1960), The concentration and isotopic abundances of carbon dioxide in the atmosphere, *Tellus*, **12**, 200-203.

Keeling C.D., Chin J.F.S., and Whorf T.P., (1996), Increased activity of northern vegetation inferred from atmospheric CO_2 measurements, *Nature*, **382**, 146-149.

Keeling C.D., Piper S.C., Bacastow R.B., Wahlen M., Whorf T.P., Heimann M., and Meijer H.A., (2005), Atmospheric CO_2 and $^{13}CO_2$ exchange with the terrestrial biosphere and oceans from 1978 to 2000: observations and carbon cycle implications, in *a history of atmospheric CO_2 and its effects on plants, animals, and ecosystems*. Editors: Ehleringer JR, Cerling T E, Dearing MD. Springer Verlag, New York.

Kuang Z.M., Margolis J., Toon G., Crisp D., and Yung Y., (2002), Spaceborne measurements of atmospheric CO_2 by high-resolution NIR spectrometry of reflected sunlight: an introductory study, *Geophys. Res. Lett.*, **29**, doi:1029/2001GL014298.

Kuze A. and Chance K.V., (1994), Analysis of cloud-top height and cloud coverage from satellites using the O_2 A-band and B-bands, *J. Geophys. Res.*, **99**, 14481-14491.

McPherson R.D., Bergan K.H., Kistler R.E., Rasch G.E., and Gordon D.S., (1979), The NMC operational global data assimilation system, *Mon. Wea. Rev.*, **107**, 1445-1461.

Meier A., Toon G.C., Rinsland C.P., Goldman A., and Hase F., (2004), *Spectroscopic atlas of atmospheric microwindows in the middle infra-red* (2nd edition), IRF Technical Report No.48, ISSN 0284-1738, Kiruna.

Meier A., Goldman A., Manning P.S., Stephen T.M., Rinsland C.P., Jones N.B., and Wood S.W., (2004), Improvements to air mass calculations for ground-based infrared measurements, *J. Quant. Spectrosc. Radiat. Trans.*, **83**, 109-113.

Miller C.E. and Brown L.R., (2004), Near infrared spectroscopy of carbon dioxide I. $^{16}O^{12}C^{16}O$ line positions, *J. Mol. Spectrosc.*, **228**, 329-354.

Miller C.E., Montgomery M.A., Onorato R.M., Johnstone C., McNicholas T.P., Kovaric B., and Brown L.R., (2004), Near infrared spectroscopy of carbon dioxide. II: $^{16}O^{13}C^{16}O$ and $^{16}O^{13}C^{18}O$ line positions, *J. Mol. Spectrosc.*, **228**, 355-374.

Miller C.E., Brown L.R., Toth R.A., Benner D.C., and Devi V.M., (2005), Spectroscopic challenges for high accuracy retrievals of atmospheric CO_2 and the Orbiting Carbon Observatory (OCO) experiment, *Comptes Rendus Physique* **6**, 876-887.

O'Brien D.M., Mitchell R.M., English S.A., and Da Costa G.A., (1998), Airborne measurements of air mass from O_2 A-band absorption spectra, *J. Atmos. Ocean. Technol.*, **15**, 1272-1286.

Park J.H., (1997), Atmospheric CO_2 monitoring from space, *Appl. Opt.*, **36**, 2701-2712.

Peterson D.B. and Margitan J.M., (1995), *Upper atmospheric satellite correlative measurement program (UARS-CMP) balloon data atlas*, NASA, Washington, DC.

Picone J.M., Hedin A.E., Drob D.P., and Aikin A.C., (2002), NRLMSISE-00 empirical model of the atmosphere: statistical comparison and scientific issues, *J. Geophys. Res.*, **107**, 1468-1483.

Pougatchev N.S., Connor B.J., and Rinsland C.P., (1995), Infrared measurements of the ozone vertical distribution above Kitt Peak, *J. Geophys. Res.*, **100**, 16689-16698.

Rayner P.J. and O'Brien D.M., (2001), The utility of remotely sensed CO_2 concentration data in surface source inversions, *Geophys. Res. Lett.*, **28**, 175-178.

Rinsland C.P., Jones N.B., Connor B.J., Logan J.A., Pougatchev N.S., Goldman A., Murcray F.J., Stephen T.M., Pine A.S., Zander R., Mahieu E., and Demoulin P., (1998), Northern and southern hemisphere ground-based infrared spectroscopic measurements of tropospheric carbon monoxide and ethane, *J. Geophy. Res.*, **103**, 28197-28217.

Rodgers, C.D., (1976), Retrieval of atmospheric temperature and composition from remote measurements of thermal radiation, *Rev. Geophys. Space. Phys.*, **14**, 609-624.

Rodgers, C.D., (1990), Characterization and error analysis of profiles retrieved from remote sounding measurements, *J. Geophys. Res.*, **95**, 5587-5595.

Rodgers, C.D., (2000), *Inverse methods for atmospheric sounding: Theory and practice*, Singapore: World Scientific.

Rodgers C.D. and Connor B.J., (2003), Intercomparison of remote sounding instruments, *J. Geophys, Res.*, **108**, 4116, doi: 10.1029/2002JD002299.

Rothman L.S., Jacquemart D., Barbe A., Benner D.C., Birk M., Brown L.R., Carleer M.R., Chackerian Jr. C., Chance K., Coudert L.H., Dana V., Devi V.M., Flaud J.M., Gamache R.R., Goldman A., Hartmann J.M., Jucks K.W., Maki A.G., Mandin J.Y., Massie S.T., Orphal J., Perrin A., Rinsland C.P., Smith M.A.H., Tennyson J., Tolchenov R.N., Toth R.A., Auwera J.V., Varanasi P., and Wagner G., (2005), The HITRAN 2004 molecular spectroscopic database, *J. Quant. Spectrosc. Rad. Transfer.* **96**, 139-204.

Russell J.M., Gordley L.L., Deaver L.E., Thompson R.E., and Park J.H., (1994), An overview of the Halogen Occultation Experiment (HALOE) and preliminary results, *Adv. Space Res.*, **14**, 9-13.

Toth R.A., Brown L.R., Miller C.E., Devi V.M., and Benner D.C., (2006), Self-broadened widths and shifts of $^{12}C^{16}O_2$: 4750-7000 cm^{-1}, *J. Mol. Spectrosc.*, **239**, 243-271.

Toth R.A., Brown L.R., Miller C.E., Devi V.M., and Benner D.C., (2006), Line strengths of $^{12}C^{16}O_2$: 4550–7000 cm^{-1}, *J. Mol. Spectrosc.*, **239**, 221-242.

Turquety S., Hadji-Lazaro J., Clerbaux C., Hauglustaine D.A., Clough S.A., Cassé V., Schlüssel P., and Mégie G., (2004), Operational trace gas retrieval algorithm for the Infrared Atmospheric Sounding Interferometer, *J. Geophys. Res.,* **109**, D21301, doi:10.1029/2004JD004821.

Washenfelder R.A., Wennberg P.O., and Toon G.C., (2003), Tropospheric methane retrieved from ground-based near-IR solar absorption spectra, *Geophys. Res. Lett.,* **30**, 2226, doi:10.1029/2003GL017969.

Washenfelder R.A., Toon G.C., Blavier J.F., Yang Z., Allen N.T., Wennberg P.O., Vay S.A., Matross D.M., and Daube B.C., (2006), Carbon dioxide column abundances at the Wisconsin Tall Tower site, *J. Geophys. Res.*, **111**, D22305, doi:10.1029/2006JD007154.

Wiacek A., (2006), First trace gas measurements using Fourier transform infrared solar absorption spectroscopy at the University of Toronto Atmospheric Observatory, Ph.D. thesis, University of Toronto.

Yang Z., Toon G.C., Margolis J.S., and Wennberg P.O., (2002), Atmospheric CO_2 retrieved from ground-based near IR solar spectra, *Geophys. Res. Lett.*, **29**, 1339, doi:10.1029/2001GL014537.

Yang Z., Wennberg P.O., Cageao R.P., Pongetti T.J., Toon G.C., and Sander S.P., (2005), Ground-based photon path measurements from solar absorption spectra of the O_2 A-band, *J. Quant. Spectrosc. Radiat. Trans.*, **90**, 309-321.

Chapter 6

Simultaneous Atmospheric Measurements Using Two Fourier Transform Infrared Spectrometers at the Polar Environment Atmospheric Research Laboratory (PEARL) during Spring 2006

6.1 Introduction

The Atmospheric Chemistry Experiment (ACE), also known as SCISAT-1, is a Canadian-led satellite mission developed for remote sensing of the Earth's atmosphere from a circular, low Earth orbit (altitude 650 km, inclination 74º). An infrared Fourier Transform Spectrometer (ACE-FTS) together with a dual, UV-visible-near-infrared spectrophotometer named Measurement of Aerosol Extinction in Stratosphere and Troposphere Retrieved by Occultation (ACE-MAESTRO), are the main two scientific instruments onboard SCISAT-1. They measure the concentrations of more than 30 atmospheric constituents, using spectroscopy from space [*Bernath et al.*, 2005; *Bernath* 2006; *Boone et al.*, 2005]. Details of the mission and instrumentation are given in Chapter 2.

The 2006 Canadian Arctic ACE Validation Campaign, the third held in Eureka, is a part of the calibration and validation program for the ACE mission [*Kerzenmacher et al.*, 2005; *Walker et al.*, 2005; *Manney et al.*, 2007; *Sung et al.*, 2007; *Fu et al.*, in preparation]. The campaign took place at the Polar Environment Atmospheric Research Laboratory (PEARL, 86.42°W, 80.05°N, 610 meters above seal level) in Eureka, Nunavut, Canada from February 17th to March 31st, 2006. A combination of 10 scientific instruments (Table 6.1) including terrestrial versions of the ACE-FTS (Portable Atmospheric Research Interferometric Spectrometer for the Infrared, PARIS-IR) [*Fu et al.*, 2007] and ACE-MAESTRO (MAESTRO-G) [*Kerzenmacher et al.*, 2005; *McElroy et al.*, 2007] were deployed at the campaign site and used to observe total columns, partial columns, and vertical profiles of most of the ACE target species, as well as temperature, and pressure. This work will focus on the observations made by PARIS-IR, Meteorological Service of Canada (MSC) DA8 FTS

[*Donovan et al.*, 1997; *Farahani et al.*, 2007] and ACE-FTS. Further descriptions of other instruments are provided in the references listed in Table 6.1.

Table 6.1 Instruments used in the 2006 Canadian Artic ACE Validation Campaign.

On-Site Instruments	**Campaign Instruments**
MSC[a] Eureka DA8 FTS	PARIS-IR
MSC[a] DIAL[b]	MAESTRO-G[c]
MSC[a] ozonesondes[d]	MSC[a] SPS-G[e]
MSC[a] Brewer spectrophotometer[f]	UT-GBS[g]
	Service d'Aéronomie SAOZ[h]
	MSC[a] Brewer spectrophotometer[f,i]

[a] Meteorological Service of Canada

[b] DIfferential Absorption Lidar [*Bird et al.*, 1996]

[c] Measurement of Aerosol Extinction in the Stratosphere and Troposphere Retrieved by Occultation- Ground [*Kerzenmacher et al.*, 2005; *McElroy et al.*, 2007]

[d] [*Davies et al.*, 2000]

[e] SunPhotoSpectrometer-Ground [*McElroy*, 1995]

[f] [*Savasktiouk* and *McElroy*, 2005]

[g] University of Toronto Ground-Based Spectrometer [*Bassford et al.*, 2001, 2005]

[h] Système d'Analyse par Observations Zénithales [*Pommereau and Goutail*, 1988]

[i] Second Brewer spectrophotometer deployed for campaign

The campaign measurements started with the return of sunlight to Eureka when polar sunrise occurred on February 20th, 2006. At and after sunrise, the Arctic atmosphere is perturbed by chemical reactions that are driven by solar radiation, such as chlorine activation [*Solomon* 1999; *Bernath* 2001]. In the chlorine activation process, inactive or reservoir forms of chlorine compounds such as HCl and $ClONO_2$ gases, which do not react with O_3, are converted to reactive forms such as Cl_2 by heterogeneous chemistry:

$$\mathrm{HCl} + \mathrm{ClONO_2} \rightarrow \mathrm{Cl_2} + \mathrm{HNO_3}\,(\mathrm{Solid}) \tag{6.1.1}$$

$$\mathrm{ClONO_2} + \mathrm{H_2O} \rightarrow \mathrm{HOCl} + \mathrm{HNO_3}\,(\mathrm{Solid}) \tag{6.1.2}$$

$$\mathrm{HCl} + \mathrm{HOCl} \rightarrow \mathrm{Cl_2} + \mathrm{H_2O}\,(\mathrm{Solid}) \tag{6.1.3}$$

on polar stratospheric clouds (PSCs). PSCs form at low temperatures in the polar vortex, which is a planetary-scale cyclonic circulation (an area of low atmospheric pressure characterized by inward spiraling winds that rotate counter clockwise in the northern hemisphere and clockwise in the southern hemisphere of the Earth), centered generally on the polar regions in winter and early spring. Cl_2 is easily turned into the reactive Cl radical through photolysis when sunrise occurs and Cl atoms destroy ozone in catalytic cycles such as

$$\mathrm{Cl} + \mathrm{O_3} \rightarrow \mathrm{ClO} + \mathrm{O_2} \tag{6.1.4}$$

$$\mathrm{ClO} + \mathrm{O} \rightarrow \mathrm{O_2} + \mathrm{Cl} \tag{6.1.5}$$

and other cycles involving the ClO dimer [*Solomon* 1999; *Bernath* 2001]. The first *in situ* measurements of depleted HCl giving evidence for conversion to active chlorine in the Arctic were made by *Webster et al.* in 1993. Observations of $ClONO_2$ in the Arctic also displayed evidence for heterogeneous processes on PSCs [*von Clarmann et al.*, 1993; *Oelhaf et al.*, 1994].

The removal of nitric acid, called denitrification, is an important feature of Cl-activated polar chemistry. Denitrification is most likely due to gaseous HNO_3 dissolving into PSCs, which causes the concentration of gaseous HNO_3 to decrease significantly. Large PSC particles can also sediment out of the polar vortex, but the mechanism of denitrification is not completely understood [*Solomon* 1999]. Denitrification affects ozone chemistry in the polar region [*Fahey et al.*, 1990; *Solomon* 1999; *Bernath* 2001]. For example, *Toon et al.* [1986]

demonstrated that the removal of nitric acid from the gas phase causes a reduction in NO_2 concentrations, which enhances $ClO/ClONO_2$ ratios and associated chlorine-catalyzed ozone loss.

It is now broadly accepted that changes in the amounts of chlorine and nitrogen compounds due to the chlorine activation and denitrification in the Arctic stratosphere lead to chemical depletion of ozone [*Fahey et al.*, 1990; *Müeller et al.* 1996; *Solomon* 1999; *Waibel et al.*, 1999; *Tabazadeh et al.*, 2000; *Bernath* 2001; *Mellqvist*, *et al.*, 2002; *Tilmes et al.*, 2004; *Jin et al.*, 2006]. PEARL, a primary station in the Network for the Detection of Atmospheric Composition Change (NDACC, http://www.ndsc.ncep.noaa.gov/), is located near the point of maximum stratospheric variability in the Arctic [*Harvey and Hitchman*, 1996] where there is a good chance of observing the evolution of chemical species in the stratosphere both inside and outside the Arctic vortex. Hence, PEARL is an excellent site for making observations of trace gases in the stratosphere and studying Arctic ozone chemistry.

During the 2006 Canadian Arctic ACE Validation Campaign, solar absorption spectra were recorded by PARIS-IR, DA8 FTS and ACE-FTS. These measurements were used to obtain information on the vertical column amounts of stratospheric trace gases such as O_3, HNO_3, NO_2, NO, HF, $ClONO_2$, and HCl near PEARL in spring 2006. Although PARIS-IR was deployed to Eureka in 2004 and 2005, there were major instrument changes and improvements for the 2006 campaign. In addition, optical parts in PARIS-IR were realigned in 2005. PARIS-IR's performance is expected to be different in 2006 from the performance in the 2004 and 2005 campaigns. The MSC DA8 FTS has been operating at Eureka since 1993, and was compared to the portable FTS from National Physical Laboratory (NPL) [*Murphy et al.*, 2001]. Hence, one of the goals of the campaign was to investigate the differences between the retrieved columns obtained by PARIS-IR, which is a relatively 'new' campaign instrument, and the DA8 FTS that is a permanently installed instrument making long term observations at PEARL.

To focus on the differences in the vertical columns that arise from the instrument performance, PARIS-IR and the DA8 FTS were configured to measure atmospheric absorption spectra simultaneously. This measurement strategy differs from that used in the 2004 and 2005 Canadian Arctic ACE Validation Campaigns, when PARIS-IR and the DA8 FTS recorded spectra alternately. Details on the configuration of the two ground-based FTSs in the 2006 campaign will be presented in Section 6.2. Making simultaneous measurements ensured that PARIS-IR and the DA8 FTS were sampling the same atmosphere, and thus removed any differences in vertical columns due to temporal and spatial variations. Total columns, partial columns and column ratios obtained from simultaneous atmospheric remote sensing measurements using PARIS-IR and the DA8 FTS at Eureka are reported. These results are used to compare measurements from PARIS-IR and the DA8 FTS, to evaluate the quality of ACE occultation measurements, and to probe the time evolution of the chemical constituents in the atmosphere over the Canadian high Arctic during spring 2006.

6.2 Instrumentation and Observations

PARIS-IR is a portable FTS built for atmospheric remote sensing from the ground and from airborne platforms such as high altitude balloon gondolas. It was constructed as a terrestrial version of the ACE-FTS using a similar design and incorporating flight-spare optical components from the satellite instrument [*Fu et al.*, 2007]. Hence, PARIS-IR can achieve the same spectral resolution (a maximum spectral resolution of 0.02 cm^{-1} or a maximum optical path difference (MOPD) of 25 cm) and spectral coverage (750 to 4400 cm^{-1}) as the ACE-FTS. Its maximum scanning speed is 2.5 cm/s, which makes PARIS-IR able to record a double-sided interferogram at MOPD every 20 seconds. A sandwich-type detector that consists of mercury cadmium telluride (MCT) and indium antimonide (InSb) elements is used in PARIS-IR to record spectra over its entire spectral coverage region in a single scan [*Fu et al.*, 2007]. Details of this novel instrument are given in Section 2.2.2.

An ABB-Bomem DA8 FTS, a high spectral resolution (maximum spectral resolution of 0.004 cm^{-1}, MOPD=250 cm) Michelson interferometer using dynamic alignment techniques, was installed at PEARL in February 1993 [*Donovan et al.*, 1997; *Farahani et al.*, 2007]. Two detectors, MCT and InSb, are used to cover the spectral range from 700 to 5100 cm^{-1}. DA8 FTS measurements are made using a sequence of nine optical filters to improve the Signal-to-Noise Ratio (SNR). The filters, the spectral ranges, and the detectors used in the DA8 FTS are shown in Table 2.3 and further details regarding this instrument are available in Section 2.2.5.

A sun-tracking mirror system which is permanently mounted on the roof of PEARL was used to direct the solar beam into the FTS laboratory. To observe the atmosphere simultaneously using the two spectrometers, the solar beam (diameter ~14 cm) was split into two parts. One third of the solar beam was directed through the input window of PARIS-IR using a flat pickoff mirror. The rest of the solar beam was directed into the DA8 FTS. The SNR and retrieved total columns from several spectra recorded in shared beam mode and in whole beam mode were compared at the beginning of the intensive phase. Differences in total columns between the two modes, which are generally about 1% in total columns, are small. PARIS-IR has a shorter acquisition time per spectrum (20 seconds) than the DA8 FTS (about 190 seconds). Hence, all of the individual spectra recorded using PARIS-IR during the interval of about 13 minutes required by the DA8 FTS to finish a single measurement (co-addition of four spectra per measurement) were co-added in order to further ensure simultaneity.

The campaign was carried out in two phases: the intensive and extended phases. The intensive phase was from February 17th to March 8th, 2006. During this time, measurements were made by all of the scientific instruments, including PARIS-IR and the DA8 FTS, when weather conditions allowed. Also, daily MSC ozonesonde balloons were launched. After the intensive phase, PARIS-IR was shipped back to its home station, the Waterloo Atmospheric Observatory (WAO). The extended phase continued from March 9th to March 31st, 2006 with measurements by the DA8 FTS, by several of the UT-visible grating spectrometers, and by weekly MSC ozonesonde flights. During the entire campaign, ACE-FTS recorded spectra by solar occultation, as described in Chapter 2, and provided thirteen measurements that are within 500 km of PEARL.

6.3 Spectral Analysis and Retrievals

The spectra measured by the ACE-FTS are analysed using a least squares fitting approach to obtain Volume Mixing Ratio (VMR) profiles of trace gases in the Earth's atmosphere, along with pressure and temperature profiles [*Boone et al.*, 2005]. The ACE-FTS version 2.2 data contains temperature and pressure profiles and VMR profiles with 3-4 km vertical resolution, for about 30 atmospheric constituents, as described in Section 2.1.1.

The spectra measured using FTSs on the ground were analyzed using SFIT2 (version 3.91) [*Pougatchev et al.*, 1995; *Rinsland et al.*, 1998]. SFIT2 makes use of the Optimal Estimation Method (OEM) [*Rodgers* 1976, 1990, 2000; *Rodgers* and *Connor*, 2003] to include *a priori* VMR profiles of atmospheric constituents as a function of altitude in the retrievals. The details of OEM and SFIT2 have been introduced in Chapter 1. The spectral ranges (called microwindows, MW) used in the retrievals are shown in Table 6.2. All of the spectroscopic line parameters used in the retrievals are from the HIgh resolution TRANsmission molecular absorption database (HITRAN) 2004 [*Rothman et al.*, 2004].

A model atmosphere is used in the SFIT2 program to simulate spectra. A forward model named FSCATM [*Gallery et al.*, 1983; *Meier et al.*, 2004] was applied to generate the model atmospheres using *a priori* VMR estimates and pressure and temperature profiles. FSCATM carries out refractive ray tracing and a calculation of the air mass distribution, which is the number of molecules as a function of altitude, for each model atmosphere. A combination of climatological estimates from the HALogen Occultation Experiment (HALOE) v.19 satellite data from 1992 to 2005 [*Russell et al.*, 1994; *Grooß et al.*, 2005], Michelson Interferometer for Passive Atmospheric Sounding (MIPAS) reference profiles measured from 2002-2004 [*Carli et al.*, 2004], Stratospheric Processes And their Role in Climate 2000 Report Climatology (SPARC2000) [*SPARC*, 2002], Eureka ozonesonde archive, MkIV balloon FT-IR spectrometer obtained in northern mid-latitudes by G.C. Toon [*Peterson and Margitan*, 1995], and the *a priori* profiles constructed by A. Meier in 1998 for the NDACC station at Kiruna, were used to construct the *a priori* estimates of VMR profiles and columns. Pressure and temperature profiles were obtained from the daily radiosondes launched from the Eureka weather station, National Centers for Environmental Prediction (NCEP)/National Center for Atmospheric Research analyses provided by the NASA Goddard Space Flight Centre automailer (obtained from the Goddard Automailer science@hyperion.gsfc.nasa.gov) [*McPherson et al.*, 1979; *Kalnay et al.*, 1996] and the Mass-Spectrometer-Incoherent-Scatter model (MSIS-2000) [*Picone et al.*, 2002]. From surface to 35 km, the radiosonde measurements were used. NCEP covers from 35 km to 50 km and the output of MSIS is used from 50 km to 100 km.

Table 6.2 Species, microwindows, spectral ranges of microwindows, interfering species, and filters used in ground-based observations.

Species	Microwindow	Spectral Range (cm^{-1})	Interfering species	Filter[b]
O_3	1120[a]	1104.78 - 1105.08	CH_3D, CHF_2Cl, CCl_2F_2, H_2CO_2, HDO, $^{16}O^{16}O\,^{18}O$	S6
		1119.73 - 1119.95	CHF_2Cl, N_2O, $^{16}O^{16}O\,^{18}O$	
		1121.67 - 1122.03	$^{16}O^{16}O\,^{18}O$, H_2CO_2, CHF_2Cl, N_2O, H_2O	
		1122.84 - 1123.06	$^{16}O^{16}O\,^{18}O$, H_2CO_2, CHF_2Cl, CH_3D, CH_4, H_2O	
	2775	2775.78 - 2775.88	HCl, N_2O, CH_4	S3
HNO_3	868	867.00 - 869.20	H_2O, OCS, NH_3, CO_2	S6
	872	871.80 - 874.00	H_2O, OCS, NH_3, CO_2, C_2H_4, Cl_2F_2	S6
$ClONO_2$	780	779.85 - 780.45	CO_2, O_3, HNO_3, CCl_4	S6
HF	4038	4038.78- 4039.10	H_2O, CH_4, HDO	S1
HCl	2725[a]	2727.72 - 2727.84	O_3, CH_4, HDO, CO_2	S3
		2775.78 - 2775.88	O_3, CH_4, N_2O	
NO[c]	1903	1899.92 - 1900.15	CO_2, N_2O, H_2O, OCS, O_3	S5
NO_2	2914	2914.60 - 2914.70	CH_4, OCS, CH_3D	S3

[a] Several spectral ranges from individual spectrum were used in the retrievals simutaneously, also known as multi-microwindow fitting.

[b] Filters were placed in front of the entrance aperture of the DA8 FTS to improve signal-to-noise ratio.

[c] PARIS-IR has no results for NO from the 2006 Canadian Arctic Validation Campaign.

6.4 Latitudes and Longitudes of Sampled Atmosphere

The knowledge of which part of the Arctic atmosphere was observed by the two ground-based FTSs during an observation day is need for the discussions in Section 6.5. In this section, the calculation of the distances between the sampled atmosphere and the PEARL, together with the latitudes and longitudes of sampled atmosphere, will be given.

The schematic diagram of the distance between the sampled atmosphere and PEARL is shown in Figure 6.1. The distance AC can be written as

$$\mathrm{AC} = \left\{ \mathrm{SZA} - \sin^{-1}\left[\frac{\mathrm{OC} \times \sin(\pi - \mathrm{SZA})}{\mathrm{OC} + \mathrm{BC}} \right] \right\} \times \mathrm{OA} \qquad (6.4.1)$$

using the law of sines and law of summation of angles, in which, AC (in km) is the distance between the ground location of the sampled atmosphere and PEARL. SZA is the Solar Zenith Angle (in radians) which is calculated using the program "sun_moon.exe" provided by A. Meier. OA = OC are the Earth's radius and the radius at the north pole of 6356.766 kilometers is used. BC is the altitude of atmosphere that is sampled. Since the target species are mainly located in the stratosphere, BC is equal to 25 km in our calculation.

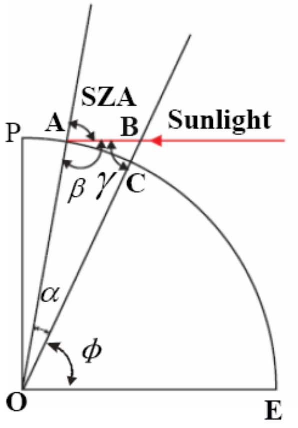

Figure 6.1 A schematic diagram of the distance between sampled atmosphere and PEARL. It shows a cross section of the Earth. O: Center of the Earth; A: Location of PEARL; B: Sampled atmosphere; C: Location of point B on the ground; SZA: Solar Zenith Angle; E: A point on the Equator; P: North Pole.

According to the definition of latitude, which is the angle at the center of the Earth between the any point on the Earth's surface and the plane of the equator, together with the geometry shown in Figure 6.1, the latitude of PEARL is

$$\angle \mathrm{AOE} = 80.05° = \alpha + \phi \ . \tag{6.4.2}$$

Hence, the latitude of the sampled atmosphere at point C is

$$\angle \mathrm{COE} = \phi = 80.05° - \alpha \ . \tag{6.4.3}$$

In the triangle ΔOAB (Figure 6.1), α can be written as

$$\alpha = \mathrm{SZA} - \sin^{-1}\left[\frac{\mathrm{OA} \times \sin(\pi - \mathrm{SZA})}{\mathrm{OC} + \mathrm{BC}}\right] \tag{6.4.4}$$

by using the law of sines and law of summation of angles.

Substituting Eq. (6.4.4) into Eq. (6.4.3), the latitude of sampled atmosphere at point C can be written as

$$\mathrm{Lat}_{\mathrm{c}} = \phi = 80.05° - \left\{\mathrm{SZA} - \sin^{-1}\left[\frac{\mathrm{OA} \times \sin(\pi - \mathrm{SZA})}{\mathrm{OC} + \mathrm{BC}}\right]\right\} \times \frac{180^{\mathrm{o}}}{\pi}. \tag{6.4.5}$$

During each measurement day, the FTSs measured several different parts of the atmosphere because the sunlight has a different optical path due to the rotation of the Earth. At solar noon on an observation day (Table 6.3), that is when the sun is on the meridian at Eureka, the sampled atmosphere is located at the same longitude as that of PEARL (86.42°W), as indicated in Figure 6.2. At other times, the longitude of the sampled atmosphere $\mathrm{Long}_{\mathrm{c}}$ can be calculated using

$$\mathrm{Long}_{\mathrm{c}} = -86.42^{\mathrm{o}} - \mathrm{HA}. \tag{6.4.6}$$

The negative sign (-86.42°) indicates a location west of the Greenwich Meridian in longitude. HA is the hour angle (in degrees) shown in Figure 6.2, and is calculated as

$$\mathrm{HA} = [T_{\mathrm{x}} \text{ (in hour)} - T_{\mathrm{SN}} \text{ (in hour)}] * 15^{\mathrm{o}} / \text{hour}, \tag{6.4.7}$$

in which, T_x is the observation time and T_{SN} is the local solar noon time for the day when the observation was made (Table 6.3).

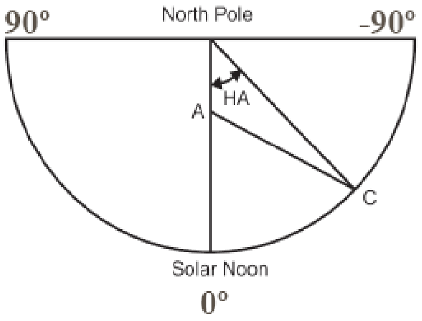

Figure 6.2 A schematic diagram of the Hour Angles (HA). A: Location of PEARL; C: Location of point B on the ground.

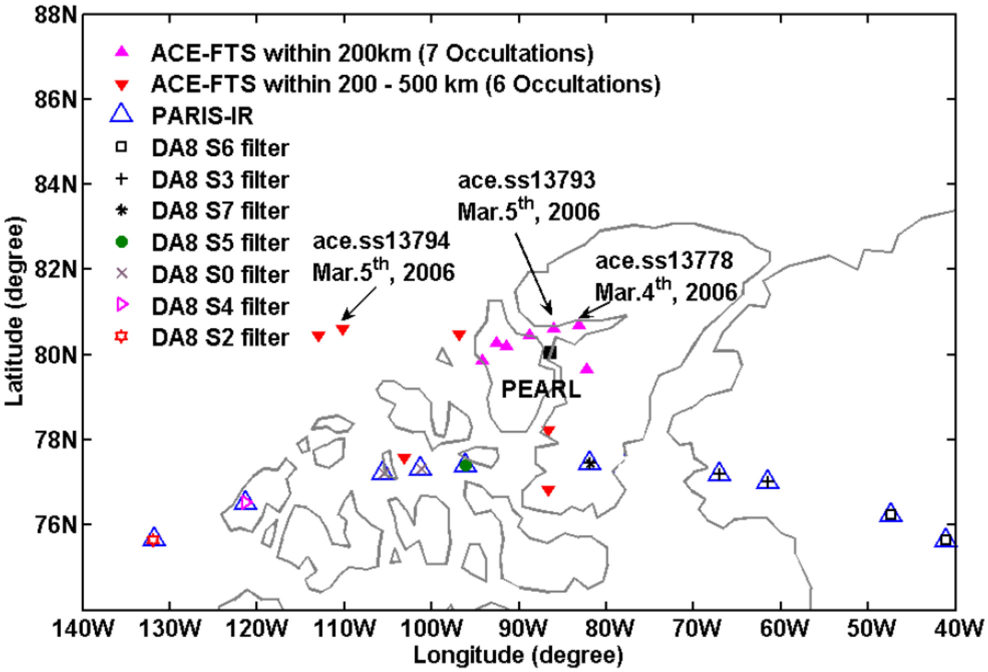

Figure 6.3 Locations of sampled atmosphere at 25 km height by two ground-based FTSs observing simultaneously on March 4th, 2006 are shown. In addition, the locations (noted using the 30 km geometric tangent points) of the 13 ACE-FTS occultations within 500 km of PEARL during the period February 21st to March 31st, 2006 are indicated. Location of PEARL is indicated with a black solid square.

Table 6.3 The sunrise, sunset and solar noon times at PEARL, Eureka, during the 2006 Canadian Arctic ACE Validation Campaign [a].

Day	**Feb. 2006**			**Mar. 2006**		
	sunrise	**sunset**	**solar noon**	**sunrise**	**sunset**	**solarnoon**
	hhmm	**hhmm**	**hhmm**	**hhmm**	**hhmm**	**hhmm**
1				0945	1615	1300
2				0933	1626	1259
3				0922	1637	1259
4				0911	1647	1259
5				0900	1658	1259
6				0850	1708	1259
7				0840	1717	1258
8				0830	1727	1258
9				0820	1736	1258
10				0810	1746	1258
11				0800	1755	1257
12				0751	1804	1257
13				0741	1813	1257
14				0732	1822	1257
15				0723	1831	1257
16				0713	1839	1256
17				0704	1848	1256
18				0655	1857	1256
19				0646	1906	1256
20	1254	1308	1301	0637	1914	1255
21	1158	1404	1301	0627	1923	1255
22	1131	1430	1300	0618	1932	1255
23	1111	1450	1300	0608	1941	1254
24	1053	1507	1300	0559	1950	1254
25	1037	1523	1300	0550	1959	1254
26	1023	1537	1300	0540	2008	1254
27	1009	1550	1259	0530	2018	1254
28	0957	1603	1300	0520	2027	1253
29				0510	2037	1253
30				0500	2047	1253
31				0450	2057	1253

[a] Time of sunrise, sunset, and solar noon are local times and obtained from the Astronomical Application Department of U.S. Naval Observatory using the following link: http://aa.usno.navy.mil/.

Hence, the distances between sampled atmosphere and PEARL, the latitudes and longitudes of sampled atmosphere of each measurement can be calculated by using Eqs. (6.4.1), (6.4.5), and (6.4.6), respectively. The calculations of latitude and longitudes of sampled atmosphere for the observations made March 4th, 2007 were carried out and are shown in Figure 6.3.

6.5 Results and Discussion

The spectra recorded using PARIS-IR, DA8 FTS and ACE-FTS during the 2006 Canadian Arctic ACE Validation Campaign were analyzed to obtain the amounts of trace gases, utilizing the methods given in Section 6.3. The results for seven trace gases (O_3, HNO_3, HCl, $ClONO_2$, NO_2, NO, HF) from these observations will be discussed in the following sections. In the Section 6.5.1, the comparisons of results between two ground-based FTSs, PARIS-IR and the DA8 FTS will be reported. In Section 6.5.2, the results from the ground-based observations are used to evaluate the quality of ACE-FTS occultation measurements. Finally, the results from three FTSs will be utilized in probing the time evolution of chemical constituents in the atmosphere over the Canadian high Arctic during the spring 2006.

6.5.1 Comparisons between PARIS-IR and the DA8 FTS

Atmospheric absorption spectra were simultaneously recorded using PARIS-IR and the DA8 FTS during the 2006 Canadian Arctic ACE Validation Campaign. Like other FTSs in the NDACC network, the DA8 FTS at PEARL records each spectral range during an observation day with a specified filter, as shown in Table 2.3. This strategy improves the SNR of recorded spectra, but provides fewer observed species at each observation time due to the limited spectral ranges of each filter. In addition, at the beginning of the campaign, each day is short as shown in Table 6.3 and the weather also affects the measurements through the campaign. The DA8 FTS was therefore not always able to finish a complete set of measurements. Not all of the target species were measured every day using two ground-based FTSs.

Unlike the DA8 FTS, PARIS-IR records a broad spectral range of 750 to 4400 cm^{-1} simultaneously, that is, it is able to determine the vertical columns for all of the investigated trace gases from each observation. Results from PARIS-IR should therefore provide information with higher temporal resolution than those from the DA8 FTS. For example, on March 4th, 2006, ten observations were made using PARIS-IR and the DA8 FTS simultaneously. Figure 6.3 shows that the two ground-based FTSs sampled the atmosphere in different locations for the ten observations. Each observation was taken in approximately 13 minutes. The vertical columns of O_3 are available from all ten observations made using PARIS-IR on that day. In contrast, only two spectra in the spectral range of the S6 Filter (Table 2.3) were recorded by the DA8 FTS containing MWs around 1120 cm^{-1}. Hence, only two ozone columns were reported from the observations using the DA8 FTS from MW1120 on March 4th, 2006. As indicated in Figure 6.3 for the rest of time on that day, the DA8 FTS recorded atmospheric absorption spectra in spectral ranges other than the one covered by the S6 Filter. Hence, the differences between PARIS-IR and the DA8 FTS in the spectral coverage of each observation resulted in different temporal resolutions for the observed vertical columns of target species. Furthermore, PARIS-IR provided column amounts with a wider spatial coverage than those made using the DA8 FTS. For example, the ozone columns retrieved from MW1120 from ten observations measured by PARIS-IR on March 4th, 2006 provide the ozone distributions in a rectangle about 40ºW to 140ºW and 74ºN to 78ºN, while the results from the MW1120 recorded by the DA8 FTS show the distribution of ozone in the area around 40ºW to 50ºW and 74ºN to 78ºN.

The total columns of six species (O_3, HNO_3, HCl, NO_2, $ClONO_2$, HF) from PARIS-IR and the DA8 FTS were compared, as shown in Table 6.4 (PARIS-IR did not measure NO). The comparisons were performed in two ways. One is to use the daily averaged values in the comparisons and the other is to utilize the individual measurements in the comparisons. For the former method, the daily averaged total columns were calculated for any given species measured by the two FTSs, and the percentage differences for the given species measured by two spectrometers were calculated for each measurement day using

$$\mathrm{P}_x = \frac{[\overline{\mathrm{C}}_{\mathrm{Px}} - \overline{\mathrm{C}}_{\mathrm{Dx}}]}{\overline{\mathrm{C}}_{\mathrm{Px}}} \times 100 , \qquad (6.5.1.1)$$

where, $\overline{\mathrm{C}}_{\mathrm{Px}}$ and $\overline{\mathrm{C}}_{\mathrm{Dx}}$ are the daily mean values of observed total columns of the given species x (x can be O_3, HNO_3, HCl, NO_2, $ClONO_2$, or HF) observed by PARIS-IR and the DA8 FTS, respectively. All of the percentage differences were then averaged to obtain the results shown in the third column of Table 6.4, with the 1σ standard deviation of the mean differences in total columns shown in parentheses. In the second method used in the comparison, the differences of individual measurements were calculated using

$$\mathrm{P}_x = \frac{[\mathrm{C}_{\mathrm{Px}} - \mathrm{C}_{\mathrm{Dx}}]}{\mathrm{C}_{\mathrm{Px}}} \times 100 , \qquad (6.5.1.2)$$

where, C_{Px} and C_{Dx} are the individual values of simultaneously observed total columns. All of these differences of individual measurements were averaged to obtain the results which are shown in the fourth column of Table 6.4, together with the 1σ standard deviations.

As shown in Table 6.4, for all six of the investigated species the comparisons using daily average values show larger differences (up to 17%) between two FTSs than those using the individual observations recorded simultaneously. The variations of the measured total columns during each observation day, which arise from temporal and spatial differences in Arctic atmospheric composition, is the explanation for these phenomena. For example, the daily trends in ozone total columns, as shown in the enlarged views in Figure 6.4, were averaged to obtained daily mean values of ozone for March 4th, 5th, and 6th, 2006 respectively. The daily averaged total columns of ozone from PARIS-IR represent ozone amounts over broad geographical areas. However, the DA8 FTS data set contains only two total ozone columns per day for the March 4th to 6th, 2006, because of the sequence of filters used. The daily averages of ozone from the DA8 FTS represent the ozone distribution on the east side of Eureka (Figure 6.3) near sunrise (Figure 6.4). The daily averages for the two instruments therefore cover different regions at different times.

Table 6.4 Comparisons of total columns observed by the DA8 FTS and PARIS-IR from February 21st to March 8th, 2006

Species	Microwindow	Mean Percentage Differences [a]	
		Comparison Using Daily Mean Value[a]	Comparison Using Individual Measured Value[a]
O_3	1120	-6.33(±8.07)%	2.84(±5.71)%
	2775	-3.56(±3.87)%	0.03(± 4.76)%
HNO_3	868	-5.11(±9.59)%	-0.11(±2.95)%
	872	-2.22(±7.34)%	-1.94(±2.60)%
NO_2	2914	-2.84(±6.97)%	-0.08(±3.23)%
HCl	2725	-7.84(±2.91)%	-3.22(±2.71)%
HF	4038	-5.31(±3.22)%	-1.45(±6.77)%
$ClONO_2$	780	-17.62(±10.10)%	-4.28(±6.70)%

[a] See text for calculation method description.

In 1999, an instrument comparison campaign was held at Eureka and the retrieved vertical columns from the portable National Physical Laboratory (NPL) FTS (a Bruker 120 M) were compared with those from the DA8 FTS at PEARL [*Murphy et al.*, 2001]. The comparisons show that the differences between the NPL FTS and the DA8 FTS have a consistent systematic bias of about 3% for HCl, HNO_3 and O_3, and 7% for HF. The large difference between instruments for HF was attributed to an instrument lineshape problem and a zero level problem (when the atmosphere has 100% absorption the signal should go zero) [*Murphy et al.*, 2001]. In addition, the non-linearity of the MCT detector was found to be causing a major part of the differences in the retrieved HNO_3 columns between the NPL FTS and the DA8 FTS [*Murphy et al.*, 2001]. The differences from the 2006 Canadian Arctic ACE Validation Campaign generally show smaller values than those reported in the 1999 comparison, although the mean differences show systematically lower column values for five species (HNO_3, HCl, NO_2, $ClONO_2$, HF) and higher column values for O_3 from PARIS-IR than from the DA8 FTS. The 2006 campaign likely benefits from the fact that the software packages used to derive detector nonlinearity and baseline corrections for the two FTSs were both from the same company (ABB-Bomem, who built both instruments), ensuring a degree of internal consistency.

Comparisons between PARIS-IR and two FTSs with higher spectral resolutions were carried out in summer 2005 at the University of Toronto [*Wunch et al.*, 2007]. One of these FTSs was the Toronto Atmospheric Observatory Fourier Transform Spectrometer (TAO-FTS), an ABB-Bomem DA8 FTS with the same specifications as the Eureka DA8 FTS. Total column differences for O_3 and HCl between PARIS-IR and the TAO-FTS were about 1% to 4% (Figure 4.2), respectively, consistent with the agreement between PARIS-IR and the Eureka DA8 FTS in this work.

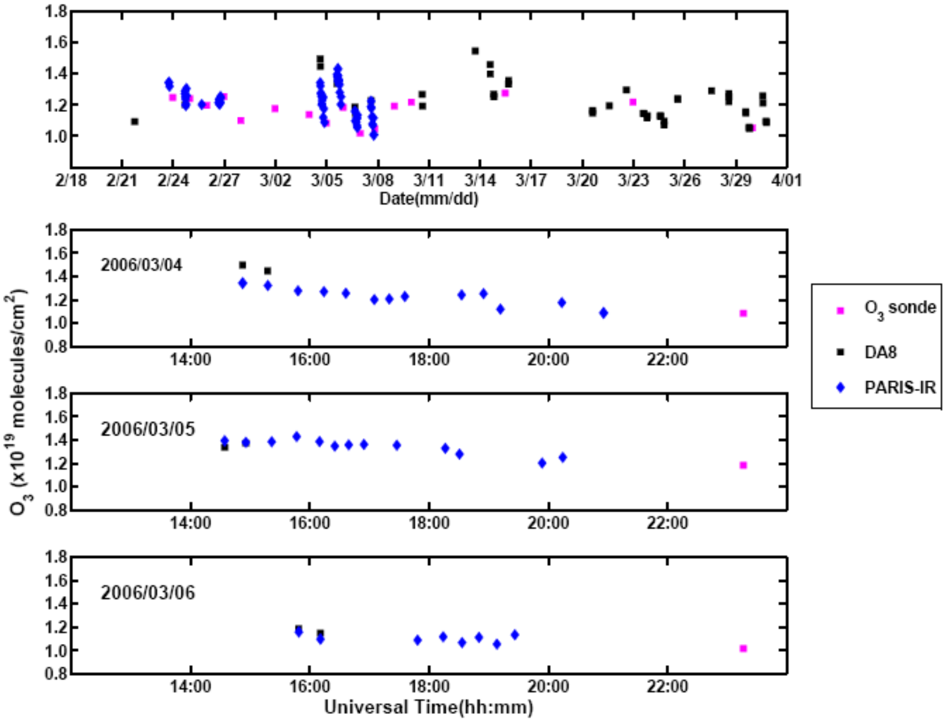

Figure 6.4 O_3 total columns obtained from the spectra near 1120 cm^{-1} recorded using PARIS-IR and the DA8 at PEARL from during the 2006 Canadian Arctic ACE Validation Campaign, together with ozonesonde measurements. Enlarged views of daily observations on March 4th to 6th, 2006 are shown.

OEM, the method used in the SFIT2 spectral analysis program, provides a method to compute the major uncertainties in the retrievals of vertical columns such as smoothing error, retrieval noise error and model parameter error [*Rodgers* 1976, 1990, 2000; *Rodgers* and *Connor* 2003]. Smoothing error, also known as null space error in the Rodger's OEM formalism, arises from the limited altitude resolution of the observing system. Retrieval noise error is due to measurement noise in the spectra. The forward model parameters such as spectral background, slope and instrumental line shape also generate uncertainties in the retrievals and these contributions are grouped together as model parameter error. Table 6.5 summarizes these errors in the observations using PARIS-IR and the DA8 FTS. The methods for estimating these errors are discussed in Section 1.7.

Table 6.5 Uncertainties in the retrievals of total vertical columns obtained from measurements by the DA8 FTS and PARIS-IR

Species	**MW**	**Smoothing Error**		**Retrieval Noise Error**		**Model Parameter Error**		**Degrees of Freedom**	
		PAR [a]	DA8 [b]	PAR [a]	DA8 [b]	PAR [a]	DA8 [b]	PAR [a]	DA8 [b]
O_3	1120	7.9%	5.4%	2.9%	2.5%	0.5%	0.3%	3.6	4.2
	2775	12.3%	8.7%	0.4%	3.7%	0.5%	0.2%	2.2	2.5
HNO_3	868	14.7%	13.5%	1.5%	2.9%	0.2%	0.1%	1.5	1.7
	872	14.5%	13.7%	1.5%	2.9%	0.3%	0.1%	1.6	1.9
NO_2	2914	25.1%	22.7%	2.8%	3.7%	0.1%	0.1%	1.7	1.9
HCl	2725	7.5%	7.4%	0.8%	2.7%	0.3%	0.1%	1.7	1.7
HF	4038	6.8%	5.5%	1.3%	2.5%	0.2%	0.1%	1.7	1.7
$ClONO_2$	780	16.1%	14.2%	3.0%	2.7%	0.1%	0.1%	1.0	0.9
NO	1903	N/A	10.9%	N/A	3.9%	N/A	0.1%	N/A	1.2

[a] PAR: PARIS-IR

[b] DA8: DA8 FTS

The spectral resolution of a measurement affects the amount of vertical information obtained from the spectral line shape of a measured species [*Rodgers* 2000]. With higher spectral resolution, more precise vertical information can be obtained, as discussed in Chapters 1 and 5. As shown in Table 6.5, the results from the DA8 FTS have higher values of Degrees Of Freedom for Signal (DOFS), the number of independent quantities obtained from the observations (the vertical partial columns in the specified altitude range, in this case), than those from PARIS-IR, since the DA8 FTS has a spectral resolution 10 times higher than that of PARIS-IR. The DOFS can be improved by choosing high quality microwindows, i.e., spectral segments which contain many absorption lines of the investigated species with only few and weak absorption features from interfering species. The microwindows used in this work generally improved the retrievals of O_3 and HCl compared to those carried out in the instrument comparison campaign at University of Toronto [*Wunch et al.* 2007] in terms of DOFS.

According to the Rodger's OEM theory which is described in Chapter 1, the averaging kernel is the derivative of a derived parameter with respect to its *a priori* state value, i.e., when this derivative is small (nearly 0) all of the information comes from the *a priori* and when it is large (near 1) then the information in the retrieval comes mainly from the measured spectra [*Rodgers* 1976, 1990, 2000]. The typical averaging kernel profiles of seven investigated species are shown in Figure 6.5. For all of the seven investigated species, the retrievals show good performance, since the averaging kernel values are close to 1 in the altitude ranges where most of the species are located. For example, the averaging kernel values from the O_3 retrievals using spectral segments near 1120 cm^{-1} (MW 1120) are close to 1 from 10 to 60 km for both FTSs, as shown in Figure 6.5. More than 80% of the total ozone is present in the altitude range of 10 to 60 km.

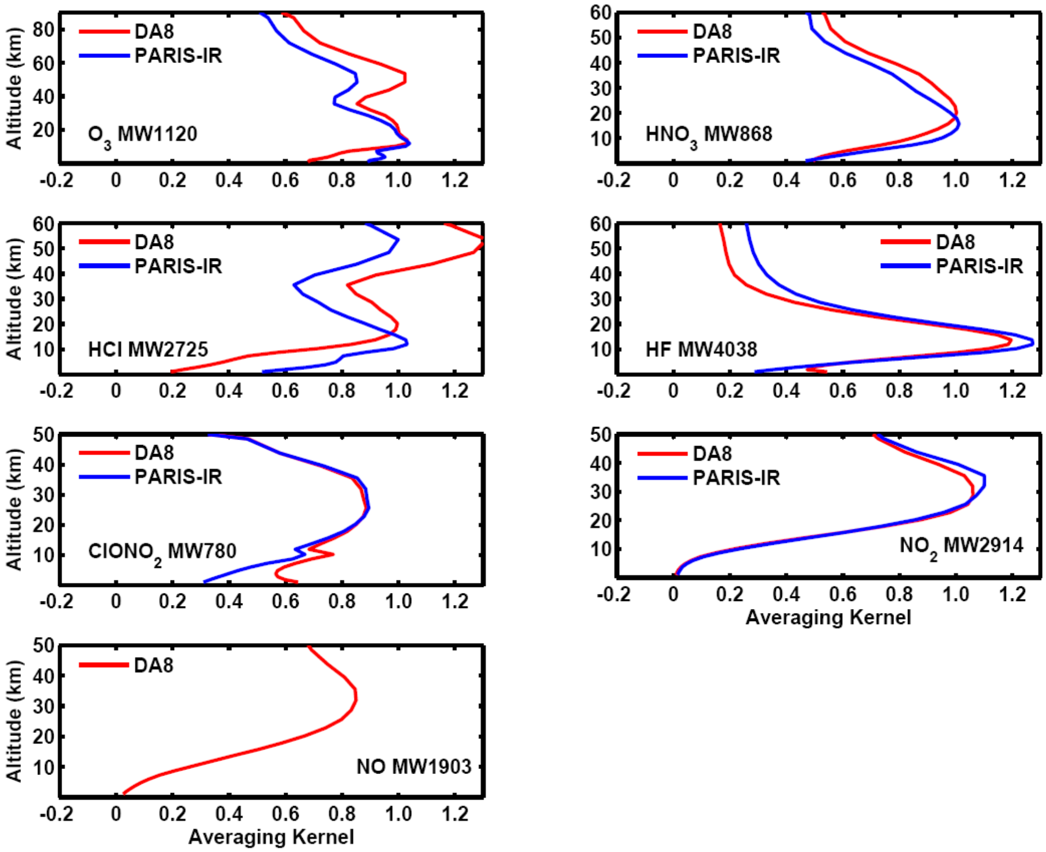

Figure 6.5 Averaging Kernels of PARIS-IR and the DA8 FTS.

6.5.2 Partial Column Comparisons between ACE-FTS Measurements and Ground-Based Observations using Two FTSs

Ground-based observations provide retrieved concentration profiles of trace gases with limited vertical resolution (DOFS about 1 to 4 as shown in Table 6.5, half width at half maximum for averaging kernels about 15 to 30 km as shown in Figure 6.5), much coarser than the vertical resolution (about 3 km) of observations from ACE-FTS. Because of this, the present comparisons are restricted to partial column abundances rather than profiles. As shown in *Sung et al.* [2007], the comparisons of partial columns from ground-based instruments with ACE-FTS results poses difficulties for molecules with maximum VMR in the troposphere (such as N_2O or CH_4), particularly for an FTS with the resolution of PARIS-

IR. Thus, the comparisons were restricted to molecules where the VMR peaks in the stratosphere.

Version 2.2 of the ACE retrievals including the ozone update [*Boone et al.*, 2005] is used here. This version is the latest release of ACE-FTS results from the ACE mission, and the ozone update shows improved agreement with other datasets [*Dupuy et al.*, in preparation for *Atmos. Chem. Phys.*]. There were thirteen occultation measurements within 500 km of PEARL during the 2006 Canadian Arctic ACE Validation Campaign. Coincidences occurred on eight days for DA8 FTS and seven days for PARIS-IR, with respectively, nine and eight ACE occultations meeting the criteria that they occurred on the same day within 500 km from PEARL. The partial columns C_x of seven trace gases were calculated for ACE-FTS using

$$C_x = \sum_{i=\mathrm{bottom}}^{i=\mathrm{top}} \rho(i) \times \mathrm{VMR}_x(i) \times Z(i), \tag{6.5.2.1}$$

where, x stands for O_3, HCl, $ClONO_2$, HF, HNO_3, NO_2, or NO.; $\rho(i)$ (in molecules/cm^3), $\mathrm{VMR}_x(i)$, and $Z(i)$ (in cm) are the number density of air, the volume mixing ratio of the species x in the ith layer, and the thickness of the ith layer. In the database of the version 2.2 ACE-FTS retrievals, ρ and VMR_x are reported on an altitude grid with 150 layers (spanning 0.5 to 150 km with a constant thickness of 1 km). However, occultations made by the ACE-FTS usually have different altitude ranges due to various factors such as clouds that block the field-of-view during observations. Hence, in order to make a valid comparison, the partial columns from PARIS-IR and the DA8 FTS for the investigated species x were determined in the same altitude range as in the 13 ACE-FTS occultations. The partial columns from the ACE-FTS are shown together with their altitude ranges, measurement dates, and occultation names in Table 6.6.

The heterogeneity of the Arctic atmosphere can be seen in the ACE-FTS observations. For example, two measurements named ss13793 and ss13794, in which the ss indicates the measurements were carried out at sunset, and 5 digits give the orbit numbers, were made within 500 km of PEARL by the ACE-FTS on March 5th, 2006 (Figure 6.3). The observation times for ss13793 and ss13794 were 21:22:04 and 22:59:47 (in universal time), respectively. The observed partial columns (Table 6.6) show percentage differences of -8.11%, -6.79%, -38.06%, -12.32%, -14.88%, 1.96%, and 7.67% for O_3, HCl, $ClONO_2$, HF, HNO_3, NO_2, and NO, respectively. The partial column differences between ss13793 and ss13794 can be attributed to the spatial differences (about 400 km) between the two observations (Figure 6.3), and shows the heterogeneity of the Arctic atmosphere because the time difference between these two observations is only about 1.5 hours.

In addition, observations made by the ACE-FTS also show differences in measured partial columns due to different measurement times. For example, the observation ss13778, whose measurement time is 20:56:26 (in universal time) on March 4th, 2006, was made about 24 hours earlier than the observation ss13793. The distance between ss13778 and ss13793 is about 30 km (Figure 6.3), and both of them are within 100 km of PEARL (Table 6.6). The observed partial columns show percentage differences of -18.14%, -16.83%, -71.18%, -40.51%, -37.45%, 11.14%, and -3.21%, for O_3, HCl, $ClONO_2$, HF, HNO_3, NO_2, and NO, respectively.

In the altitude ranges of the partial columns measured by the ACE-FTS, the retrievals from PARIS-IR and the DA8 FTS have averaging kernel values generally larger than 0.5 (as shown in Figure 6.5), which indicates that retrieved columns of the investigated species are mainly obtained from observations rather than *a priori* information. The partial columns from the DA8 FTS and PARIS-IR, which were determined in the same altitude ranges as those of the ACE-FTS, were divided by the partial columns of ACE-FTS to obtain the ratios in Table 6.7. The partial columns from the individual ground-based observations with measurement time closest to those of the ACE-FTS observations were used in these calculations.

Table 6.6 Partial columns observed by ACE-FTS during the 2006 Canadian Arctic ACE Validation Campaign

Date	Time	Occult.	Distance	O_3	HCl	$ClONO_2$	HF	HNO_3	NO_2	NO
mm/dd	**hh:mm:ss**[a]	**Name**[b]	**Δ**[c] **in km**	**molecules /cm^2**						
2/22	21:32:40	ss13631	449	1.1646×10^{19}	4.4257×10^{15}	1.5903×10^{15}	1.9223×10^{15}	2.6874×10^{16}	0.8151×10^{15}	2.2761×10^{15}
2/23	20:20:45	ss13645	201	1.1136×10^{19}	4.4358×10^{15}	1.5824×10^{15}	1.9217×10^{15}	2.6225×10^{16}	1.2500×10^{15}	2.8668×10^{15}
2/26	20:00:13	ss13689	92	1.1103×10^{19}	4.3949×10^{15}	1.8289×10^{15}	2.0582×10^{15}	2.5816×10^{16}	0.9698×10^{15}	2.2107×10^{15}
2/28	20:51:34	ss13719	119	1.0994×10^{19}	4.3367×10^{15}	2.0231×10^{15}	2.0782×10^{15}	2.5891×10^{16}	0.7822×10^{15}	2.1822×10^{15}
3/1	21:17:13	ss13734	202	1.1631×10^{19}	4.4074×10^{15}	2.4271×10^{15}	2.2977×10^{15}	2.7763×10^{16}	1.2075×10^{15}	2.2530×10^{15}
3/4	20:56:26	ss13778	95	0.9404×10^{19}	3.9714×10^{15}	1.4044×10^{15}	1.7299×10^{15}	2.1749×10^{16}	1.1683×10^{15}	2.3525×10^{15}
3/5	21:22:04	ss13793	64	1.1110×10^{19}	4.6399×10^{15}	2.4041×10^{15}	2.4306×10^{15}	2.9895×10^{16}	1.0381×10^{15}	2.4280×10^{15}
3/5	22:59:47	ss13794	445	1.0277×10^{19}	4.3447×10^{15}	1.7413×10^{15}	2.1639×10^{15}	2.6022×10^{16}	1.0589×10^{15}	2.6297×10^{15}
3/6	21:47:43	ss13808	63	1.0540×10^{19}	4.3723×10^{15}	2.2347×10^{15}	2.2577×10^{15}	2.6079×10^{16}	1.0059×10^{15}	2.4636×10^{15}
3/6	23:25:25	ss13809	497	1.0212×10^{19}	4.2115×10^{15}	1.6180×10^{15}	2.0166×10^{15}	2.4378×10^{16}	1.0539×10^{15}	2.3264×10^{15}
3/7	22:13:21	ss13823	98	1.0256×10^{19}	4.3300×10^{15}	1.8834×10^{15}	2.2221×10^{15}	2.3588×10^{16}	1.1856×10^{15}	2.4563×10^{15}
3/8	22:38:59	ss13838	152	1.1407×10^{19}	4.5224×10^{15}	1.7710×10^{15}	2.2175×10^{15}	2.7366×10^{16}	1.1370×10^{15}	2.5993×10^{15}
3/13	23:09:33	ss13912	357	1.2004×10^{19}	4.9258×10^{15}	3.0328×10^{15}	2.8421×10^{15}	3.5076×10^{16}	1.3169×10^{15}	2.2828×10^{15}
Altitude Range (km)				9.5 - 84.5	11.5 - 47.5	14.5 - 30.5	13.5 - 44.5	10.5 - 31.5	17.5 - 35.5	24.5 - 84.5

[a] Universal time.

[b] Occultation names which are used by the ACE Science Operation Centre to name occultations [type of measurement (sr = sunrise and ss = sunset) + orbit number].

[c] Δ is distance from 30 km altitude tangent point of ACE-FTS occultation measurement to PEARL

Table 6.7 Ratios of partial columns ([ACE-FTS]/[ground-based FTS]) obtained during the 2006 Canadian Arctic ACE Validation Campaign

Date	Time	Occultation	O$_3$		HCl		ClONO$_2$		HF		HNO$_3$		NO$_2$		NO	
mm/dd	**hh:mm:ss[a]**	**Δ[b] in km**	**AD[c]**	**AP[d]**	**AD**	**AP**	**AD**	**AP**	**AD**	**AP**	**AD**	**AP**	**AD**	**AP**	**AD**	**AP**
2/22	21:32:40	ss13631 (449)	-	-	-	-	-	-	-	-	-	-	-	-	-	-
2/23	20:20:45	ss13645 (201)	-	0.93	0.91	1.00	-	1.01	0.87	0.89		0.92	1.31	1.20	-	-
2/26	20:00:13	ss13689 (092)	-	1.00	0.88	1.01		0.91	1.00	0.99		0.94	0.96	0.96	-	-
2/28	20:51:34	ss13719 (119)	-	-	-	-	-	-	-	-	-	-	-	-	-	-
3/1	21:17:13	ss13734 (202)	-	-	-	-	-	-	-	-	-	-	-	-	-	-
3/4	20:56:26	ss13778 (095)	0.70[e]	0.94	0.82	0.95	0.54[e]	0.92	-	0.90	0.74[e]	0.94	1.11	0.92	1.17	-
3/5	21:22:04	ss13793 (064)	0.90	0.99	0.89	1.03	0.85	0.95	1.02	1.17	1.09	1.13	1.18	1.07	1.21	-
3/5	22:59:47	ss13794 (445)	0.84	0.91	0.83	1.01	0.62	1.05	0.91	1.05	0.95	0.98	1.20	0.88	1.31	-
3/6	21:47:43	ss13808 (063)	1.00	1.01	0.94	1.02	1.08	1.18	1.09	1.18	1.07	1.13	0.96	0.89	1.05	-
3/6	23:25:25	ss13809 (497)	0.97	0.98	0.91	0.99	0.78	0.85	0.98	1.06	1.00	1.06	1.00	0.94	0.99	-
3/7	22:13:21	ss13823 (098)	0.93	1.06	0.92	1.06	0.77	0.84	1.05	1.10	0.89	0.98	1.19	0.78	1.14	-
3/8	22:38:59	ss13838 (152)	-	-	-	-	-	-	-	-	-	-	-	-	-	-
3/13	23:09:33	ss13912 (357)	0.93	-	0.84	-	1.01	-	0.88	-	-	-	1.32	-	1.06	-
Mean Values			0.90	0.98	0.88	1.01	0.77	0.96	0.98	1.04	0.96	1.01	1.14	0.96	1.13	-

[a] Universal time.

[b] Δ is distance from 30 km altitude tangent point of ACE-FTS occultation measurement to PEARL.

[c] Ratio of [ACE-FTS]/[DA8]

[d] Ratio of [ACE-FTS]/[PARIS-IR]

[e] The large differences between the DA8 FTS and the ACE-FTS are caused by the heterogeneity of the Artic atmosphere. See text for details.

The trace gases have average differences of about 10% between the DA8 FTS and the ACE-FTS except for $ClONO_2$, a trace gas involved in many heterogeneous chemical processes that often occur in a strong polar vortex [*Solomon* 1999; *Toon et al.*, 1999]. The discrepancies between ground-based measurements and the observations made by the ACE-FTS are mainly due to the heterogeneity of the Arctic atmosphere and the differences in measurement time. The results from PARIS-IR show better agreement than those of the DA8 FTS with the ACE-FTS due to better temporal coincidences. The average differences for all of the investigated species for ACE-FTS, and PARIS-IR are within 4%, as shown in Table 6.7. In previous work carried out by *Mahieu et al.* [2005], HCl and $ClONO_2$ measurements made by ACE-FTS were compared to ground-based FTS observations and showed column ratios ([ACE-FTS]/[Ground FTS]) spanning from 0.99 to 1.07 and 0.79 to 1.09, respectively. The comparisons carried out in this work are consistent with those in *Mahieu et al.* [2005].

6.5.3 Time Evolution of Trace Gases and Ozone Chemical Depletion during the 2006 Canadian Arctic ACE Validation Campaign

The satellite observations, together with meteorological analyses, have been used to study the Arctic vortex, temperature and trace gas evolution in 2004-2005, 2005-2006 and 2006-2007 winters [*Manney et al.*, 2007]. In that study, the 2005-2006 winter in the Arctic had a very strong, prolonged major Stratospheric Sudden Warming (SSW) beginning in early to mid January, 2006, that ended in the middle to late February, 2006. After the SSW, a pole-centered strong vortex redeveloped quickly in the lower mesosphere and the upper stratosphere. Figures 1 to 3 of *Manney et al.* [2007] show that the Arctic vortex in the stratosphere extends to about 60° N. Figures 4 and 12 of *Manney et al.* [2007] show cold temperatures (about 190 to 220 K) in the stratosphere (about 20 to 50 km) over Eureka during the entire 2006 Canadian Arctic ACE Validation Campaign.

Figure 6.6 is a contour plot of scaled potential vorticity (sPV in units of $10^{-4}s^{-1}$) as a function of time from February 21st to March 31st, 2006 over PEARL. sPV is the scaled

Rossby-Ertel potential vorticity (PV), which is a measure used to describe the intensity of the polar vortex [*Dunkerton and Delisi*, 1986; *Manney et al.*, 1994]. The larger sPV, the stronger the polar vortex is. The sPV values used in Figure 6.6 are the Derived Meteorological Products (DMPs) calculated from the Goddard Earth Observing System version 4.03 (GEOS-4) and provided by G.L. Manney. *Manney et al.* [2007] found that the sPV values at the edge of vortex in the stratosphere are about 1.2 to $1.6\times10^{-4}s^{-1}$. The sPV profiles shown in Figure 6.6 are produced for each sunrise and sunset during the campaign. In the upper stratosphere (about 50 km), the sPV values are larger than $2\times10^{-4}s^{-1}$ during entire campaign, and indicate the Arctic vortex is strong. In the middle stratosphere (about 30 km) the sPV values are larger than $1.6\times10^{-4}s^{-1}$, and indicate that the Arctic vortex has formed. In the lower stratosphere (about 18 km) the sPV values are generally about 1.2 to $1.6\times10^{-4}s^{-1}$, and indicate that the vortex is weak and ill-defined. During the entire 2006 Canadian Arctic ACE Validation Campaign, the redeveloping vortex was continuously over Eureka, but in the lower stratosphere, the vortex was weak and ill-defined compared to higher altitudes.

The observations carried out using three FTSs (ACE-FTS, PARIS-IR, and the DA8 FTS) measured column densities of the stratospheric trace gases within the Arctic vortex on 2006 (the locations of sampled atmosphere shown in Figures 6.3 and 6.7 of this work, Arctic vortex range in the stratosphere shown in Figures 1 to 3 of *Manney et al.* [2007]). The meteorological conditions in the stratosphere affect the trace gases in the Arctic because polar stratospheric clouds form at temperatures below 195 K, [*Solomon* 1999; *Bernath* 2001]. Heterogeneous chemistry on these PSCs results in ozone depletion. The temperature dependence of chlorine activation is discussed by *Kawa et al.* in [1996].

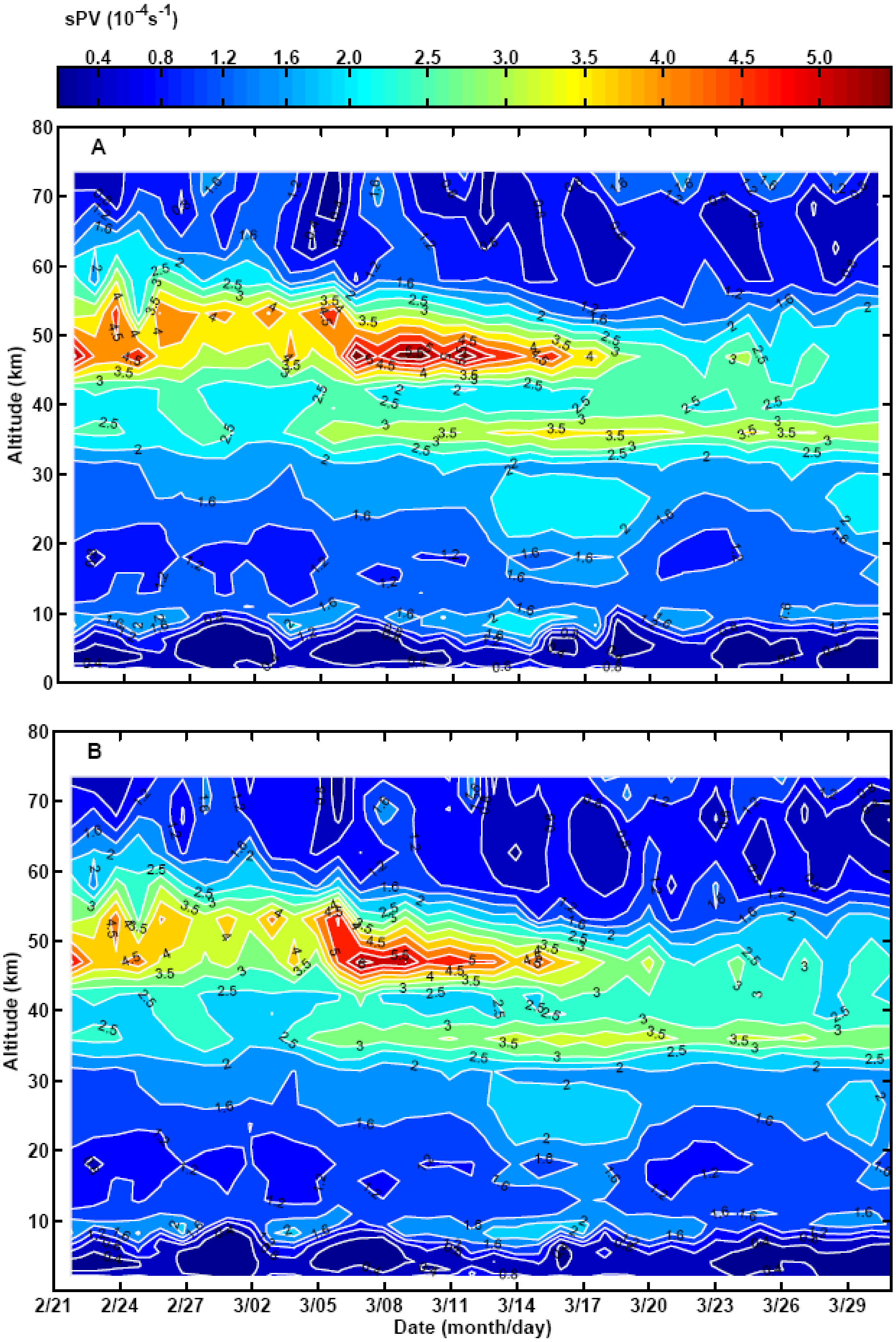

Figure 6.6 Cross-sections above Eureka of scaled potential vorticity (sPV, $10^{-4}s^{-1}$) from GEOS-4 as a function of time from February 21st to March 31st, 2006 are shown. A: at sunrise; B: at sunset.

PARIS-IR

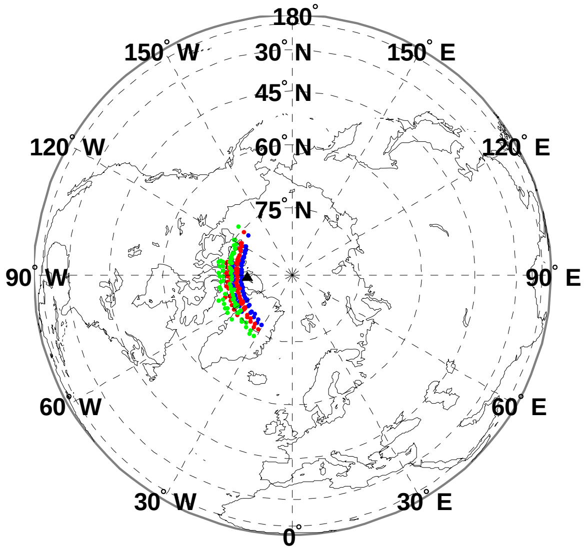

DA8 FTS

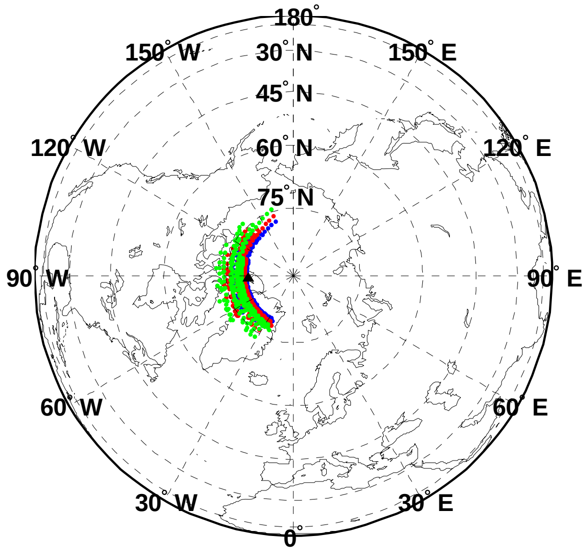

Figure 6.7 Locations of sampled atmosphere by PARIS-IR and the DA8 FTS. Location of PEARL is indicated with a black triangle. Blue dots, red dots and green dots indicate locations of sampled atmosphere at 14 km, 26 km, and 46 km height, respectively. PARIS-IR made observations from February 21st to March 7th, 2006. The DA8 FTS made observations from February 21st to March 30th, 2006.

The O_3, $ClONO_2$, HCl, HNO_3, and HF atmospheric height profiles of concentrations have similar shapes, with peak values in the stratosphere [*Toon et al.*, 1992; *Mellqvist et al.*, 2002]. HF has been used as a tracer in the stratosphere, since it is a long-lived species and does not have any known stratospheric sinks [*Toon et al.*, 1992; *Mellqvist et al.*, 2002]. In addition, the ACE-FTS provides partial columns of these species that are very nearly total column densities. The partial columns to total column percentages for O_3, HCl, $ClONO_2$, HNO_3, and HF are 92%, 98%, 94%, 93%, and 91%, respectively. In order to remove most of the dynamical effects, such as diabatic descent and tropopause and stratospause height changes, the partial columns of O_3, $ClONO_2$, HCl, and HNO_3 from ACE-FTS, PARIS-IR, and the DA8 FTS, were normalized by taking ratios with the partial columns of HF, and the results are shown in Figure 6.8.

The columns of $ClONO_2$, HCl, HNO_3, and O_3 cannot be measured simultaneously with those of HF with the DA8 FTS operated using the observation strategy of NDACC. The daily mean values of partial columns were used for the DA8 FTS. For PARIS-IR, simultaneous measurements were used to compute the ratios, and these ratios were then averaged to obtain the daily mean column ratios of [HCl]/[HF], [$ClONO_2$]/[HF], [HNO_3]/ [HF], and [O_3]/[HF]. As shown in Figure 6.8, PARIS-IR and the DA8 FTS have similar trends.

HCl and $ClONO_2$ are the major chlorine reservoir species (they do not react with ozone) but can form active compounds such as ClO in the cold atmospheric conditions within the polar vortex [*Webster et al.*, 1993; *von Clarmann et al.*, 1993; *Oelhaf et al.*, 1994; *Toon et al.*, 1999; *Solomon* 1999; *Mellqvist et al.*, 2002]. ClO is a key chemical in ozone depletion [*Solomon* 1999; *Bernath* 2001]. Based on previous studies, chlorine activation is characterized by a decrease in the ratios of [HCl]/[HF], [$ClONO_2$]/[HF], or [HCl+$ClONO_2$]/[HF], and is associated with a decrease in the ratios of [O_3]/[HF]. For example, *Toon et al.* in [1999] discussed the connection between the decreases in the column ratios of [O_3]/[HF] and [HCl]/[HF], [$ClONO_2$]/[HF], [HNO_3]/[HF] with the low temperature in the vortex. The observations, which were carried out using the ground-based FTS at Ny Ålesund (78.9°N, 11.9°E) in spring 1992 and 1997 together with the FTS at Fairbanks

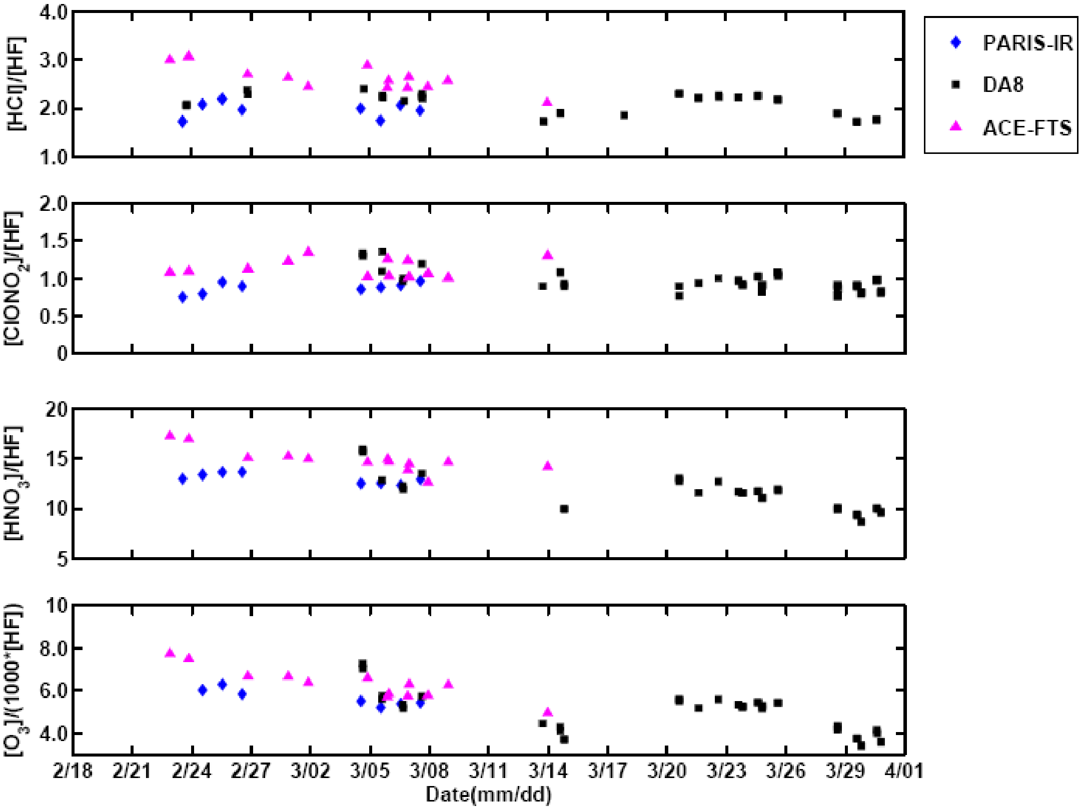

Figure 6.8 Time evolution of partial columns of $ClONO_2$, HCl, HNO_3, and O_3, normalized with HF from the observations using ACE-FTS, PARIS-IR, and the DA8 FTS during the 2006 Canadian Arctic ACE Validation Campaign.

(65.1ºN, 147.4ºW) in spring 1997, were utilized in the work of *Toon et al*. [1999]. In addition, *Mellqvist et al.* demonstrated in 2002 that chlorine activation correlates with ozone depletion, using the observations from Harestua (60.2°N, 10.8°E), Kiruna (67.8°N, 20.4°E), Esrange (67.9°N, 21.1°E), and Ny Ålesund (78.9°N, 11.9°E) during the winter of 1999-2000. The observations made by ACE-FTS, PARIS-IR, and the DA8 FTS show decreases in the [HCl]/[HF], [$ClONO_2$]/[HF] and [O_3]/[HF] ratios (Figure 6.8). Although there are differences in the individual column ratios between the observations of ACE-FTS and those from two ground-based FTSs (PARIS-IR and the DA8 FTS), especially at the beginning of the campaign (February 21st to 25th, 2006), these differences are most likely due to the heterogeneous Arctic atmosphere and temporal differences in the observations. These ratios indicate that during the 2006 campaign, chlorine activation occurred over Eureka, which was inside the polar vortex in spring 2006. The deceases of $ClONO_2$ and O_3 in the Arctic stratosphere (65º N to 80º N) during the 2006 campaign were also observed by the Microwave Limb Sounder (MLS) on Aura which were shown in Figures 7 to 9 of *Santee et al.* (submitted to J. Geophs. Res.). *Santee et al.* carried out the study of the evolution of reactive and reservoir chlorine, nitric acid gas and ozone during the 2004-2005 and 2005-2006 winters in the Arctic stratosphere using the observations from the Microwave Limb Sounder (MLS) on Aura and the ACE-FTS on SCISAT-1.

HNO_3 is a major nitrogen reservoir in the atmosphere, and can be removed from the polar stratosphere by denitrification processes such as HNO_3 dissolving in sulfate aerosols [*Solomo*n 1999; *Bernath* 2001]. Denitrification occurs less frequently in the Arctic than in the Antarctic, since it requires extremely low temperatures to form PSCs (around 195 K) [*Solomon* 1999]. In exceptionally cold winters such as 2004-2005, denitrification in the Arctic was observed using ACE-FTS measurements [*Jin et al.*, 2006]. Ground-based and satellite observations suggest that denitrification also occurred near Eureka during the 2006 campaign (Figure 6.8), since the $[HNO_3]/[HF]$ ratio generally decreased. *Manney et al.* [2007] showed that in the 2005-2006 winter the meteorological conditions were very similar to those in the 2003-2004 winter, and that after a SSW the Arctic vortex quickly redeveloped and had much colder temperatures in the stratosphere compared to those in ‘normal’ winters. Chlorine deactivation is the process in which active chlorine compounds such as ClO convert to chlorine reservoir forms such as $ClONO_2$ through reactions with nitrogen dioxide (NO_2) [*Waibel et al.*, 1999; *Tabazadeh et al.*, 2000]. The amount of NO_2 can be reduced via conversion of NO_2 into HNO_3 catalyzed by aerosol surfaces. The reduction will be permanent due to the removal of the HNO_3 from the atmosphere by sedimenting PSCs particles. It results in a delay on the deactivation of chlorine compounds, and prolongs the polar ozone depletion in the stratosphere [*Solomon* 1999; *Waibel et al.*, 1999; *Tabazadeh et al.*, 2000].

Based on observations from three FTSs, the ratios of [O_3]/[HF] generally decreased during the 2006 campaign. The DA8 FTS, the only FTS providing results throughout the entire campaign, gave a value at the end of the campaign that was about 70% of the value at the beginning (Figure 6.8). This is mainly due to the combined effects of chlorine activation and denitrification, which results in the chemical removal of ozone in the Arctic atmosphere [*Solomon* 1999; *Toon et al.*, 1999; *Mellqvist et al.*, 2002]. Despite wavelike variations, the total amount of ozone also decreased by about 10% during the campaign, according to the observations of the DA8 FTS (Figure 6.4), with 1.201×10^{19} molecules/cm^2 on February 24th, 2006 and 1.087×10^{19} molecules/cm^2 on March 30th, 2006. In addition, the ozonesondes (a balloon instrument that measures ozone *in situ*) also reported a decrease of about 15% in the total amount of ozone near Eureka. According the ozonesonde measurements, the total vertical column of ozone was about 461 DU (1.240×10^{19} molecules/cm^2) on February 24th, 2006 and 391 DU (1.051×10^{19} molecules/cm^2) on March 29th, 2006. The decrease in total ozone column is less severe than the partial column of [O_3]/[HF], suggesting that dynamical effects may have mitigated the chemical loss, especially in the lower stratosphere and the troposphere where the Arctic vortex was the ill-defined [*Manney et al.*, 2007]. In a weak Arctic vortex the air is not isolated, and horizontal meridional transport might bring air masses richer in O_3 than HF from lower latitudes to the Arctic [*Toon et al.*, 1999].

6.6 Summary and Conclusions

The 2006 Canadian Arctic ACE Validation Campaign made measurements for the ACE satellite mission at PEARL, Eureka from February 17th to March 31st in 2006. The DA8 FTS and PARIS-IR observations were performed simultaneously so that instrument performance could be compared directly. The solar beam was shared between the two FTSs, and spectral co-additions were performed over the same time intervals to ensure simultaneity. From these spectra, vertical total columns and partial columns of O_3, $ClONO_2$, HCl, HNO_3, NO, NO_2, and HF were retrieved using the SFIT2 (version 3.91) program. The mean differences in vertical total columns of O_3, HNO_3, NO_2, HCl, HF, and $ClONO_2$ from the observations between PARIS-IR and the DA8 FTS are 2.84%, -1.94%, -0.08%, -3.22%, -1.45% and -4.28%, respectively. These differences can be attributed to the non-linearity of the detectors, zero levels of the observed spectra, and instrumental line shapes, together with the different spectral resolutions. Other factors have been removed by using the same analysis program, spectroscopic parameters, spectral regions, and *a priori* information to analyze the spectra recorded by PARIS-IR and the DA8 FTS.

The ground-based observations using the DA8 FTS and PARIS-IR were used to validate the observed version 2.2 results of the ACE-FTS. The results from PARIS-IR agree better with the ACE-FTS than those the DA8 FTS for all of the investigated species. This has been attributed to the better coincidence with the ACE-FTS observations, and the ground-based measurements are within 4% of partial column ratios. The differences can be explained by the heterogeneity of the Arctic atmosphere and temporal differences between the measurements.

The results from three FTSs are utilized in probing the time evolution of chemical constituents in the atmosphere over Eureka in spring 2006. Chlorine activation was evident from the decrease in $ClONO_2$ and HCl [*von Clarmann et al.*, 1993; *Oelhaf et al.*, 1994; *Solomon* 1999; *Mellqvist et al.*, 2002], and denitrification from the decrease in the amount of HNO_3 [*Solomon* 1999; *Tabazadeh et al.*, 2000; *Bernath* 2001; *Jin et al.*, 2006] was observed by ACE-FTS, PARIS-IR and the DA8 FTS. Ozone depletion during the 2006 campaign was caused by chemical removal inside the Arctic vortex over Eureka [*Manney et al.*, 2007].

6.7 References

Bassford M.R., McLinden C.A., and Strong K., (2001), Zenith-Sky Observations of Stratospheric Gases: The sensitivity of air mass factors to geophysical parameters and the influence of tropospheric clouds, *J. Quant. Spectrosc. Radiat. Transfer*, **68**, 657-677.

Bassford M.R., Strong K., McLinden C.A., and McElroy C.T. (2005), Ground-based measurements of ozone and NO_2 during MANTRA 1998 using a New Zenith-Sky spectrometer, *Atmos. Ocean.*, **43**, 325-338.

Bernath P.F., (2001), The Atmospheric Chemistry Experiment (ACE): an overview, Spectroscopy from Space, Kluwer Academic Publishers, 147-161.

Bernath P.F., McElroy C.T., Abrams M.C., Boone C.D., Butler M., Camy-Peyret C., Carleer M., Clerbaux C., Coheur P.-F., Colin R., DeCola P., DeMazière M., Drummond J.R., Dufour D., Evans W.F.J., Fast H., Fussen D., Gilbert K., Jennings D.E., Llewellyn E.J., Lowe R.P., Mahieu E., McConnell J.C., McHugh M., McLeod S.D., Michaud R., Midwinter C., Nassar R., Nichitiu F., Nowlan C., Rinsland C.P., Rochon Y.J., Rowlands N., Semeniuk K., Simon P., Skelton R., Sloan J.J., Soucy M.-A., Strong K., Tremblay P., Turnbull D., Walker K.A., Walkty I., Wardle D.A., Wehrle V., Zander R., and Zou J., (2005), Atmospheric Chemistry Experiment (ACE): Mission overview, *Geophys. Res. Lett.*, **32**, L15S01, doi:10.1029/2005GL022386.

Bernath P.F., (2006), Atmospheric Chemistry Experiment (ACE): analytical chemistry from orbit, *Trends Anal. Chem.*, **25**, 647-654.

Bird J.C., Carswell A.I., Donovan D.P., Duck T.J., Pal S.R., Whiteway J.A., and Wardle D.I., (1996), Stratospheric studies at the Eureka NDSC station using a Rayleigh/Raman differential absorption lidar, paper presented at XVIII Quadrennial Ozone Symposium-96, Univ. of L'Aquila, L'Aquila, Italy.

Boone C.D., Nassar R., Walker K.A., Rochon Y., McLeod S.D., Rinsland C.P., and Bernath P.F., (2005), Retrievals for the atmospheric chemistry experiment Fourier transform spectrometer, *Appl. Opt.*, **44**, 7218-7231.

Carli B., Alpaslan D., Carlotti M., Castelli E., Ceccherini S., Dinelli B.M., Dudhia A., Flaud J.M., Hoepfner M., Jay V., Magnani L., Oelhaf H., Payne V., Piccolo C., Prosperi M., Raspollini P., Remedios J., Ridolfi M., and Spang R., (2004), First results of MIPAS/ENVISAT with operational Level 2 code, *Adv. Space Res.*, **33**, 1012-1019.

Davies J., Tarasick D.W., McElroy C.T., Kerr J.B., Fogal P.F., and Savastiouk V., (2000), Evaluation of ECC Ozonesonde Preparation Methods from Laboratory Tests and Field Comparisons during MANTRA, *Proceedings of the Quadrennial Ozone Symposium*, Hokkaido University, Sapporo, Japan, July 3-8, 2000. Bojkov RD, Kazuo S. eds., 137-138.

Donovan D.P., Fast H., Makino Y., Bird J.C., Carswell A.I., Davies J., Duck T.J., Kaminski J.W., McElroy C.T., and Mittermeier R.L., (1997), Ozone, Column ClO, and PSC measurements made at the NDSC Eureka observatory (80°N, 86°W) during the spring of 1997, *Geophys. Res. Lett.*, **24**, 2709-2712.

Dunkerton T.J. and Delisi D.P., (1986), Envolution of potential vorticity in the winter stratosphere of January-February 1979, *J. Geophys. Res.*, **91**, 1199-1208.

Dupuy E., Walker K.A., and Kar J., Validation of ozone measurements from the Atmospheric Chemistry Experiment (ACE), (in preparation for *Atmos. Chem. Phys.*)

Fahey D.W., Kelly K.K., Kawa S.R., Tuck A.F., Loewenstein M., Chan K.R., and Heidt L.E., (1990), Observations of denitrification and dehydration in the winter polar stratospheres, *Nature*, **344**, 321-344.

Farahani E., Fast H., Mittermeier R.L., Makino Y., Strong K., McLandress C., Shepherd T.G., Chipperfield M.P., Hannigan J.W., Coffey M.T., Mikuteit S., Hase F., Blumenstock T., and Raffalski U., (2007), Nitric acid measurements at Eureka obtained in winter 2001–2002 using solar and lunar Fourier transform infrared absorption spectroscopy: Comparisons with observations at Thule and Kiruna and with results from three-dimensional models, *J. Geophys. Res.*, **112**, D01305, doi:10.1029/2006JD007096.

Fu D., Walker K.A., Sung K., Boone C.D., Soucy M-A, and Bernath P.F., (2007), The Portable Atmospheric Research Interferometric Spectrometer for the Infrared, PARIS-IR, *J. Quant. Spectrosc. Radiat. Trans.*, **103**, 362-370.

Fu D., Mittermeier R., Sung K., Walker K.A., Boone C.D., Bernath P.F., Fast H., and Strong K., Simultaneous atmospheric measurements using Fourier transform infrared spectrometers at the Polar Environment Atmospheric Research Laboratory (PEARL) during spring 2006, (in preparation for *Atmos. Chem. Phys.*).

Gallery W.O., Kneizys F.X., and Clough S.A., (1983), Air mass computer program for atmospheric transmittance/radiance calculation: FSCATM, *Environ. Res. Pap.*, **828** (AFGL-TR-83-0065), U.S. Air Force Geophysics Laboratory, Bedford, Massachusetts.

Grooß J.U. and Russell III J., (2005), Technical note: A stratospheric climatology for O_3, H_2O, CH_4, NO_x, HCl and HF derived from HALOE measurements, *Atmos. Chem. Phys.*, **5**, 2797-2807.

Harvey V.L. and Hitchman M.H. (1996), A climatology of the Aleutian high, *J. Atmos. Sci.*, **53**, 2088-2101.

Jin J.J., Semeniuk K., Manney G.L., Jonsson A.I., Beagley S.R., McConnell J.C., Rinsland C.P., Boone C.D., Walker K.A., and Bernath P.F., (2006), Denitrification in the Arctic winter 2004/2005: Observations from ACE-FTS, *Geophys. Res. Lett.*, **33**, L19814, doi:10.1029/2006GL027687.

Kalnay E., Kanamitsu M., Kistler R., Collins W., Deaven D., Gandin L., Iredell M., Saha S., White G., Woollen J., Zhu Y., Leetmaa A., Reynolds B., Chelliah M., Ebisuzaki W., Higgins W., Janowiak J., Mo K., Ropelewski C., Wang J., Jenne R., and Joseph D., (1996), The NCEP/NCAR 40-year reanalysis project, *Bull. Amer. Meteor. Soc.*, **77**, 437-471.

Kawa S.R., Newman P.A., Lait L.R., Schoeberl M.R., Stimpfle R.M., Kohn D.W., Webster C.R., May R.D., Baumgardner D., and Dye J.E., (1997), Activation of chlorine in sulfate aerosol as inferred from aircraft observations, *J. Geophys. Res.*, **102**, 3223-3226.

Kerzenmacher T.E., Walker K.A., Strong K., Berman R., Bernath P.F., Boone C.D., Drummond J.R., Fast H., Fraser A., MacQuarrie K., Midwinter C., Sung K., McElroy C.T., Mittermeier R.L., Walker J., and Wu H., (2005), Measurements of O_3, NO_2 and Temperature during the 2004 Canadian Arctic ACE Validation Campaign, *Geophys. Res. Lett.*, **32**, L16S07, doi:10.1029/2005GL023032.

Mahieu E., Zander R., Duchatelet P., Hannigan J.W., Coffey M.T., Mikuteit S., Hase F., Blumenstock T., Wiacek A., Strong K., Taylor J.R., Mittermeier R.L., Fast H., Boone C.D., McLeod S.D., Walker K.A., Bernath P.F., and Rinsland C.P., (2005), Comparisons between ACE-FTS and ground-based measurements of stratospheric HCl and $ClONO_2$ loadings at northern latitudes, *Geophys. Res. Lett.*, **32**, L15S08, doi:10.1029/2005GL022396.

Manney G.L., Daffer W.H., Strawbridge K.B., Walker K.A., Boone C.D., Bernath P.F., Kerzenmacher T., Schwartz M.J., Strong K., Sica R.J., Krüger K., Pumphrey H.C., Froidevaux L., Lambert A., Santee M.L., Livesey N.J., Remsberg E.E., Mlynczak M.G., and Russell III J.R., The high Arctic in extreme winters: vortex, temperature, and MLS and ACE-FTS trace gas evolution, *Atmos. Chem. Phys.*, **7**, 10235-10285.

Manney G.L., Zurek R.W., O'Neill A., and Swinbank R., (1994), On the motion of air through the stratospheric polar vortex, *J. Atmos. Sci.*, **51**, 2973-2994.

McElroy C.T., (1995), A spectroradiometer for the measurement of direct and scattered solar irradiance from on-board the NASA ER-2 high-altitude research aircraft, *Geophys. Res. Lett.*, **22**, 1361-1364.

McElroy C.T., Nowlan C.R., Drummond J.R., Bernath P.F., Barton D.V., Dufour D.G., Midwinter C., Hall R.B., Ogyu A., Ullberg A., Wardle D.I., Kar J., Zou J., Nichitiu F., Boone C.D., Walker K.A., and Rowlands N., (2007), The ACE-MAESTRO instrument on SCISAT: description, performance, and preliminary results, *Appl. Opt.*, **46**, 4341 – 4356.

McPherson R., Bergman K., Kistler R., Rasch G., and Gordon D., (1979), The NMC operational global data assimilation system, *Mon. Wea. Rev.*, **107**, 1445-1461.

Meier A., Goldman A., Manning P.S., Stephen T.M., Rinsland C.P., Jones N.B., and Wood S.W., (2004), Improvements to air mass calculations for ground-based infrared measurements, *J. Quant. Spectrosc. Radiat. Trans.*, **83**, 109-113.

Mellqvist J., Galle B., Blumenstock T., Hase F., Yashcov D., Notholt J., Sen B., Blavier J.F., Toon G.C., and Chipperfield M.P., (2002), Ground-based FTIR observations of chlorine activation and ozone depletion inside the Arctic vortex during the winter of 1999/2000, *J. Geophys. Res.*, **107**, doi:10.1029/2001JD001080.

Müeller R., Crutzen P.J., Grooß J.U., Brühl C., Russell J.M., and Tuck A.F., (1996), Chlorine activation and ozone depletion in the Arctic vortex: Observations by the Halogen Occultation Experiment on the Upper Atmosphere Research Satellite, *J. Geophys. Res.*, **101**, 12531-12554.

Murphy C., Bell W., Woods P., Demoulin Ph., Galle B., Mellqvist J., Arlander W., Notholt J., Goldman A., Toon G.C., Blavier J.F., Sen B., Coffey M.T., Hannigan J.W., Mankin W.G., Jones N., Griffith D., Meier A., Blumenstock T., Fast H., Mittermeier R., and Makino Y., (2001), Validation of NDSC measurements of ozone, reservoir compounds and dynamical tracers: Results of a series of side-by-side instrument intercomparisons, paper presented at 2001 Symposium, Network for the Detection of Stratospheric Change, Arcachon, France.

Oelhaf H., Clarmann T.V., Fischer H., and Friedl-Vallon F., (1994), Stratospheric $ClONO_2$ and HNO_3 profiles inside the Arctic vortex from MIPAS-B limb emission spectra obtained during EASOE, *Geophys. Res. Lett.*, **21**, 1263-1266.

Peterson D.B. and Margitan J.J., (1995), Upper atmospheric satellite correlative measurement program (UARS-CMP) balloon data atlas, NASA, Washington, DC.

Picone J.M., Hedin A.E., Drob D.P., and Aikin A.C., (2002), NRLMSISE-00 empirical model of the atmosphere: statistical comparison and scientific issues, *J. Geophys. Res.*, **107**, 1468-1483.

Pommereau J.P. and Goutail F., (1988), O_3 and NO_2 ground-based measurements by visible spectrometry during Arctic winter and spring, *Geophys. Res. Lett.*, **15**, 891-894.

Pougatchev N.S., Connor B.J., and Rinsland C.P., (1995), Infrared measurements of the ozone vertical distribution above Kitt Peak, *J. Geophys. Res.*, **100**, 16689-16698.

Rinsland C.P., Jones N.B., Connor B.J., Logan J.A., Pougatchev N.S., Goldman A., Murcray F.J., Stephen T.M., Pine A.S., and Zander R., (1998), Northern and southern hemisphere ground-based infrared spectroscopic measurements of tropospheric carbon monoxide and ethane, *J. Geophy. Res.*, **103**, 28197-28217.

Rodgers C.D., (1976), Retrieval of atmospheric temperature and composition from remote measurements of thermal radiation, *Rev. Geophys. Space Phys.*, **14**, 609-624.

Rodgers C.D., (1990), Characterization and error analysis of profiles retrieved from remote sounding measurements, *J. Geophys. Res.*, **95**, 5587-5595.

Rodgers C.D., (2000), *Inverse methods for atmospheric sounding: Theory and practice*, World Scientific, Singapore.

Rodgers C.D. and Connor B.J., (2003), Intercomparison of remote sounding instruments, *J. Geophys. Res.*, **108**, 4116, doi: 10.1029/2002JD002299.

Rothman L.S., Jacquemart D., Barbe A., Benner C., Birk M., Brown L.R., Carleer M.R., Chackerian Jr.C., Chance K., Coudert L.H., Dana V., Devi V.M., Flaud J.M., Gamache R.R., Goldman A., Hartmann J.M., Jucks K.W., Maki A.G., Mandin J.Y., Massie S.T., Orphal J., Perrin A., Rinsland C.P., Smith M.A.H., Tennyson J., Tolchenov R.N., Toth R.A., Vander J., Varanasi P., and Wagner G., (2005), The HITRAN 2004 molecular spectroscopic database, *J. Quant. Spectrosc. Rad. Transfer.*, **96**, 139-204.

Russell J.M., Gordley L.L., Deaver L.E., Thompson R.E., and Park J.H., (1994), An overview of the Halogen Occultation Experiment (HALOE) and preliminary results, *Adv. Space Res.*, **14**, 13-20.

Santee M.L., MacKenzie I.A., Manney G.L., Chipperfield M.P., Bernath P.F., Walker K.A., Boone C.D., Froidevaux L., Livesey N.J., and Waters J.W., (2007): A study of stratospheric chlorine partitioning based on new satellite measurements and modeling, submitted to *J. Geophys. Res.*

Savasktiouk V. and McElroy C.T., (2005), Brewer spectrophotometer total ozone measurements made during the 1998 Middle Atmosphere Nitrogen Trend Assessment (MANTRA) campaign, *Atmos. Ocean.*, **43**, 315–324.

Solomon S., (1999), stratospheric ozone depletion: a review of concepts and history, *Rev. Geophys.*, **37**, 275-315.

SPARC, SPARC Assessment of Upper Tropospheric and Stratospheric Water Vapour, pp. 312, Stratospheric Processes and their Role in Climate, WCRP-113, WMO-TD No 1043, SPARC Report 2, Verrieres Le Buisson Cedex, 2000.

Sung K., Skelton R., Walker K.A., Boone C.D., Fu D., and Bernath P.F., (2007), N_2O and O_3 Arctic column amounts from PARIS-IR observations: Retrievals, characterization and error analysis, *J. Quant. Spectrosc. Radiat. Trans.*, **107**, 385-406.

Tabazadeh A., Santee M.L., Danilin M.Y., Pumphrey H.C., Newman P.A., Hamill P.J., and Mergenthaler J.L., (2000), Quantifying denitrification and its effect on ozone recovery, *Science*, **288**, 1407-1411.

Tilmes S., Müller R., Grooß J.U., and Russell III, J.M., (2004), Ozone loss and chlorine activation in the Arctic winters 1991–2003 derived with the tracer-tracer correlations, *Atmos. Chem. Phys.*, **4**, 2181–2213.

Toon G.C., Farmer C.B., Schaper P.W., Lowes L.L., Norton R.H., Schoeberl M.R., Lait L.R., and Newman P.A., (1992), Evidence for subsidence in the 1989 Arctic winter stratosphere from airborne infrared composition measurements, *J. Geophys. Res.*, **97**, 7963-7970.

Toon G.C., Sen B., Salawitch R., Osterman G., and Notholt J., (1999), Ground-based observations of Arctic O_3 loss during spring and summer 1997, *J. Geophys. Res.*, **104**, 26497-26510.

Toon O.B., Pinto J., Hamill P., and Turco R.P., (1986), Condensation of HNO_3 and HCl in the winter polar stratosphere, *Geophys. Res. Lett.*, **13**, 1284-1287.

von Clarmann T., Fisher H., Firedl-Vallon F., Linden A., Oelhaf H., Piesch C., and Seefeldner M., (1993), Retrieval of stratospheric O_3, HNO_3 and $ClONO_2$ profiles from 1992 MIPAS-B limb emission spectra: Method, results, and error analysis, *J. Geophys. Res.*, **98**, 20495-20506.

Walker K.A., Randall C.E., Trepte C.R., Boone C.D., and Bernath P.F., (2005), Initial validation comparisons for the Atmospheric Chemistry Experiment (ACE-FTS), *Geophys. Res. Lett.*, **32**, L16S04, doi:10.1029/2005GL022388.

Waibel A.E., Carslaw P.T., Oelhaf K.S., Wetzel H., Crutzen G., Poeschl P.J., Tsias U., Reimer A., and Fischer E.H., (1999), Arctic ozone loss due to denitrification, *Science*, **283**, 2064-2068.

Webster C.R., May R.D., Toohey D.W., and Avallone L.M., (1993), Chlorine chemistry on polar stratospheric cloud particles in the Arctic winter, *Science*, **261**, 1130-1133.

Wunch D., Taylor J.R., Fu D., Bernath P., Drummond J.R., Midwinter C., Strong K., and Walker K.A., (2007), Simultaneous ground-based observations of O_3, HCl, N_2O, and CH_4 over Toronto, Canada by three Fourier transform spectrometers with different resolutions, *Atmos. Chem. Phys.*, **7**, 1275–1292.

Chapter 7

Summary and Future Work

This work has investigated the concentrations of O_3, HNO_3, NO_2, NO, HCl, $ClONO_2$, HF, $COCl_2$, O_2, CO_2, CH_4 retrieved from measurements by satellite-borne, balloon-borne or ground-based Fourier Transform Spectrometers (FTSs) in order to study several important atmospheric science topics such as ozone depletion and global warming. The results have been reported, have been submitted or will be submitted for publication in the scientific literature [*Fu et al.*, 2007a; 2007b; 2007c; 2007d].

Chapter 1 presented an overview of the observations carried out using FTSs and the basic principles used in the retrieval of concentrations of atmospheric gases from spectra with a focus on ground-based observations. The characteristic features of three types of platforms (satellite-based, balloon-borne, ground-based), four types of viewing geometries (solar occultation, nadir viewing, glint viewing, ground-based solar viewing), six measurement sites (Waterloo, Kitt Peak, Eureka, Toronto, Kiruna, Vanscoy), and five FTSs used in the measurements are introduced in Chapter 2.

Chapter 3 presented the first study of the global distribution of atmospheric phosgene and discussed reasons for the observed distribution pattern. The study was carried out using solar occultation measurements from a total of 5614 measured profiles from the satellite-borne Atmospheric Chemistry Experiment FTS (ACE-FTS) spanning the period February 2004 through May 2006. In addition, comparisons between observations from the ACE mission and previous measurements made in 1980s and 1990s were carried out. The phosgene concentrations measured by the ACE-FTS display a zonally symmetric pattern with the maximum concentration located approximately over the equator, at about 25 km in altitude, and decreasing towards the poles. A layer of enhanced concentration of phosgene spans the lower stratosphere at all latitudes, with volume mixing ratios of 20 to 60 pptv. The distribution pattern of atmospheric phosgene has been attributed to the insolation, the lifetime of phosgene and the Brewer-Dobson circulation. The observations from ACE-FTS show lower phosgene concentrations than were obtained from previous observations in the 1980s and 1990s. This is due to a significant decrease in the chlorinated hydrocarbon source species. Discrepancies in the results between current model predictions and observations made by ACE-FTS and the JPL MkIV spectrometer were noted. Improvements in chemical transport model calculations are needed to improve our understanding of the evolution of atmospheric phosgene.

Portable Atmospheric Research Interferometric Spectrometer for the Infrared (PARIS-IR) is a copy of the ACE-FTS that was designed for ground-based and balloon-borne measurements. Chapter 4 presented the PARIS-IR configuration used for its first balloon flight as a part of the Middle Atmosphere Nitrogen TRend Assessment (MANTRA) 2004 balloon payload. Useful engineering information, detailing the thermal performance of the instrument during the flight, was obtained from this balloon campaign. As part of the MANTRA 2004 program, a ground-based inter-instrument comparison campaign was carried out with the goals of assessing instrument performance, and evaluating data processing routines and retrieval codes. Based on the results from the inter-comparison campaign, PARIS-IR provides measurements of similar quality for stratospheric species as obtained from the University of Toronto FTS. For future balloon flights, a new solar tracker system must be built for PARIS-IR. The new tracker system must be able to direct sunlight into the PARIS-IR instrument independently without input from the balloon payload pointing system. To verify the performance of this new tracker system, sufficient pre-flight tests are recommended.

The goals of Chapter 5 were to investigate the suitable spectral resolution, spectral ranges, spectroscopic parameters and the optical components for a possible future satellite mission called Carbon Cycle science by Fourier Transform Spectroscopy (CC-FTS). The CC-FTS mission will improve our understanding of the sources and sinks of greenhouse gases in the Earth's atmosphere by monitoring total and partial columns of CO_2, CH_4, N_2O, and CO in the near infrared. The molecular O_2 column density will also be measured to obtain the effective optical path of each measurement and will be used to normalize the column densities of the other gases. To achieve these goals, ground-based Fourier transform spectra recorded at Kiruna, Kitt Peak, and Waterloo were used in the investigations. Dry air volume mixing ratios of CO_2 and CH_4 were retrieved from ground-based observations. Based on these results, a Fourier transform spectrometer with a spectral resolution of 0.1 cm^{-1}, operating between 2000 and 15000 cm^{-1}, is suggested as the primary instrument for the mission. Deficiencies in the spectroscopic parameters of the investigated greenhouse gases were noted during this study. Recently, *Devi et al.* [2007] made improvements in the CO_2 spectroscopic parameters for the 6348 cm^{-1} band by considering line mixing and by using speed-dependent Voigt line shape functions. By improving the spectroscopic parameters (as was done in the work by *Devi et al.* [2007]), it is possible to obtain precisions of ~0.3 % in remote sensing measurements of CO_2. New laboratory measurements to improve the spectroscopic line parameters are required to improve the atmospheric retrievals for CH_4, O_2 and CO_2 (in spectral regions other than 6348 cm^{-1} band).

Chapter 6 presented atmospheric observations made with PARIS-IR, ACE-FTS and the Eureka DA8 FTS at the Polar Environment Atmospheric Research Laboratory (PEARL) from from February 17th to March 31st, 2006 during the 2006 Canadian Arctic ACE Validation Campaign. Mean differences in vertical total columns of O_3, HNO_3, NO_2, HCl, HF, and $ClONO_2$ obtained from PARIS-IR and DA8 FTS measurements are 2.84%, -1.94%, -0.08%, -3.22%, -1.45% and -4.28%, respectively. For all of the species investigated, the results from PARIS-IR agreed better with the ACE-FTS than did those from the DA8 FTS. Chorine activation and denitrification in the Arctic atmosphere were observed by the three FTSs in the extremely cold stratosphere near Eureka, Nunavut, Canada. The observed ozone depletion during the 2006 campaign was attributed to chemical removal. In summer 2006, a new Bruker 125 FTS was installed at PEARL. It was used record Arctic atmospheric spectra simultaneously with PARIS-IR and DA8 FTS during the 2007 Canadian Arctic ACE Validation Campaign. A study is under way to investigate the differences in the retrieved columns from these three ground-based FTSs in order to evaluate the performance of the newly installed instrument.

References

Devi V.M., Benner D.C., Brown L.R., Miller C.E., and Toth R.A., (2007), Line mixing and speed dependence in CO_2 at 6348 cm^{-1}: positions, intensities and air- and self-broadening derived with constrained multispectrum analysis, *J. Mol. Spectrosc.*, **242**, 90-117.

Fu D., Walker K.A., Sung K., Boone C.D., Soucy M-A, and Bernath P.F., (2007a), The Portable Atmospheric Research Interferometric Spectrometer for the Infrared, PARIS-IR, *J. Quant. Spectrosc. Radiat. Trans.*, **103**, 362-370.

Fu D., Boone C.D., Bernath, P.F., Walker K.A., Nassar R., Manney G.L., and S.D. McLeod (2007b), Global phosgene observations from the Atmospheric Chemistry Experiment (ACE) mission, Geophys. Res. Lett., **34**, L17815, doi:10.1029/2007GL029942.

Fu D., Sung K., Walker K.A., Boone C.D., and Bernath P.F., (2007c), Ground-based solar absorption studies for the Carbon Cycle science by Fourier Transform Spectroscopy (CC-FTS) mission, Submitted to *J. Quant. Spectrosc. Radiat. Trans.*

Fu D., Mittermeier R., Sung K., Walker K.A., Boone C.D., Bernath P.F., Fast H., and Strong K., (2007d), Simultaneous atmospheric measurements using Fourier transform infrared spectrometers at the Polar Environment Atmospheric Research Laboratory (PEARL) during spring 2006, in preparation for *Atmos. Chem. Phys.*